Università degli Studi di Torino

UNIVERSITÀ
DI TORINO

Scuola di Scienze della Natura
Dipartimento di Fisica

Ph.D. Thesis

Unveiling the (anti-)hypertriton properties with ALICE at the LHC

Francesco Mazzaschi

Supervisor Prof. Massimo Masera

Co-supervisor Dott. Maximiliano Puccio

30 May, 2023

CERN-THESIS-2023-095
30/05/2023

Francesco Mazzaschi
Unveiling the (anti-)hypertriton properties with ALICE at the LHC
Ph.D. Thesis, 30 May, 2023
Supervisors: Prof. Massimo Masera and Dott. Maximiliano Puccio

Università degli Studi di Torino
Scuola di Scienze della Natura
Dipartimento di Fisica
Via P.Giuria, 1 - 10125 Torino

Abstract

A Large Ion Collider Experiment (ALICE) is one of the four experiments installed at the CERN Large Hadron Collider (LHC). ALICE was designed and built to study a phase of the matter called Quark Gluon Plasma, which is formed in heavy-ion collisions at ultra-relativistic energies. The extreme energy densities reached in hadronic collisions at the LHC lead to a significant production of baryonic states. Among the thousands of particles produced, light (anti-)hypernuclei are of special interest. Indeed, the study of their internal structure represents a direct probe to investigate the strong interaction among hyperons and the ordinary matter.

This thesis project is focused on the study of the properties of the lightest known hypernucleus, the hypertriton ($^{3}_{\Lambda}\mathrm{H}$) which is a bound state of a proton, a neutron and a Λ. The most precise measurements to date of the $^{3}_{\Lambda}\mathrm{H}$ lifetime and Λ separation energy are performed by exploiting the large Pb–Pb data sample collected by ALICE during 2018. The $^{3}_{\Lambda}\mathrm{H}$ signal is extracted for the first time with a machine learning technique, allowing for a significant improvement in the discrimination between signal and background. The combined measurements confirm that the $^{3}_{\Lambda}\mathrm{H}$ is a loosely bound state with a large wave function radius extending up to $\sim$ 5 fm.

In the second part of this thesis, the first measurement of the $^{3}_{\Lambda}\mathrm{H}$ production in p–Pb collisions is presented. Given the large spread of its wave function, the measured $^{3}_{\Lambda}\mathrm{H}$ yield in p–Pb collisions is a sensitive observable to test the nucleosynthesis in hadronic collisions and is a powerful tool for discriminating between different production models of nuclei. The $^{3}_{\Lambda}\mathrm{H}$ signal is extracted again with a machine learning approach, leading to a significance higher than 4 σ. The value of the yield favours a coalescence model to describe the nucleosynthesis, demonstrating that the $^{3}_{\Lambda}\mathrm{H}$ wave function directly influences its nuclear production mechanism in hadronic collisions.

In the last part of this thesis a new algorithm for tracking the $^{3}_{\Lambda}\mathrm{H}$ and fully reconstruct its decay topology is presented: this method relies on the high granularity of the upgraded Inner Tracking System of ALICE, installed for the Run 3 of the LHC. Finally, the possibility to characterise the properties of $A \geq 4$ hypernuclei with the proposed NA60+ experiment is discussed, using the $^{5}_{\Lambda}\mathrm{He}$ as a use case.

Contents

1 High Energy Nuclear Physics 1
- 1.1 Quantum Chromodynamics . . . 1
- 1.2 Quark Gluon Plasma . . . 4
- 1.3 Heavy-Ion Collisions . . . 7
  - 1.3.1 The collision geometry . . . 7
  - 1.3.2 Collision evolution . . . 9
- 1.4 Signatures of the QGP in heavy-ion collisions . . . 11
  - 1.4.1 Hard probes . . . 12
  - 1.4.2 Electroweak probes . . . 12
  - 1.4.3 Soft probes . . . 13

2 Hypertriton 17
- 2.1 Hypernuclei . . . 17
  - 2.1.1 Probing the core of neutron stars . . . 19
- 2.2 Hypertriton properties . . . 20
  - 2.2.1 Decay channels of the $^{3}_{\Lambda}$H . . . 21
  - 2.2.2 $^{3}_{\Lambda}$H structure . . . 22
- 2.3 Production of (anti-)(hyper-)nuclei at the LHC . . . 24
  - 2.3.1 Statistical Hadronization Models . . . 25
  - 2.3.2 Coalescence Models . . . 29
  - 2.3.3 $^{3}_{\Lambda}$H production in small systems . . . 32

3 A Large Ion Collider Experiment 35
- 3.1 The Large Hadron Collider . . . 35
- 3.2 The ALICE detector . . . 38
  - 3.2.1 The Inner Tracking System . . . 39
  - 3.2.2 The Time Projection Chamber . . . 41
  - 3.2.3 V0 system . . . 41
- 3.3 Data acquisition and reconstruction in ALICE . . . 42
  - 3.3.1 Trigger system . . . 42
  - 3.3.2 Event reconstruction . . . 43
  - 3.3.3 Particle identification . . . 47
  - 3.3.4 Centrality determination . . . 47
  - 3.3.5 ALICE offline software . . . 49

4 Machine learning 51
4.1 Supervised learning 51
  4.1.1 Receiver Operating Characteristic 52
4.2 Boosted Decision Trees 54
  4.2.1 XGBoost 55
  4.2.2 Tuning the BDT 56
  4.2.3 Feature importance 58

5 Precision measurements of the ${}^{3}_{\Lambda}\mathrm{H}$ lifetime and B_{Λ} 59
5.1 Data sample 59
  5.1.1 Event selection 59
  5.1.2 Monte Carlo 62
5.2 ${}^{3}_{\Lambda}\mathrm{H}$ (${}^{3}_{\overline{\Lambda}}\overline{\mathrm{H}}$) reconstruction 64
  5.2.1 Track selection 64
  5.2.2 Decay vertex reconstruction 64
5.3 ${}^{3}_{\Lambda}\mathrm{H}$ selection with machine learning 68
  5.3.1 Training sample 69
  5.3.2 Training and testing of the BDT 73
  5.3.3 Application to data 76
5.4 Signal extraction 79
  5.4.1 Probing the mass shaping effect 83
5.5 Measurement of $\tau_{{}^{3}_{\Lambda}\mathrm{H}}$ 83
  5.5.1 Absorption correction 84
  5.5.2 Lifetime determination 85
  5.5.3 Systematic uncertainties 87
5.6 Measurement of B_{Λ} 92
  5.6.1 Systematic uncertainties 94
5.7 Final results 97
  5.7.1 Testing the CPT symmetry 98

6 First measurement of ${}^{3}_{\Lambda}\mathrm{H}$ production in p–Pb collisions 103
  6.0.1 Monte Carlo sample 104
6.1 ${}^{3}_{\Lambda}\mathrm{H}$ (${}^{3}_{\overline{\Lambda}}\overline{\mathrm{H}}$) reconstruction 105
  6.1.1 Training and testing of the BDT 108
  6.1.2 Choice of the BDT threshold 109
6.2 Measurement of ${}^{3}_{\Lambda}\mathrm{H}$ production in p–Pb collisions 112

7 New avenues in hypernuclear physics 123
7.1 Tracking hypernuclei with ALICE 123
  7.1.1 Upgrade of the ITS 123
  7.1.2 The ${}^{3}_{\Lambda}\mathrm{H}$ matching algorithm 126
7.2 Heavier hypernuclei with NA60+ 128
  7.2.1 Production of ${}^{5}_{\Lambda}\mathrm{He}$ 131

8 Conclusions 135

9 Appendix 139
9.1 Blast-Wave distribution 139
9.2 Maxwell-Boltzmann distribution 139
9.3 Transverse momentum and mass exponential distributions 140

Bibliography 141

1

High Energy Nuclear Physics

Strong interaction is one of the four fundamental forces. It is responsible to keeep bound the protons and neutrons inside nuclei, and quarks inside nucleons. The High Energy Nuclear Physics (HENP) was born to investigate the behaviour of the strong interactions and the constituents of the hadronic matter under extreme temperatures and energy densities. In such conditions, quarks can not bind together and a peculiar state of matter, called Quark Gluon Plasma (QGP), is formed. Such a plasma, consisting of free quarks and gluons, existed for a fleeting moment at the birth of the Universe, about 1 microsecond after the Big Bang [1][2]. This type of primordial matter can be recreated in the laboratory through ultra-relativistic heavy-ion collisions. The theory underlying HENP is the subject of this chapter. In the following, the natural units are used, thus: $\hbar = c = k_b = 1$.

1.1 Quantum Chromodynamics

The necessity to have a theoretical framework capable to explain the large particle zoo observed between the 1950s and 1960s led to the development of a new model proposed independently by Gell-Mann[3] and Zweig[4][5] in 1964. Such a model, which is one of the foundations of the current Standard Model (SM), was based on the assumption that hadrons are bound states of finer constituents called quarks. Under this assumption, Gell-Mann and Zweig were able to explain for the first time the large amount of particle discoveries, and to predict the existence of the Ω baryons starting from three quark families (u, d, s). Nevertheless, despite the phenomenological success, the original quark model could not explain the discovery of the Δ^{++} hadron, which should have been forbidden due to the Pauli principle. The only way to solve this issue was to introduce a new quantum number, the colour charge [6], as an additional degree of freedom. The resulting extended Quark Model successfully predicted a modification in the ratio R [7], defined as the interaction cross section of electron and positron going into hadrons and going into muon pairs:

$$R = \frac{\sigma(e^+e^- \to hadrons, s)}{\sigma(e^+e^- \to \mu^+\mu^-, s)} = n_c \sum Q_f \tag{1.1}$$

where n_c is the number of possible colour charges, Q_f is the electric charge of the quark family f, and s is the available energy in the centre of mass frame. The

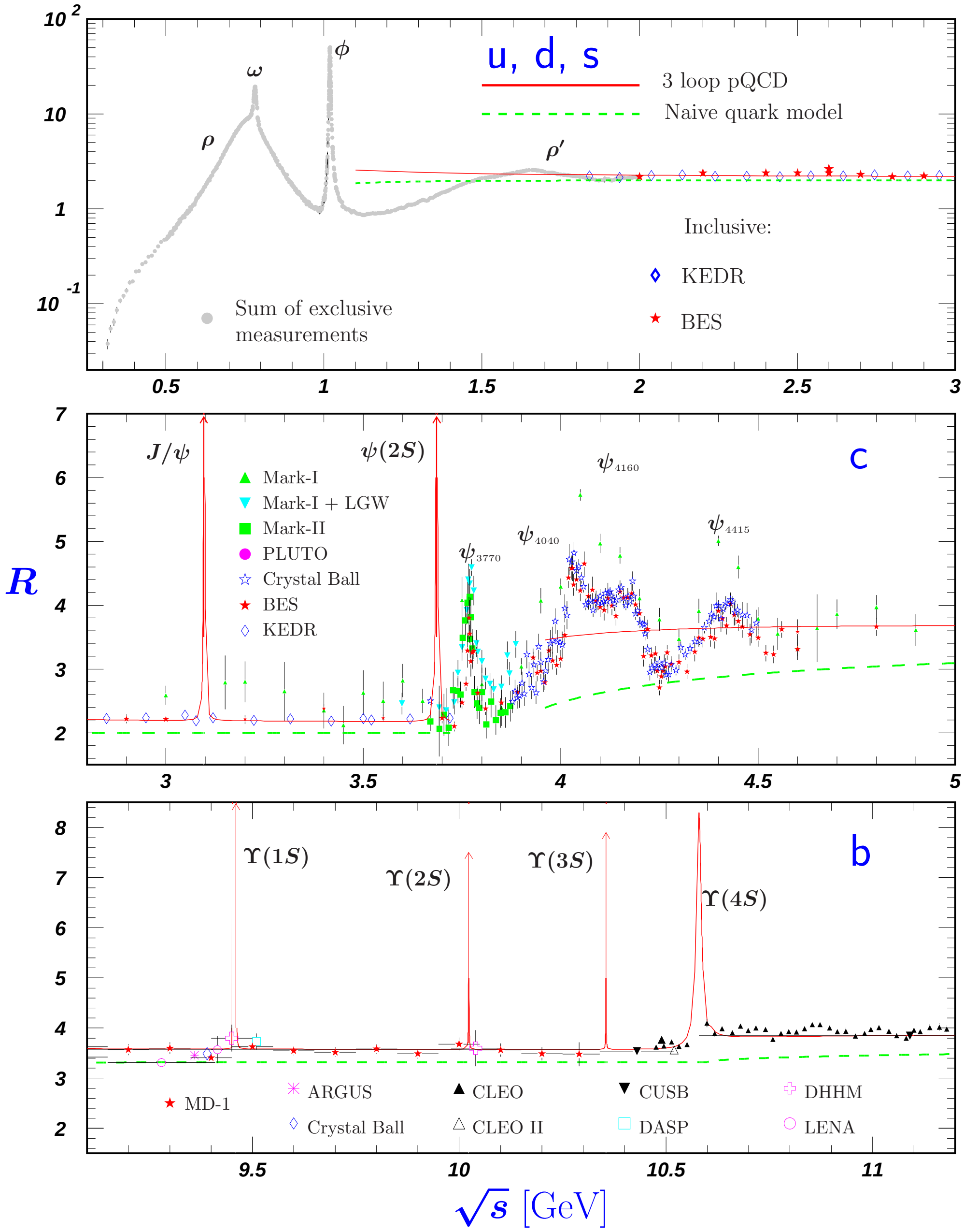

Fig. 1.1: R ratio as a function of the $\sqrt{s}$ of the collision between electron and positron [7]. The three pads correspond to three different regions of $\sqrt{s}$: the top pad shows the region of the u, d and s quarks resonances, the middle one the region of the c quark resonances and the bottom one the region of the b quark resonances. It is possible to observe how the ratio changes value when new flavours are available. The observed ratio fits with the Quark Model expectations with 3 quarks (green line). The red line shows how the Quark Model predictions are refined taking into account loop corrections in perturbation theory

experimental results shown in Fig. 1.1 confirm the prediction of the extended quark model, and the number of different colours turned out to be $n_c = 3$.

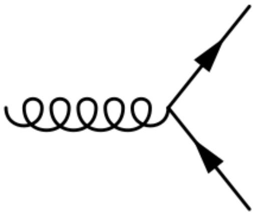

Fig. 1.2: Quark-gluon interaction vertex

All these experimental results and a systematical theoretical effort led in few years to the development of the Quantum Chromodynamics (QCD), which is nowadays the theory describing the strong interactions. In QCD, quarks represent the fundamental matter constituents which carry colour charge in three different colours: red, blue, green. Gluons act as exchange bosons of the interaction in analogy to virtual photons mediating the electromagnetic interaction in QED. There are six different quark flavours: the light flavours u (up), d (down), and s (strange) with masses in the MeV/c^2 regime and the heavy flavours c (charm), b (beauty), t (top), with masses ranging from few to hundreds GeV/c^2. QCD is a non-Abelian quantum gauge theory that postulates the invariance of its Lagrangian under local SU(3) group transformations. The QCD Lagrangian[8] can be written as:

$$\mathcal{L}_{\mathrm{QCD}} = \bar{\psi}(i\gamma^{\mu} D_{\mu} - m)\psi - \frac{1}{4} G^{a}_{\mu\nu} G^{\mu\nu}_{a} \tag{1.2}$$

with:

$$D_{\mu} = \partial_{\mu} - i g_s A^{a}_{\mu} \lambda_a. \tag{1.3}$$

$$G^{a}_{\mu\nu} = \partial_{\mu} A^{a}_{\nu} - \partial_{\nu} A^{a}_{\mu} + g_s f^{abc} A^{b}_{\mu} A^{c}_{\nu}. \tag{1.4}$$

In these equations λ_a are the Gell-Mann matrices, g_s is the strong interaction coupling constant, $A(x)$ is the gluon field and f^{abc} are the $SU(3)$ group structure constants. The first term of the Lagrangian describes the interaction between quarks and gluons in analogy with the Quantum Electrodynamics (QED) interaction vertices, as shown in Fig. 1.2: The second term of the Lagrangian describes two new interaction vertices with respect to the QED theory. Since $SU(3)$ is non-Abelian, the f_{abc} structure constants are not null, and the additional term $g_s f^{abc} A^{b}_{\mu} A^{c}_{\nu}$ represents new gluon-gluon vertices, as sketched in Fig. 1.3:

In QED the intensity of the electromagnetic interaction is ruled by the QED coupling constant. At small values of Q^2 its value is $\alpha \approx 1/137$, and it weekly increases with Q^2 because of the effects of the vacuum polarization. On the contrary in QCD the

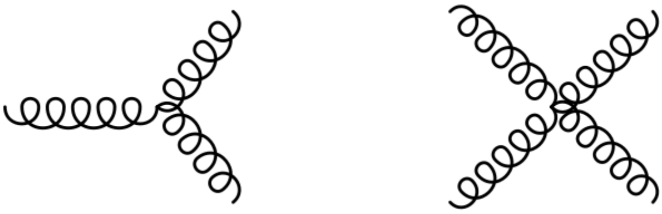

Fig. 1.3: Gluon-gluon interaction vertices

self-interaction processes lead to an opposite and steeper trend as a function of Q^2. The evolution of α_s in terms of the transferred momentum is given by the following equation:

$$\alpha_s(Q^2) = \frac{\alpha_s(\mu^2)}{1 + \alpha_s(\mu^2)(33 - 2\,n_f)\ln(Q^2/\mu^2)} \tag{1.5}$$

where n_f is the number of quark families and μ is the mass scale of the renormalization, which cannot be determined by the theory. The value of α_s decreases with increasing Q^2; at low Q^2 (long distances) α_s diverges, and it is not possible to describe the strong interaction by using a perturbative field theory (pQCD). The equation 1.5 can be arranged in terms of the parameter Λ_{QCD} which represent the energy limit for using a perturbative approach:

$$\alpha_s(Q^2) = \frac{12\pi}{(33 - 2\,n_f)\ln(Q^2/\Lambda_{\mathrm{QCD}})} \tag{1.6}$$

The figure 1.4 shows α_s as a function of Q^2 in different experimental conditions. For $Q^2 > 100$ GeV a_s is small, quarks in hadrons are weakly bound and can be treated as free particles: this behaviour is called asymptotic freedom. For small Q^2 values, α_s increase rapidly and quarks are strongly bound in hadrons, and they cannot be separated.

1.2 Quark Gluon Plasma

As described in the previous section, one of the most peculiar behaviour of the running coupling constant is the confinement of the quark matter into colour neutral hadrons. Nevertheless, under extreme high temperatures or densities it is possible to create a new phase of matter where quarks and gluons become free and are not localized in individual hadrons. Hence, a phase diagram of the QCD matter can be defined by employing observables from thermodynamics, such as the temperature (T) and the chemical potential (μ_B). Figure 1.5 shows the phase diagram predicted by the QCD theory and the values of T and μ_B. At high temperatures it is possible to

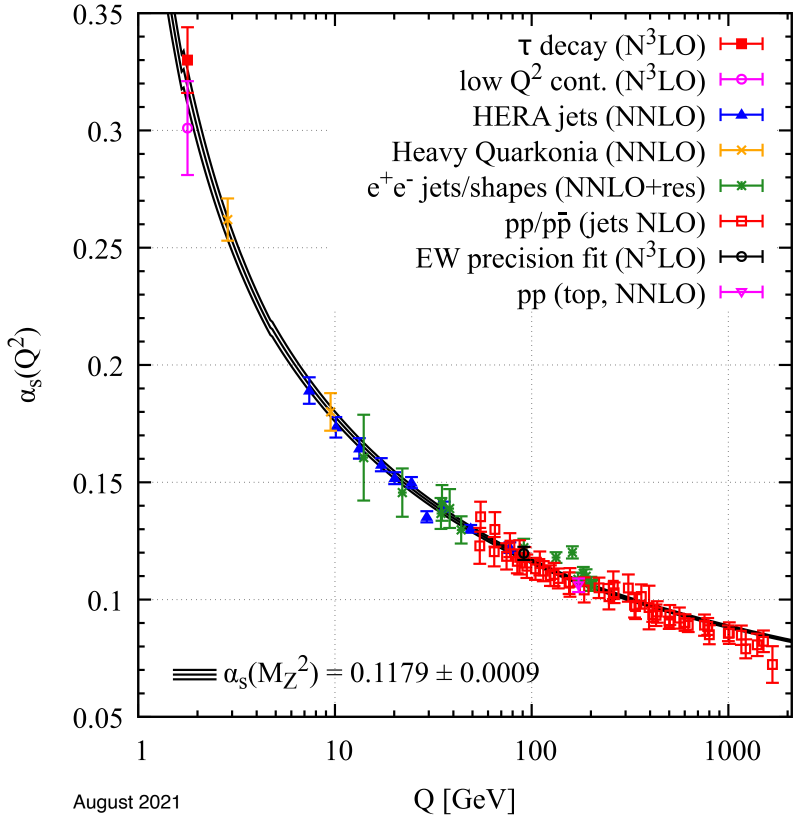

Fig. 1.4: Values of α_s in different experimental conditions [9–12] as a function of the transferred momentum, taken from [13]. The reference value at the energy scale of the Z boson mass $\alpha_s(M_Z)$ has been evaluated using the χ^2 averaging method.

create the QCD region where quarks and gluons are deconfined. This new phase of the matter has been called Quark Gluon Plasma (QGP) [14, 15].

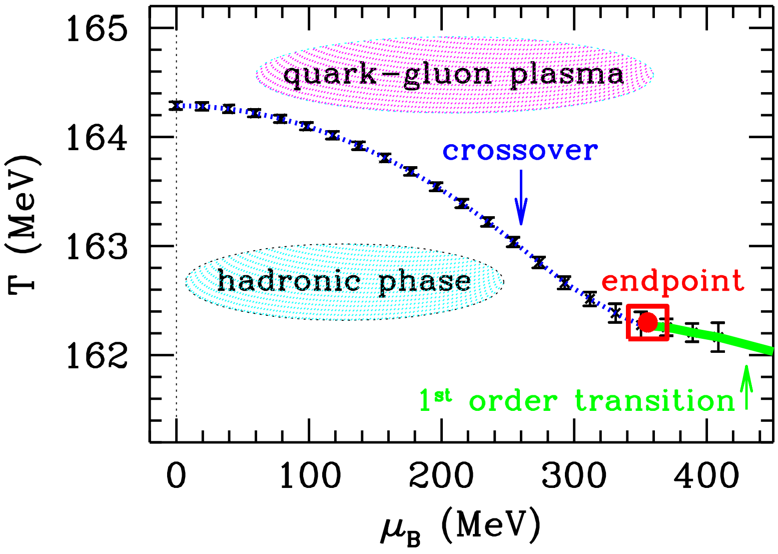

Fig. 1.5: Phase diagram of the QCD matter, taken from [16].

Looking at Fig. 1.5, the origin of the diagram corresponds to the QCD vacuum, while the ordinary nuclear matter is located at around $T = 0$ and $\mu_B \approx 1$ GeV. Moving along the T axis, for $\mu_B = 0$ and T $\approx$ 200 MeV a continuous crossover transition from hadron gas to QGP occurs in conditions that are expected be close to those existing in the primordial Universe. On the contrary, moving along the μ_B axis, for $T = 0$ and $\mu_B \approx$ 2 GeV theoretical models predict a phase transition to a colour superconductive deconfined state. This state has been hypothesized to be present in the core of neutron stars [17]. According to [18], in the early Universe the crossover transition happened from the QGP phase to hadronic matter at $\mu_B \sim$ 0.33 eV, caused by the QGP expansion and the consequent cooling.

In order to reproduce such extreme conditions in the laboratory one has first to create a system characterized by an extreme energy density. This can be done by colliding heavy ions at relativistic energies. A simple but powerful description of the energy density required to create the QGP can be performed by considering a system composed by massless quarks and gluons confined in a finite volume V [19], the MIT bag model. The energy density ϵ and pressure p under these approximations is described by the equation of state of an ideal gas:

$$p = \frac{\pi^2}{90} n_{DF} T^4, \epsilon = 3p \tag{1.7}$$

where n_{DF} is the number of degrees of freedom of the system and T is the temperature. This simple model foresees a sharp pressure increase in the first order transition from hadron gas, where $n_{DF} = 3$, to QGP where $n_{DF} = \left(16 + \frac{21}{2} n_f\right)$. A similar trend is also observed for more sophisticated calculations, such as the Hadron Resonance Gas Model [21] and the lattice QCD one [20], as shown in Fig. 1.6.

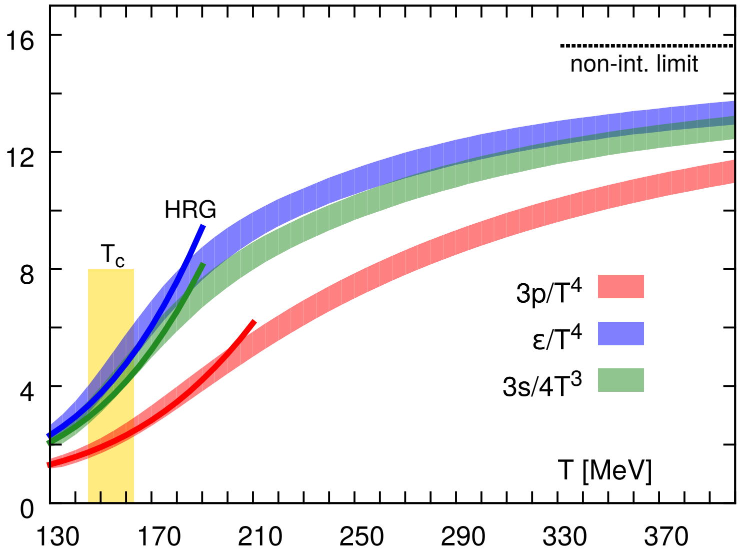

Fig. 1.6: QCD equation of state [20] as predicted by the Hadron Resonance Gas model and Lattice QCD calculations.

All the currently available QCD calculations, at vanishing or finite μ_B, predict a cross-over transition to the Quark Gluon Plasma at a pseudo-critical temperature (T_c) around 150 MeV and energy density around 1 GeV/fm^3.

1.3 Heavy-Ion Collisions

Collisions of relativistic heavy ions provide the only tool to probe matter at such high temperatures and densities in the laboratory. The first experiment of heavy-ion collisions (HIC) was performed in the 70s at the Lawrence Berkeley National Laboratory and the nuclei were accelerated at $\approx 2\ \mathrm{GeV/nucleon}$ while the first observation of a new phase of the nuclear matter (QGP) was announced at the CERN SPS in Pb-Pb central collisions at $\approx 17.3\ \mathrm{GeV/nucleon}$ [22]. Nowadays, there are two hadron colliders that carry out a HIC experimental programme: the Relativistic Heavy-Ion Collider(RHIC) at the Brookhaven National Laboratory (BNL) [23] and the Large Hadron Collider (LHC) at CERN. In addition, there are currently two accelerators with a heavy-ion physics programme at fixed target: the SuperProton Syncrotron (SPS) at CERN and the Schwerionensynchrotron (SIS) at the Gesellschaft für Schwerionenforschung (GSI).

1.3.1 The collision geometry

Thousands of particles are created when two nuclei at ultra-relativistic energy collide head-on, generating a physics event that has very complex features if compared to a proton-proton one. Over the years many models were developed in order to estimate relevant quantities in nucleus-nucleus interactions such as the impact parameter (b), the number of participating nucleons (N_{part}) or binary nucleon-nucleon collisions (N_{coll}). One of the simplest but most effective models is the Glauber model [24], which describes the collision geometry as an incoherent superposition of nucleon-nucleon interactions, as sketched in Fig. 1.7.

The model assumptions are called *Optical limit* and consist in:

- Nucleons are independent point-like objects inside nuclei.
- Protons and neutrons are subject only to the hadronic interaction: they are not distinguishable.
- Nuclei are not deflected after the collision.
- The nucleon-nucleon cross section always remains the same during all the overlapping process.

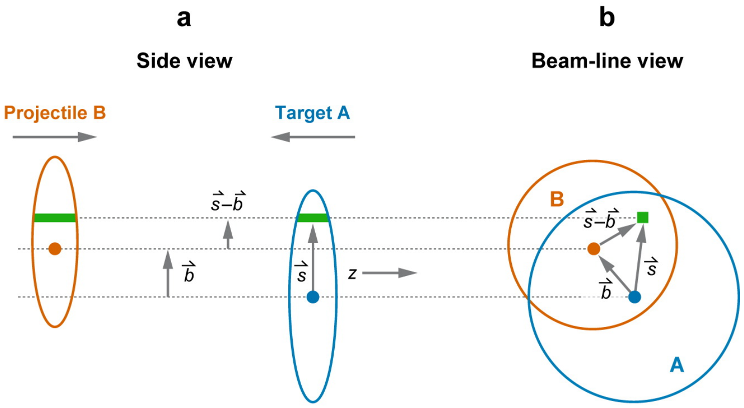

Miller ML, et al. 2007.
Annu. Rev. Nucl. Part. Sci. 57:205–43

Fig. 1.7: A sketched representation of the heavy-ion collision geometry, taken from [25]

Defining the *Thickness function* $T(\vec{s})$ as the probability to find a nucleon in the unit transverse area located at $\vec{s}$ in Fig. 1.7, given its probability density $\rho(\vec{s}, z)$:

$$T(\vec{s}) = \int \rho(\vec{s}, z)dz \tag{1.8}$$

the nuclear overlapping function can be written as:

$$T_{AB}(\vec{b}) = \int T_A(\vec{s})\, T_B(\vec{s} - \vec{b})\, d^2s \tag{1.9}$$

The input nucleon probability density is usually described by a Woods-Saxon distribution [26]:

$$\rho(r) = \frac{\rho_0}{1 + e^{(r-r_0)/\delta}} \tag{1.10}$$

where ρ_0 represents the density in the centre of the nucleus, δ is a length representing the surface thickness or skin depth of the nucleus, and r_0 is the nuclear radius. Starting from these quantities and the nucleon-nucleon cross section σ_{inel} the probability of having *n* binary collisions between the nuclei A and B, having A and B nucleons respectively, can be computed using the binomial statistics:

$$p_{AB} = \sum_{n=1}^{AB} P(n, b) = 1 - [1 - T_{AB}(\vec{b})\, \sigma_{inel}]^{AB} \tag{1.11}$$

The total nucleus-nucleus cross section σ_{tot} can be obtained by integrating the probability to observe at least one nucleon-nucleon collision p_{AB}:

$$p_{AB} = \sum_{n=1}^{AB} P(n, b) = 1 - [1 - T_{AB}(\vec{b})\, \sigma_{inel}]^{AB} \tag{1.12}$$

$$\sigma_{tot} = \int_0^\infty 2\pi\, b\, db\, [1 - [1 - T_{AB}(\vec{b})\, \sigma_{inel}]^{AB}] \tag{1.13}$$

The mean number of collisions N_{coll} is estimated as the mean value of the binomial distribution in eq. 1.11:

$$N_{\text{coll}}(b) = \sum_{n=1}^{AB} n\, P(n,b) \;= AB\, T_{AB}\, \sigma_{inel}. \tag{1.14}$$

Similarly, N_{part} can be obtained by integrating over $\vec{s}$ the contribution of the two nuclei:

$$N_{\text{part}}(b) = \int d^2s\, \{A\, T_A(\vec{s})[1-(1-T_B(\vec{b}-\vec{s})\, \sigma_{inel})^B] + B\, T_B(\vec{b}-\vec{s})[1-(1-T_A(\vec{s})\, \sigma_{inel})^A]\} \tag{1.15}$$

The last two equations show that Glauber model allows us to extract relevant parameters of a heavy-ion collision as a function of the impact parameter b, such as N_{part} and N_{coll}, starting from the knowledge of $\rho(z,\vec{s})$ and σ_{inel}. The main drawback of this model is that it uses continuous density functions for quantities that are discrete in nature, and hence fluctuate event by event. More refined estimates of N_{part} and N_{coll} are obtained with Glauber Monte Carlo (GMC) Models [25], where the colliding nuclei geometry is generated by distributing their nucleons in the space according to their nuclear density functions. A random impact parameter is then drawn from the distribution $d\sigma/db = 2\pi b$. Finally, the nuclei collision is treated as a sequence of independent binary nucleon-nucleon collisions. In the simplest version of the Monte Carlo approach, a nucleon-nucleon collision takes place if the distance of the nucleons d in the plane orthogonal to the beam axis satisfies $d \leq \sqrt{\sigma_{inel}/\pi}$. As shown in Fig. 1.8, as the nucleon-nucleon cross section becomes more point like, the optical and GMC cross sections converge to the same values, while for high input σ_{inel} the former overshoots the estimated nucleus–nucleus inelastic cross section. The value of σ_{inel} at $\sqrt{s_{\text{NN}}}$ = 5.02 TeV (the energy of the latest ALICE Pb–Pb sample) is obtained by interpolating pp data at different centre-of-mass energies and results to be $\sigma_{inel} = 70 \pm 5$ mb [27].

1.3.2 Collision evolution

The QGP formation and expansion is characterized by a complex evolution in space-time. The evolution of the collision, as shown in Fig. 1.9, is characterized by five different phases which can be described as follows [28]:

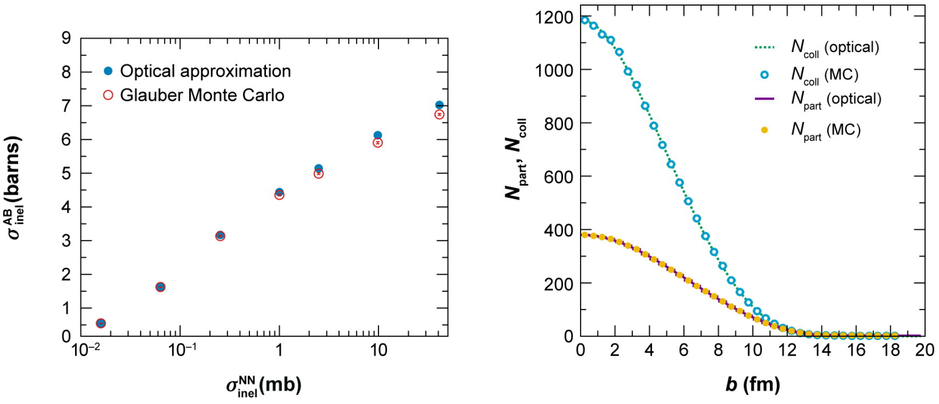

Miller ML, et al. 2007.
Annu. Rev. Nucl. Part. Sci. 57:205–43

Fig. 1.8: (Left) The total cross section, calculated in the optical approximation and with a Glauber Monte Carlo (MC) both with identical nuclear parameters as a function of σ_{inel}, the inelastic nucleon-nucleon cross section. (Right) N_{coll} and N_{part} as a function of impact parameter, calculated in the optical approximation (lines) and with a Glauber Monte Carlo (symbols).

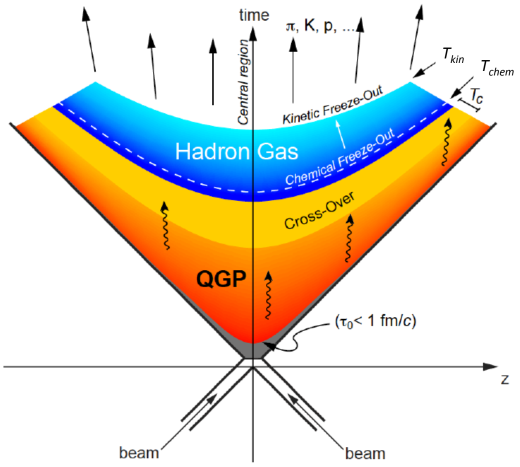

Fig. 1.9: Evolution of the fireball with from QGP formation to the hadronization phase.

- **Collision**: before the collision, the nuclei are Lorentz contracted ($\gamma \approx 2700$ at the LHC), and the overlap lasts for a very short time: $\tau_c = 2R/\gamma \approx 0.004\ fm/c$.

- **Pre-Equilibrium**: this is the phase characteristic of the hard processes (high Q^2) between colliding quarks. The constituent partons of nuclei undergo several interactions, losing their energy in the mid-rapidity region and escaping at forward rapidities. The obtained system at mid-rapidity is a hot and interacting medium with an almost null μ_{B}, the QGP. The particles are produced at a time τ_f that can be estimated using the Heisenberg uncertainty principle $\tau_f \approx \frac{\hbar}{m_{\mathrm{T}}}$ where $m_{\mathrm{T}} = \sqrt{m^2 + p_{\mathrm{T}}^2}$ is the transverse mass and p_{T} is the momentum in the transverse plane of the collision. The mean value of m_{T} is calculated starting from the rapidity distribution of the particles produced and their transverse energy E_T:

$$m_\mathrm{T} = \frac{dE_\mathrm{T}/dy}{dN/dy} \tag{1.16}$$

where rapidity y is defined as:

$$y = \frac{1}{2}\log(\frac{E+p_z}{E-p_z}) \tag{1.17}$$

At the LHC $\tau_f \approx 0.1\ fm/c$. In heavy-ion collisions at RHIC and LHC the energy densities can be inferred by using the Bjorken approximation described in [29] leading to the values of $\epsilon \sim 5.4 \mathrm{GeV}/\mathrm{fm}^3$ and $\epsilon \sim 15 \mathrm{GeV}/\mathrm{fm}^3$ respectively. These values are much higher than the one required to reach the phase transition (computed in Sec. 1.2), such that the formation of the QGP state is expected.

- **Quark Gluon Plasma**: after the particle production the medium reaches the thermal equilibrium at a time τ_{eq}. If the temperature of the system approaches $T_C \approx$ 150 MeV the medium undergoes the phase transition from hadron gas to QGP. At the LHC, τ_{eq} is estimated to be $\approx 0.3\ fm/c$.

- **Hadronization**: when the plasma expands under the thermal pressure gradients generated at the system boundaries and cools down another phase transition occurs ($\tau \approx 10\ fm/c$ at LHC): quarks and gluons hadronize and baryons, mesons and nuclei are produced. After the possible mixed phase the system appears as a gas of hadrons.

- **Freeze out**: When the particle densities are too low to permit inelastic scatterings the abundance of different hadronic species is fixed. This condition is called *chemical freeze-out*. At a certain point ($\tau \geq 15\ fm/c$ at LHC) also elastic scatterings cease and the particle momentum spectra are defined: this condition is named kinetic freeze-out.

1.4 Signatures of the QGP in heavy-ion collisions

Due to its short lifetime, a direct observation of the QGP is impossible. However, during the last decades numerous experimental evidences of the QGP have been observed in different experiments at SPS, RHIC, and at the LHC. In this section, few signatures of the QGP will be outlined briefly. Three different kinds of probes have been exploited to study the QGP, each of them is sensitive to different frames of the QGP evolution: hard probes, electroweak probes, and soft probes.

1.4.1 Hard probes

Hard probes represent an important tool to investigate the properties of the QGP, as they are produced in the early stages after the collision, where high exchanges of momentum take place. As the system evolves and the energy density decreases, hard probes can no longer be produced. Since these processes involve high transferred Q^2, they can be studied by using the pQCD. When such hard processes occur, either gluons and quarks with high momentum or heavy-flavoured quarks (charm and beauty) are created. Since hard probes can be produced only in the first stages of the collision, they experience the evolution dynamics of the medium. Hence, hard probes permit us to investigate the parton propagation and the energy loss in the QGP. Finally quarks and gluons produced in the early stages of the collision hadronize, bringing to the formation of open heavy-flavoured particles, quarkonia and jets. Open heavy-flavoured particles are hadrons composed of a heavy quark (c or b) and light quarks (d, u or s), such as D and B mesons. Similarly, quarkonia are hadrons formed by a quark and an anti-quark with the same flavour such as the J/Ψ ($\mathrm{c\bar{c}}$). Jets are instead narrowly collimated bunches of hadrons. The effects of the energy loss in the QGP and the dynamics of heavy-quark hadronization can be studied with the comparison of the transverse-momentum differential production yields in nucleus-nucleus collisions with those obtained in pp collisions, in which QGP is not expected to form. The difference is typically quantified with the help of the nuclear modification factor, R_{AA}, defined as:

$$R_{AA} = \frac{1}{N_{coll}} \frac{d^2N_{AA}/(dydp_{\mathrm{T}})}{d^2N_{pp}/(dydp_{\mathrm{T}})} \tag{1.18}$$

The latest measurements of D mesons R_{AA} from ALICE [30, 31] are shown in Fig. 1.10. The R_{AA} trends are well described by theoretical calculations of charm-quark transport and energy loss in a hydrodynamically expanding QGP. Two additional evidences of the QGP formation, which will only be mentioned here, are the observation of quarkonia [32, 33] and jets suppression [34, 35] due to the interaction with the medium.

1.4.2 Electroweak probes

Electroweak probes are particles that carry no colour charge, such as leptons, photons, Z and $\mathrm{W}^{\pm}$ bosons. Since at the extreme energy-density characterizing HIC all the interactions but the strong one are negligible, the electroweak probes are not affected by the presence of the medium, and they carry direct information about the initial state of the collision. For this reason, no modification of the production spectra of these particles is foreseen in HIC. The CMS Collaboration measurements of the Z boson R_{AA} in Pb–Pb collisions at $\sqrt{s_{\mathrm{NN}}} = 2.76$ TeV [34] and $\sqrt{s_{\mathrm{NN}}} = 5.02$

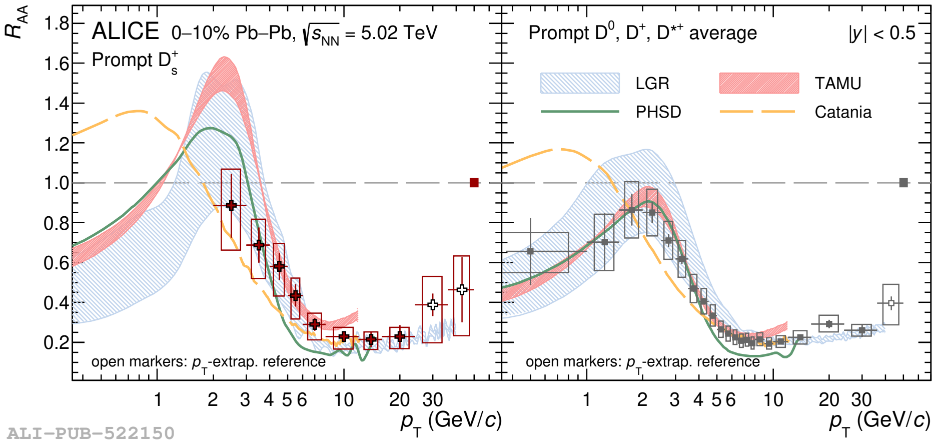

Fig. 1.10: Nuclear modification factor R_{AA} from [30, 31] of prompt D_s^+ mesons (left panel) and non-strange D mesons (right panel) in the 0–10% centrality interval in Pb–Pb collisions at $\sqrt{s_{\mathrm{NN}}} = 5.02$ TeV compared with theoretical calculations based on charm-quark transport in a hydrodynamically expanding QGP. The boxes represent the total systematic uncertainties. The colour bands represent the theoretical uncertainty when available.

TeV [36] confirm the expected behaviour, since the R_{AA} is compatible with unity. Furthermore, the study of direct photon (i.e. photons not coming from hadron decays) production is particularly interesting because thermal photons are emitted by the QGP, and are therefore sensitive to the medium temperature. However, thermal photons can not be distinguished from direct photons coming from other sources and all direct photons must be studied together. The first measurement of direct-photon production in Pb–Pb collisions performed by the ALICE collaboration can be found in [37]: the direct photon production spectra follow the trend indicated by the models including effects of the QGP formation.

1.4.3 Soft probes

Soft probes are low momentum hadrons representing the majority of the particles produced in a collision ($\approx 99\%$). They are produced in the latest stages of the collision, when the energy density of the system is highly degraded and therefore their study can be performed only with non-perturbative QCD techniques. A strong signature of the QGP can be observed by looking at the transverse momentum distributions of low momentum hadrons. Assuming a Boltzmann-Gibbs distribution for the particle emission at kinetic freeze-out, the particle spectra for the species i can be modelled as:

$$\frac{1}{m_{\mathrm{T}}}\frac{\mathrm{d}^2 N_i}{\mathrm{d}m_{\mathrm{T}}\mathrm{d}y} \propto e^{-\frac{m_{\mathrm{T}}}{T_{slope}}} \tag{1.19}$$

where T_{slope} is a fit parameter. Taking into account only the thermal component of the spectra and assuming a common emission temperature, the spectra of all

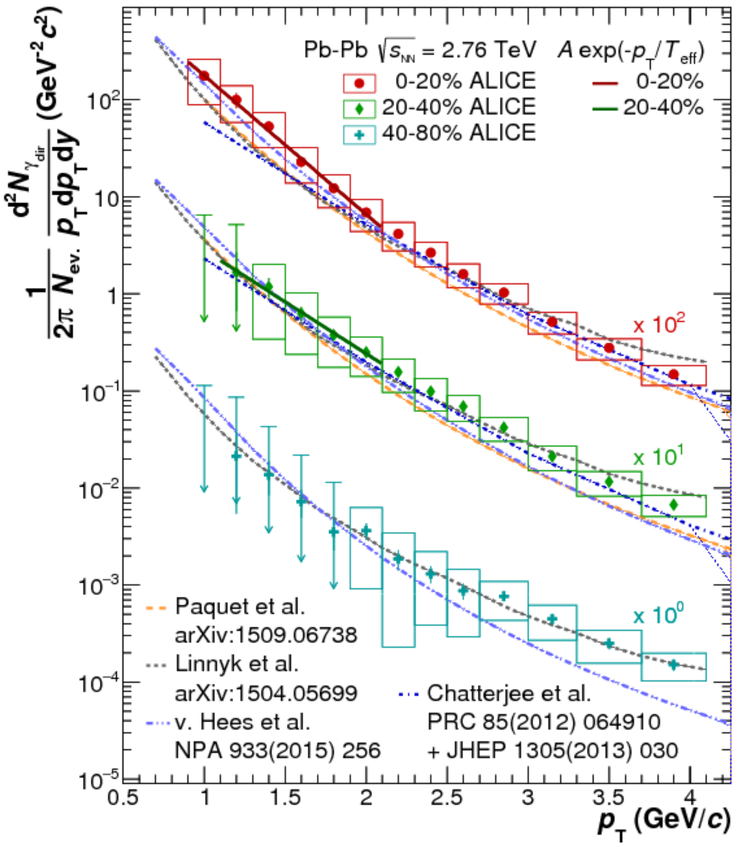

Fig. 1.11: Comparison of model calculations with the direct photon spectra in Pb–Pb collisions at $\sqrt{s_{\mathrm{NN}}}$ = 2.76 TeV for the 0–20% (scaled by a factor 100), the 20–40% (scaled by a factor 10) and 40–80% centrality classes. All models include a contribution from pQCD photons. For the 0–20% and 20–40% classes the fit with an exponential function is shown in addition

the particle species should have the same slope. This simple prediction, called m_{T} scaling, has not been observed in HIC at RHIC [38] and LHC [39, 40] energies, where different T_{slope} have been extracted for different particle species. In particular, as shown in Fig. 1.12, the slope of the spectra decreases with the mass of the particle. The breaking of the m_{T} scaling can be explained by adding a component to the measured temperature for each particle species:

$$T_{slope} = T_{kin} + \frac{1}{2} m \langle v_{\perp} \rangle^2 \tag{1.20}$$

where T_{kin} is the temperature at kinetic freeze–out and the additional term keeps into account the mean kinetic energy acquired by the particles of the species i due to a collective expansion along the transverse plane. This behaviour has been called radial flow, and it is well described by hydrodynamical calculations describing the QGP expansion (HKM [41], Krakow [42]).

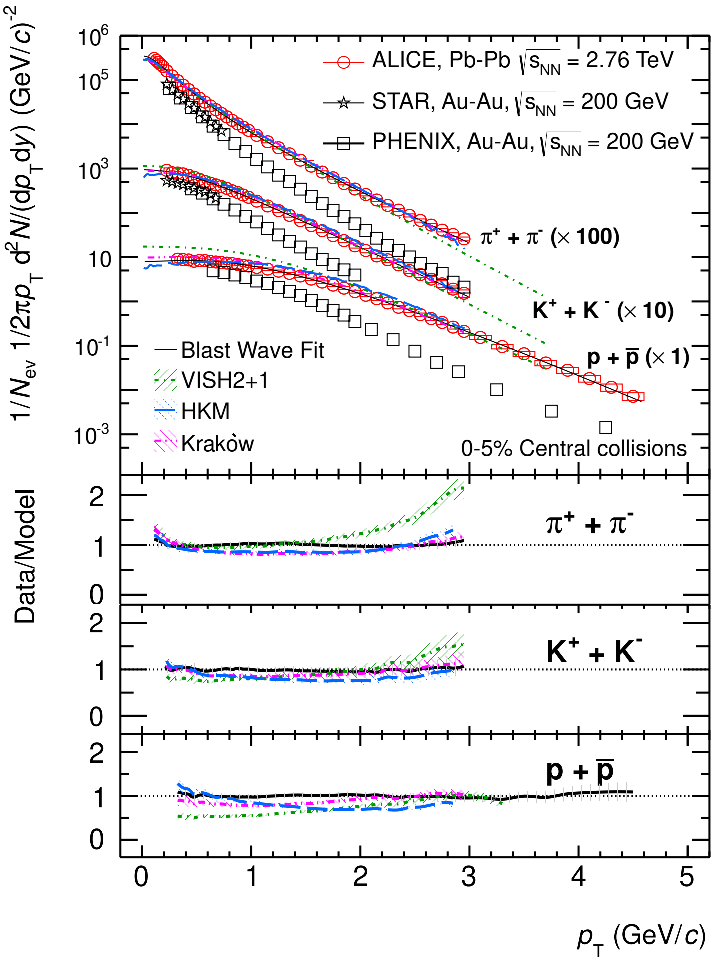

Fig. 1.12: Transverse momentum distributions of the sum of positive and negative particles (box: systematic errors; statistical errors smaller than the symbol for most data points), fitted individually with a blast wave function, compared to RHIC data and hydrodynamic models.

Another evidence of the QGP can be observed by studying eventual azimuthal anisotropies in the particle production spectra. In particular, in a collision between two nuclei overlapping only partially, a correlation between the emission angles of the particles and the impact parameter can be found. Such behaviour can be studied by looking at the azimuthal (ϕ) anisotropies of the particle spectra employing a Fourier decomposition of the azimuthal distribution $\frac{dN}{d\phi}$:

$$\frac{dN}{d\phi} \approx 1 + 2\sum_{n=1}^{\infty} v_n \cos(n(\phi - \psi_N)) \tag{1.21}$$

where v_n is the Fourier coefficient and ψ_N is the azimuthal angle of the reaction plane. The presence of an expanding QGP medium translates the initial geometrical anisotropy into strong pressure gradients parallel to the plane defined by the beam direction and the impact parameter vector. The flow of particles created by these pressure gradients is called elliptic flow, and it contributes to the second coefficient of the Fourier expansion of Eq. 1.21 (v_2). A measurement of the v_2 performed by ALICE [43] is shown in Fig. 1.13 and it is in agreement with hydrodynamical computation. Furthermore, from this comparison it is possible to extract relevant parameters of the medium such as the shear viscosity over entropy η/s, the bulk viscosity over entropy ζ/s and its lifetime.

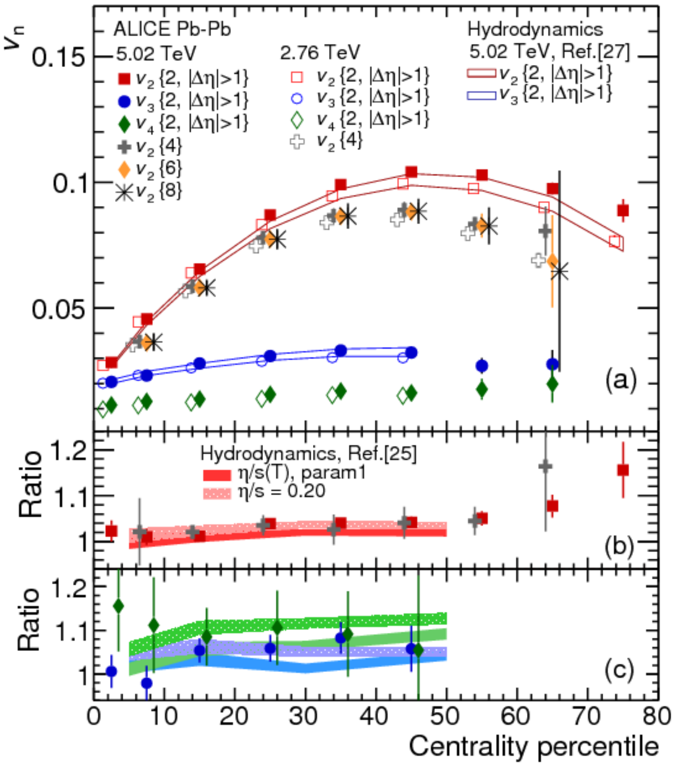

Fig. 1.13: Anisotropic flow v_n integrated over the p_{T} range $0.2 < p_{\mathrm{T}} < 5.0$ GeV/, as a function of event centrality. Measurements for Pb–Pb collisions at $\sqrt{s_{\mathrm{NN}}} = 5.02$ (2.76) TeV are shown by solid (open) markers. The ratios of v_n (green) between Pb–Pb collisions at 5.02 TeV and 2.76 TeV, are shown in the lower panels. Various hydrodynamic calculations are also presented, showing a good agreement with data for low ζ/s values. The statistical and systematical uncertainties are summed in quadrature.

Finally, hadrochemistry, the study of particle species abundances, is a fundamental tool for understanding the mechanisms driving hadron production. This contributes to shed light on the latest stages of the collision, when the chemical and kinematic freeze–out occur. Hadron and nuclei synthesis at the LHC, both from experimental and theoretical point of view, will be discussed in the next chapter.

Hypertriton

2

Among the thousands of particles produced at the LHC in all collision systems, hypernuclei represent one of the most exotic and interesting objects. Hypernuclei were first observed in cosmic rays in 1953 [44] and are formed by a mix of protons, neutrons and unstable baryons containing strange quarks called hyperons. After almost 70 years since their discovery, hypernuclei are still a source of fascination for nuclear physicists since their production is very rare and the measurement of their properties is extremely challenging. The lightest hypernucleus, the hypertriton ($^{3}_{\Lambda}$H), is formed by a proton, a neutron and a Λ hyperon, and it is the main focus of this thesis. In the following, the main properties of the $^{3}_{\Lambda}$H, as well as its tight connections with the astro-nuclear physics, will be discussed. Finally, our current understanding on the $^{3}_{\Lambda}$H production mechanisms in high-energy hadronic collisions will be presented.

2.1 Hypernuclei

Hypernuclei are bound states of non-strange and strange baryons. The only hypernuclei observed so far contain a Λ or a Σ baryon inside, but future experiments will be able to access more rare hypernuclei composed by Ξ and Ω baryons. The discovery of the lightest hypernucleus, the hypertriton ($^{3}_{\Lambda}$H), was published in 1952 by the Polish physicists Marion Danysz and Jerzy Pniewski [44]. Their event, first reported at a meeting of the Polish Academy of Sciences in October 1952, was observed in a balloon-flown, 600 μm thick, glass-backed Ilford G5 emulsion plate. With the innovation of stacks of stripped emulsion pellicles the first complete event of $^{3}_{\Lambda}$H was reported in the following year [45]. The observed decay channel, the one studied in this thesis, is: $^{3}_{\Lambda}\mathrm{H} \rightarrow ^{3}\mathrm{He} + \pi^{-}$, and the event is shown in Fig. 2.1

Since then, a dedicated hypernuclear programme has started and many hypernuclei have been observed, up to the $^{208}_{\Lambda}$Pb [46], allowing for the extension of the nuclear chart to a third dimension, the strangeness one. The reason why a complete characterization of the hypernuclear chart is so important is that hypernuclei represent a unique experimental probe for studying the interaction between strange and non-strange baryons (Y–N), which is still poorly known. This is not only interesting per se, but it gives us insights on the core of neutron stars, as it will be shown in the

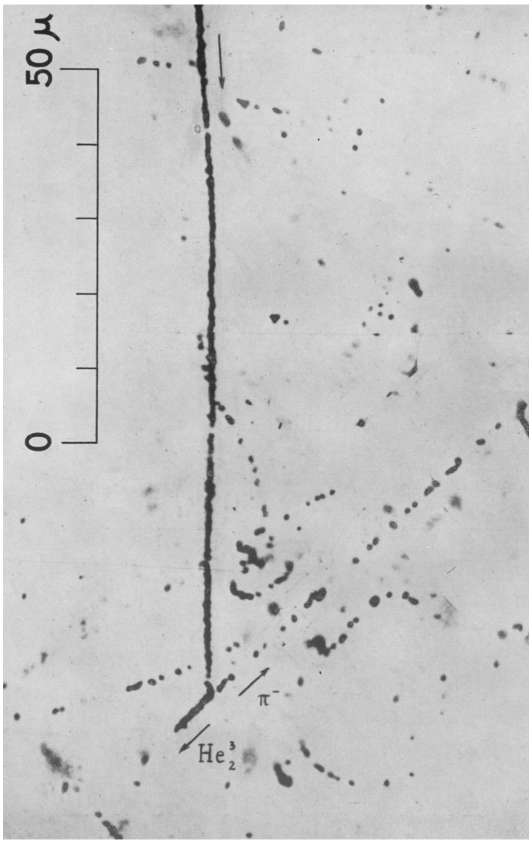

Fig. 2.1: The first observation of the ${}^3_\Lambda$H two-body charged decay channel ${}^3_\Lambda\mathrm{H} \rightarrow {}^3\mathrm{He} + \pi^-$, reported by Bonetti et al. [45].

next section. After the first cosmic-rays experiments, hypernuclei have started to be produced in the laboratory with reactions producing Λ on a nuclear target, such as:

- *Strangeness exchange:* $K^- + p \rightarrow \Lambda + n$
- *Associated production:* $\pi^+ + n \rightarrow \Lambda + K^+$
- *Photo- or electro-production:* $\gamma + p \rightarrow \Lambda + n$, or $e^- + p \rightarrow e^- + \Lambda + n$.

This second generation of hypernuclear experiments allowed for the determination of the energy level of nearly all p-shell Λ-hypernuclei both by γ-ray spectroscopy from the decay of low-lying excited states and by missing-mass measurements with magnetic spectrometers at KEK (SKS), JLab (Hall A and Hall C) and LNF-INFN (FINUDA) [47, 48]. Finally, hypernuclei have been studied in the third generation of experiments, which study the production of hypernuclei in high-energy hadronic collisions. As it will be outlined in the next sections, measuring hypernuclei at accelerators provides a unique opportunity to study the properties of these exotic objects and its counterparts, the anti-hypernuclei, as well as to

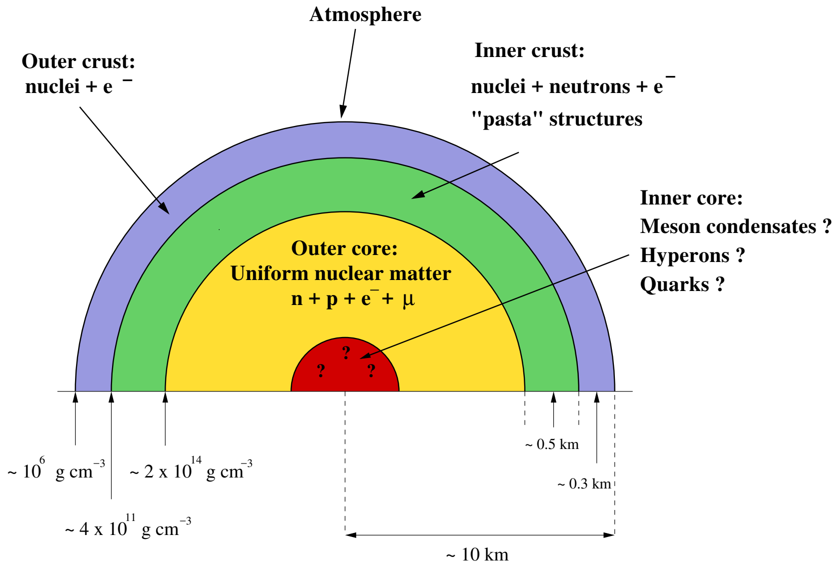
Atmosphere
Outer crust:
nuclei + e⁻
Inner crust:
nuclei + neutrons + e⁻
"pasta" structures
Inner core:
Meson condensates ?
Hyperons ?
Quarks ?
Outer core:
Uniform nuclear matter
n + p + e⁻ + μ
? ? ?
~ 10⁶ g cm⁻³
~ 2 x 10¹⁴ g cm⁻³
~ 4 x 10¹¹ g cm⁻³
~ 0.5 km
~ 0.3 km
~ 10 km

Fig. 2.2: Schematic representation of the internal structure of a neutron star, taken from [49].

understand the nucleosynthesis in the hot and dense matter created in high-energy hadronic collisions.

2.1.1 Probing the core of neutron stars

Neutron stars (NSs) are unique objects to test the fundamental properties of matter under extreme conditions of density, isospin asymmetry and temperature. NSs are among the densest objects in the Universe, with a density of about 10^{14} g/cm^3 and a radius of about 10 km, and they are supported mainly by the neutron degeneracy pressure [49]. Nevertheless, the expected densities span over a wide range as the internal structure can be described as an onion-like, as sketched in Fig. 2.2.

Due to the high value of density at the centre of a NS and the rapid increase of the nucleon chemical potential with density, the appearance of hyperons is energetically favourable in the inner core of the NSs. The creation of hyperons in NSs has been hypothesized for the first time in [50], and after that many authors have studied theoretically the phenomenon with different techniques [51–53]. These approaches agree that hyperons may appear in the inner core of neutron stars, as the nucleon chemical potential is large enough to make the conversion of nucleons into hyperons energetically favourable. This conversion should relieve the Fermi pressure of the system: the equation of state (EoS) of the NSs with and without hyperons is shown in the left panel of Fig. 2.3. The lower pressure due to the presence of hyperons is usually referred to as the "softening" of the EoS. The softer the EoS, the lower is the maximum mass a NS can reach, as shown in the right panel of Fig. 2.3. Hence, the formation of high-mass NSs should be inhibited by the presence of hyperons in

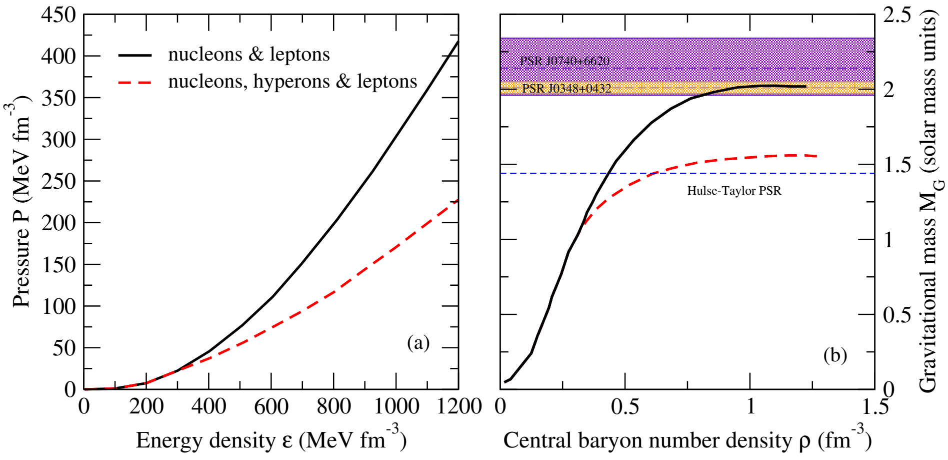

Fig. 2.3: Left panel: the equation of state of a NS with hyperons (red) and without hyperons (black). Right panel: the NSs mass as a function of the central baryon number density with hyperons (red) and without hyperons (black). The mass of the Hulse-Taylor pulsar and the observed PSR J1614-2230 [54] and PSR J0348+0432 [55] are shown with horitzontal lines and bands.

the inner core. This is incompatible with the observation of NSs heavier than two solar masses [54, 55], constituting what is referred to as the NSs "hyperon puzzle". Many attempts were made to solve this puzzle, e.g. by introducing three-body forces leading to an additional repulsion that can counterbalance the large gravitational pressure and allow for larger star masses [56, 57]. Ultimately, to constrain the parameter space of such models, a detailed knowledge of the Y–N interaction and of the three-body Y–N–N interaction is mandatory. Numerous particle correlation analyses [58, 59] directly contribute to the determination of such interactions. In a complementary approach, the lifetime and the binding energy of a hypernucleus reflect the strength of the Y–N interaction [60], and their measurement can be exploited to constrain the Y–N potential and significantly contributing to the solution of the hyperon puzzle.

2.2 Hypertriton properties

As mentioned in the previous section, the hypertriton ($^{3}_{\Lambda}$H) is the lightest hypernucleus, being composed by a proton, a neutron and a Λ hyperon. Due to its light mass, $^{3}_{\Lambda}$H is the most abundant hypernucleus produced in high-energy hadronic collisions. While the first observation of $^{3}_{\Lambda}$H was made in the early 50s [44], the discovery of its counterpart, the antihypertriton ($^{3}_{\bar{\Lambda}}\overline{\mathrm{H}}$), has been achieved only in 2010 at the Relativistic Heavy-Ion Collider (RHIC) by the STAR Collaboration [61].

In the following section, the main properties of the $^{3}_{\Lambda}$H will be discussed, such as its decay channels, binding energy and its lifetime.

2.2.1 Decay channels of the ${}^{3}_{\Lambda}\mathrm{H}$

A Λ hypernucleus in the ground state can decay with two different mechanisms: non-mesonic (NMWD) and mesonic (MWD) weak decays. While the former decay mode is predominant for A $>$ 5 hypernuclei, the latter is by far the dominant process for the ${}^{3}_{\Lambda}\mathrm{H}$ [62]. In the NMWD, the hypernucleus decays through processes which involve a weak interaction of the Λ with one or more core nucleons N. When the pion emitted in $\Lambda \rightarrow p + \pi^{-}$ reaction is virtual, it can be absorbed by the nuclear medium, resulting in a non-mesonic decay as:

$$\Lambda N \rightarrow NN. \tag{2.1}$$

In the MWD, Λ hyperon decays into a nucleon and a pion inside the nuclear medium, following the weak decay mode in the free space:

$$\Lambda \rightarrow p + \pi^{-}, \tag{2.2}$$

or

$$\Lambda \rightarrow n + \pi^{0}. \tag{2.3}$$

The most complete calculation of MWD (Γ_{MWD}) and NMWD (Γ_{NMWD}) rates is presented in [60]. In this paper, the authors compute Γ_{MWD} and Γ_{NMWD} starting from the ${}^{3}_{\Lambda}\mathrm{H}$ wave function and solving the ${}^{3}_{\Lambda}\mathrm{H}$ three-body Faddeev equations, which describe all the possible interactions in a system of three particles in a fully quantum mechanical formulation. The equations are solved by employing realistic NN and Y-N interactions. The results are listed in Table 2.1: it is worth noting that the six MWD channels are not independent, but according to the empirical $\Delta I = 1/2$ rule [63], the following ratios for decay rates result:

$$\frac{\Gamma({}^{3}_{\Lambda}\mathrm{H} \rightarrow {}^{3}\,\mathrm{He} + \mathrm{pi}^{-})}{\Gamma({}^{3}_{\Lambda}\mathrm{H} \rightarrow {}^{3}\,\mathrm{H} + \mathrm{pi}^{0})} = \frac{\Gamma({}^{3}_{\Lambda}\mathrm{H} \rightarrow \mathrm{p} + \mathrm{d} + \mathrm{pi}^{-})}{\Gamma({}^{3}_{\Lambda}\mathrm{H} \rightarrow \mathrm{n} + \mathrm{d} + \pi^{0})} \frac{\Gamma({}^{3}_{\Lambda}\mathrm{H} \rightarrow \mathrm{p} + \mathrm{p} + \mathrm{n} + \mathrm{pi}^{-})}{\Gamma({}^{3}_{\Lambda}\mathrm{H} \rightarrow \mathrm{p} + \mathrm{n} + \mathrm{n} + \mathrm{pi}^{0})} = 2. \tag{2.4}$$

From Tab. 2.1, one can compute the branching ratio for the decay channel analysed in this work, i.e. the decay of the ${}^{3}_{\Lambda}\mathrm{H}$ into a ${}^{3}\mathrm{He}$ and a π^{-}: $\mathrm{B.R.}({}^{3}_{\Lambda}\mathrm{H} \rightarrow {}^{3}\,\mathrm{He} + \pi^{-}) \simeq 0.25$. Finally, the total decay width $\Gamma_{{}^{3}_{\Lambda}\mathrm{H}}$ can be expressed in terms of the hypertriton lifetime $\tau_{{}^{3}_{\Lambda}\mathrm{H}}$ as:

$$\Gamma_{{}^{3}_{\Lambda}\mathrm{H}} = \frac{\hbar}{\tau_{{}^{3}_{\Lambda}\mathrm{H}}} \tag{2.5}$$

where $\hbar$ is the reduced Planck constant equal to $6.582 \times 10^{16}\mathrm{eV} \cdot \mathrm{s}$.

Channel	$\Gamma(sec^{-}1)$	Γ/Γ_{tot}
	Mesonic	
$^3\mathrm{He} + \pi^-$	$0.146 \cdot 10^{10}$	0.38
$^3\mathrm{He} + \pi^0$		
d+p+π^-	$0.235 \cdot 10^{10}$	0.62
d+n+π^0		
p+p+n+π^-	$0.368 \cdot 10^{8}$	0.01
p+n+n+π^0		
	Non Mesonic	
d+n	$0.67 \cdot 10^{7}$	$2 \cdot 10^{-3}$
p+n+n	$0.57 \cdot 10^{8}$	0.01

Tab. 2.1: Partial mesonic and non mesonic decay rates of the ${}^3_\Lambda$H.

2.2.2 ${}^3_\Lambda$H structure

More than 60 years after its discovery, the ${}^3_\Lambda$H structure still represents an open question for the nuclear physics community. As the ${}^3_\Lambda$H represents a direct probe of the Y–N interaction, since the beginning of the study of this system one of the main goal of the experimentalists has been to measure the energy that keeps the hyperon bound to the nucleus. This quantity, which is called Λ separation energy B_Λ, for the ${}^3_\Lambda$H is the energy required to separate the Λ hyperon from the deuteron. The first precision measurement of B_Λ was published in 1973 by Juric et al. [64]: the value of B_Λ was found to be incredibly small, 130 ± 50 keV, hinting that ${}^3_\Lambda$H is an extreme weakly bound state and that the Y–N interaction is very shallow. In the same years, the first measurements of the ${}^3_\Lambda$H lifetime ($\tau_{{}^3_\Lambda\mathrm{H}}$) [65, 66] were found to be compatible with the free Λ hyperon one (τ_Λ = 263.2 ± 2 ps [13]), and therefore consistent with the picture of the ${}^3_\Lambda$H as a weakly bound state. After these measurements, few theoretical calculations were performed, all starting from the assumption of $\mathrm{B}_\Lambda \sim 130$ keV, and they were used to compute the ${}^3_\Lambda$H radius, lifetime, spin, and branching ratios [60, 67, 68]. A B_Λ value of around 100 keV provides a strong constraint on the ${}^3_\Lambda$H structure and in particular on its size: the ${}^3_\Lambda$H radius under this assumption should be ~ 10 fm [68, 69], more than five times larger than the deuteron one. This is why the ${}^3_\Lambda$H has been reasonably approximated as a bound state of a Λ and a deuteron.

Then, in recent years, the study of the ${}^3_\Lambda$H structure triggered new interest in the community because of the connection with the hadrochemistry of the neutron stars, as explained in Sec. 2.1.1, and because of the new experimental measurements of $\tau_{{}^3_\Lambda\mathrm{H}}$ and B_Λ in ultrarelativistic heavy-ion collisions and in relativistic ion fragmentation experiments [70]. In particular, the STAR Collaboration measured both $\tau_{{}^3_\Lambda\mathrm{H}}$ [71, 72] and B_Λ [73] in Au+Au collisions at the RHIC. All the STAR measurements seem to indicate that surprisingly ${}^3_\Lambda$H could be more compact than expected: the

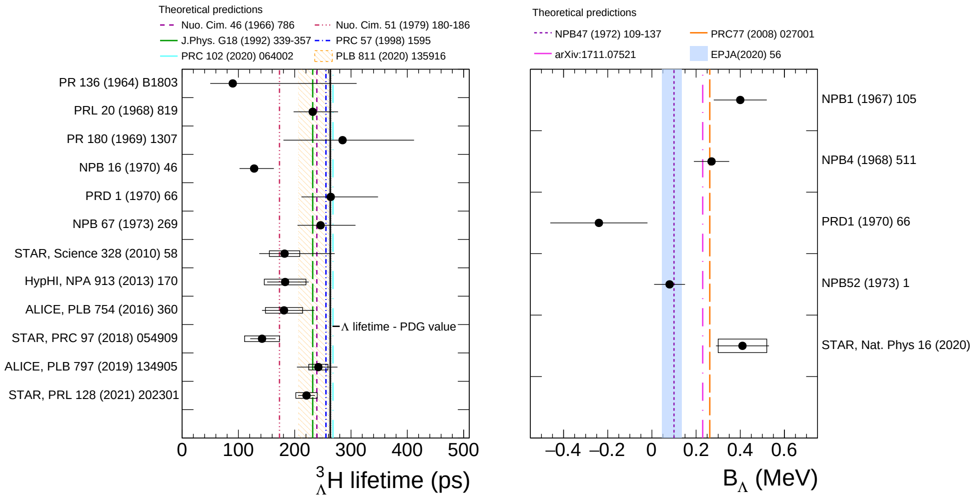

Fig. 2.4: Collection of the $^{3}_{\Lambda}\mathrm{H}$ lifetime (left) and B_{Λ} (right) measurements obtained with different experimental techniques. The horizontal lines and boxes are the statistical and systematic uncertainties respectively. The dashed-dotted lines are the corresponding theoretical predictions.

average of the two STAR lifetime measurements is more than 2σ lower than the free Λ lifetime, while the B_{Λ} value, even if affected by a large uncertainty, is more than 3 times larger than the reference value of 130 keV (1.7σ). The ALICE Collaboration published two measurement of the $\tau_{^{3}_{\Lambda}\mathrm{H}}$ in Pb–Pb collisions at $\sqrt{s_{NN}} = 2.76$ TeV and $\sqrt{s_{NN}} = 5.02$ TeV, and the last measurement, which has an uncertainty of 17% (compared with 35% of the first one), is compatible within 1σ with the free τ_{Λ} [74, 75]. The collections of the measurements of both $\tau_{^{3}_{\Lambda}\mathrm{H}}$ and B_{Λ} are shown in Fig. 2.4, together with few theoretical predictions. The new experimental measurements of the $^{3}_{\Lambda}\mathrm{H}$ properties triggered a new interest also in the theoretical community, and several new calculations based on modern effective field theories have been published [76, 77]. In particular, the relation between $\tau_{^{3}_{\Lambda}\mathrm{H}}$ and B_{Λ} has been investigated. In [76], the authors employed a pionless effective field theory to compute the $^{3}_{\Lambda}\mathrm{H}$ decay rate as a function of B_{Λ}, finding that the full $^{3}_{\Lambda}\mathrm{H}$ rate ($\Gamma_{^{3}_{\Lambda}\mathrm{H}}$) should be close to the free Λ one with little sensitivity to B_{Λ}, as shown in Fig. 2.5.

Different conclusions are drawn in [77], where the $^{3}_{\Lambda}\mathrm{H}$ three-body wave functions are generated in a chiral effective field theory approach to calculate the decay rate: values of $\tau_{^{3}_{\Lambda}\mathrm{H}}$ for different B_{Λ} values are reported in Tab. 2.2.

B_{Λ} (keV)	$\Gamma(^{3}_{\Lambda}\mathrm{H} \rightarrow ^{3}\mathrm{He} + \pi^{-})$ (GHz)	$\tau_{^{3}_{\Lambda}\mathrm{H}}$ (ps)
69	0.975	234 ± 27
135	1.197	190 ± 22
159	1.265	180 ± 21
410	1.403	163 ± 18

Tab. 2.2: $\Gamma(^{3}_{\Lambda}\mathrm{H} \rightarrow ^{3}\mathrm{He} + \pi^{-})$ (GHz) and $\tau_{^{3}_{\Lambda}\mathrm{H}}$ (ps) calculated for several B_{Λ} values (keV), up to $\mathrm{B}_{\Lambda} = 410$ keV from [77].

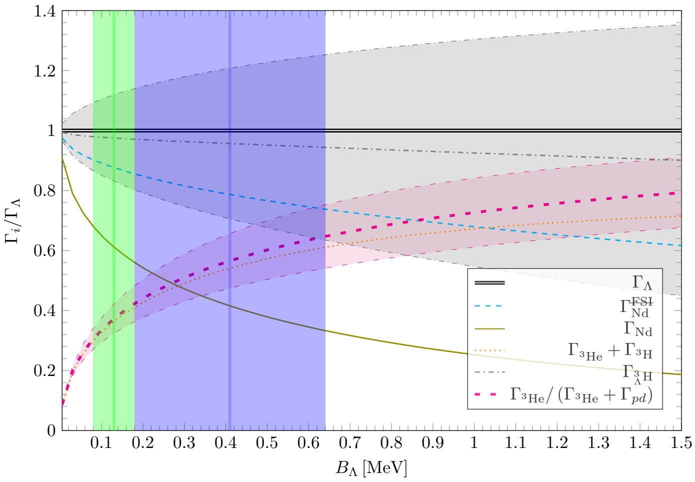

Fig. 2.5: Partial decay widths Γ_i in units of the free Λ width Γ_Λ as a function of B_Λ. The experimental values from [64] and [73] are indicated by the shaded light (green) and dark (blue) rectangular areas, respectively. The EFT uncertainties are shown by bands.

The general outcome of all these papers is that precision measurements of $\tau_{^3_\Lambda\mathrm{H}}$ and B_Λ are needed to definitely address the question of the $^3_\Lambda$H structure and compactness, which is the key for understanding the nature of the Y–N interaction.

Finally, an interesting tool for understanding the strength of the Y–N interaction comes from the study of the available proton-Λ scattering data [78–81] and correlation function [82]. In [83], the authors have employed the proton-Λ measured cross sections to constrain the Y–N interaction within a next to leading order (NLO) chiral effective field theory. The B_Λ of the $^3_\Lambda$H can be extracted from the fit to the proton-Λ cross sections shown in Fig. 2.6, resulting of the order of 90 keV. These calculations have also been employed for the study of the proton-Λ correlation function measured by ALICE in [82], resulting in a qualitative agreement with the data.

2.3 Production of (anti-)(hyper-)nuclei at the LHC

As discussed in the previous sections, since the beginning of the last decade (anti-)hypernuclei have started to be studied in high energy hadronic collisions. This led to new exciting results, like the discovery of the antihypertriton ($^3_\Lambda\overline{\mathrm{H}}$) [61], and few new open questions. One of the main point to be addressed is the production mechanism of ordinary nuclei and hypernuclei in such collisions. Two classes of models are employed to describe such production mechanism: the Statistical Hadronization Models (SHMs) and the coalescence models. The following two

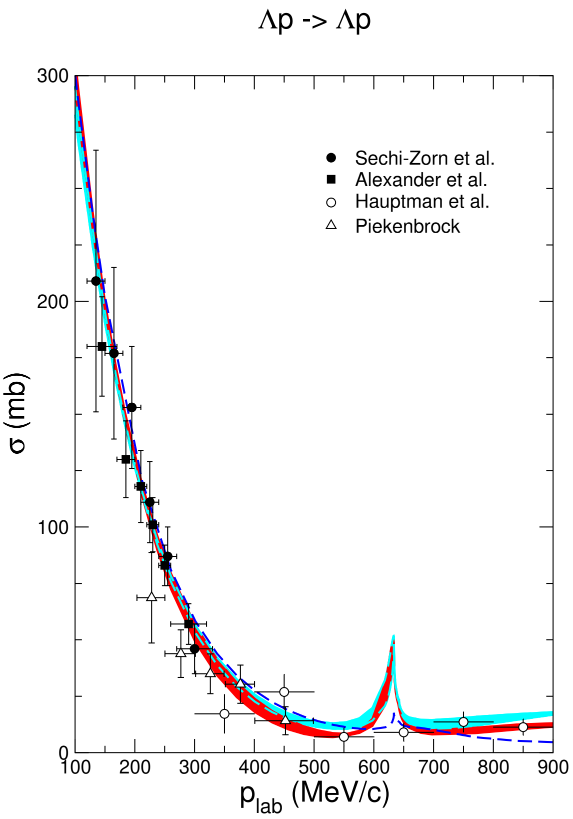

Fig. 2.6: Proton-Λ cross sections measured by [78–81] compared with the NLO chiral effective field theory predictions (blue and red bands) [83].

sections are dedicated to briefly explain the assumptions and the results predicted by this two successful models.

2.3.1 Statistical Hadronization Models

The Statistical Hadronization Models (SHMs), also known as Thermal Models, have the purpose to describe the abundances of different particle species produced in the collision between particles. The original idea behind the SHMs was formulated by Fermi [84], and more than 70 years later it has been developed by many authors. One of the first prototypes of the SHM was proposed by Hagerdorn [85] in 1968, and it was able to describe the abundances of different particle species produced in pp collisions. The general principle of the Hagerdorn model, as well as the modern SHMs, is that the final state of the interaction is composed by all the particle states compatible with the conservation laws imposed by the theory. The relative abundance of different particle states is set by the maximization of the total phase space filled by the system, to which each particle species contributes according to its partition function. These models, even if originally developed for describing pp collisions, are suitable for HICs where the presence of an expanding medium that eventually reaches the thermal equilibrium seems appropriate for the statistical hadronization approach. Few attempts have also been made to apply the SHM approach to e^+e^- collisions [86].

In the modern formulation of the SHMs, depending on the system size, two different approaches are used: if the system under study is characterized by a large volume, such as HIC, a Grand Canonical formalism is used. On the other hand in small systems a canonical approach has to be followed. The two approaches will be described in the following sections.

Grand Canonical SHM

The Grand Canonical approach will be described in this section following the implementation from [87]. The size of the system created in relativistic HIC ($\sim 10\ fm/c$) is large enough to allow the use of the Grand Canonical approach. This formalism can be used in the central rapidity region where are located most of the detectors of ALICE: this region can be considered in equilibrium with a thermal reservoir (the rest of the medium created in a HIC). Hence, quantities like energy, baryon number, charge and isospin are conserved on average. Within the Grand Canonical formalism the parameters describing the equilibrium condition of a HIC include the temperature T, the volume V, and the chemical potentials μ_i. The partition function of the system can be written as:

$$Z(T, V, \mu) = Tr\left[e^{-\beta(H-\Sigma_i Q_i \mu_i)}\right] \tag{2.6}$$

with

$$\mu = \sum_i Q_i \mu_{Q_i} \quad \text{and} \quad \beta = \frac{1}{T} \tag{2.7}$$

where V is the volume of the system at the equilibrium, H is the Hamiltonian and μ_{Q_i} is the chemical potential associated to the conserved quantum number Q_i. In the formulation adopted in [87], the main conserved quantum numbers are the electric charge Q, the strangeness content of the system S and the baryon number B. The Hamiltonian H used in the partition function is the one of a Hadron Resonance Gas. This Hamiltonian is chosen because it successfully predicts the behaviour of a strongly interacting medium and reproduces the EoS calculated with lattice QCD over a wide temperature range, as shown in Sec. 1.2. The partition function of the system is the product of the partition functions of all the available particle states in the Hadron Resonance Gas:

$$Z(T,V,\mu) = \prod_i Z_i(T,V,\mu_i) \quad \rightarrow \quad \log Z(T,V,\mu) = \sum_i \log Z_i(T,V,\mu_i). \tag{2.8}$$

Each partition function is defined by the spin–statistics theorem as follows:

$$\log Z_i(T,V,\mu_i) = \frac{Vg_i}{2\pi^2}\int_0^{\infty} \pm p^2\, dp\, \log\left[1 \pm \lambda_i(T,\mu_i)e^{-\beta\epsilon_i}\right] \tag{2.9}$$

where $(+)$ is used for bosons (following the Bose-Einstein distribution) and $(-)$ for fermions (following the Fermi-Dirac distribution). The g_i constant is the degeneracy state i and ϵ_i is the energy of one particle of the species i with momentum $p(\epsilon_i = \sqrt{p^2+m_i^2})$. The *fugacity* λ_i term encloses the dependence on the chemical potentials:

$$\lambda_i(T,\mu_i) = e^{\beta(B_i\mu_B + S_i\mu_S + Q_i\mu_Q)} = e^{\beta\mu_i} \tag{2.10}$$

where B_i, S_i and Q_i are the baryon number, the strangeness content and the electric charge associated with the particle species i and μ_B , μ_S and μ_Q are the quantum charges chemical potentials. Expanding the logarithm and integrating over the momentum, the partition function for the particle i becomes:

$$\log Z_i(T,V,\mu_i) = \frac{VTg_i}{2\pi^2}\sum_{k=1}^{\infty}\frac{(\pm 1)^{k+1}}{k^2}\lambda_i^k m_i^2 K_2(\beta k m_i) \tag{2.11}$$

where $(+)$ is used for bosons, the $(-)$ for fermions and the K_2 is the second kind modified Bessel function of second order. The average number of particles for the species i for a system described by the Grand Canonical ensemble, is defined as:

$$\langle N_i\rangle^{th}(T,V,\mu_i) = \frac{1}{\beta}\frac{\partial}{\partial\mu_i}\log Z_i(T,V,\mu_i)\frac{VTg_i}{2\pi^2}\sum_{k=1}^{\infty}\frac{(\pm 1)^{k+1}}{k}\lambda_i^k m_i^2 K_2(\beta k m_i). \tag{2.12}$$

This equation does not consider the feed–down contributions from all the other particle species (resonances) j in the thermal system that can decay strongly or electromagnetically in a final state containing particles of the species i. Therefore, the total yield is:

$$\langle N_i\rangle(T,V,\mu) = \langle N_i\rangle^{th}(T,V,\mu_i) + \sum_j \Gamma_{j\rightarrow i}\langle N_j\rangle^{th}(T,V,\mu_j) \tag{2.13}$$

where $\Gamma_{j\rightarrow i}$ is the decay rate of the state j into the final state i. The Eq. 2.12 and 2.13 indicate the 5 free parameters of the model: the temperature T, the volume V and the chemical potentials μ_B, μ_Q and μ_S. The knowledge of the initial collision conditions give the possibility to fix two of them: in Pb-Pb collisions no net strangeness is present ($\mu_S = 0$) and μ_Q is fixed by the initial electric charge asymmetry. The dependence on the volume V of the system can also be removed

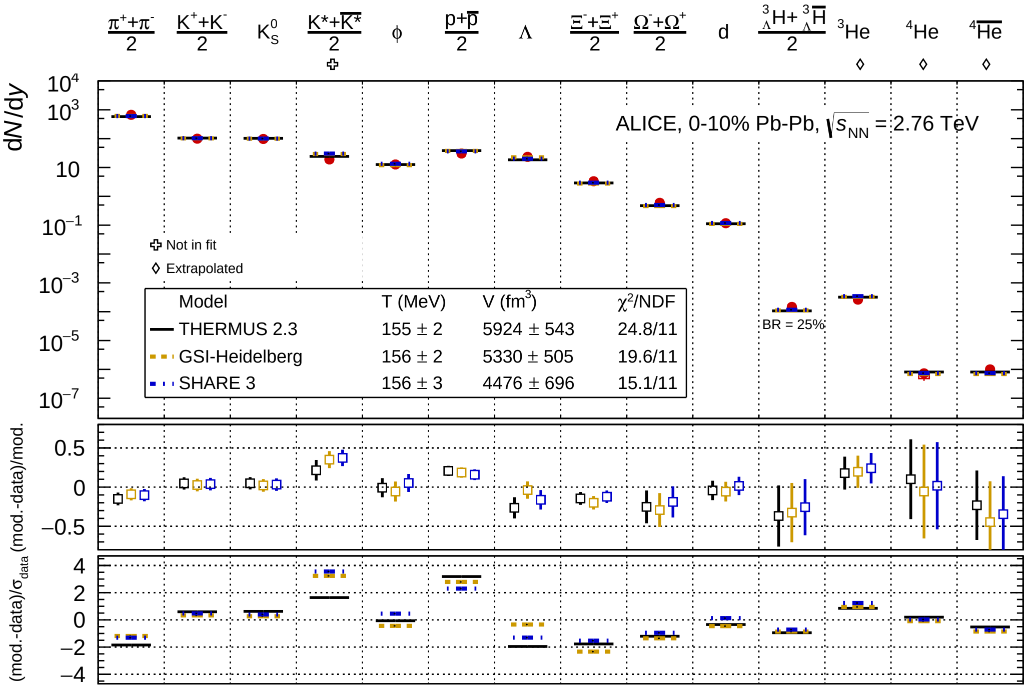

Fig. 2.7: Thermal model fit to the light-flavoured hadron yields in central Pb–Pb collisions at $\sqrt{s_{\mathrm{NN}}}$ = 2.76 TeV [91], with three different SHM implementations: THERMUS (black line), GSI-Heidelberg (yellow line) and SHARE (blue line).

by measuring the ratio between the yields of different particle species (relative abundances), which depends only on the temperature of the system and on the baryon chemical potential.

By setting the chemical freeze–out temperature and the baryon chemical potential the properties of each particle species can be inferred from the SHMs including the production yield. This mechanism can be naturally applied to the study of the light (hyper-) nuclei production in HICs. In principle one would not expect to see any light nuclei in such collisions, since the chemical freeze-out temperature is much higher than their binding energy. However, the thermal model is blind to the internal structure of hadrons. The SHM is used to predict hadron yields in a collision, going from pions to light nuclei. The success of the model is shown in Fig. 2.7: a thermal fit has been performed to describe all the light-flavoured hadrons measured in central (0–10%) Pb–Pb collisions at $\sqrt{s_{\mathrm{NN}}}$ = 2.76 TeV up to the $^{3}_{\Lambda}\mathrm{H}$. The fits are performed with three slightly different implementations of the SHM: THERMUS [88], GSI-Heidelberg [89] and SHARE [90]. For all of them, the fits provide a chemical freeze-out temperature $T_{chem} = 156$ MeV [91].

Canonical suppression in small collision systems

In small collision systems, where the typical number of particles produced is up to few tens, the conditions for the grand canonical approach are not satisfied, and the description of the collision can be performed only by using the canonical ensemble [92, 93]. While a complete description of the canonical SHM is given in Refs. [94, 95], here we will focus on the results and the main consequences on the hadron yields in small collision systems. In the canonical approach, the ensemble is represented by an ideal hadron resonance gas (HRG) in the Boltzmann approximation and in full chemical equilibrium. The three quantum charges previously considered - the baryon number B, the electric charge Q, and the strangeness S - are fixed exactly to particular values which are conserved exactly across a correlation volume V_c. The mean particle multiplicity for the species j calculated under this assumption $\langle N_j^{th} \rangle^{ce}$ can be written in terms of the Gran Canonical multiplicity $\langle N_j^{th} \rangle^{gce}$ as:

$$\langle N_j^{th} \rangle^{ce} = \frac{Z(B - B_j,\, Q - Q_j,\, S - S_j)}{Z(B, Q, S)} \langle N_j^{th} \rangle^{gce}, \tag{2.14}$$

where $Z(B, Q, S)$ is the canonical partition function. The final particle yields, $\langle N_j \rangle^{ce}$, are then calculated after including the feed-down from the decays of unstable resonances as it is done in Eq. 2.13. Looking at Eq. 2.14, the factor before $\langle N_j^{th} \rangle^{gce}$ is the chemical factor, which reflects the exact conservation of the charges. The chemical factor reflects the so-called canonical suppression of the yields of particles carrying conserved charges, relative to their Grand Canonical values. The effect is stronger for multi-charged particles, such as multi-strange hyperons or light (hyper-)nuclei. Fig. 2.8 shows the effect of the canonical suppression for the deuteron over proton ratio, as a function of the average charged pion multiplicity of the collision ($\mathrm{d}N_\pi/\mathrm{d}y$). The study has been performed by varying both the correlation volume V_c and the chemical freeze-out temperature T_{chem}.

The canonical suppression mechanism is able to reproduce the ALICE measurements of d/p from central Pb–Pb collisions at $\sqrt{s_{\mathrm{NN}}}$ = 2.76 TeV to pp collisions at s = 900 GeV.

2.3.2 Coalescence Models

The second approach used to describe the (hyper-)nuclei yields is given by the coalescence models. Like the SHMs, coalescence models do not provide a dynamic theory of the interactions that cause the nucleosynthesis, but provide a powerful description of the formation process. The fundamental idea behind the coalescence approach is that nuclei constituents which are close enough in phase space at the kinematic freeze-out can bind to form a nucleus. In 1961 Pearson and Butler [96] proposed the first coalescence model to explain the deuteron formation in proton-

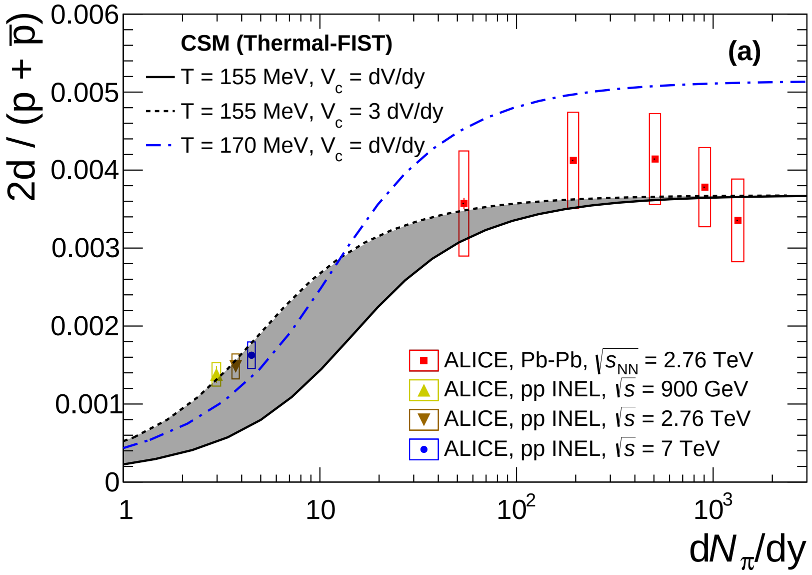

Fig. 2.8: Predictions for d/p as a function of charged pion multiplicity $\mathrm{d}N_\pi/\mathrm{d}y$ obtained with *Thermal-Fist* package, implemented in [95]. Predictions are reported for $T = 155$ MeV and $V_c = \mathrm{d}V/\mathrm{d}y$ (black solid lines), $T = 155$ MeV and $V_c = 3\ \mathrm{d}V/\mathrm{d}y$ (black dashed lines) and $T = 170$ MeV and $V_c = \mathrm{d}V/\mathrm{d}y$ (blue dash-dotted lines). Experimental points corresponds to the available ALICE measurements at the time of the publication of Ref. [95], from which this picture is taken.

nucleus collisions in terms of the production spectra of its constituent nucleons (a proton and a neutron). Taking into account the p-n force and the nuclear optical potential, it is possible to evaluate the deuteron invariant momentum spectrum $E_d\frac{d^3N_d}{dp_d^3}$ as:

$$E_d\frac{d^3N_d}{dp_d^3} = B_2(E_p\frac{d^3N_p}{dp_p^3})(E_n\frac{d^3N_n}{dp_n^3}) \tag{2.15}$$

where $E_p\frac{d^3N_p}{dp_p^3}$ and $E_n\frac{d^3N_n}{dp_n^3}$ are the proton and the neutron invariant momentum spectrum and B_2 is the coalescence parameter that encodes the dependence from the nucleon mass, the binding energy of the final state, and the depth of the potential well. The model has been extended in 1963 by Schwarzchild and Zupancic [97] to evaluate the production probability of a light nucleus composed by A nucleons in a nucleus-nucleus collision. The equation 2.15 for a nucleus of the species i becomes:

$$E_d\frac{d^3N_i}{dp_i^3} = B_A(E_p\frac{d^3N_p}{dp_p^3})^A \tag{2.16}$$

In Eq. 2.16, the proton spectrum is assumed to be identical to the spectrum of the constituent neutron: this approximation is particularly useful for experiments that do not have hadronic calorimeters at mid-rapidity for the identification of neutrons, and it is well justified in high-energy hadronic collisions at mid-rapidity where the isospin symmetry is fulfilled. The new proportionality constant B_A is no longer related to the binding energy of the nucleus and the nuclear optical potential, but it is interpreted as a function of the radius p_0, which is the maximum distance between two nucleons at which coalescence can happen. In the simplest formulation of the coalescence models, only the momentum space is considered (not the space-time) and the coalescence parameter can be expressed neglecting the spin:

$$B_A = \left(\frac{4}{3}\,\pi\,p_0^3\right)^{A-1}\frac{m_i}{m_p^A}, \tag{2.17}$$

where p_0 is the aforementioned radius and m_i and m_p are the nucleus and proton mass, respectively.

A more realistic coalescence model can be found in [98], where authors explore the system size (or charged particle multiplicity) dependence of different (hyper-)nuclei ratios by taking into account the finite size of their internal wave functions. In this approach, the formation probability of a light nucleus is given by the overlap of the nucleon phase-space distribution functions in the emission source with the Wigner function of the light nucleus, which is obtained from the Wigner transform of its internal wave function. The phase-space distributions of nucleons are taken from a thermalized expanding spherical fireball of kinetic freeze-out temperature T_k and radius R:

$$f_{\mathrm{p,n}}(\vec{x},\vec{p}) = \frac{N_{\mathrm{p,n}}}{(2\pi)^3(mT_kR^2)^{3/2}}e^{-\frac{p^2}{2mT_k}}e^{-\frac{x^2}{2R^2}} \tag{2.18}$$

where m is the mass of the nucleon and $N_{\mathrm{p,n}}$ is the number of protons or neutrons. From the full calculation the d/p, ^{3}He/p, ^{3}He/^{3}H and the $^3_\Lambda$H/ Λ ratios are extracted. For example, the d/p ratio is given by:

$$\frac{N_{\mathrm{d}}}{N_{\mathrm{p}}} \approx \frac{3N_{\mathrm{n}}}{4(mT_kR^2)^{3/2}}\left[1+\left(\frac{1.6\text{ fm}}{R}\right)^2\right]^{-3/2}, \tag{2.19}$$

where the last factor in the above equation describes the suppression of deuteron production due to its finite size relative to that of the nucleon emission source, and the factor $\frac{N_{\mathrm{p,n}}}{(2\pi)^3(mT_kR^2)^{3/2}}$ corresponds to the d/p ratio in the limit of large nucleon emission source.

Finally, for A=3 nuclei, coalescence can arise both from the overlap of three nucleons and the overlap of an A=2 nucleus with a nucleon. These two contributions are treated separately in [98] and called three-body and two-body coalescence, respectively. The d/p, ^{3}He/p, ^{3}He/^{3}H ratios as a function of the charged particle multiplicity are shown in Fig. 2.9: coalescence models are able to reproduce the available ALICE measurements at the time of the publication of Ref. [98].

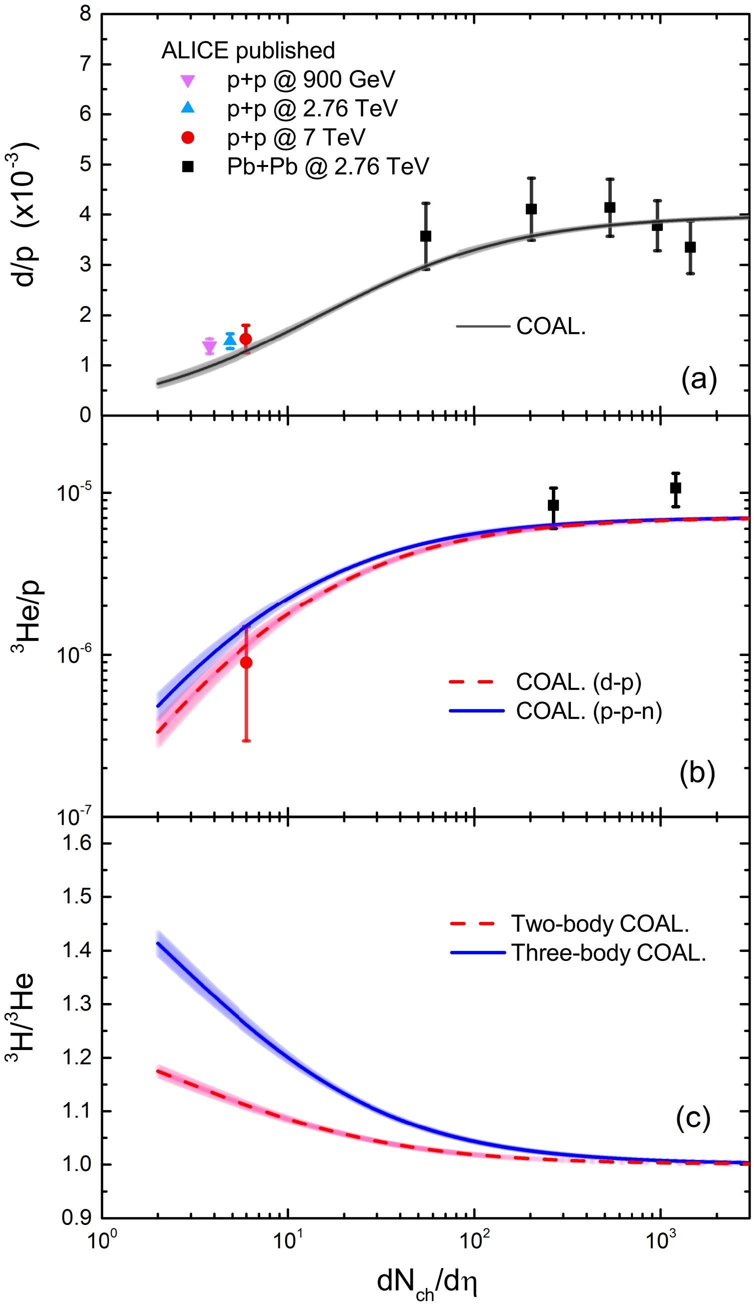

Fig. 2.9: Yield ratios d/p, ^{3}He/p and ^{3}H/^{3}He as a function of charged particle multiplicity. Experimental data are measured in pp collisions at $\sqrt{s}$ = 0.9, 2.76 and 7 TeV [99] and in Pb–Pb collisions at 2.76 [100]. Lines are the predictions of the coalescence model, with theoretical uncertainties on the emission source radius given by the shaded bands. For ^{3}He/p and ^{3}H/^{3}He the magenta and the blue lines correspond to two-body and three-body coalescence, respectively.

2.3.3 $^{3}_{\Lambda}\mathrm{H}$ production in small systems

Both the coalescence and the statisticals model have been used to successfully describe the nuclei production at the LHC. The d/p ratio as a function of the charged

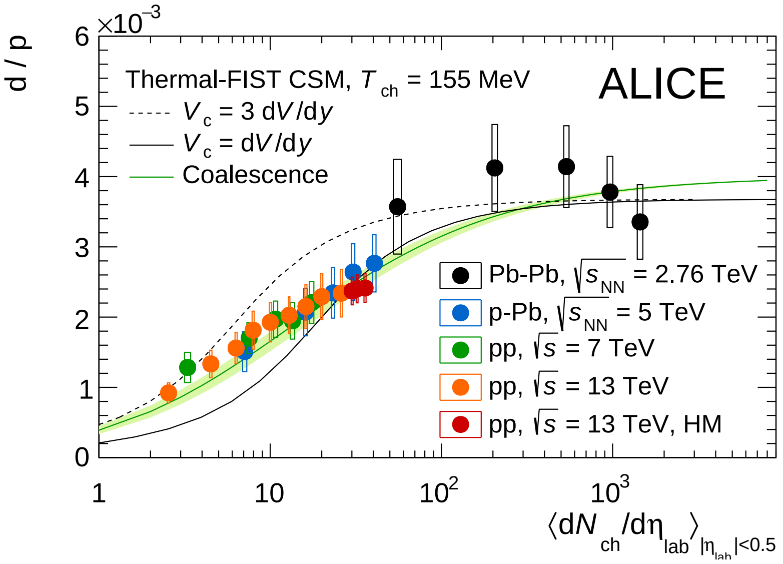

Fig. 2.10: Ratio between the p_T-integrated yields of (anti)deuterons and protons as a function of multiplicity. The measurements are performed in high-multiplicity pp collisions at $\sqrt{s}$ = 13 TeV, in minimum bias pp collisions at $\sqrt{s}$ = 13 TeV and at $\sqrt{s}$ = 7 TeV, in p–Pb collisions at $\sqrt{s_{NN}}$ = 5.02 TeV, and in Pb–Pb collisions at $\sqrt{s_{NN}}$ = 2.76 TeV. Vertical bars and boxes represent statistical and systematic uncertainties, respectively. The two black lines are the theoretical predictions of the Thermal-FIST CSM [95] for two sizes of the correlation volume VC. The green line represents the expectation from the coalescence model [98]

.

particle multiplicity has been reproduced quantitatively from 900 GeV pp to 5.02 TeV Pb–Pb collisions, as it is shown in Fig. 2.10. In spite of these remarkable results, there are still important open questions that need to be addressed: can we define a range of validity for the parameters and the assumptions of the models? Can coalescence and SHMs coexist? While SHM provides a statistical description of our ensemble, coalescence is able to predict the yield ratios starting from microscopic information. On the other hand, SHMs are able to reproduce the particle species yield and not only the ratios in terms of their constituents (while coalescence does not).

The study of the ${}^{3}_{\Lambda}\mathrm{H}$ production in small systems can help us to shed light on some of these questions. If ${}^{3}_{\Lambda}\mathrm{H}$ is as weakly bound as described in 2.2.2, its wave function can extend up to a radius of $\sim$ 5-6 fm. Hence, the size of the ${}^{3}_{\Lambda}\mathrm{H}$ wave function is much larger than the hadron emission radius estimated with a femtoscopic technique in pp or p–Pb collisions (1–2 fm, [101, 102]). For this reason, the ${}^{3}_{\Lambda}\mathrm{H}$ yield in small systems predicted by the coalescence model, where the ratio of nucleus size to source size directly influences its yield (as shown in Eq. 2.19), is suppressed with respect to the statistical hadronization model expectations, where the nuclear size does not enter explicitly and particles are treated as point-like objects. The ${}^{3}_{\Lambda}\mathrm{H}/\Lambda$ ratio

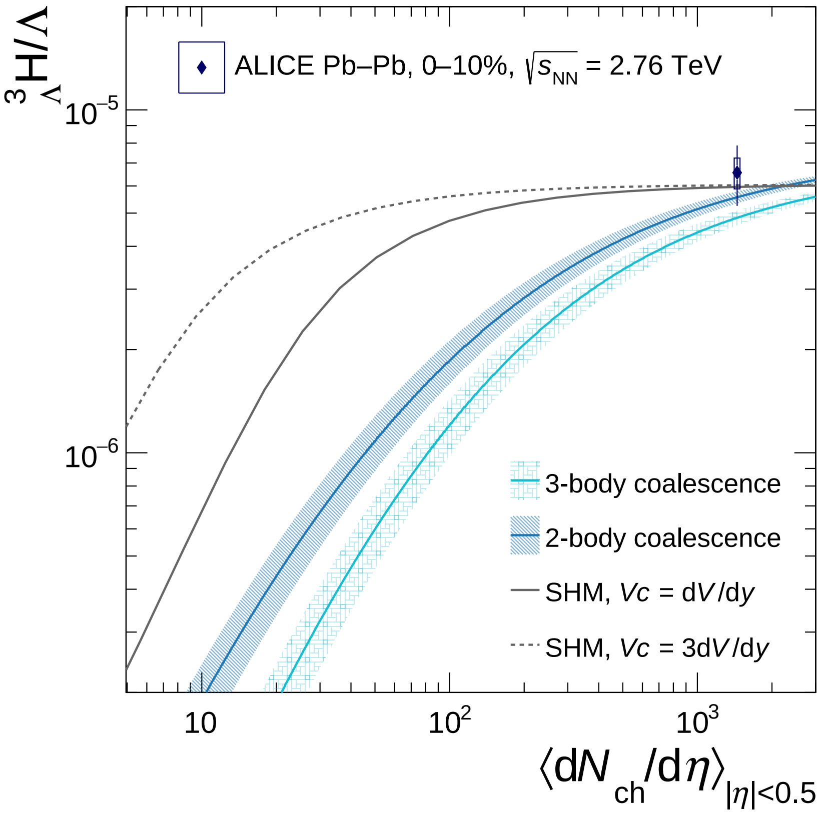

Fig. 2.11: The $^3_\Lambda$H/Λ The expectations for the canonical statistical hadronization(with two different V_c) and coalescence (2-body and 3-body) models. The ALICE measurement in Pb–Pb collisions at $\sqrt{s_{\rm NN}}$ = 2.76 TeV is also shown.

prediction as a function of the charged particle multiplicity is shown in Fig. 2.11 for both the models.

In small systems, where the charged particle multiplicity is lower than 30, the separation between coalescence and SHM is clearly visible. Hence, the measurement of $^3_\Lambda$H production in p–Pb collisions, which is a subject of this thesis and will be described in Chap. 6, is a powerful tool for probing the nucleosynthesis mechanism in high-energy hadronic collisions.

A Large Ion Collider Experiment

3

The Large Hadron Collider is the most powerful accelerator ever built for particle physics. Thanks to its 27 km ring, the LHC can deliver pp and heavy-ion collisions at the highest energies ever achieved. The LHC is operated by the European Organization for Nuclear Research (CERN) and is located in the Canton of Geneva, Switzerland. A significant part of the LHC physics programme is devoted to the study of the properties of the Quark Gluon Plasma, that can be produced through relativistic heavy ion collisions. As mentioned in the previous sections, the LHC can provide Pb–Pb collisions at a centre of mass energy per nucleon pair of 5.02 TeV. The ALICE (A Large Ion Collider Experiment) detector has been designed to profit from the unique opportunities offered by the LHC heavy ion programme. A description of the LHC and ALICE setup during the Run 2 of the LHC (2015-2018) will be given in this chapter, while the current status of ALICE, and in particular of its inner tracking system, will be briefly discussed in Chap. 7.

3.1 The Large Hadron Collider

The Large Hadron Collider (LHC) is the final component of CERN accelerator complex (Figure 3.1), which progressively accelerates particles to higher energies. Each machine in this chain increases the energy of a particle beam and then injects it into the next machine. Protons and heavy ions are brought to their collision energies through different acceleration chains. Protons are obtained from a source of ionized hydrogen and are then accelerated up to 50 MeV by LINAC 2 (or LINAC 4 for LHC Run 3). The beam is then directed to the Proton Synchrotron Booster (PSB), which increases the proton energy to 1.4 GeV and injects the beam bunches into the Proton Synchrotron (PS). The Proton Synchrotron boosts protons up to 25 GeV before injecting them into the Super Proton Synchrotron (SPS), where protons are accelerated up to 450 GeV. After passing through the SPS, protons finally reach the LHC and are accelerated up to a record energy of 6.8 TeV [104][105].

"The CERN heavy ion programme is based on the use of $^{208}\mathrm{Pb}$ ions. The production of lead-ion beams at the LHC starts with a 2-centimeter-long pure lead sample that weighs 500 milligrams. In the first stage, the lead sample is heated to about 500 degrees Celsius to vaporize a small number of atoms. An electric current is then used

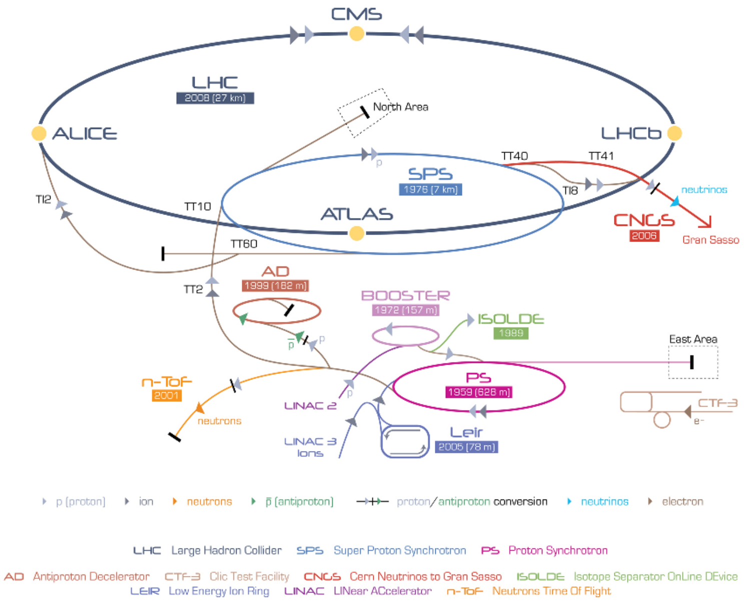
CMS
LHC
2008 (27 km)
North Area
ALICE
LHCb
TT40
TT41
SPS
1976 (7 km)
TI8
neutrinos
TI2
TT10
ATLAS
CNGS
2006
Gran Sasso
TT60
AD
1999 (182 m)
TT2
BOOSTER
1972 (157 m)
ISOLDE
1989
East Area
n-ToF
2001
PS
1959 (628 m)
LINAC 2
CTF3
e−
neutrons
LINAC 3
Ions
Leir
2005 (78 m)
p
p̄
p (proton)
ion
neutrons
p̄ (antiproton)
proton/antiproton conversion
neutrinos
electron
LHC Large Hadron Collider
SPS Super Proton Synchrotron
PS Proton Synchrotron
AD Antiproton Decelerator
CTF3 Clic Test Facility
CNGS Cern Neutrinos to Gran Sasso
ISOLDE Isotope Separator OnLine DEvice
LEIR Low Energy Ion Ring
LINAC LINear ACcelerator
n-ToF Neutrons Time Of Flight

Fig. 3.1: View of the CERN accelerator complex and the LHC experiments [103]

to remove a few of the electrons from each atom to obtain ${}^{208}_{82}\mathrm{Pb}^{29+}$ ions, which are accelerated up to 4.2 MeV per nucleon in the Linear Accelerator 3 (LINAC3). Then, a carbon foil is used to further ionize the ${}^{208}_{82}\mathrm{Pb}^{29+}$ into a ${}^{208}_{82}\mathrm{Pb}^{54+}$ beam, which is then injected into the Low Energy Ion Ring (LEIR). LEIR increases the beam's energy to 72 MeV and injects it into the PS. From this point onwards the accelerating chain used for proton beams is the same to the one describe above. Before reaching the LHC, the lead ions are ionized again by a second foil to obtain fully ionized Pb ions [106].

The LHC ring is made up of 1232 dipole magnets and 392 quadrupole magnets that respectively guide and focus two counter-rotating beams in separate vacuum pipes. The superconductive magnets operate at a temperature of 1.9 K, and deliver a peak magnetic field value of 8.33 T. Proton and ion beams are accelerated in the ring and brought to collisions in the four interaction points corresponding to the four major LHC experiments. The performance of the collider is evaluated using the instantaneous luminosity L, which is related to the number of events per second R and the cross-section σ of the process by the following formula:

$$R = L\sigma \tag{3.1}$$

The luminosity does not depend on the nature of the studied process but only on the beam parameters, and it can be expressed as:

$$L = \frac{N_b N^2 f_{rev} \gamma}{4\pi \epsilon_n \beta^*} F, \tag{3.2}$$

where N_b is the number of bunches in the collider ring, N is the number of charges in each bunch, f_{rev} is the revolution frequency of the beam, γ is the relativistic factor, F is a geometrical factor, ϵ_n is the normalized emittance and β^* is the value of the amplitude function at the interaction point (IP) where the luminosity is estimated. The ALICE apparatus requires a peak luminosity of $L = 10^{27}$ cm^{-2}s^{-1} in Pb-Pb collisions [107][108]. Figure 3.2 shows the integrated luminosities collected by ALICE for different trigger configurations during the Pb–Pb period in Run 2 at the end of 2018.

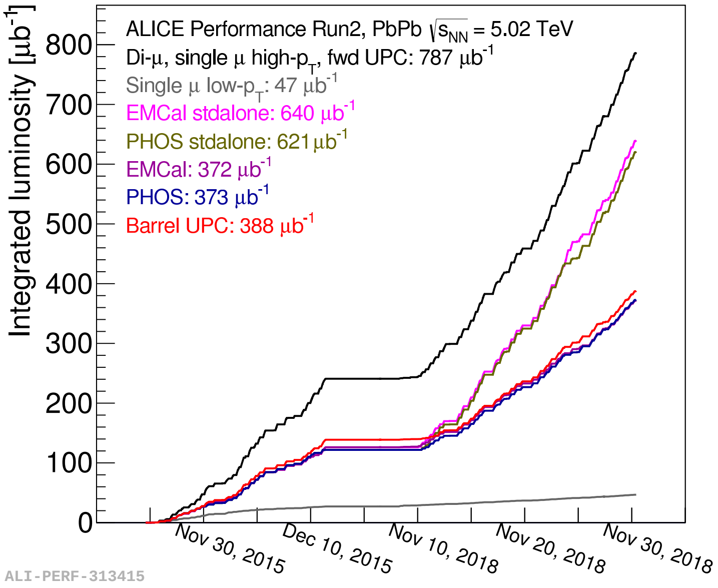

Fig. 3.2: ALICE integrated luminosity for different trigger configurations.

Each collision takes place in a narrow region around the nominal interaction point, and the actual position of the collision is called *primary vertex*. The primary vertex displacement is due to the finite shape of the bunches, and assuming a 3D Gaussian profile for the bunches the vertex RMS is computed as:

$$\sigma_{xyz}^{ver} = \frac{\sigma_{xyz}^{b}}{\sqrt{2}} \tag{3.3}$$

where σ_{xyz}^{b} and σ_{xyz}^{ver} are the bunches and the vertex RMS, respectively. For the ALICE experiment, assuming that the z axis coincides with the beam axis, typical values for the vertex dispersion are $\sigma_{xy}^{ver} \approx 50$ μm and $\sigma_{z}^{ver} \approx 5$ cm.

The LHC physics programme started in 2009 delivering pp collisions up to $\sqrt{s} =$ 7 TeV, p-Pb at $\sqrt{s_{\rm NN}}$ = 5.02 TeV and Pb–Pb at $\sqrt{s_{\rm NN}}$ = 2.76 TeV, before ending in 2013 with the Long Shutdown 1 (LS1). During the LS1, the LHC has been upgraded in order to increase the collision energy. The Run 2 started in 2015 and the LHC delivered Pb-Pb collisions at $\sqrt{s_{\mathrm{NN}}}$ = 5.02 TeV, p-Pb collisions at $\sqrt{s_{\mathrm{NN}}}$ = 8 TeV and pp collisions at $\sqrt{s} = 13$ TeV. In December 2018 the LHC Long Shutdown 2 started, allowing for the detectors upgrade in view of LHC Run 3 physics programme, that started in 2022. The analysis of the data collected in Run 2 for the study of the ${}^{3}_{\Lambda}\mathrm{H}$ properties is the main topic of this thesis, while the last chapter will be dedicated to the developments ongoing for the analyses of hypernuclei during the LHC Run 3.

3.2 The ALICE detector

ALICE, the LHC experiment devoted to heavy-ion physics at CERN [107], requires an excellent tracking system with a large acceptance and outstanding Particle IDentification (PID) capabilities over a wide momentum range. When ALICE was planned, the expected number of charged particles produced per rapidity unit in a LHC Pb-Pb central collision was estimated to be between 2000 and 8000 [109]. Consequently, the ALICE detectors were designed with high granularity [110, 111]. The ALICE apparatus is shown in Figure 3.3 and has a weight of ≈ 1000 tons, with dimensions of 26 m length, 16 m height, and 16 m width.

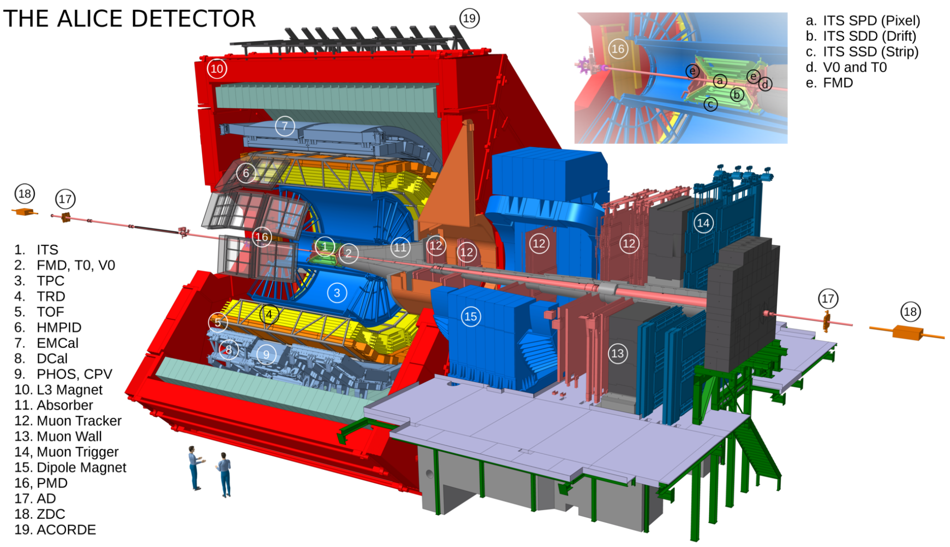
THE ALICE DETECTOR
1. ITS
2. FMD, T0, V0
3. TPC
4. TRD
5. TOF
6. HMPID
7. EMCal
8. DCal
9. PHOS, CPV
10. L3 Magnet
11. Absorber
12. Muon Tracker
13. Muon Wall
14, Muon Trigger
15. Dipole Magnet
16, PMD
17. AD
18. ZDC
19. ACORDE
a. ITS SPD (Pixel)
b. ITS SDD (Drift)
c. ITS SSD (Strip)
d. V0 and T0
e. FMD

Fig. 3.3: Schematic view of the ALICE layout.

ALICE comprises three different parts: the central barrel, a forward muon spectrometer, and a set of detectors at forward and backward rapidity for trigger and event characterization. The central barrel has an optimized detector sequence for particle reconstruction and identification, covering a wide pseudo-rapidity region from $-0.9 < \eta < 0.9$ and is surrounded by a solenoidal magnet with a peak magnetic field of 0.5 T parallel to the beam axis. The detectors, from the innermost to the outermost, include the Inner Tracking system (ITS), the Time Projection Chamber (TPC), the Transition Radiation Detector (TRD), the Time Of Flight (TOF) detector, the High-Momentum Particle IDentification detector (HMPID), the Photon Spectrometer (PHOS), the Electromagnetic Calorimeter (EMCal), a Di-Jet Calorimeter (DCal), and the ALICE Cosmic Ray Detector (ACORDE).

The forward muon spectrometer consists of a complex arrangement of absorbers, a large dipole magnet, and fourteen planes of Resistive Plate Chambers (RPC). It covers the pseudo-rapidity range of $-4 < \eta < 2.5$. The other detectors mainly serve for global event characterization and triggering and include the Photon Multiplicity Detector (PMD), the Forward Multiplicity Detector (FMD), the Cherenkov T0 detector, the plastic scintillator V0 detector, and the Zero Degree Calorimeter (ZDC).

The ALICE coordinate system is a right-handed orthogonal Cartesian system with the origin located at the nominal beam Interaction Point 2. The x axis is aligned with the horizontal accelerator plane, pointing to the center of the LHC, and the y axis is perpendicular to the accelerator plane, pointing upward. Consequently, the z axis is parallel to the beam direction, and its positive direction is defined by the chirality of the system. The azimuthal angle ϕ increases counter-clockwise, starting from $\phi = 0$ for x axis looking towards the Compact Muon Solenoid (CMS) side, and the polar angle θ increases from z ($\theta = 0$) to -z ($\theta = \pi$).

In the following subsections, the detectors of ALICE that are relevant for the analysis of ${}^{3}_{\Lambda}$H will be described in more detail.

3.2.1 The Inner Tracking System

The Inner Tracking System is the closest detector to the primary vertex, covering a distance from the beam line from r = 3.9 cm for the innermost pixel layer up to r = 43 cm for the outermost strip layer [112, 113]. The ITS barrel is composed of 6 cylindrical layers of silicon detectors using three different technologies: two layers of pixel, drift and strip detectors. The layout of the ITS is shown in Figure 3.4.

The main tasks of the ITS are the localization of the primary vertices with a resolution better than 100 μm, the reconstruction of the secondary vertices from hyperons and B and D meson decays, the tracking and the identification of charged particles with p_{T} < 200 MeV/c. In addition, the ITS helps to improve the momentum and angle resolution for particles tracked by the TPC. The three technologies used in the ITS are described in the following.

Silicon pixel detectors (SPDs) constitute the two innermost layers of the ITS. SPDs are highly segmented in order to obtain a good impact parameter resolution and to withstand the high multiplicity environment typical of ion collisions.

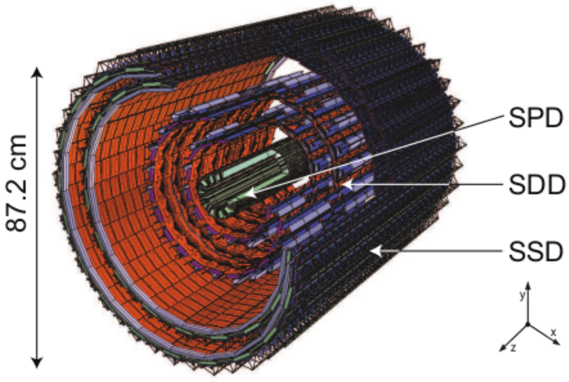

Fig. 3.4: Layout of the ALICE Inner Tracking System, with three different subdetectors: Silicon Pixel Detector (SPD), Silicon Drift Detector (SDD) and Silicon Strip Detector (SSD).

Silicon drift detectors (SDDs): they are the intermediate two layers of the ITS. The SDD use the time necessary to electrons, produced by ionizing particle crossing the detector, to drift towards the collecting anodes to determine the position of the particle along the drift direction. This technology provides a good resolution with a limited number of readout channels and a low material budget.
Silicon strip detectors (SSDs): they are the outer layers of the ITS and are equipped with double sided silicon detectors, which provide a two-dimensional measurement of the track position. Their spacial information are used for the matching of the tracks from the ITS to the TPC, being the closest layers to the TPC.

Further details on the ITS sub-detectors are given in Tab. 3.1.

Parameter	**SPD**	**SDD**	**SSD**
Material budget per layer (%X_0)	1.14 - 1.14	1.13 - 1.26	0.83 - 0.86
Spatial resolution $r\phi$ (μm)	12	35	20
Spatial resolution z (μm)	100	25	830
Two track resolution $r\phi$ (μm)	100	200	300
Two track resolution z (μm)	850	600	2400
Active cell size (μm^2)	50×425	202×294	95×40000
Number of readout channels (k)	9835	133	2603

Tab. 3.1: Details about the material budget and spatial resolution of the ITS sub-detectors.

The identification of low momentum particles via specific energy loss is entrusted to the SDDs and SSDs, which are equipped with ADC readout electronics. The ITS allows a primary and secondary vertex reconstruction with a resolution better than 100 μm and extends the tracking of particles with p_{T} lower than 80 MeV/c.

3.2.2 The Time Projection Chamber

The ALICE Time Projection Chamber (TPC) is the main detector of the central barrel covering a sensitive volume of 88 m^3. The TPC is 500 cm long, and the inner and the outer radius are of 80 and 250 centimetres respectively. The acceptance coverage in pseudo-rapidity of the TPC is $|\eta| < 0.9$. Charged particles that travel in the TPC ionise the gas along their path, liberating electrons that drift towards the end plates of the detector. Each end plate is equipped with 36 readout chambers, arranged in 18 sectors, covering 20° in azimuth each. The gas mixture employed to fill the TPC during the LHC Run 2 is composed by Ar and CO_2. A schematic view of the TPC layout is shown in Figure 3.5.

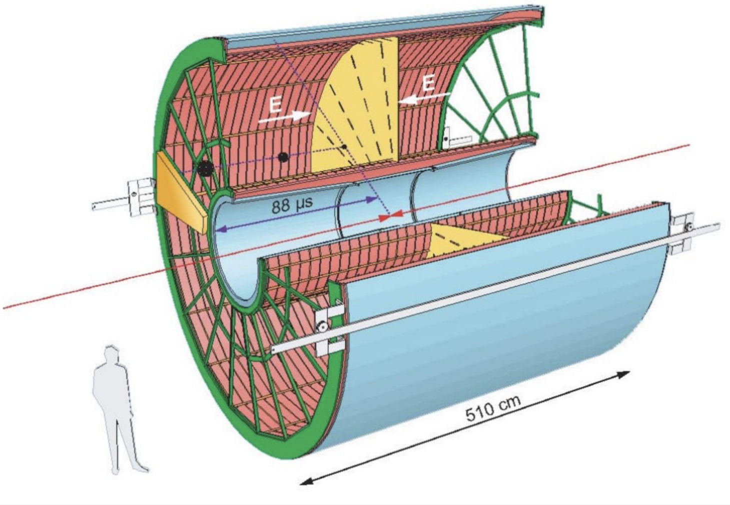

Fig. 3.5: Layout of the ALICE Time Projection Chamber.

Within the drift volume of the TPC, an electric field of 400 V/cm is achieved by applying -100 kV at the central electrode that divide the gas volume into two specular drift regions. The finely segmented field cage at the inner and outer wall of the TPC provides a very high level of homogeneity of the drift field. The end-cap readout chambers are composed by a system of Multi Wire Proportional Chambers (MWPC) with cathode pad readout. Each sector is segmented by pads organized in rows and the longitudinal coordinate is given by the drift time. Thanks to this segmentation, charged particles can be tracked and identified with up to 159 3-dimensional space points (TPC clusters), including also the specific energy loss information for the particle identification.

3.2.3 V0 system

The V0 [114] system consists in two arrays of scintillator counters, V0A and V0C, covering the pseudo-rapidity regions of $2.8 < \eta < 5.1$ and $-3.7 < \eta < -1.7$, respectively. The V0A is located 340 cm from the nominal interaction point, on the opposite side to the muon spectrometer, while the V0C is placed in front of the hadronic absorber, 90 cm from the interaction point. Each of the V0 arrays is segmented in four rings in the radial direction, and each ring is divided in eight sections in the azimuthal direction, as shown in Figure 3.6.

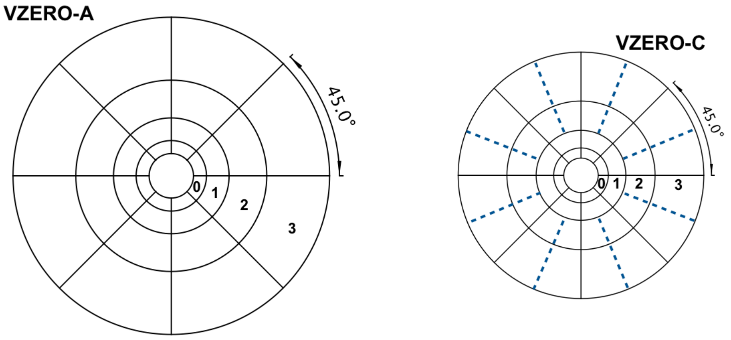

Fig. 3.6: Sketches of V0A (left) and V0C (right) arrays showing their segmentation. Scintillator thicknesses are 2.5 and 2 cm, respectively. The scintillator segments on both sides of the dashed lines are connected to the same photomultiplier tube.

The main function of the V0 detectors is to provide the Minimum bias trigger (defined in the following section) of ALICE and to separate beam-beam interactions from background events such as beam-gas interactions. Furthermore, the signal collected in V0s is also used to estimate the beam luminosity and the charged-particle multiplicity in all collision systems.

3.3 Data acquisition and reconstruction in ALICE

3.3.1 Trigger system

The ALICE trigger system is composed by a low level hardware trigger, handled by the Central Trigger Processor (CTP) [115] and a software trigger managed by the High-Level Trigger [116] system (HLT). The CTP is in charge of taking a decision for every bunch crossing and providing a trigger signal to the readout electronics of the detectors in case of positive trigger conditions. Owing to the different requirements of the ALICE detectors, there are three global levels implemented in the ALICE hardware trigger: L0, L1 and L2. The fastest level of the trigger, L0, has a latency of 900 ns and provides a strobe to detectors with fast electronics. Furthermore L0 is in charge of inhibiting data taking for all detectors in an affected cluster. The next trigger level, L1, arrives at the detector 6.5 μs after the interaction takes place, where most of the trigger inputs are available, and therefore major rate reductions can be made. The final decision is taken after 88 μs, thanks to the L2 trigger, which gathers input coming from slow detectors such as the TPC. If the L2 decision is positive, events are sent to the HLT and to the Data Acquisition (DAQ) system. It is worth to mention that a dedicated trigger level, called LM, provides the strobe to the TRD only, with a latency of 650 ns.

When the CTP trigger signal is propagated, the raw data from the detectors are collected through optical connections into local computers nodes, which are connected to all the ALICE subdetectors. The raw data in the nodes are processed to build a fraction of the full event. Each fraction is then sent, with a data rate up to 20 GB/s, to the Global Data Collectors (GDCs) where they are assembled, together with the HLT output, in the full event.

The HLT performs an online reconstruction of the data, including clusterization and track reconstruction employing fast algorithm such as Cellular Automata [117] and Kalman Filters [118]. The reconstructed event is further selected by the HLT, and events are further compressed. When the event building in the GDC is terminated, the data are stored in a local disk pool waiting to be transferred to the CERN computing centre. The data rate of the full chain during LHC Run 1 and 2 was about 2 GB/s after the HLT compression. In Figure 3.7 the compression factor (also called compression ratio) of the events after the HLT is shown as a function of the number of clusters found in the TPC for a given event [119].

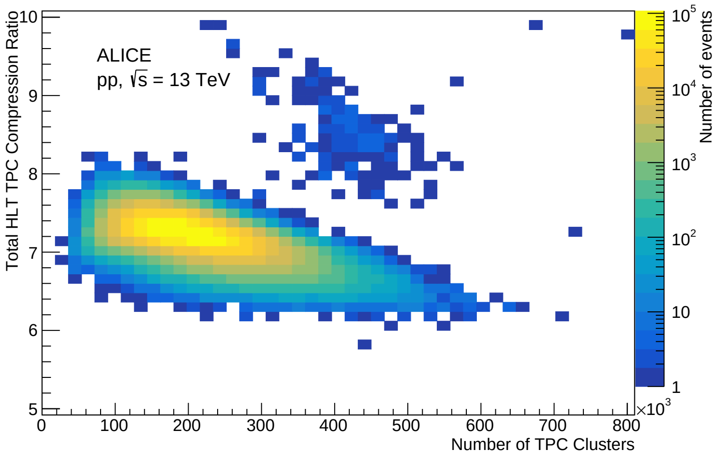

Fig. 3.7: Total HLT TPC data compression ratio in Run 2 on 2017 pp data as a function of the input data size expressed in terms of the number of TPC clusters.

3.3.2 Event reconstruction

The offline event reconstruction starts at the single detector level: all the signals collected in each sub-detector are converted into a space-time information and adjacent particle hits are merged to form a *cluster*. Additional information, such as

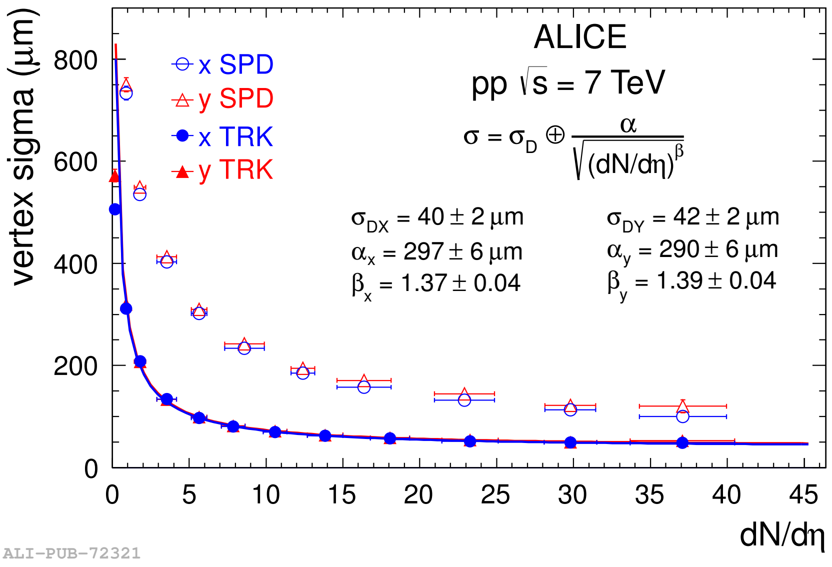

Fig. 3.8: Primary vertex position resolution in pp collision at $\sqrt{s} = 7$ TeV with SPD-tracklets (SPD) and full tracks (TRK) [108].

the TPC signal amplitude employed for PID, are directly attached to the cluster. After the clusterization step, primary vertex and track reconstruction start.

The primary vertex can be reconstructed either by using only the ITS SPD, or globally by exploiting the full reconstructed tracks. While the latter method is more accurate, the former is employed for a first estimate of the primary vertex position which is used by the tracking algorithm to speed up the process. The SPD reconstruction algorithm starts as follows: two clusters belonging totwo different layers of the SPD within the same azimuthal acceptance window are connected to form a segment called *tracklet*. The primary vertex position is then estimated by minimizing the distance of closest approach among all the tracklets and removing the outliers. If only one tracklet is found, e.g. in pp collisions, the z position of the vertex can still be computed by exploiting the nominal beam line position in the transverse plane as a constraint. Similarly, the global primary vertex reconstruction is obtained by minimising the distance among the full tracks: the resolution on the primary vertex position obtained by using SPD tracklets and full tracks is shown in Fig. 3.8. The resolution depends on the charged particle multiplicity: in Pb-Pb collisions a resolution of 10 μm is obtained, while the average resolution in pp collisions is around $\sim$ 150 μm [108].

The track reconstruction for the central barrel detectors is based on the Kalman Filter algorithm, which is described in detail in [120]. The reconstruction starts by building the first track seeds in the outermost pads of the TPC which are then propagated inwards: the track parameters are updated at each step with every closest cluster found by the Kalman filter, until the inner wall of the TPC is reached. The TPC

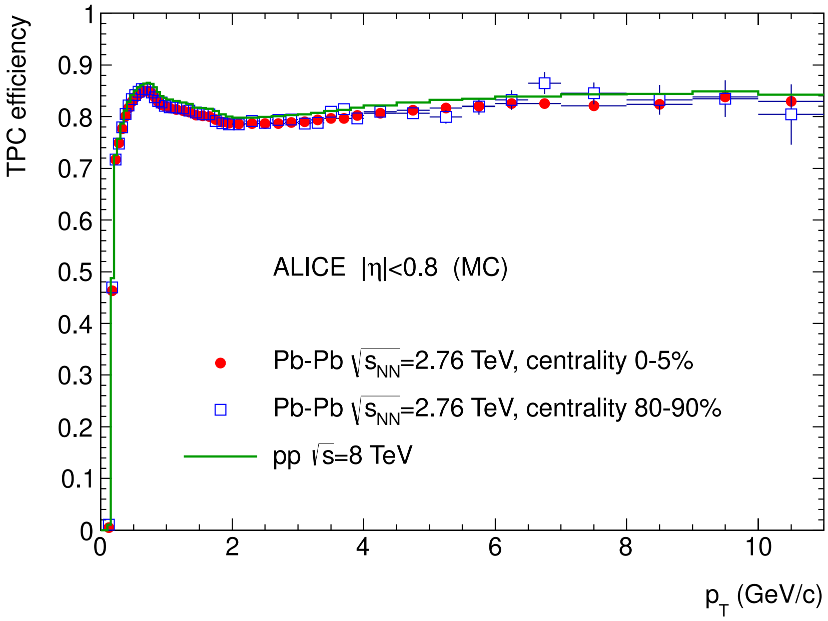

Fig. 3.9: TPC reconstruction efficiency as a function of the transverse momentum in pp and Pb–Pb collisions from [108].

reconstruction efficiency as a function of the transverse momentum computed using Monte Carlo (MC) events is shown in Fig. 3.9: the drop for $p_{\mathrm{T}} <$ 0.5 GeV/c is caused by energy loss in the detector material.

The reconstructed TPC tracks are then propagated to the outermost layer of the ITS, becoming the seeds for track finding in the ITS. Each seed is propagated inward and updated at each ITS layer by all clusters within a distance window, taking into account positions and errors. The result of each update is iteratively saved as a new seed: for each TPC track a tree of track hypotheses in ITS is built. Once the complete tree of prolongation candidates for the TPC track is built, the candidates are sorted according to their reduced χ^2: only the highest quality candidate from each hypothesis tree is added to the reconstructed event. A special treatment is applied to the track seeds with shared clusters: first an attempt is made to find alternative candidates in the involved trees. In the case of a failure, the worse track of the two (in terms of χ^2) is labeled with a flag indicating that it may contain wrongly matched ("fake") clusters. The ITS-TPC matching efficiencies as a function of p_{T} are shown in Fig. 3.10 for both data and MC in pp collisions at $\sqrt{s} = 7$ TeV (left panel) and Pb–Pb collisions at $\sqrt{s_{\mathrm{NN}}}$ = 2.76 TeV (right panel) [108].

Finally, a standalone ITS reconstruction is performed with those clusters that were not used in the ITS–TPC tracks, with an algorithm similar to the TPC standalone one. The ITS standalone tracking is employed to recover the TPC reconstruction efficiency drop at low p_{T}, where particles are affected by energy loss and multiple scattering in the detector material. The tracks obtained with clusters in both the ITS and the

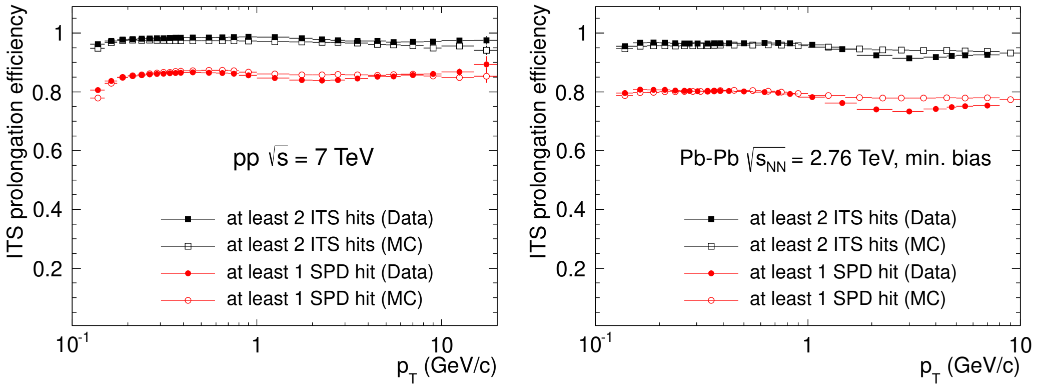

(a) **(b)**

Fig. 3.10: ITS–TPC matching efficiency vs. p_{T} for data and Monte Carlo for pp (left) and Pb–Pb (right) collisions from [108].

TPC detectors are then back-propagated outwards to match the clusters in the TRD and in the TOF and the signals in EMCAL, PHOS and HMPID. Then, an inward fit is performed on the full tracks which are finally propagated to the point of closest approach to the beam line. At this stage, if the number of tracks is greater than two, the global primary vertex algorithm is employed to compute the best vertex position. Fig. 3.11 shows the resolution on $1/p_{\mathrm{T}}$ for tracks, which is related to the p_{T} resolution by the formula:

$$\frac{\sigma_{p_{\mathrm{T}}}}{p_{\mathrm{T}}} = \frac{\sigma_{1/p_{\mathrm{T}}}}{1/p_{\mathrm{T}}} \tag{3.4}$$

Tracks can be reconstructed with a resolution between 1% and 10% in the momentum range from 0.1 to 100 GeV/c.

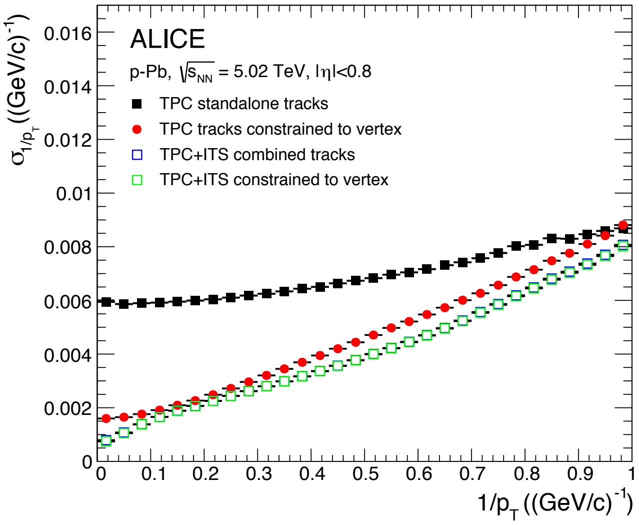

Fig. 3.11: Resolution on the $1/p_{\mathrm{T}}$ parameter as a function of $1/p_{\mathrm{T}}$ in p-Pb collisions. The resolution is reported for $1/p_{\mathrm{T}}$ because this quantity can be extracted directly from the Kalman filter fit.

The reconstruction of the secondary vertices, which has been extensively employed in this work, will be described in the next chapter.

3.3.3 Particle identification

The ALICE detector is suited for the identification of charged particles (PID). PID is performed in a wide range of transverse momentum by using the information from the ITS, the TPC, the TOF and the HMPID. The ITS and the TPC provide the Particle Identification measuring the specific energy loss of the charged particles while the TOF detector uses the time of flight. Finally, the HMPID gives the $\beta = v/c$ of the particles from the measurement of the Cerenkov angle. In the following, only the PID with TPC, which is relevant for this work, will be described. The TPC determines the specific energy loss ($\mathrm{d}E/\mathrm{d}x$) and the momentum of each particle traversing the detector gas. The charge deposited by the passing particle is measured by up to 159 padrows through the ionisation process. The energy loss as a function of the momentum in TPC can be derived starting from the Bethe-Bloch formula, and parametrized following the work of the ALEPH collaboration[121] as:

$$f(\beta\gamma) = \frac{P_1}{\beta^{P_4}}\left(P_2 - \beta^{P_4} - \ln\left(P_3 + \frac{1}{(\beta\gamma)^{P_5}}\right)\right), \tag{3.5}$$

where β is the particle velocity, γ is the Lorentz factor and P_{1-5} are parameters obtained from a fit to the experimental data. A more empirical but effective parametrization for the response function is given employing splines, as it is shown in Fig. 3.12. To assess if a track is compatible with a specific particle species, $^{3}\mathrm{He}$ or π in the case of $^{3}_{\Lambda}\mathrm{H}$ decays, the difference between the measured S_{meas} and the expected S_{exp} signal is computed as:

$$n\sigma^{^3\mathrm{He},\pi} = \frac{|S_{meas} - S_{exp}|}{\sigma^{^3\mathrm{He},\pi}} \tag{3.6}$$

where $\sigma^{^3\mathrm{He},\pi}$ is the resolution on the energy loss signal for each species. The $\mathrm{d}E/\mathrm{d}x$ resolution is about 5.2% in pp collisions and 6% in Pb–Pb collisions [108].

3.3.4 Centrality determination

As already discussed in Section 1.3.1, the geometry of heavy-ion collisions is characterized by the impact parameter b, which connects the centre of the two colliding nuclei in the plane transverse to the beam direction. However, this quantity cannot be measured directly but a Glauber Model has to be used to correlate the impact parameter to other variables, such as the energy deposited in the ZDCs or the charged particle multiplicity [122]. A useful quantity to describe the collision is the centrality, which is defined as the percentile of the hadronic cross section corresponding to a particle multiplicity, or an energy deposited above a given threshold. Following

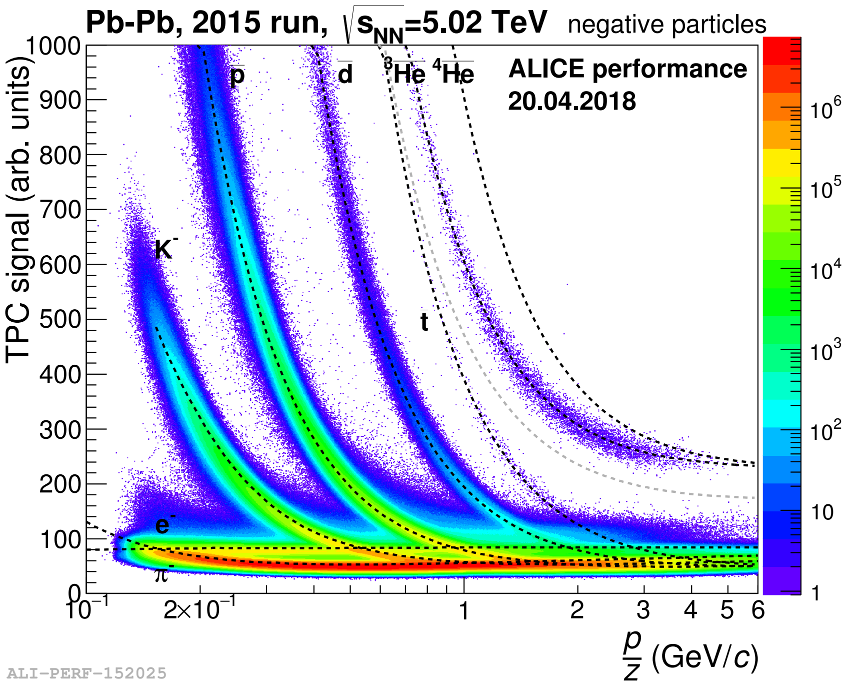

Fig. 3.12: Specific energy loss as a function of the rigidity (p/z) for different anti-particles in Pb–Pb collisions at $\sqrt{s_{\mathrm{NN}}}$ = 5.02 TeV from [108].

this definition, centrality can be expressed as a percentage of the total hadronic interaction cross section of the colliding nuclei σ_{AA}:

$$c(b) = \frac{1}{\sigma_{AA}} \int_0^b \frac{d\sigma}{db'} db', \tag{3.7}$$

where $\sigma_{AA} = \int_0^\infty \frac{d\sigma}{db'} db'$. Assuming a monotonic dependence on the impact parameter of both the charged particle multiplicity (N_{ch}) and the energy deposit at zero degrees (E_{ZDC}), the centrality could be expressed as:

$$c(b) \approx \frac{1}{\sigma_{AA}} \int_d^\infty \frac{d\sigma}{dN'_{ch}} dN'_{ch} \approx \frac{1}{\sigma_{AA}} \int_0^{E_{ZDC}} \frac{d\sigma}{dE'_{ZDC}} dE'_{ZDC} \tag{3.8}$$

Under the same assumption the total cross section can be replaced with the number of observed events n:

$$c(b) \approx \frac{1}{\sigma_{AA}} \int_d N_{ch}^{\infty} \frac{dn}{dN'_{ch}} dN'_{ch} \approx \frac{1}{\sigma_{AA}} \int_0^{E_{ZDC}} \frac{dn}{dE'_{ZDC}} dE'_{ZDC} \tag{3.9}$$

The centrality determination from the particle multiplicity can be performed with the V0 detectors as shown in Figure 3.13. The distribution of the sum of the signal provided by the V0A and V0C detectors is fitted with a function taken from a MC Glauber model (see Sec. 1.3.1) to connect this experimental quantity with the impact parameter of the collision.

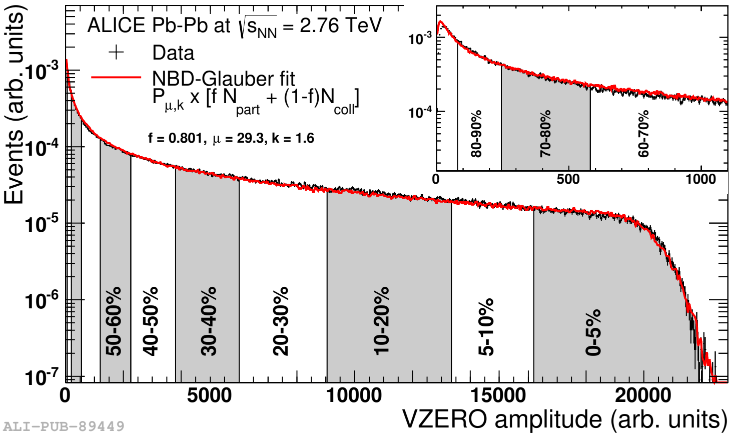

Fig. 3.13: Distribution of the V0A+V0C amplitude. The centrality percentiles are determined integrating the distribution while the red line represents the Glauber fit.

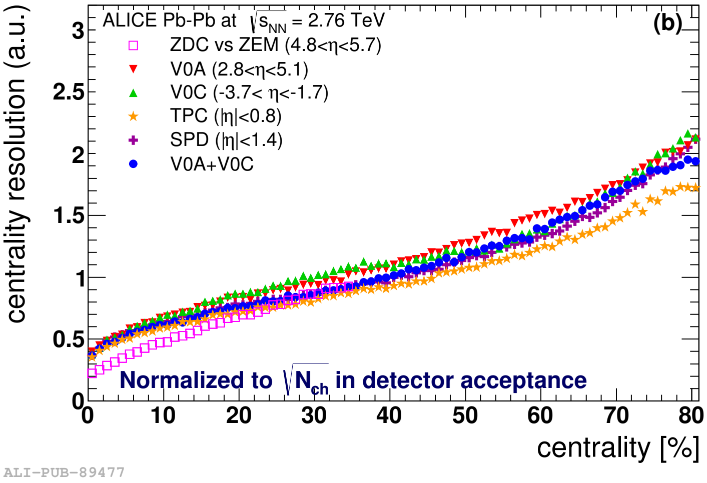

Fig. 3.14: Centrality resolution for different estimators in the ALICE experiment [122].

The same fit can be performed on the distribution of the number of the clusters on the second layer of SPD or on the distribution of the number of TPC tracks. The performance of the difference centrality estimators are compared in Fig.3.14.

3.3.5 ALICE offline software

The ALICE offline software is based on the ROOT package, which is developed and maintained at CERN [123]. ROOT is an object-oriented programme originally designed for particle physics research, even though it is also used in other applications such as astronomy and data mining. It is mainly written in C++ but integrated with other languages such as Fortran, Python, and R. The ALICE software is included in a custom extension of the ROOT package named AliRoot. AliRoot is specifically designed to provide a set of classes and macros to analyze data coming from the ALICE experiment. It also allows full simulations of pp, p-Pb and Pb-Pb collisions using event generator codes such as PYTHIA [124] and HIJING [125] and different transport codes (FLUKA [126], GEANT3 [127], GEANT4 [128]). The geometry and material budget of the experimental apparatus are precisely coded by means of the ROOT geometrical modeler. Finally, the code employed by users in the analysis is contained in the AliPhysics framework, developed by the ALICE data analysis group. The reconstruction of the collected data, the data analyses, and the MC simulations are performed by exploiting the Worldwide LHC Computing Grid (WLCG) [129], a federation of 170 computing centers in 42 countries designed to cope with the data collected by all the LHC experiments.

4

Machine learning

The term *machine learning* (ML) is employed to define a very wide range of algorithms that can automatically learn patterns from the data without requiring an ad-hoc programming (just like human learning does) [130] [131]. Since this definition is extremely general, in the last fifteen years ML techniques have been applied to solve a tremendous amount of problems in different fields: medicine, biology, finance, marketing, robotics, just to cite a few of them. Nowadays, ML has become a very popular tool in High-Energy Physics for dealing with the large amount of data produced by the experiments, and ML techniques have been successfully employed in all the High-Energy Physics (HEP) sectors: triggering, track reconstruction, particle identification, event and candidate selection. In this work, the ${}^{3}_{\Lambda}\mathrm{H}$ signal selection has been performed by using a popular ML algorithm, the Boosted Decision Tree (BDT). This chapter is dedicated to briefly introduce the main concepts of ML and to describe the BDT algorithm.

4.1 Supervised learning

Supervised learning is a subcategory of ML well known in HEP. Supervised learning algorithms are employed for discriminating between two or more classes, signal and background in our case, starting from a set of examples called *training set*. Each element of the training sample, a ${}^{3}_{\Lambda}\mathrm{H}$ candidate in the case of this thesis, has a label containing its class (signal / background), which is known a priori: the training process fixes the internal parameters of the learning algorithm in order to maximize the separation power among the classes. In this thesis, the training set will be composed by Monte Carlo ${}^{3}_{\Lambda}\mathrm{H}$ particles, which will be labelled as signal, and fake ${}^{3}_{\Lambda}\mathrm{H}$ candidates extracted from real data, which will be labelled as background (see Sec. 5.3.1). The goal of the training is to teach to the model a common pattern in data that can be used to classify properly an independent sample, in our case the real data sample. The output of the supervised model, or *score*, is evaluated starting from the candidate properties, which are called *features*. The score is related to the candidate probability of belonging to the different classes. The example in figure 4.1 shows the score distribution for a binary classification model. In order to define which candidates are members of a class and which of the other, it is necessary to choose a score $threshold$: candidates below threshold will be classified as belonging

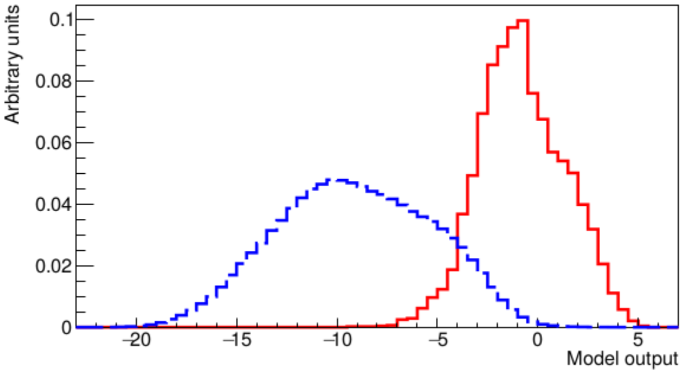

Fig. 4.1: Generic output of a supervised model for a binary classification problem

to the *blue class* and those above as *red class* members. Binary classification models are widely used in particle physics because are well suited to discriminate between the signal and the background distributions.

In order to evaluate the performance of the model the entire labelled data sample is split in two parts: the first one is used to build the training set, the second one represents the *test set*. The test set does not participate in the training process, but it is only used to give an unbiased estimation of the algorithm performance. One of the most common metrics employed for testing the model is the Receiver Operating Characteristic (ROC) [132].

4.1.1 Receiver Operating Characteristic

In a sample containing a positive class P and a negative class N (in HEP they are the signal and the background classes, respectively) the ROC curve is built by plotting the *true positive rate* (TPR) against the *false negative rate* (FPR), as a function of the score threshold.

To give a definition of TPR and FPR, we observe that the elements of the sample can be either classified as positive or negative. This classification may be either correct or wrong, leading to four possible cases as illustrated in Fig. 4.2.

Hence a *true positive* is an element belonging to class P, correctly classified as such, while a *false positive* is an element belonging to class N, wrongly classified as positive. Similarly a *true negative* is an element belonging to class N, correctly classified as such, and a *false negative* is and element belonging to class P, wrongly classified as negative.

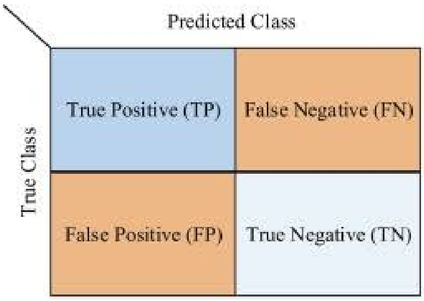

True Class \ Predicted Class		
	True Positive (TP)	False Negative (FN)
	False Positive (FP)	True Negative (TN)

Fig. 4.2: Table illustrating the definition of TPR and FPR, taken from [133]

The overall number of the elements that belong to class P is the sum of the *true positives* and the *false negatives*, while the overall number of the elements that belong to class N is the sum of the *true negatives* and the *false positives*. The TPR is the ratio between the number of the *true positive* elements and the overall number of elements that belong to class P. The FPR is the ratio of the *false positive* elements and the overall number of elements that belong to class N, namely:

$$TPR = \frac{\sum TP}{\sum TP + \sum FN} \qquad\qquad FPR = \frac{\sum FP}{\sum FP + \sum TN} \tag{4.1}$$

In our case, TPR and FPR represent the signal selection and the background rejection efficiencies respectively. The ROC curve is the set of TPR and FPR values that a model can assume for all the possible values of the threshold. An example of ROC curve is in Fig. 4.3. The dashed line represents the ROC curve of a purely random classifier; a good classifier stays as far away from that line as possible toward the top-left corner.

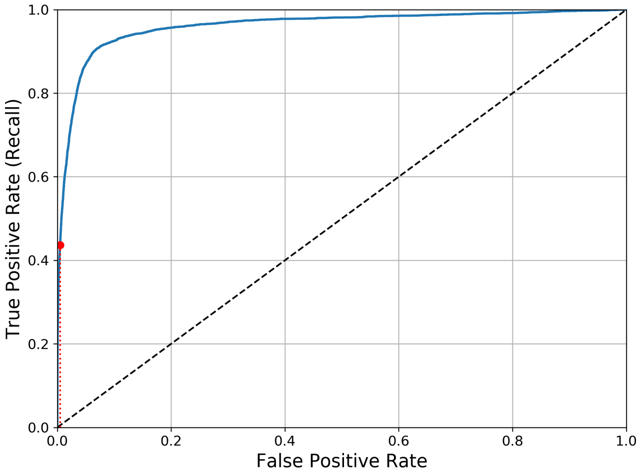

Fig. 4.3: Example of a ROC curve taken from [131]. The red dashed line represents the FPR and TPR for a fixed threshold value.

The most common way employed to evaluate the performance of a classifier is to compute the area under the ROC curve, called AUC: a perfect classifier will have a ROC AUC equal to 1, whereas a random classifier will have a ROC AUC equal to 0.5. The ROC AUC gives a global estimation of the model performance and it is not related to the choice of the threshold value: hence it does not provide any information on the best score threshold to be used for the signal selection. Furthermore, the ROC AUC is independent of the relative abundances of the classes candidates in the dataset used for its evaluation: this is particularly useful for this thesis, where the signal in the training set is far more abundant than in the real data (see Sec 5.1.2).

4.2 Boosted Decision Trees

Boosted Decision Trees(BDT) [134] are a family of ML algorithms employed both for solving classification and regression problems. The usage of BDTs has become very popular in the HEP community in the last years, thanks to their impressive versatility and robustness. The core of every BDT model is the decision tree algorithm (DT). A DT is a flowchart-like binary structure where an internal node represents a feature(or candidate), the branch represents a decision rule, and each leaf node represents the outcome. The topmost node in a decision tree is known as the root node. The DT works by combining a sequence of simple binary tests (each branch of the tree), to classify a data point in terms of its features. Each test consists in a linear threshold applied to one of the features which helps the model to predict the belonging class of every candidate. Figure 4.4 shows a simple example of how the DT works. The training of a DT consists in the automatic procedure that builds the tree recursively starting from the training set. At each building step, the feature and its threshold value that maximizes the separation power between the classes are chosen. This step is then repeated iteratively over the data until all the candidates in a node belong to the same class or an external stopping condition occurs.

The main flaw of the DT is that it is prone to the so-called *overfitting*: this means that the model is able to perfectly classify the training set if deep enough (the depth is defined as the length of the longest path from a root to a leaf), but it does not generalize well to new data. Overfitting occurs when the model memorizes the training set rather than learning a general pattern in the data. To overcome this problem, BDT algorithms combine numerous shallow trees using for each a subsample of features. In particular, in the *boosting* procedure the DTs are constructed sequentially taking care of compensating the misclassified candidates of the previous trees. The resulting model, the BDT, maintains high performances both on the training and the test set.

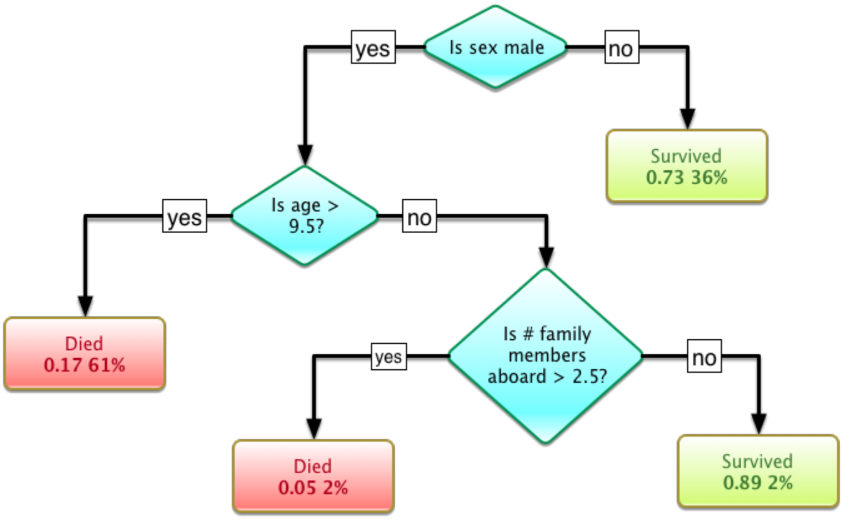

Fig. 4.4: Simple scheme of a decision tree. This example uses the Titanic data set for predicting whether a passenger will survive or not. The model uses 3 features from the data set, namely sex, age and sibsp (number of spouses or children along). The decision tree is drawn upside down with its root at the top. In the image, the text in black represents the test, namely *internal node*, based on which the tree splits into *branches*. The end of the branch that does not split anymore is the decision/*leaf*, in this case, whether the passenger died or survived, represented as red and green text respectively. Since this DT is not a perfect classifier, the DT leaves contain samples from both the classes. Under each leaf node is probability of survival given as a decimal value and the percentage of the samples filtered into each leaf.

4.2.1 XGBoost

One of the most efficient way to perform the boosting is known as *Gradient Boosting* [131]. The first step of this technique is to define an *objective function* $f(\vec{\theta})$, where $\vec{\theta}$ are the undetermined parameters that we need to learn from data. The function $f(\vec{\theta})$ indicates how good are the coefficients of model $\vec{\theta}$ at fitting the training data. The objective function is composed by the training loss $\mathrm{L}(\vec{\theta})$, which measures how predictive the model is with respect to the training data, and an additional regularization term used to control the complexity of the model. A common choice of $\mathrm{L}(\vec{\theta})$ is the mean squared error, which is given by:

$$\mathrm{L}(\vec{\theta}) = \sum_i (y_i - \bar{y}_i)^2$$

where y_i is the label of the training candidate and $\bar{y}_i$ is the corresponding prediction of the model. Then the Gradient Boosting algorithm tries to minimize $f(\vec{\theta})$ by using the gradient descent method[135]. The optimization of the objective function is performed iteratively and at each stage the tree that minimizes the loss for the current model configuration is built. The algorithm used in this thesis is an optimized implementation of Gradient Boosting available in the popular Python library *XGBoost* [136], which stands for Extreme Gradient Boosting. This package was initially developed by Tianqi Chen as a part of the Distributed (Deep) Machine Learning Community (DMLC), and it aims at being extremely fast, scalable and portable. Indeed, XGBoost is often an important component of the winning entries in ML competitions. The XGBoost Classifier works assigning to each candidate a score related to its features for each tree. The output of the BDT is given by the sum of all the tree scores, as exemplified in Figure 4.5.

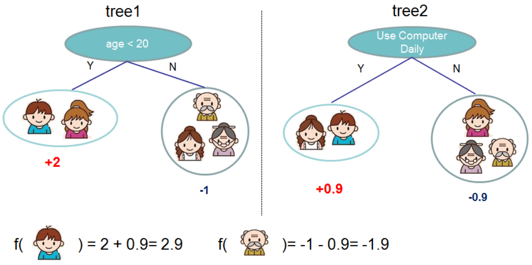

Fig. 4.5: Score assignment in the XGBoost BDT: the algorithm tries to determine whether someone will like a hypothetical computer game. The prediction scores of each individual tree are summed up to get the final score.

4.2.2 Tuning the BDT

The XGBoost Classifier has many hyperparameters that control the complexity of the model. Their tuning is important to enhance the performance of the BDT and to prevent overfitting. In this thesis, the tuning is based on calculating the *k-fold cross validation error* for different combinations of the parameters. In the k-fold cross-validation [131], the training sample is randomly divided into k equal sized subsamples. The training is then performed k times, each time excluding one of the subsamples from the training data and using it as a validation sample. The metrics employed to evaluate the BDT performance on the validation set is the ROC AUC score. The k ROC AUCs are then averaged to produce a single performance estimation. An example of 5-fold cross-validation is shown in Figure 4.6.

This process is repeated multiple times, for different combinations of the hyperparameters. The hyperparameter configuration that maximises the average ROC AUC among k folds is then chosen for the final training of the BDT. The sampling of the hyperparameter space can be done randomly or following a grid search scheme, but in this thesis a more refined approach has been employed, called *Bayesian optimization* [137, 138]. The Bayesian optimization is a method for finding a minimum/maximum of a computational expensive target function ***f(x)***, in this case the cross-validation error. The method works by building a posterior distribution of functions for describing ***f(x)*** starting from a multivariate Gaussian distribution. As the number of observations grows, the posterior distribution improves, and the algorithm becomes more certain of which regions in the parameter space are worth exploring and which are not. This procedure is designed to minimize the number of

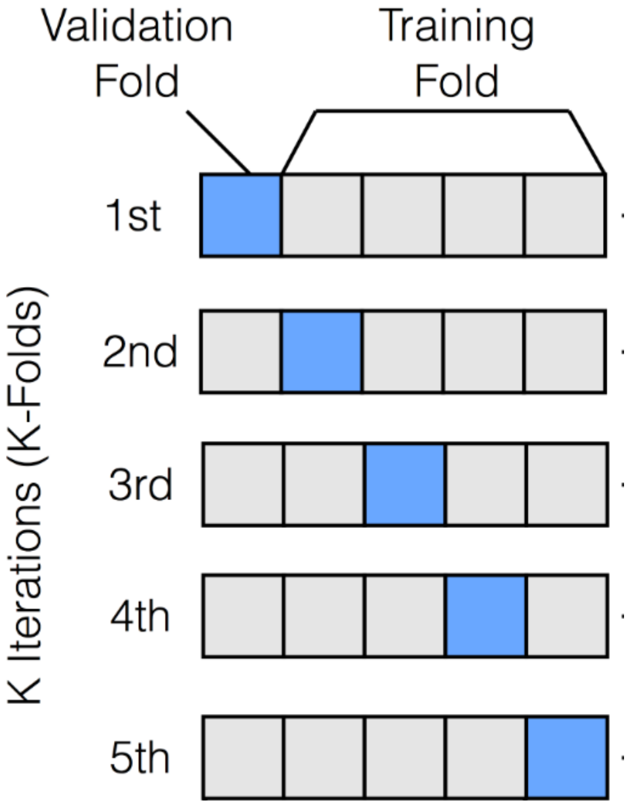

Fig. 4.6: Schematization of the 5-fold cross-validation procedure

steps required to find a point that is close to the minimum. A brief description of the hyperparameters that have been optimized in this thesis is reported hereafter:

- n_estimators: Number of trees in the BDT
- max_depth: Maximum depth of a tree
- eta: learning rate of the algorithm: it controls the step size of the gradient descent algorithm
- gamma: Minimum loss reduction required to make a further partition on a leaf node of the tree. The larger gamma is, the more tolerant to data-model deviation the algorithm will be
- min child weight: it is related to the minimum number of candidates needed in a node in order to be split
- colsample_bytree: it specifies the fraction of features used in each tree
- subsample: it specifies the fraction of candidates to be subsampled in each tree.

4.2.3 Feature importance

One of the main advantages of using a BDT with respect to more complex algorithms such as Deep Neural Networks is that the interpretability of the model is easier. In particular, it is possible to evaluate exactly the impact of each feature on the model output, the so-called *feature importance*. In recent years, the evaluation of the feature importance for tree models made important step forward thanks to an innovative method based on game theory [139]. The SHAP (SHapley Additive exPlanations) method is an approach that allows us to evaluate the contribution of each feature to the model output. The SHAP method is based on the Shapley value, a concept introduced by Lloyd Shapley in 1953 [140]. The Shapley value is a measure of the contribution of each player to the total value of a coalition. In the context of machine learning, the Shapley value is used to evaluate the contribution of each feature to the model output, and it is calculated by averaging the marginal contributions of each feature to the model output. The marginal contribution of a feature is the difference in the model output when the feature is present or absent. The variables that are more important for the model are those that have a higher marginal contribution, and Shapley values consequently. An example of SHAP feature importance is shown in Fig. 4.7.

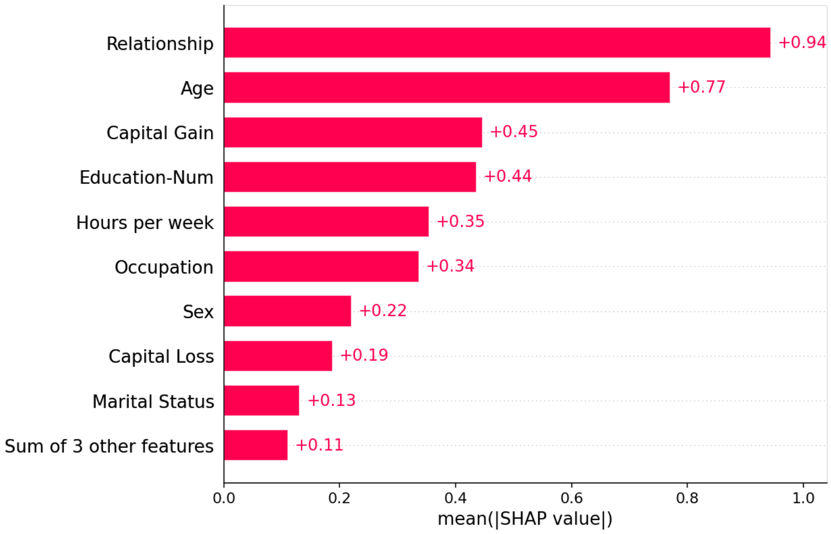

Fig. 4.7: SHAP feature importance for the BDT trained on the adult census income dataset available in the Scikit-learn library [141]. The features are ordered by their mean SHAP value.

5

Precision measurements of the ${}^{3}_{\Lambda}\mathrm{H}$ lifetime and B_{Λ}

In this Chapter, the most precise measurements to date of the ${}^{3}_{\Lambda}\mathrm{H}$ lifetime ($\tau_{{}^{3}_{\Lambda}\mathrm{H}}$) and Λ separation energy B_{Λ} are presented. The measurements have been performed by analysing the Pb–Pb data sample collected by ALICE at $\sqrt{s_{\mathrm{NN}}}$ = 5.02 TeV during 2018, and by selecting the ${}^{3}_{\Lambda}\mathrm{H}$ signals with BDTs. The measurements have been published with a letter on arXiv [142] and are currently under review for publication in Physical Review Letters.

5.1 Data sample

The measurements presented in this Chapter are based on the data sample collected by ALICE during 2018, the last year of the LHC Run 2 data taking. The data sample consists of Pb–Pb collisions at $\sqrt{s_{\mathrm{NN}}}$ = 5.02 TeV with an interaction rate peak of 7.5 kHz. Two magnetic field configurations were employed during the data taking: +0.5 T and -0.5 T. Three different triggers were used to select the events of interest:

- the *Minimum bias trigger*(MB): requires a hit in the SPD or in either two V0 detectors (V0A or V0C): this corresponds to at least one charged particle anywhere in 8 units of pseudorapidity.

- the *Central trigger*: a threshold into the charge deposited in the V0 detectors is set to select the most central collisions. The Central Trigger collects the events in the 0-10% centrality interval.

- the *Semi-Central trigger*: uses the V0 detectors to select the semi-peripheral collisions. It collects the events in the 30-50% centrality interval.

5.1.1 Event selection

The triggered events are selected offline, to reduce possible biases due to different data taking conditions. First, only the primary vertices within a fiducial region of ± 10 cm in the beam direction (z coordinate) from the nominal interaction points are considered: this guarantees a symmetric acceptance and the rejection of beam-gas background events. The distribution of the vertex position in the beam direction is shown in Fig. 5.1.

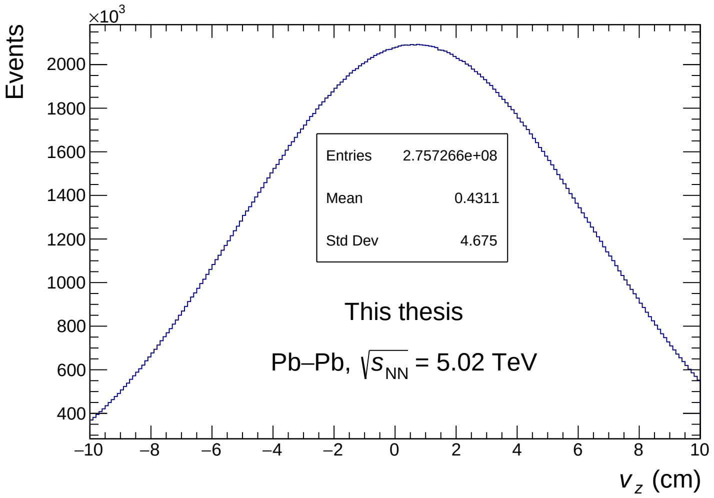

Fig. 5.1: Vertex position in the beam direction: selection of the primary vertices within a fiducial region of ± 10 cm. A shift with respect to the nominal interaction point position is observed in all the Run 2 Pb–Pb analyses, due to an offset of the LHC machine.

Beam-gas events are further rejected by using the V0s time information, as explained in detail in [108]. Few additional selections are applied to reduce the contribution of pileup events, i.e. events containing more than one primary collision vertex: these events could potentially bias the determination of the primary vertex, and consequently the measurement of the decay length of the $^3_\Lambda$H candidate. The first selection is performed on the The first pileup tagging method is based on the maximum distance between two SPD vertices: if two vertices are spaced more than 8 mm the event is tagged as pileup and it is removed. Further methods are applied to reduce the presence of pileup for vertices closer than 8 mm. The first one is based on the number of reconstructed SPD primary vertices with more than n contributors. The quantity of SPD tracklets used to determine the vertex position is the number of contributors. In case a vertex is constructed using only a few tracklets, it may be a fake. Based on previous analyses on the relationship between the number of tracks and the false positive pileup tagging, the value of the parameter n is adjusted to 5 for events with more than 50 tracklets, 3 for events with less than 20 tracklets, and 4 for all other events. This method removes the pileup of collisions occurring either during the same bunch crossing or out of bunch pileup within the SPD readout time (300 ns). The second selection employed to reduce the pileup contribution is based on the position of the global primary vertex. In fact, it has been observed that in presence of pileup events the primary vertex reconstruction algorithms might fail to find the correct primary vertex.

Tab. 5.1: Summary of the event selection applied for to the data sample employed for this analysis.

Data sample	Selections
Pb–Pb 2018	$\lvert V_z\rvert \leq 10$cm
	Reject multiple SPD vertices with more than n contributors
	$\lvert\Delta V_z\rvert \leq 20\sigma_{\mathrm{track}}$, $\lvert\Delta V_z\rvert \leq 10\sigma_{\mathrm{SPD}}$ and $\lvert\Delta V_z\rvert \leq 0.2$ cm

In the left panel of Fig. 5.1 the raw distribution of the difference (ΔV_z) between the reconstructed vertex position obtained with the SPD based method and the track based vertex finding algorithm is shown. The presence of events in which the outcomes of the two methods is different is clearly visible. These discrepancies are filtered at the level of the event selection, picking only events where ΔV_z is less than 20 σ_{track} and 10 σ_{SPD}, where σ_{track} and σ_{SPD} are the resolution of the primary vertex computed with the track based and the SPD only vertex finding algorithms respectively. Furthermore, the ΔV_z is required to be less than 0.2 cm. The effect of these selections is shown in the right panel of Fig.5.2.

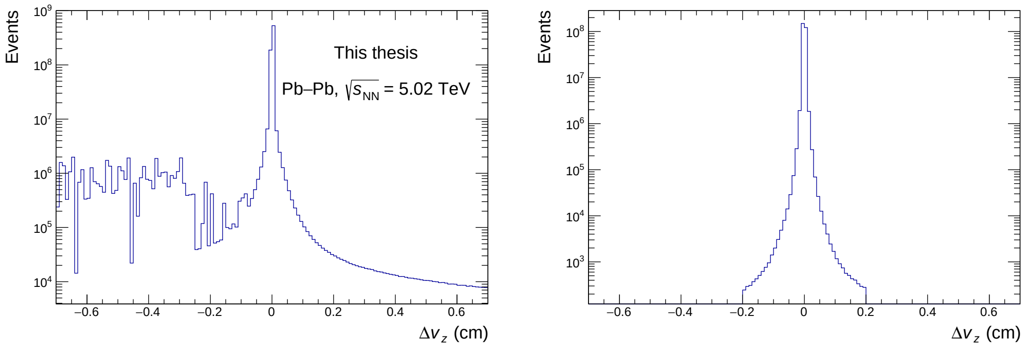

Fig. 5.2: Primary vertex position in the beam direction: ΔV_z distribution before and after the event selection.

The event selections previously described and used in this analysis are summarized in Table: 5.1.

The number of collisions passing the event selection is $\sim$ 270 million. The centrality of each collision is determined through the V0M estimator, as it is explained in Section 3.3.4. The centrality distribution of the selected events is shown in Fig. 5.3: the enhancements in the central (0-10%) and semi-central (30-50%) regions are due to the central and semi-central triggers respectively.

For the analysis of $\tau_{^3_\Lambda\mathrm{H}}$ and B_Λ all the selected events in the 0-90% centrality interval are used.

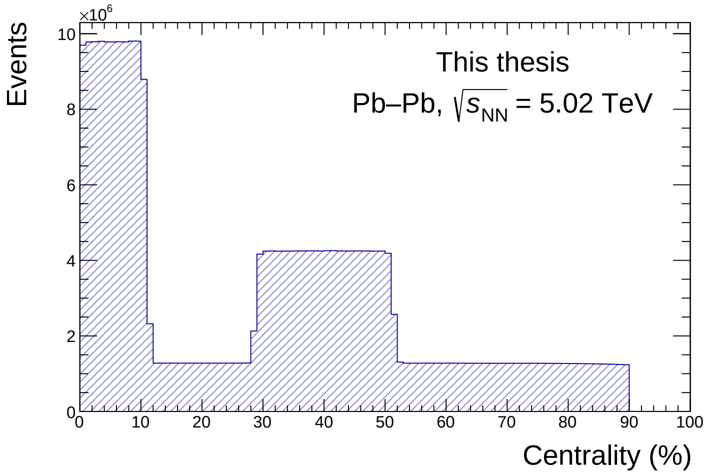

Fig. 5.3: Centrality distribution of the analysed events.

5.1.2 Monte Carlo

A dedicated Monte Carlo sample has been produced to perform the $^{3}_{\Lambda}\mathrm{H}$ and $^{3}_{\overline{\Lambda}}\overline{\mathrm{H}}$ selection and to compute the efficiency and acceptance corrections. The Pb–Pb MC events are generated by using the HIJING[125] event generator. As HIJING does not include hypernuclei, 20 $^{3}_{\Lambda}\mathrm{H}$ and $^{3}_{\overline{\Lambda}}\overline{\mathrm{H}}$ are injected for each event with uniform transverse momentum and rapidity distributions. The $^{3}_{\Lambda}\mathrm{H}$ decay is simulated by the transport code, the GEANT4[128] simulation package, using a decay time constant generated by sampling an exponential distribution with $\tau_{^{3}_{\Lambda}\mathrm{H}}$ chosen equal to τ_{Λ}. The proper decay length ct of the $^{3}_{\Lambda}\mathrm{H}$ can be evaluated as:

$$ct = \frac{M}{p}L \tag{5.1}$$

where M is the mass of the particle, p is the momentum, L is the decay length of the particle in the laboratory frame, and t is the decay time in the rest frame of the $^{3}_{\Lambda}\mathrm{H}$. For a neutral particle, L can be simply computed as the distance between the production and decay vertex:

$$L = \sqrt{(x_{\mathrm{PV}} - x_{\mathrm{SV}})^2 + (y_{\mathrm{PV}} - y_{\mathrm{SV}})^2 + (z_{\mathrm{PV}} - z_{\mathrm{SV}})^2}, \tag{5.2}$$

where PV and SV stand for production and decay vertex respectively. However, for the $^{3}_{\Lambda}\mathrm{H}$, the curvature given by the presence of the magnetic field B should be potentially taken into account. In this case, the decay length in the laboratory frame is given by:

$$L = \sqrt{\text{arc length}^2 + (z_{\mathrm{PV}} - z_{\mathrm{SV}})^2}, \tag{5.3}$$

where the arc length is given by:

$$\text{arc length} = 2R \times arcsin\left(\frac{\sqrt{(x_{\mathrm{PV}} - x_{\mathrm{SV}})^2 + (y_{\mathrm{PV}} - y_{\mathrm{SV}})^2}}{2R}\right), \tag{5.4}$$

with R being the curvature radius of the particle, which is defined as:

$$R = \frac{p_{\mathrm{T}}}{q\mathrm{B}}. \tag{5.5}$$

In our case, taking a B field of 0.5 T, in the transverse momentum range between 1.5 and 10 GeV/c, the curvature radius is between 10 and 67 m, to be compared with the typical decay length of the ${}^{3}_{\Lambda}\mathrm{H}$ which is of the order of $\sim$ 10 cm. This means that the curvature of the ${}^{3}_{\Lambda}\mathrm{H}$ can be neglected, and that the decay length L can be evaluated by using the Eq. 5.2.

The p_{T} and ct input distributions of the ${}^{3}_{\Lambda}\mathrm{H}$ (${}^{3}_{\overline{\Lambda}}\overline{\mathrm{H}}$) sample are shown in Fig. 5.4. The input p_{T} distribution, which is uniform in the range 1.5-10 GeV/c, will be reweighted afterwards in Sec. 5.3.1. The transport of ${}^{3}_{\Lambda}\mathrm{H}$ and ${}^{3}_{\overline{\Lambda}}\overline{\mathrm{H}}$ in the detector material is simulated by GEANT4[128] simulation package. The MC simulation of a full Pb–Pb event, from the generation of the kinematics of the different particles to their transport through the detector volumes, is expensive in terms of computing resources. For this reason only a fraction of the total collected statistics is generated in the MC samples. For this reason the number of events in the MC samples is a fraction of 10% of the collected data. The centrality of the simulated events is computed starting from the impact parameter (b) of the collision provided by HIJING. In order to optimize the use of the computing resources, three MC samples anchored to the 2018 Pb–Pb data sample with different b intervals were produced. These three MC productions correspond to the 0-10%, 10-50% and 50-90% V0 centrality intervals.

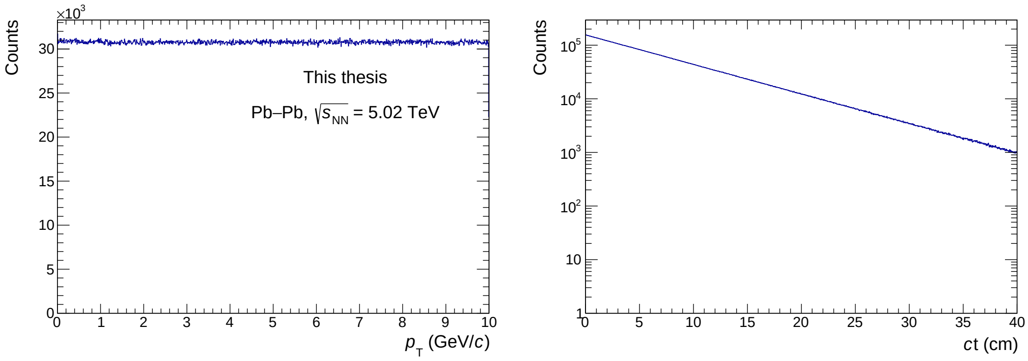

Fig. 5.4: Input p_{T} and ct distributions of the ${}^{3}_{\Lambda}\mathrm{H}$ sample in the MC production.

Variable	Selection
$\|\eta\|$	<0.8
n^{clus}_{TPC}	>70
TPC refit	True
χ^2/n^{clus}_{TPC}	≤ 5

Tab. 5.2: Track selection criteria.

5.2 $^{3}_{\Lambda}\mathrm{H}$ ($^{3}_{\Lambda}\overline{\mathrm{H}}$) reconstruction

5.2.1 Track selection

As anticipated in Sec. 2.2.2, the $^{3}_{\Lambda}\mathrm{H}$ is identified by reconstructing the invariant mass of its decay products. The decay channel analysed in this thesis is the two-body charged one, in which the $^{3}_{\Lambda}\mathrm{H}$ decays into a $^{3}\mathrm{He}$ and a π^{-} with an expected B.R. of $\sim$ 0.25. Since at the LHC energies particles and anti-particles are produced in equal numbers, also the $^{3}_{\Lambda}\overline{\mathrm{H}}$ decay products ($^{3}\overline{\mathrm{He}}$ and π^{+}) are reconstructed. **In the following, $^{3}_{\Lambda}\mathrm{H}$ and $^{3}_{\Lambda}\overline{\mathrm{H}}$ will be summed together and simply referred to as $^{3}_{\Lambda}\mathrm{H}$:** only in Sec. 5.7.1 the $^{3}_{\Lambda}\mathrm{H}$ and $^{3}_{\Lambda}\overline{\mathrm{H}}$ results will be discussed separately. Before the decay vertex reconstruction, few track selections are applied to all the tracks in the event.

First, only tracks with pseudorapidity $|\eta| < 0.8$ are considered, as in this acceptance region the track reconstruction and PID are fully efficient in ALICE. Furthermore, to guarantee a track momentum resolution better than $\sim$ 3% and a TPC dE/dx resolution of $\sim$ 6%, the selected tracks are required to have at least 70 clusters in the TPC. The TPC refit step, which is the last part of the global tracking algorithm (see Sec 3.3.2), is also required. Finally, the χ^2 per TPC cluster is computed in the track fitting procedure and is required to be less than 5. A summary of the track selections is reported in Table 5.2.

5.2.2 Decay vertex reconstruction

As anticipated in Sec. 2.2.2, the decay channel analysed in this thesis is the two-body charged one, in which the $^{3}_{\Lambda}\mathrm{H}$ decays into a $^{3}\mathrm{He}$ and a π^{-} with an expected B.R. of $\sim$ 0.25. The $^{3}_{\Lambda}\mathrm{H}$ reconstruction is performed starting by the invariant mass of its decay products.

The reconstruction of the $^{3}_{\Lambda}\mathrm{H}$ is performed after the primary vertex reconstruction, by exploiting the so-called *V0 finder* algorithm implemented in AliROOT. The V^0 finder was originally developed for the reconstruction of neutral particles decaying into two charged daughters, such as the K_S^0 and the Λ. The basic principle of the algorithm is the matching between two tracks of different sign which are close in the phase space and supposedly come from the decay of the same mother particle. Moreover, the daughter tracks are required to pass some loose quality selection criteria before being stored as V^0 candidates. A simple sketch of the ${}^3_\Lambda$H decay topology is shown in Fig. 5.5.

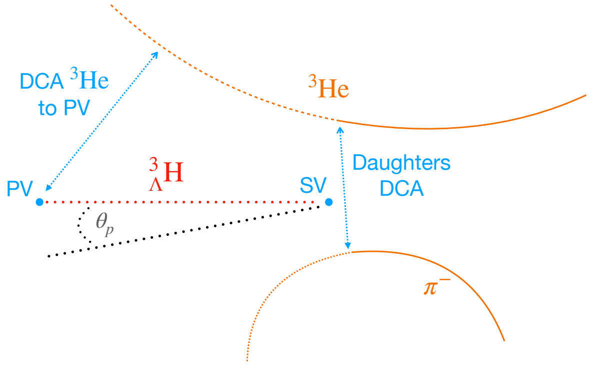

Fig. 5.5: Sketch of the ${}^3_\Lambda$H decay topology.

Few topological variables that are employed to select the ${}^3_\Lambda$H candidates are shown in the sketch and described in the following:

- the *Distance of closest approach* (DCA) between the daughter tracks ($\mathrm{DCA}_{\mathrm{daugh}}$),
- the DCA of the daughter tracks from the primary vertex ($\mathrm{DCA}^{\mathrm{PV}}$). Usually the selection is performed by looking at the DCA projection in the transverse plane, namely $\mathrm{DCA}^{\mathrm{PV}}_{\mathrm{xy}}$,
- the *Cosine of the Pointing Angle*($\cos(\theta_p)$), where θ_p is the angle between the total momentum vector of the daughter pair and the straight line connecting the primary and secondary vertices.

The V^0 finder algorithm has two different implementations in AliROOT: the offline V^0 and the on-the-fly V^0. The first one is executed after the full track reconstruction while the on-the-fly V^0 is already operated during the track fitting. In this thesis, a customized version of the offline V^0 finder is employed for the ${}^3_\Lambda$H reconstruction. The main difference with respect to the standard V^0 finder is that extremely loose selections are applied to the decay topology: the main selection will be performed afterwards by using a machine learning approach. The topological selections applied at the V^0 level are listed in Tab. 5.3: loose selections are applied to the DCA of the daughter tracks and to the $\cos(\theta_p)$.

Variable	Selection
$\mathrm{DCA_{daugh}}$	<1.5 cm
$\mathrm{DCA_{xy}^{PV}}$	>0.01 cm
$\cos(\theta_p)$	>0.9

Tab. 5.3: Topological selections applied at the V^0 level.

The choice of applying soft selections at the V^0 level has a major drawback: the increase in computing time with respect to the standard V^0 finder is more than a factor of 10. To speed up the secondary vertex reconstruction, a dedicated selection on the $^3\mathrm{He}$ and π^- PID is applied during the vertexing procedure. The PID is performed by using the TPC dE/dx information, and by selecting only the daughter tracks with either $n\sigma^{^3\mathrm{He}} = \frac{|S_{meas}-S_{exp}|}{\sigma^{^3\mathrm{He}}} < 4$ or $n\sigma^{\pi} = \frac{|S_{meas}-S_{exp}|}{\sigma^{\pi}} < 4$. To do that, while the π PID is well tuned for all the ALICE data samples, the PID response of the $^3\mathrm{He}$ needs to be carefully calibrated. The calibration is performed in two steps: first the TPC signal of the $^3\mathrm{He}$ candidates is fitted in several rigidity (p/z) intervals by using a Gaussian function and two exponential distributions to model the tails. An example of $^3\mathrm{He}$ signal extraction is shown in Fig. 5.6: the background on the left side of the peak is due to residual triton contamination. Before the signal extraction, a selection on the number of TPC clusters ($\mathrm{n_{clus}^{TPC}} > 100$) is applied to reduce the background due to low quality tracks.

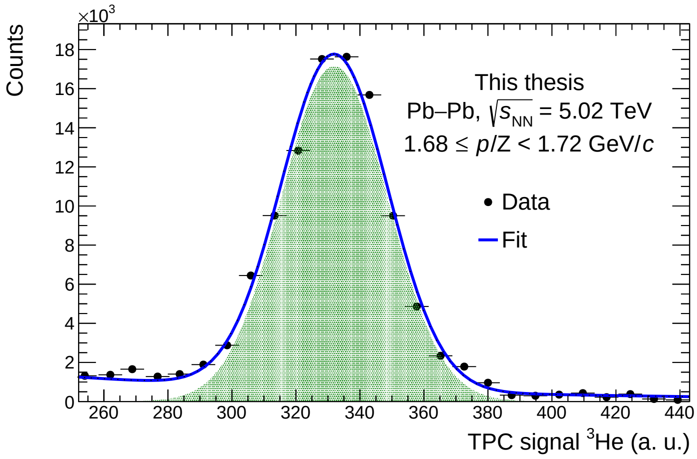

Fig. 5.6: Example of $^3\mathrm{He}$ TPC signal extraction for $1.68 \leq p/z < 1.72$ GeV/c.

In the second step, the mean of the Gaussian distribution with its error is plotted as a function of the rigidity, and the resulting distribution is fitted with the Bethe-Bloch ALEPH parametrisation already described in Sec. 3.3.3. The resulting parametrization is shown in Fig. 5.7. The resolution is extracted with a weighted average of the width of the Gaussian distribution as a function of the rigidity and amounts to $\sim 5\%$.

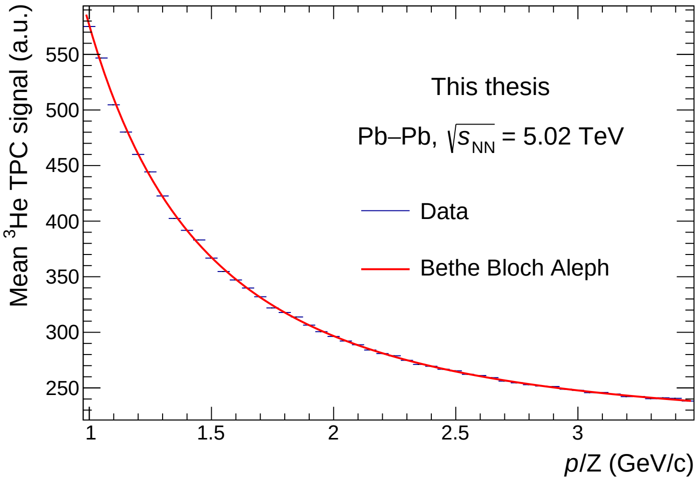

Fig. 5.7: Bethe-Bloch ALEPH [121] parametrization applied to the ^{3}He TPC signal.

The vertexing procedure starts by matching the PID selected ^{3}He track with a PID selected π track of opposite sign: if the doublet satisfies the selections reported in Tab. 5.3, the secondary vertex is fitted by minimizing the relative distance between the daughter tracks. Finally the $^{3}_{\Lambda}$H momentum and energy is reconstructed by combining the information of the two daughter particles. The application of the PID selection to the daughter tracks during the vertexing procedure reduces significantly the computing time: the time needed to reconstruct the $^{3}_{\Lambda}$H candidates using the CERN Grid over the full 2018 ALICE data sample is $\sim$ one day, while it is more than 2 weeks without the PID selection.

After the vertexing, a dedicated interface (analysis task) has been developed to store the topological (e.g $\cos(\theta_p)$), kinematic (e.g. p_{T}), and PID (e.g. $n\sigma^{^{3}\mathrm{He}}$) variables of the reconstructed $^{3}_{\Lambda}$H candidates into ROOT trees. When running over MC productions, few extra variables (e.g. p_{T} of the generated $^{3}_{\Lambda}$H particle) are included in the tree to evaluate the reconstruction efficiency and the resolutions of the reconstructed variables. The efficiency after the vertexing step (also called *pre-selection efficiency*), which includes also the geometrical acceptance of the detector, is shown in Fig. 5.8 as a function of the p_{T} and the ct of the $^{3}_{\Lambda}$H candidates. The efficiency is evaluated by comparing the number of reconstructed $^{3}_{\Lambda}$H candidates with the number of generated $^{3}_{\Lambda}$H particles in the MC sample.

The efficiency grows with the momentum according to the single track efficiency shown in Fig. 3.9, while the efficiency as a function of the ct slightly increases up to $\sim$ 0.35.

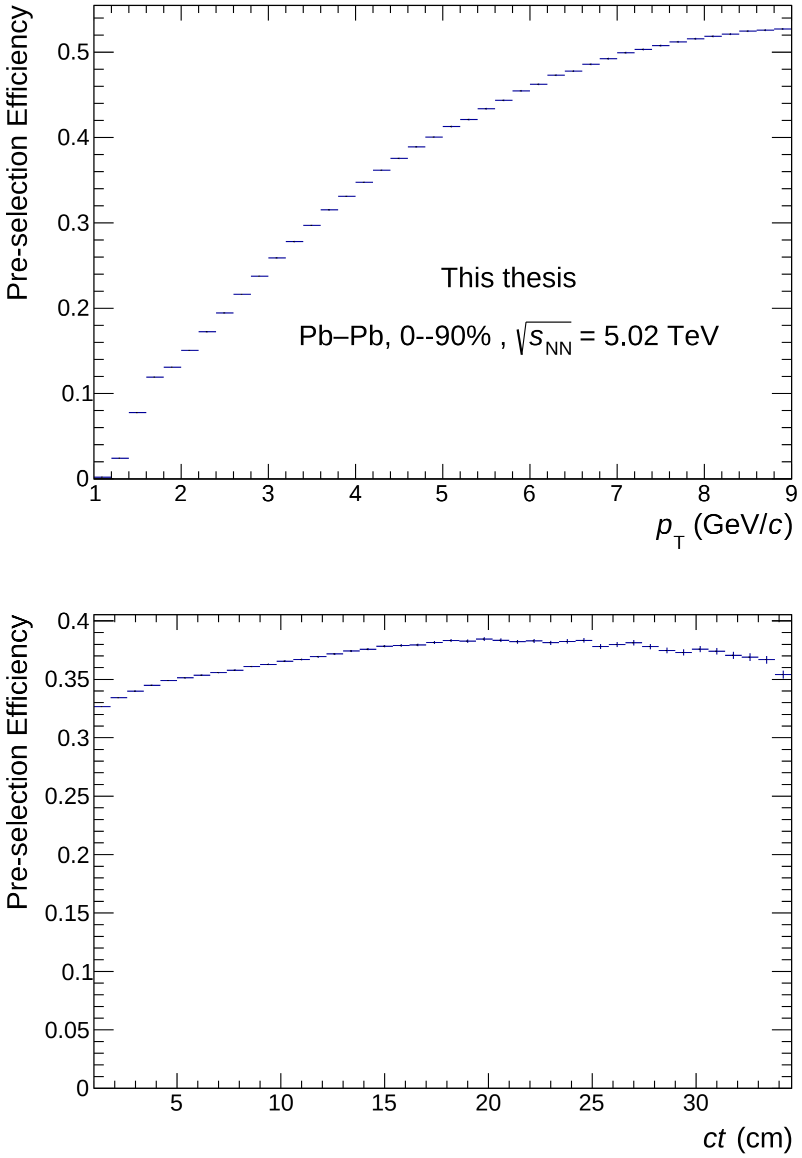

Fig. 5.8: Efficiency of the ${}^{3}_{\Lambda}\mathrm{H}$ reconstruction as a function of the p_{T} and the ct of the ${}^{3}_{\Lambda}\mathrm{H}$ candidates.

5.3 ${}^{3}_{\Lambda}\mathrm{H}$ selection with machine learning

The reconstructed and pre-selected ${}^{3}_{\Lambda}\mathrm{H}$ candidates are stored in ROOT trees that are downloaded to a local server for the offline analysis. As mentioned in the previous Chapter, the ${}^{3}_{\Lambda}\mathrm{H}$ selection is entrusted to the BDT classifier from the XGBoost package [136]. Unfortunately, the XGBoost package is not available in the ROOT framework, so the BDT training and evaluation is performed using the XGBoost Python API. The ROOT Tree files have been converted into a tabular Python format (Pandas Dataframe [143]) using the uproot [144] package. The Pandas Dataframe can be directly used as input for the XGBoost model. The hipe4ml (Heavy-Ion Physics Environment for

Machine Learning) [145] package has been developed to simplify the application of machine-learning techniques for analyses similar to those performed in this work. The library is built on top of commonly used Python packages. In hipe4ml, the typical steps needed to perform a ML analysis in particle physics, such as the data preparation, the model training, the hyperparameter optimization and the model evaluation are implemented in a user-friendly form.

As all the supervised machine learning algorithms, the BDT needs to be trained on a sample of ${}^{3}_{\Lambda}\mathrm{H}$ candidates that are correctly labelled as signal or background. In the following, the signal and the background samples are described.

5.3.1 Training sample

Signal

The signal component of the training sample is composed by the ${}^{3}_{\Lambda}\mathrm{H}$ candidates available in the enriched MC. The MC ${}^{3}_{\Lambda}\mathrm{H}$ candidates undergo to the same reconstruction and selection steps that are applied to the data: the quality of the data-MC agreement has been studied and validated in several V^0 analyses where the abundance of particles produced allows a detailed comparison, and it will also be assessed in the systematic evaluation. The ${}^{3}_{\Lambda}\mathrm{H}$ candidates in the Monte Carlo sample are injected with a flat transverse momentum distribution in the p_{T} interval 0-10 GeV/c. This is done because the ${}^{3}_{\Lambda}\mathrm{H}$ p_{T} shape is poorly known and to collect a large sample also in high p_{T} regions. In order to obtain a transverse momentum distribution closer to the physical one and that could be utilized in the training process and for the computation of the efficiency, the signal p_{T} distribution is reweighted by using the rejection sampling technique. The ${}^{3}_{\Lambda}\mathrm{H}$ p_{T} distribution is sampled from a Blast Wave (B-W) function, which describes the particle production in a thermalized expanding medium. More details on the B-W are given in Appendix. 9. The parameters of the B-W (except for the mass) are taken from the fit to the ${}^{3}\mathrm{He}$ p_{T} spectra published in [146]. The choice of the ${}^{3}\mathrm{He}$ is motivated by the fact that its mass is close to that of the hypertriton and, unlike the ${}^{3}_{\Lambda}\mathrm{H}$ case, helium B-W fits are published and cover the whole centrality interval(0-90%). Five B-W fits are extracted from the ${}^{3}\mathrm{He}$ analysis and they are shown in Fig. 5.9.

The five different p_{T} shapes are employed to reweight the ${}^{3}_{\Lambda}\mathrm{H}$ signal in the MC. The final MC sample is further reweighted to take into account the different centrality distribution between real data and MC: this effect turns out to be negligible for the measurements presented in this Chapter. The final p_{T} distribution is shown in Fig. 5.10.

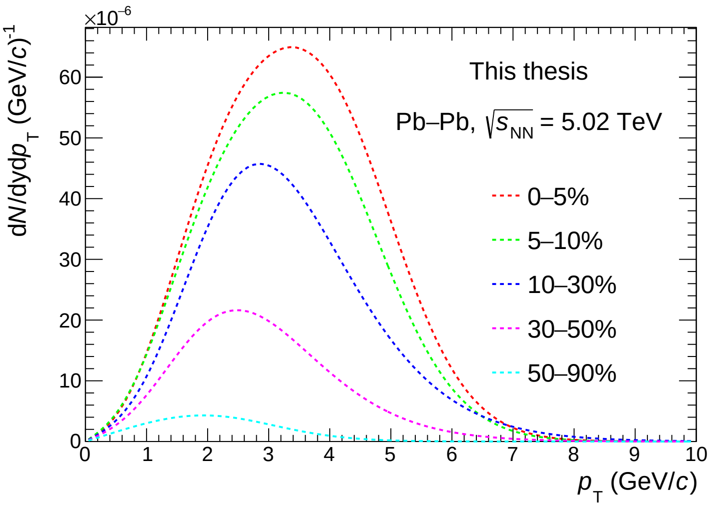

Fig. 5.9: Blast Wave distributions from the analysis of the $^3\mathrm{He}$ production in five centrality classes [146]. These distributions are employed to reweight the p_T shape of the $^3_\Lambda\mathrm{H}$ candidates in the MC.

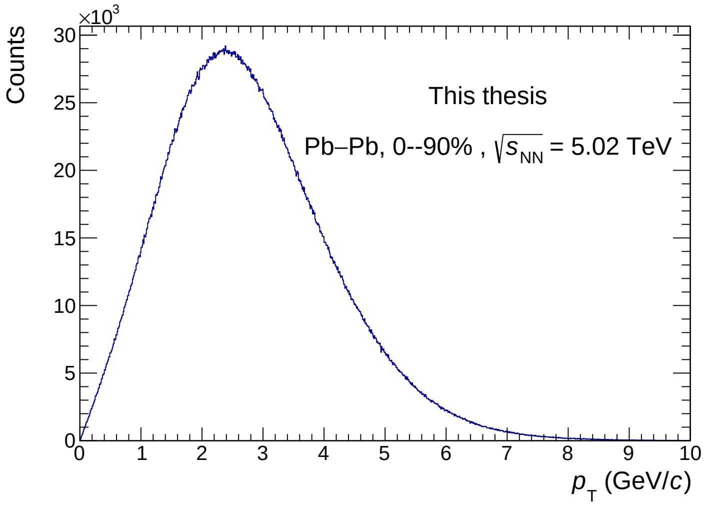

Fig. 5.10: Transverse momentum distribution of the $^3_\Lambda\mathrm{H}$ candidates in the MC sample after the B-W reweighting.

Background

The choice of the background sample is crucial for the BDT training. In this work, the background is extracted directly from the real data sample. The idea behind this decision is to use real data, where feasible, to avoid a loss in the model predictive power caused by possible shortcomings of the simulations in describing the real events. In this work, the background sample is built by pairing an $^3\mathrm{He}$ and a pion tracks of the same sign (like-sign background, or LS) satisfying the same selection criteria as the $^3_\Lambda\mathrm{H}$ candidates. A modification on the V^0 finder is implemented to allow the pairing and the fitting of tracks of the same sign. The usage of the LS background is fundamental also in the model evaluation, as it allows to assess that the BDT is not creating a fake hypertriton invariant mass peak in the background distribution.

The number of signal and background candidates composing the training set is reported in Table 5.4: the imbalance between the two classes is not a problem for the BDT training, as it is well known that the algorithm is not sensitive to the class imbalance (as well as the ROC-AUC metric employed to evaluate the model performance). However, to speed up the training process only 20% of the background candidates are employed for the training.

Training candidates in the 0-90% centrality interval	
Signal	2×10^6
Background	3×10^7

Tab. 5.4: Number of signal and background candidates that compose the training set.

The variables, or features, used to train the BDT involve the topology, the kinematics, and the PID of the ${}^3_\Lambda$H candidates and are listed hereafter:

- $\cos(\theta_p)$: defined in Sec. 5.2.2
- $\mathrm{DCA_{daugh}}$: defined in Sec. 5.2.2
- $\mathrm{DCA^{PV}}\ {}^3\mathrm{He}$: defined in Sec. 5.2.2
- $\mathrm{DCA^{PV}}\ \pi$: defined in Sec. 5.2.2
- $\mathrm{DCA^{PV}_{xy}}\ {}^3\mathrm{He}$: defined in Sec. 5.2.2
- $\mathrm{DCA^{PV}_{xy}}\ \pi$: defined in Sec. 5.2.2
- $\mathrm{n}\sigma_{\mathrm{TPC}}\ {}^3\mathrm{He}$: defined in Sec. 3.3.3
- $\mathrm{n}\sigma_{\mathrm{TPC}}\ \pi$: defined in Sec. 3.3.3
- $\mathrm{n^{clus}_{TPC}}\ {}^3\mathrm{He}$: number of TPC clusters of the ${}^3\mathrm{He}$ track
- p_{T}: transverse momentum of the ${}^3_\Lambda$H candidate

The distribution normalised to the number of candidates of the training variables for the signal and the background samples are shown in Fig. 5.11: it is expected that the features which present the stronger discrepancies between signal and background (such as the $\cos(\theta_p)$) will be more important for the discrimination in the training process.

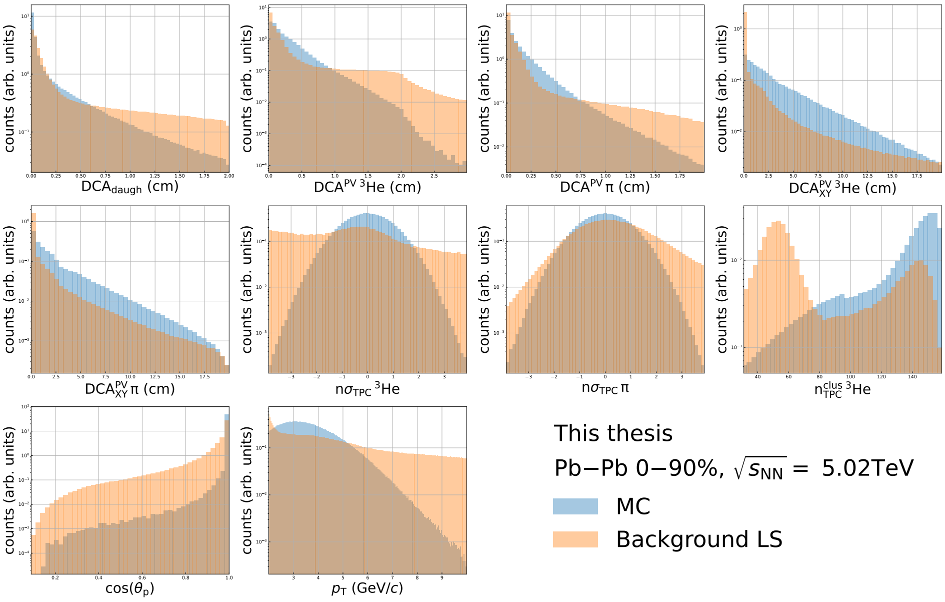

Fig. 5.11: Normalised distribution of the training variables for the signal (from MC) and the background (from real data) samples.

A similar plot is shown in Fig. 5.12: in this case the training variable distributions are shown for the LS and the real data samples. As the signal of the $^3_\Lambda$H is very small with respect to the combinatorial background, it is important to verify that LS and real data distributions are similar. If it were not the case, the learning process would be biased. As it can be verified qualitatively from the figure, the distributions of all the training variables result to be compatible between the two samples.

Figure 5.13 reports the linear correlations between the features and the invariant mass. Variables that carry the same physical information, such as those related to the DCAs of the daughter tracks, are strongly correlated as expected. Moreover, there are some differences in the variable correlations between signal and background candidates, which could be exploited by the model to discriminate signal from background. It is also useful to evaluate the correlations between the training features and the invariant mass that could produce a distortion in the signal extraction. The correlations with the invariant mass in Figure 5.13 are not significantly relevant but requires further investigations, as it will be discussed in 5.3.3.

Finally, the training set is randomly split in two parts: the first one is used to train the BDT, while the second one is used to evaluate the model performance, and it is called the test set. As the feature distributions change as a function of ct, different trainings are performed in all the ct intervals in which we expect to extract the $^3_\Lambda$H

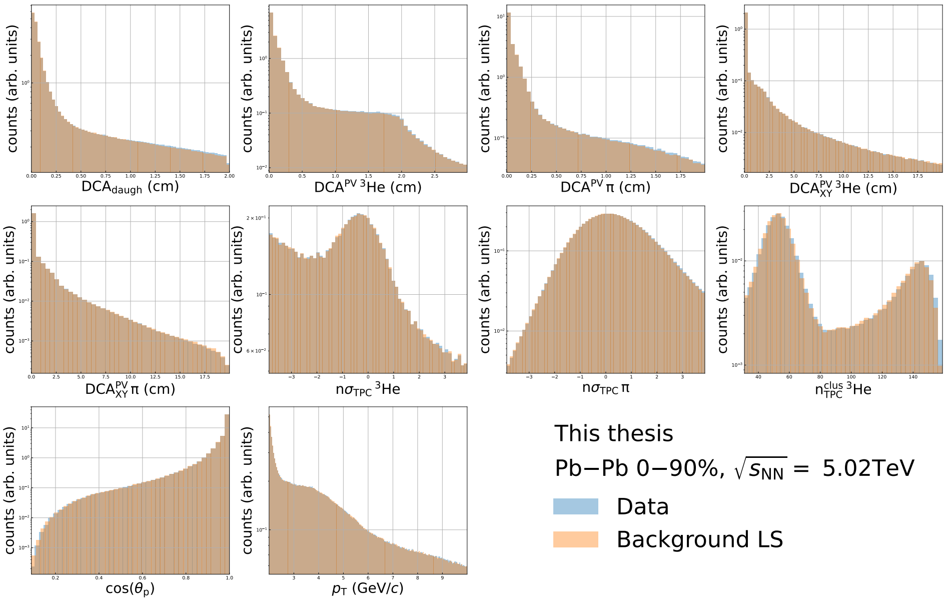

Fig. 5.12: Normalized distribution of the training variables for the LS background and the real data samples.

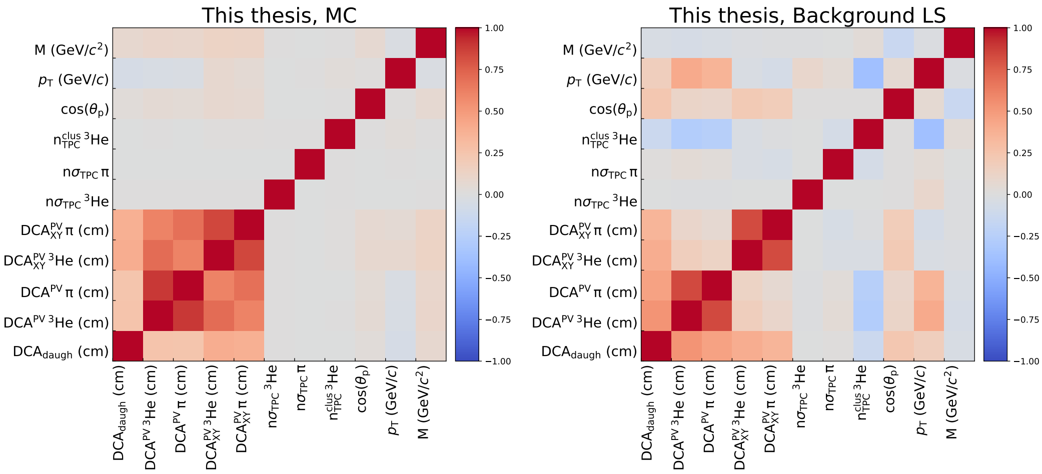

Fig. 5.13: Linear correlations between the training variables and the $^3_\Lambda$H invariant mass, for signal (left) and background (right) candidates. The colours, from red (fully correlated) to blue (fully anti-correlated), indicate the correlation level.

signal. Hence, nine different BDTs are trained, one for each ct interval, ranging from 1 to 35 cm.

5.3.2 Training and testing of the BDT

As mentioned in the previous section, the BDT is trained using the XGBoost [136] implementation of the gradient boosting algorithm. The model hyper-parameters, are optimized by minimizing the cross-validation error computed with the ROC AUC metrics as described in 4.2.2. A Bayesian optimizer, described in Sec. 4.2.2, is used to reduce the number of iterations needed to find the optimal hyper-parameters configuration. As the training is performed in the ct intervals, the hyper-parameters should be optimized for each ct interval separately. However, similar values of the hyper-parameters are found in all the ct bins, therefore the same hyper-parameters are employed for all the bins. The best hyper-parameters configuration is reported in Table 5.5.

Hyper-parameter	Optimization range	Values
max_depth	[3, 20]	9
n_estimators	[50, 800]	280
learning_rate	[0.01, 0.3]	0.098
gamma	[0.3, 1.1]	0.446
min_child_weight	[1, 12]	5.75
subsample	[0.5, 0.9]	0.74
colsample_by_tree	[0.5, 0.9]	0.57

Tab. 5.5: Optimized hyper-parameters for the BDT.

After the training process, the performance of the BDT are evaluated both on the training and the test set. It is important to verify that the model is not over-fitting the training set, and that the performance on the test set is similar to the one on the training set. The ROC curves for the training and the test sets are shown in Figure 5.14 in the ct interval between 1 and 2 cm.

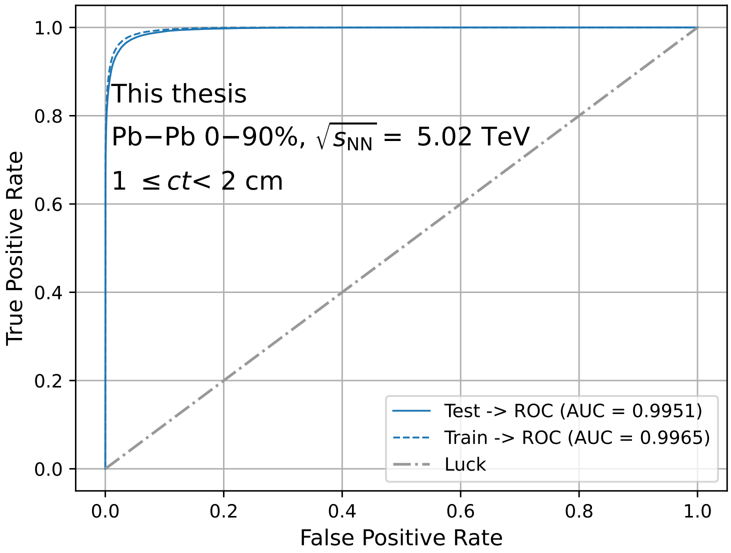

Fig. 5.14: ROC curves for the training and the test sets for ct between 1 and 2 cm.

The values of the ROC AUCs are similar for the training and the test sets, and they are always above 0.99, which demonstrates that the ${}^{3}_{\Lambda}\mathrm{H}$ can be easily selected over a wide ct range by the XGBoost Classifiers employed in this thesis. As already mentioned, the BDT returns a score for each candidate, which is related to the probability of the candidate of being signal or background. In Fig. 5.15 the BDT outputs for the training and test sets are shown: the red distributions represent the signal candidates, while the blue ones represent the background candidates.

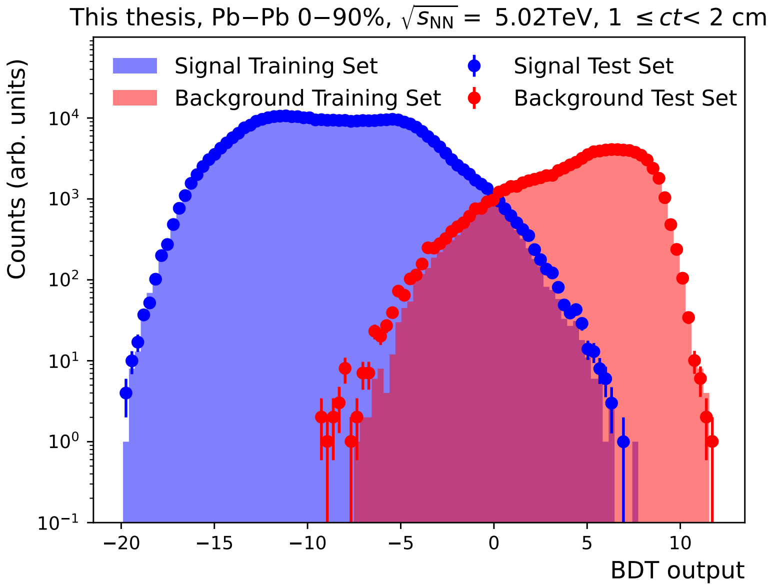

Fig. 5.15: Normalized BDT output distributions for the training (shaded area) and test (points with statistical errors) set. The background is reported in blue, the signal in red.

All the distributions are normalised to the same area. A high discrimination power between the two classes is always achieved, and the distributions are well separated. In all the intervals, an extremely low degree of over-fitting is observed, as the ROC-AUC of the training set are systematically higher than the ROC-AUC of the test set. This is taken into account in the next steps of the analyses and in the systematic uncertainties, as it will be explained in the next sections.

Finally, the analysis of the feature importance provide a powerful tool to assess the quality of the training. The impact of each variable on the model output is evaluated by using the Shapley values, as described in Sec. 4.2.3, and it is shown in Fig. 5.16 in two different ct intervals. For small decay lengths (top panel), the leading variable for the discrimination is the $\cos(\theta_p)$ angle. This is due to the fact that the contamination coming from ^{3}He produced at the primary vertex can be removed by the simple requirement the alignement between the sum of the momenta of the daughter tracks and the straight line connecting the primary vertex and the secondary vertex. This result is in agreement with the previous $^{3}_{\Lambda}$H analyses done in ALICE [147, 148] in which the $\cos(\theta_p)$ selection represents the "golden cut" for the $^{3}_{\Lambda}$H selection. For larger decay lengths (bottom panel), the leading variable is the number of TPC clusters of the ^{3}He. The reason is that if an extremely displaced ^{3}He track is found, it is likely that the track is the daughter of a $^{3}_{\Lambda}$H and not a

^{3}He produced at the primary vertex. The fact that different feature importance hierarchies are observed for different ct intervals motivates the choice of training multiple BDT models rather than a single one for the whole ct range.

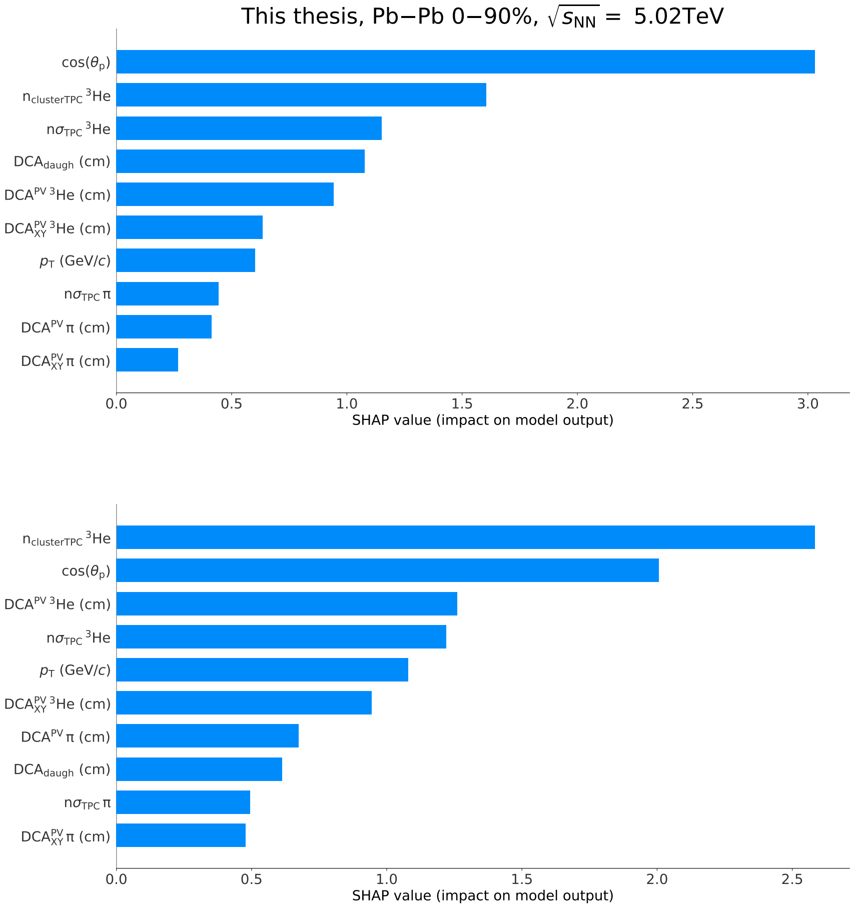

Fig. 5.16: Feature importance for the training set for ct between 1 and 2 cm (top) and 18 and 23 cm (bottom).

5.3.3 Application to data

After the training and the testing part, the BDT is finally applied to the real data sample. For each $^3_\Lambda$H candidate the BDT score is computed resulting in a continuous distribution, as shown in Fig. 5.17.

As the signal extraction is performed by fitting the invariant mass spectrum of the $^3_\Lambda$H in each ct bin, it is necessary to define a threshold value (or BDT *cut*) in order to reject the background $^3_\Lambda$H candidates maintaining a high BDT efficiency. The BDT efficiency is defined as the number of signal candidates passing the BDT cut $\mathrm{N(BDT_{out})}$ divided by the number of pre-selected candidates N:

$$\epsilon_{\mathrm{BDT}}(\mathrm{thr}) = \frac{\mathrm{N(BDT_{out} > thr)}}{\mathrm{N}}, \tag{5.6}$$

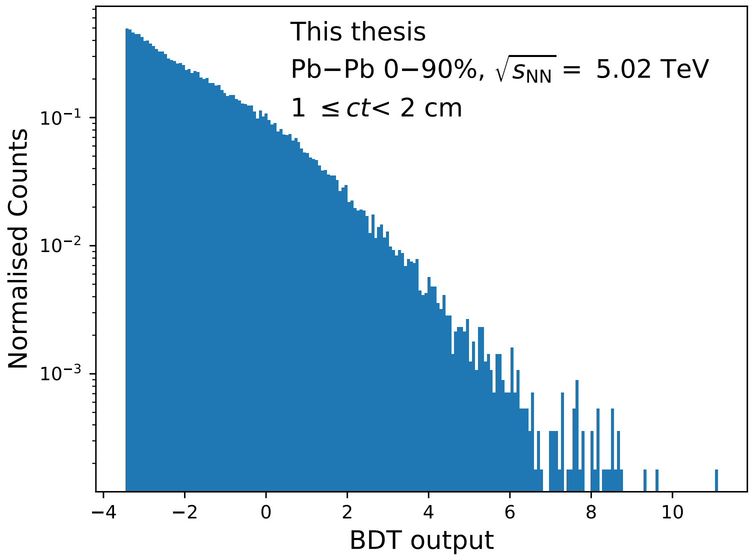

Fig. 5.17: Normalized distribution of the BDT output of the real data sample for ct between 1 and 2 cm.

The BDT efficiency is computed as a function of the BDT cut value, and it is shown in Fig. 5.18 for the ct interval between 1 and 2 cm. The BDT threshold efficiency is computed on the test set to avoid the possible over-fitting of the training set. However, for a given BDT threshold, the discrepancy between the efficiency computed with the test set and the one computed with the training set is always less than 1%.

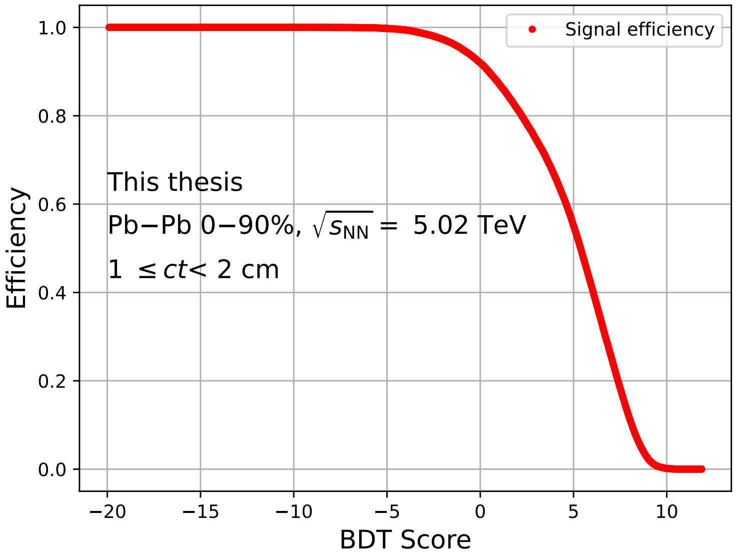

Fig. 5.18: BDT threshold efficiency as a function of the threshold (or score) for ct between 1 and 2 cm.

In order to choose the proper BDT cut, an algorithmic procedure is implemented in the ALICE code, called significance scan. The aim of the significance scan is to return in output the threshold score value that maximizes the expected significance ($\mathrm{Sign}_{\mathrm{exp}}$), defined as:

$$\mathrm{Sign}_{\mathrm{exp}} = \frac{S_{exp}}{\sqrt{S_{exp} + B_{exp}}} \tag{5.7}$$

where S_{exp} and B_{exp} are the expected signal and the background obtained with different BDT thresholds. To obtain an unbiased estimation of the $\mathrm{Sign}_{\mathrm{exp}}$ the expected signal could not be calculated extracting the raw yield from the real data sample candidates. Hence, a dedicated expected invariant mass spectrum is built in the following way:

- The **Background region** (out of 4σ from the ${}^{3}_{\Lambda}\mathrm{H}$ nominal invariant mass peak) contains the counts of the candidates from the real data sample
- The **Signal region** (complementary to the background region) is filled with *pseudodata*, which are the sum of:
  - Background counts (B_{exp}) extrapolated from the polynomial fit of the background in the side-bands
  - Signal counts (S_{exp}) extracted from the SHM expectation [89] and corrected with the current number of events in the real data, the preselection(ϵ_{presel}) and BDT(ϵ_{BDT}) efficiencies, and the expected two-body branching ratio ($\sim$ 0.25 [60]) as reported in the following equation:

$$S_{exp} = \mathrm{Yield}_{\mathrm{SHM}} \times N_{ev}^{2018} \times \epsilon_{\mathrm{presel}} \times \epsilon_{\mathrm{BDT}} \times \mathrm{B.R.}({}^{3}_{\Lambda}\mathrm{H} \rightarrow {}^{3}\,\mathrm{He} + \pi^{-}). \tag{5.8}$$

In order to find a balance between systematic and statistical uncertainties the product between $\mathrm{Sign}_{\mathrm{exp}}$ and the BDT threshold efficiency, rather than $\mathrm{Sign}_{\mathrm{exp}}$ only, is maximized. This guarantees to select a cut region in which the signal variation is stable enough to have the systematic uncertainty due to the signal extraction under control (in statistics this procedure derives from the bias-variance trade-off). Therefore, for each ct interval the BDT threshold is computed as:

$$\mathrm{BDT}_{\mathrm{thr}} = \arg\max[\mathrm{Sign}_{\mathrm{exp}} \times \epsilon_{\mathrm{BDT}}(\mathrm{thr})]. \tag{5.9}$$

The significance scan algorithm samples uniformly the BDT score range and chooses the value that maximizes the product of the expected significance and the BDT efficiency. The result obtained with this method in the ct interval between 2 and 4 cm is shown in Figure 5.19 . The left plot reports the Significance × Efficiency product as a function of the threshold value. Then the score that maximizes this product is chosen, and the right plot reports the performance expected with this technique.

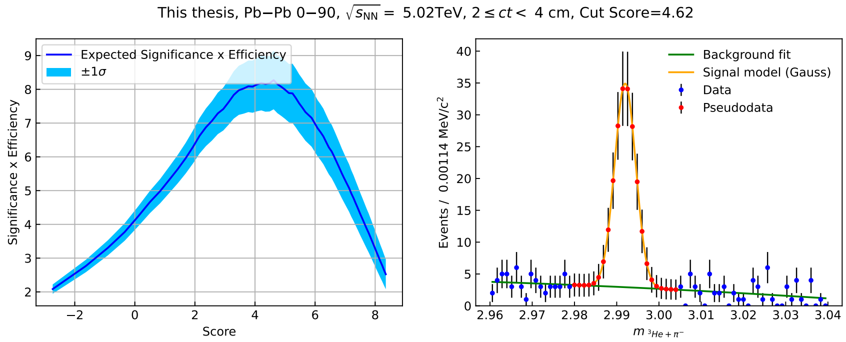

Fig. 5.19: 2≤ct <4 cm. Left: expected signal significance × BDT efficiency as a function of the threshold value applied on the BDT output. The light blue region is the confidence interval within 1σ associated to the estimation. Right: invariant mass spectrum for the performance BDT analysis. The signal region counts (red bullets) and the background region counts (blue bullets) are reported with the statistical error.

Table 5.6 reports the BDT threshold with its related efficiency for each ct bin: the BDT threshold efficiency is typically around 70 %.

ct interval (cm)	BDT threshold	BDT efficiency
$1 \leq ct < 2$	3.71	0.69
$2 \leq ct < 4$	4.62	0.76
$4 \leq ct < 6$	4.88	0.73
$6 \leq ct < 8$	4.73	0.75
$8 \leq ct < 10$	4.10	0.81
$10 \leq ct < 14$	4.23	0.77
$14 \leq ct < 18$	3.48	0.8
$18 \leq ct < 23$	4.36	0.67
$23 \leq ct < 35$	4.42	0.57

Tab. 5.6: BDT threshold and efficiency for each ct bin.

5.4 Signal extraction

The ${}^{3}_{\Lambda}\mathrm{H}$ candidates that pass the BDT selections are employed to extract the signal yield in the nine ct intervals covered by the models. The signal extraction process consists by an unbinned maximum likelihood fit of the invariant mass spectra of the ${}^{3}_{\Lambda}\mathrm{H}$ candidates in the signal region. The package employed for the fitting is RooFit, which is a ROOT based framework for statistical modeling [149]. Two relevant parameters are extracted from the spectra:

- The ${}^{3}_{\Lambda}\mathrm{H}$ signal raw yield ($N_{{}^{3}_{\Lambda}\mathrm{H}}$), that is employed for determining $\tau_{{}^{3}_{\Lambda}\mathrm{H}}$
- The ${}^{3}_{\Lambda}\mathrm{H}$ invariant mass peak position ($\mu_{{}^{3}_{\Lambda}\mathrm{H}}$), that is the key quantity for computing the B_{Λ}.

The ${}^{3}_{\Lambda}\mathrm{H}$ signal shape, which is particularly important for the extraction of $\mu_{{}^{3}_{\Lambda}\mathrm{H}}$, is determined by the momentum reconstruction scale and resolution. Hence, the ${}^{3}_{\Lambda}\mathrm{H}$ signal shape is extracted starting from the MC simulation. First, the MC candidates available in the test set undergo the same BDT selections that are applied to the real data. Then, the ${}^{3}_{\Lambda}\mathrm{H}$ signal candidates passing the optimal BDT thresholds are parametrized with two different fit functions (one of the two is used for the systematic uncertainty evaluation):

- A Kernel Density Estimator (KDE) [149, 150] function, which models the distribution of an arbitrary input dataset as a superposition of Gaussian kernels, one for each data point, each contributing 1/N to the total integral of the probability density function (pdf),
- A Double Sided Crystal Ball (DSCB) function, which consists of a Gaussian core portion and two power-law low-end tails.

A comparison between the two functions is shown in Figure 5.20: both the pdfs are able to describe the central part and the tails of the ${}^{3}_{\Lambda}\mathrm{H}$ signal shape.

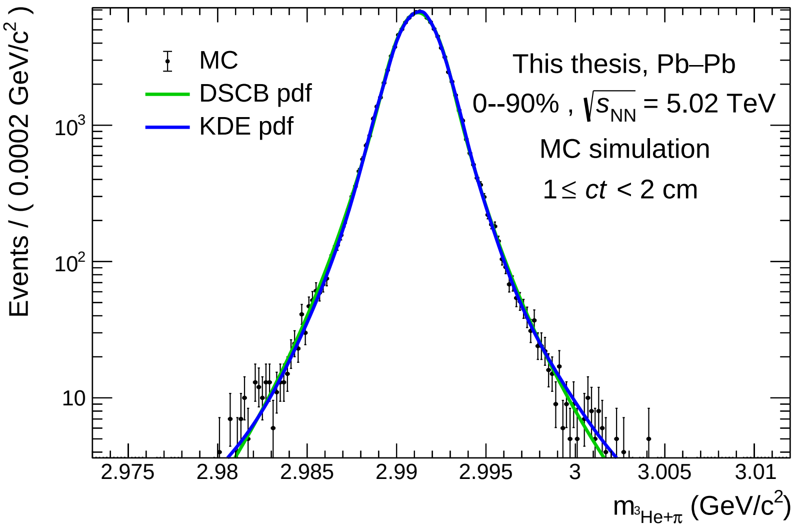

Fig. 5.20: Invariant mass distribution of the selected MC sample, for ct between 1 and 2 cm with superimposed a KDE and DSCB fitting functions. The KDE is shown in blue, while the DSCB is shown in green.

The fit to the MC spectra fixes all the internal parameters of the signal shape function, except for the parameters of interest that are the normalization and the mean value of the distribution. The background shape is extracted directly from the data: three different pdfs are employed: a linear function (default), a second order polynomial and an exponential (for the systematic uncertainty evaluation). The resulting total pdf (f_{tot}) is a superposition of the signal (f_{sig}) and background (f_{bkg}) ones:

$$f_{tot}(m; \mu_{^3_\Lambda\mathrm{H}}, N_{^3_\Lambda\mathrm{H}}, N_{bkg}, \vec{\theta}) = N_{^3_\Lambda\mathrm{H}} \cdot f_{sig}(m; \mu_{^3_\Lambda\mathrm{H}}, \vec{\theta}) + N_{bkg} \cdot f_{bkg}(m; \vec{\theta}), \tag{5.10}$$

where m is the reconstructed invariant mass, $\mu_{^3_\Lambda\mathrm{H}}$ is the $^3_\Lambda\mathrm{H}$ invariant mass peak position,$N_{^3_\Lambda\mathrm{H}}$ and N_{bkg} are the normalisations of f_{sig} and f_{bkg}, and $\vec{\theta}$ are the nuisance parameters of the total pdf. The invariant mass spectra of the selected $^3_\Lambda\mathrm{H}$ candidates on the real data are shown in Fig. 5.21 in all the nine ct intervals from 1 to 35 cm. The fitted f_{tot} is the sum of a KDE function for f_{sig} and a linear function for f_{bkg}. The free parameters of f_{sig} are $N_{^3_\Lambda\mathrm{H}}$ and $\mu_{^3_\Lambda\mathrm{H}}$, while the shape is fully constrained by the corresponding MC fit.

As shown in the figure, the $^3_\Lambda\mathrm{H}$ invariant mass spectra are well described by the total pdfs, demonstrating, in particular, a good agreement between the data and the MC invariant mass distributions. For each ct bin the significance is computed as $\mathrm{Sign} = \frac{\mathrm{S}}{\sqrt{\mathrm{S+B}}}$, where S and B are the signal and background yields in the signal region, which is defined by taking three times the width extracted from the DSCB fit of the MC signal shape. A summary of the signal extraction results is shown in 5.7: in total $\sim$ 1000 $^3_\Lambda\mathrm{H}$ and $^3_\Lambda\overline{\mathrm{H}}$ are reconstructed and selected.

ct interval (cm)	$N_{^3_\Lambda\mathrm{H}}$	$\mu_{^3_\Lambda\mathrm{H}}\mathrm{GeV}/c^2$	Sign($3\,\sigma$)
$1 \leq ct < 2$	87 ± 11	2991.1 ± 0.2	7.6 ± 1.1
$2 \leq ct < 4$	206 ± 13	2991.2 ± 0.1	13 ± 1
$4 \leq ct < 6$	145 ± 13	2991.6 ± 0.2	10 ± 1
$6 \leq ct < 8$	150 ± 13	2991.2 ± 0.2	10 ± 1
$8 \leq ct < 10$	99 ± 10	2991.5 ± 0.3	8.5 ± 1.3
$10 \leq ct < 14$	156 ± 13	2991.6 ± 0.2	10 ± 1
$14 \leq ct < 18$	79 ± 11	2991.7 ± 0.4	6.5 ± 1.1
$18 \leq ct < 23$	57 ± 10	2991.7 ± 0.4	5.5 ± 1.0
$23 \leq ct < 35$	30 ± 9	2991.2 ± 1.1	3.5 ± 0.8

Tab. 5.7: Results of the fit to the $^3_\Lambda\mathrm{H}$ invariant mass distributions in the nine ct intervals.

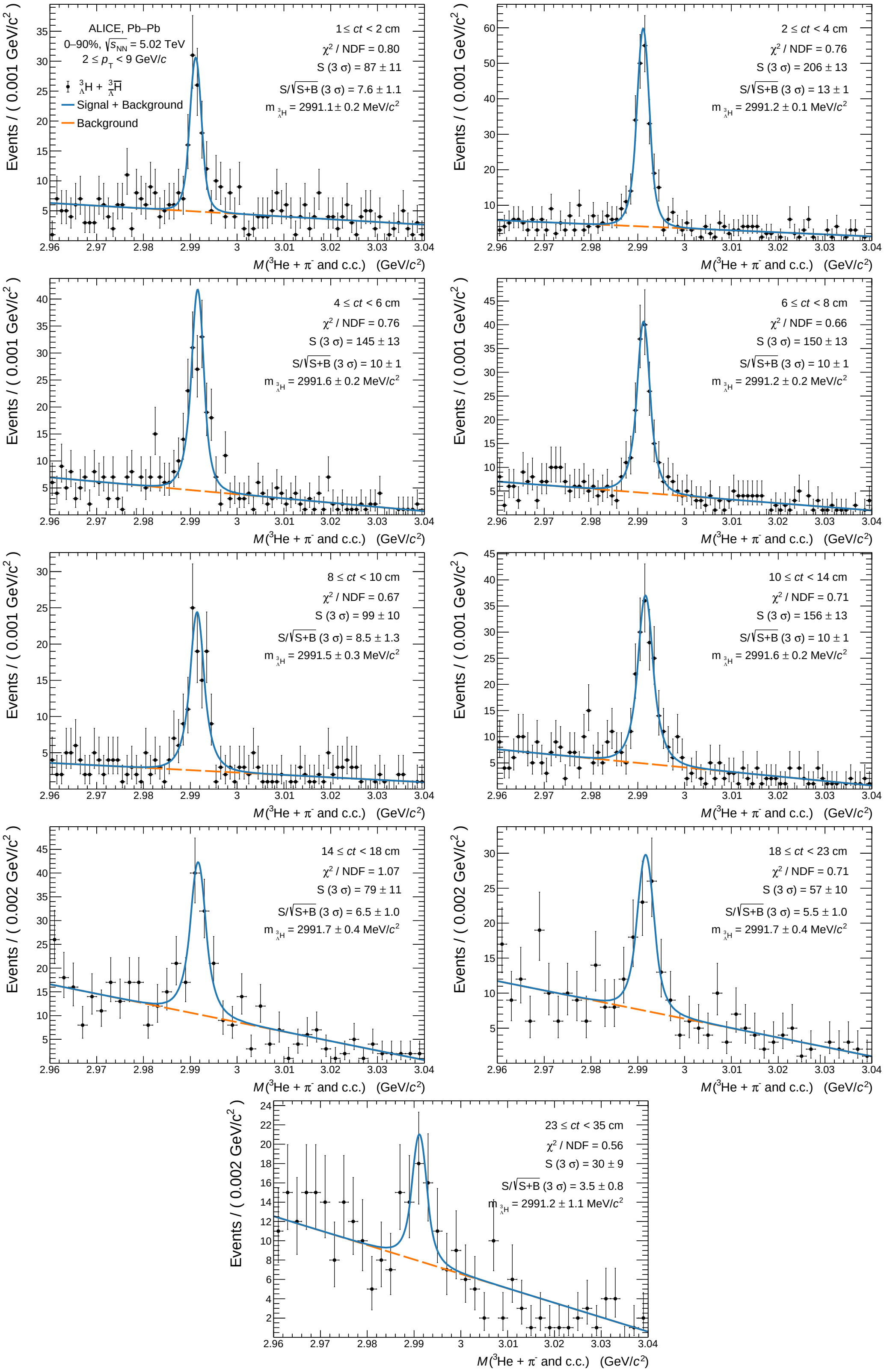

Fig. 5.21: Distribution of the invariant-mass of the $^{3}_{\Lambda}$H and $^{3}_{\bar{\Lambda}}\overline{\mathrm{H}}$ candidates in nine ct intervals from 1 to 35 cm. The statistical uncertainties of the bin counts are represented with vertical lines. The distribution is fitted with a two-component model; the blue line depicts the overall fit, and the orange dashed line displays the background component.

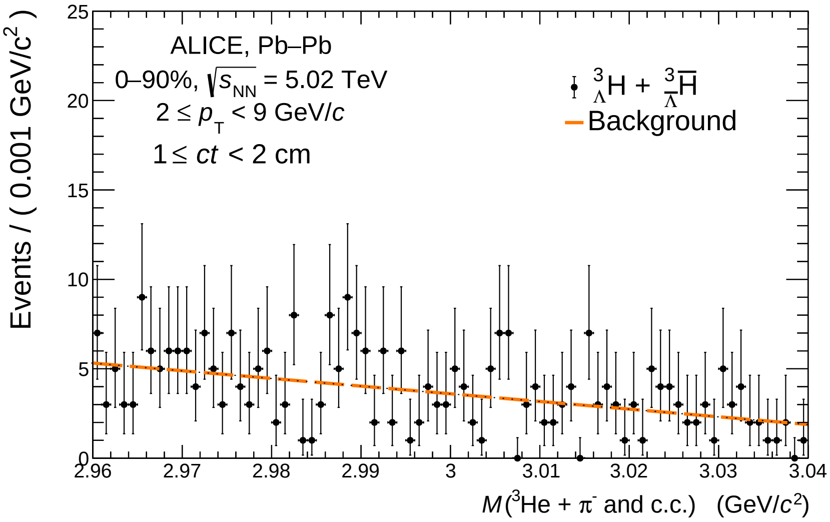

Fig. 5.22: Distribution of the invariant-mass of the LS candidates in the first ct interval. The statistical uncertainties of the bin counts are represented with vertical lines.

5.4.1 Probing the mass shaping effect

As mentioned in Section 5.3.2, the small correlation of the invariant mass with the other training features should prevent a distorsion in the signal extraction procedure. Nevertheless a further investigation needs to be done: if the machine learning model learns the $^{3}_{\Lambda}$H mass and preferentially selects candidates with an invariant mass similar to $^{3}_{\Lambda}$H one, a peak in the background will be present causing a bias in the extracted yield, which would not be only composed of signal. This behaviour is called *mass shaping*. To assess if the training process is affected by this kind of problem, the BDT is applied to the LS background available in the test set. The LS candidates are selected using the same BDT selections employed for the signal extraction and the invariant mass distribution in each ct interval is checked. The results are shown in Figure 5.22 for the first ct interval of the analysis: the invariant mass spectrum is well described by a linear background function and no peak is observed at 2.991 GeV/c^2 (the value of the $^{3}_{\Lambda}$H mass). Hence, the selection process does not involve indirectly the invariant mass feature.

5.5 Measurement of $\tau_{^{3}_{\Lambda}\mathrm{H}}$

The $^{3}_{\Lambda}$H lifetime is measured starting from the number of $^{3}_{\Lambda}$H extracted in each ct interval, as described in the previous section. Few corrections are applied to the raw $^{3}_{\Lambda}$H signals in order to obtain the final ct spectrum:

- the pre-selection efficiency, which is takes into account the vertexing efficiency and the acceptance of the ALICE detector, as described in 5.2.2;

- the BDT efficiency, which is the fraction of ${}^{3}_{\Lambda}\mathrm{H}$ candidates that pass the BDT selection in each ct interval.

A further correction, which has not been mentioned so far, needs to be applied to take into account the fraction of ${}^{3}_{\Lambda}\mathrm{H}$ that are not reconstructed because of their absorption in the ALICE detector material. In principle, this correction should be taken into account in the pre-selection efficiency, as GEANT4 naturally simulates the inelastic interactions of the particles during their transport. This is what happens for the ${}^{3}_{\Lambda}\mathrm{H}$ daughters: the ${}^{3}\mathrm{He}$ and π^{-} that are absorbed in the ALICE detector contribute to lower the ${}^{3}_{\Lambda}\mathrm{H}$ pre-selection efficiency. However, as the ${}^{3}_{\Lambda}\mathrm{H}$ inelastic cross section is poorly known, it is arbitrarily set to zero all in the GEANT4 code. This means that inelastic interactions of ${}^{3}_{\Lambda}\mathrm{H}$ are by default switched off. In the following subsection, the procedure to estimate the fraction of ${}^{3}_{\Lambda}\mathrm{H}$ absorbed in the ALICE detector material is described.

5.5.1 Absorption correction

As mentioned before, there are currently no experimental data concerning the ${}^{3}_{\Lambda}\mathrm{H}$ inelastic cross section with the material (σ^{inel}). As the ${}^{3}_{\Lambda}\mathrm{H}$ mass and momentum distribution are similar to those of the ${}^{3}\mathrm{He}$, the naive assumption is that the ${}^{3}_{\Lambda}\mathrm{H}$ absorption rate should be of the order of that of the ${}^{3}\mathrm{He}$ nucleus. However, the large size of the particle could lead to some significant variations: the only calculation available in the literature is the one performed by Evlanov et al. [151], which treats the ${}^{3}_{\Lambda}\mathrm{H}$ as a two cluster nucleus (a deuteron and a Λ) with a large RMS radius of ~ 10 fm. From this work, it can be inferred that the predicted ${}^{3}_{\Lambda}\mathrm{H}$ cross section is $\sim$ 1.5 times that of the ${}^{3}\overline{\mathrm{He}}$ ($\sigma^{inel}({}^{3}\overline{\mathrm{He}})$) measured by ALICE in [152]. The study of the ${}^{3}_{\Lambda}\mathrm{H}$ absorption is performed by using ${}^{3}\overline{\mathrm{He}}$ nuclei as a proxy, because different MC productions are available with altered $\sigma^{inel} = \sigma^{inel}({}^{3}\overline{\mathrm{He}}),\ 1.5\sigma^{inel}({}^{3}\overline{\mathrm{He}}),\ 2\sigma^{inel}({}^{3}\overline{\mathrm{He}})$. The MC production with $\sigma^{inel} = 1.5\sigma^{inel}({}^{3}\overline{\mathrm{He}})$ is employed to compute the default correction, while the other two are used to estimate a systematic uncertainty. The ${}^{3}_{\Lambda}\mathrm{H}$ absorption correction is computed as follows:

- for each ${}^{3}\overline{\mathrm{He}}$ produced in the MC, the p_{T} spectrum is reweighted according to the expected ${}^{3}_{\Lambda}\mathrm{H}$ p_{T} spectrum, as it is done in Sec. 5.1.2;

- for each ${}^{3}\overline{\mathrm{He}}$ a ct is extracted by sampling an exponential distribution with the average lifetime equal to τ_{Λ};

- when the $^{3}\overline{\mathrm{He}}$ interacts, it, as a hypertriton proxy, is considered "absorbed" if the interaction occurs before the extracted ct, i.e. before the decay of the corresponding ${}^{3}_{\Lambda}\mathrm{H}$.

The fraction of absorbed ${}^{3}_{\Lambda}\mathrm{H}$ ($f_{abs}({}^{3}_{\Lambda}\mathrm{H})$) as a function of ct is shown in Fig. 5.23 for both ${}^{3}_{\Lambda}\mathrm{H}$ and ${}^{3}_{\overline{\Lambda}}\overline{\mathrm{H}}$ separately. As the ${}^{3}_{\overline{\Lambda}}\overline{\mathrm{H}}$ cross section is expected to be larger than that of the ${}^{3}_{\Lambda}\mathrm{H}$, the ${}^{3}_{\overline{\Lambda}}\overline{\mathrm{H}}$ absorption correction is taken by rescaling $f_{abs}({}^{3}_{\Lambda}\mathrm{H})$ for $f_{abs}(^{3}\overline{\mathrm{He}})/f_{abs}(^{3}\mathrm{He})$. Both the ${}^{3}_{\Lambda}\mathrm{H}$ and ${}^{3}_{\overline{\Lambda}}\overline{\mathrm{H}}$ f_{abs} grow with ct reaching a maximum of $\sim 10\%$ in the last ct bin. Such a behaviour is expected, since more material is crossed by the particles as ct increases. As at the LHC ${}^{3}_{\Lambda}\mathrm{H}$ and ${}^{3}_{\overline{\Lambda}}\overline{\mathrm{H}}$ are produced in the same amount, the average between the two corrections f_{abs} is taken for correcting the extracted ${}^{3}_{\Lambda}\mathrm{H}$ signal.

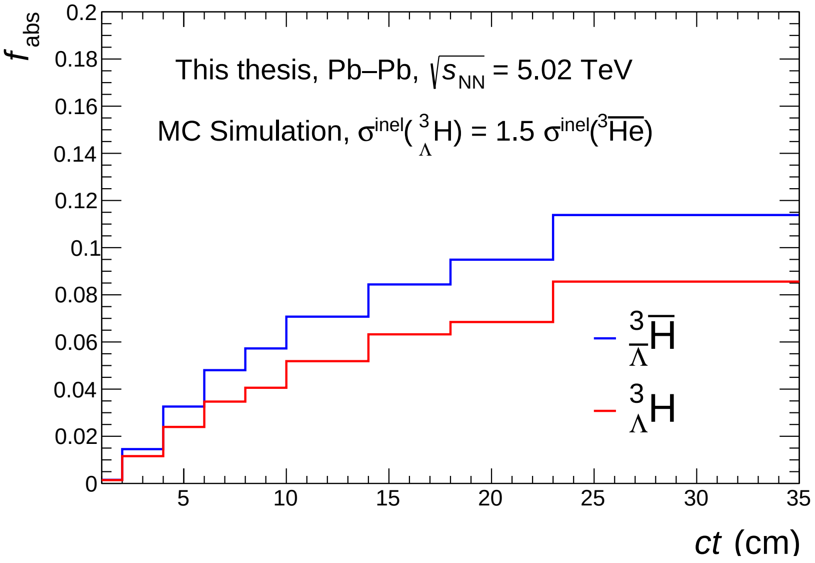

Fig. 5.23: Fraction of ${}^{3}_{\Lambda}\mathrm{H}$ and ${}^{3}_{\overline{\Lambda}}\overline{\mathrm{H}}$ absorbed in the ALICE detector material as a function of the ct.

5.5.2 Lifetime determination

The corrected ct spectrum $\mathrm{dN}/\mathrm{d}(ct)$ is obtained as:

$$\frac{\mathrm{dN}}{\mathrm{d}(ct)} = \frac{1}{\Delta ct} \cdot \frac{1}{\epsilon_{pre}} \cdot \frac{1}{\epsilon_{BDT}} \cdot \frac{1}{1 - f_{abs}} \cdot N_{{}^{3}_{\Lambda}\mathrm{H}}(ct), \tag{5.11}$$

where Δct is the width of the ct interval, ϵ_{pre} is the pre-selection efficiency, ϵ_{BDT} is the BDT efficiency and f_{abs} is the fraction of ${}^{3}_{\Lambda}\mathrm{H}$ absorbed in the ALICE detector material. The corrected spectrum is expected to follow the exponential distribution:

$$N(ct) = N_0 \cdot exp(-ct/c\tau_{{}^{3}_{\Lambda}\mathrm{H}}) \tag{5.12}$$

where N_0 is the normalization parameter and $\tau_{^3_\Lambda\mathrm{H}}$ is the average $^3_\Lambda$H lifetime. As in Sec. 5.7.1 the lifetime will be computed separately for $^3_\Lambda$H and $^3_{\Lambda}\overline{\mathrm{H}}$, in the following the sum of the two will be simply referred as τ.

An exponential χ^2 fit is performed to the corrected ct spectrum, as shown in Fig. 5.24. The fit is performed by using the integral of the function in each bin instead of the value at the bin centre to account for the different bin widths.

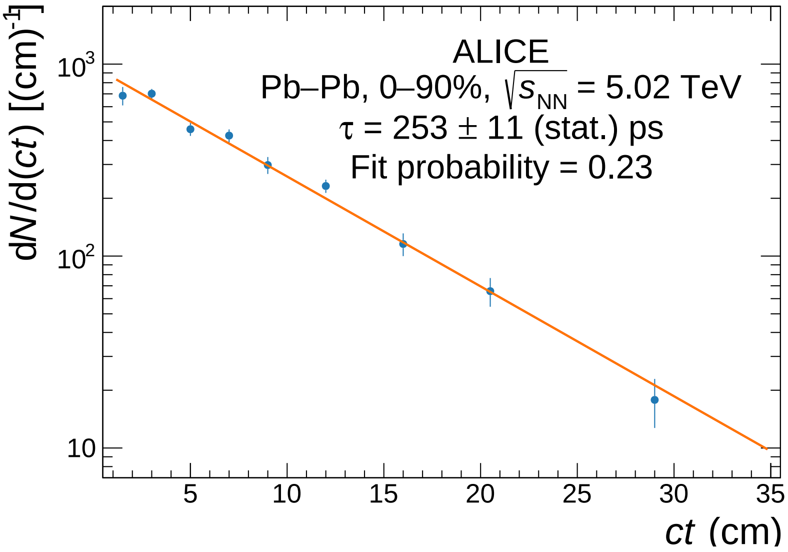

Fig. 5.24: $^3_\Lambda$H production spectrum as a function of the proper decay length , the blue points represent the measured yield, while the orange line represents the best fit to the measurement.

The fit probability shows that the obtained ct distribution is compatible with an exponential law. The value of τ extracted from the fit together with its statistical uncertainty is:

$$\tau = 253 \pm 11 \text{ ps}. \tag{5.13}$$

The statistical precision of this result improves by about a factor of 3 the previous ALICE measurement [75], and it is the most precise lifetime measurement to date. The value of τ is compatible with the previous ALICE measurement within the statistical uncertainties, as well as with the free Λ lifetime. In the following, the systematic uncertainties related to the measurement are discussed.

5.5.3 Systematic uncertainties

The systematic uncertainties on τ originate from (1) the ${}^{3}_{\Lambda}\mathrm{H}$ selection, (2) the signal extraction, (3) the absorption corrections. In order to take into account the possible correlations between (1) and (2), a combined systematic uncertainty due to the signal selection and extraction is computed. Other potential sources of systematic uncertainties are tested, such as the input p_{T} and ct shape of the ${}^{3}_{\Lambda}\mathrm{H}$ in the Monte Carlo sample, the choice of the BDT hyperparameters and the discrepancy between BDT and linear selections, all resulting in a non-significant contribution.

Signal selection and extraction

A multi-trial approach is employed to properly take into account the correlation between the BDT selection and signal extraction in the ${}^{3}_{\Lambda}\mathrm{H}$ lifetime determination, and to estimate the related systematic uncertainties. For each ct interval, a variation range of the BDT efficiency is defined, and different fit functions are used to extract the signal. In order to precisely define the BDT efficiency range, the BDT efficiency as a function of the score needs to be parametrized. In this way, for each efficiency value we want to probe, it is possible to define the corresponding BDT output. The parametrization is performed by employing polynomial splines that successfully reproduce the BDT efficiency as a function of the score. In each ct interval the spline parametrization is obtained from 0.99 down to 0.30: an example is shown in Figure 5.25.

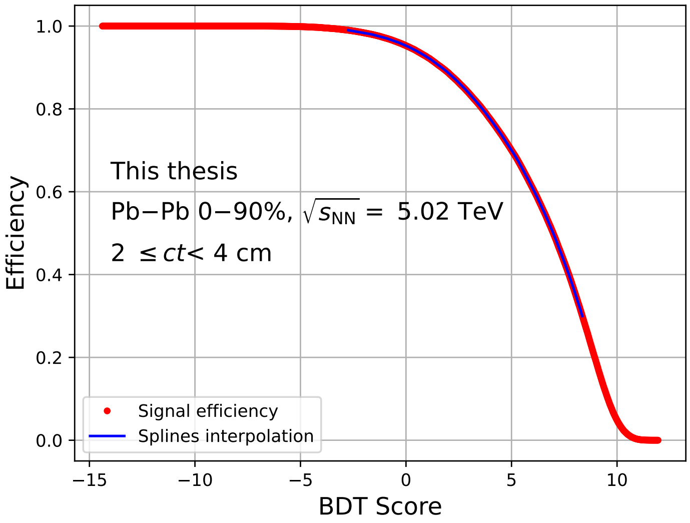

Fig. 5.25: BDT efficiency as a function of the BDT score parametrized with a spline function, in the ct interval between 2 and 4 cm.

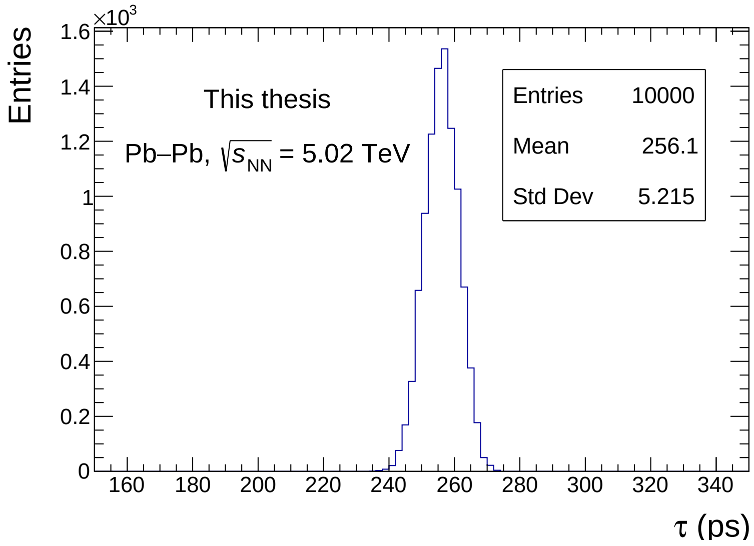

Fig. 5.26: Distribution of the τ value from the exponential fit of the ct spectra obtained by varying the BDT score selection and the signal extraction procedure. The RMS of this distribution is assigned as systematic uncertainty to the final estimation of the ${}^{3}_{\Lambda}\mathrm{H}$ lifetime.

The variation ranges defined for computing the systematic uncertainty in each ct interval are:

- a BDT efficiency range of $\pm10\%$ around the nominal value;
- three background fit functions: linear, second order polynomial and exponential;
- two signal pdfs: a KDE and a Double Sided Crystal Ball.

Hence, for each ct interval there are 21 variations of the BDT efficiency selection ($\pm10\%$ from the nominal value + the nominal value) and for each of those there are three and two variations the background and signal fit functions respectively, for a total of 126 variations. Then, for each ct bin, one random combination is extracted, and the resulting spectrum is fitted with an exponential to obtain the lifetime value. Repeating this procedure thousand times it is possible to investigate what is the effect of these systematic variations on the lifetime. The result of this study is shown in Figure 5.26: the standard deviation of the systematic distribution can be used as an estimate of the systematic uncertainty of our lifetime measurement due to the ML selection and signal extraction. The systematic uncertainty due to these contributions is 5.2 ps ($\sim$ 2.1%).

Absorption in the detector

As the ${}^{3}_{\Lambda}\mathrm{H}$ cross section with the material is poorly known, a conservative approach has been applied to evaluate the systematic uncertainty. Indeed, the ${}^{3}_{\Lambda}\mathrm{H}$ absorption cross section is varied from the nominal ${}^{3}\overline{\mathrm{He}}$ one ($\sigma^{inel} = \sigma^{inel}({}^{3}\overline{\mathrm{He}})$) up to two times the value of $\sigma^{inel} = 2\sigma^{inel}({}^{3}\overline{\mathrm{He}})$. For each cross section, the procedure to compute f_{abs} is repeated as described in Sec. 5.5.1, and the lifetime of ${}^{3}_{\Lambda}\mathrm{H}$ is recomputed. The f_{abs} correction as a function of ct for the two different cross section variations is shown in Fig. 5.27: the slope of the correction, which is the quantity relevant for the τ determination, is mildly affected by the variation of the cross section. Half of the difference between the two slopes is assigned as systematic uncertainty to the lifetime measurement, which is 3 ps ($\sim$ 1.2%).

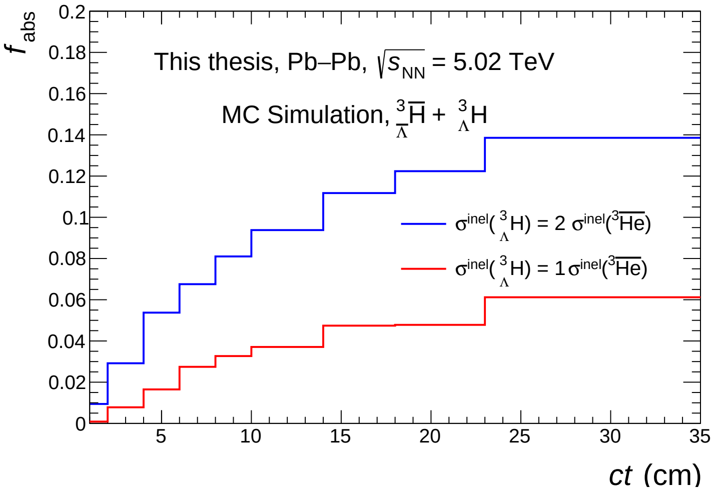

Fig. 5.27: Absorption correction as a function of the proper decay length for ${}^{3}_{\Lambda}\mathrm{H}$, for two different values of the ${}^{3}_{\Lambda}\mathrm{H}$ absorption cross section.

Additional checks

Additional checks are performed to assess the stability of the results:

- different p_{T} shapes that well describe the ${}^{3}\mathrm{He}$ data are employed for reweighting the MC sample. For each p_{T} shape the efficiency is re-computed and the training of the BDT is repeated. In particular, the Boltzmann and the m_{T}-exponential distributions from ${}^{3}\mathrm{He}$ analysis [146] are those used for the systematic uncertainty estimate. The ratio between the nominal efficiency and the efficiency obtained with the different p_{T} shapes is shown in Fig. 5.28. The difference between the efficiencies is less than 5%, and it is constant as a function of the ct. Hence, the τ values computed by assuming the different shapes differ by less than 0.2%. Furthermore, as shown in Fig. 5.16, the p_{T} is not a valuable feature for classifying the ${}^{3}_{\Lambda}\mathrm{H}$ signal: hence the difference due to the training is found to be negligible. The overall systematic uncertainty due to the p_{T} shape is found to be less than 1 ps.

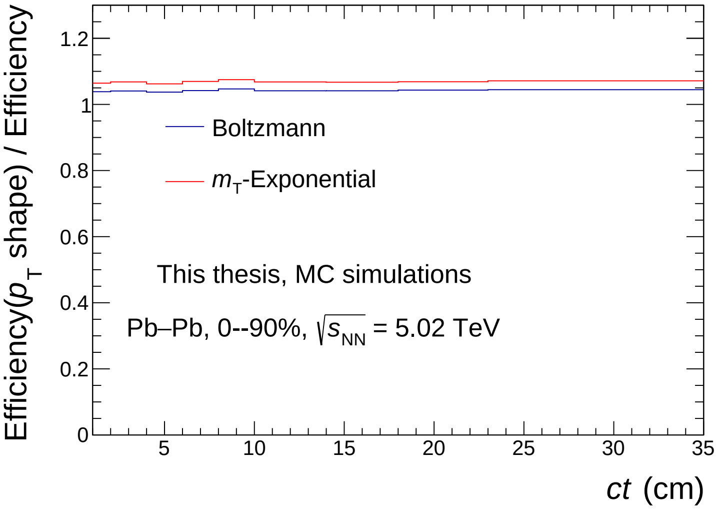

Fig. 5.28: Ratio between the efficiency obtained with the nominal p_T shape and the efficiency obtained with the Boltzmann and m T -exponential distributions.

- a potential bias coming from the choice of the BDT hyperparameters is investigated. To do that, the BDT is trained with the default hyperparameters of XGBoost, which are listed in Tab. 5.8. The lifetime is recomputed obtaining a difference of 1.5 ps, which is 4 times smaller than the RMS of the systematic distribution obtained by varying the BDT efficiency selection and the signal extraction procedure. The RMS systematic uncertainty due to the BDT hyperparameters is found to be less than 1 ps.

Hyper-parameter	Value
max depth	3
n estimators	100
learning rate	0.1
gamma	0
min child weight	1
subsample	1
colsample by tree	1

Tab. 5.8: Default XGBoost hyper-parameters.

- a potential bias coming from the BDT selection is investigated by performing the analysis employing linear topological selections. The selections, which are listed in Tab. 5.9, involve the variables that are used for training the BDT and are taken from the previous Run 2 $^{3}_{\Lambda}\mathrm{H}$ published analysis [75].

The signal extraction in the ct interval between 6 and 8 cm is shown in the left panel of Fig. 5.29, while the corrected ct spectrum of the $^{3}_{\Lambda}\mathrm{H}$ signal is shown in the right panel. The extracted value of τ is fully compatible with the ML based one, as it is included in the signal selection and extraction

Variable	Selection
$\mathrm{DCA_{daugh}}$	<1. cm
$\mathrm{DCA}^{\mathrm{PV}}\ {}^{3}\mathrm{He}$	>0.05 cm
$\mathrm{DCA}^{\mathrm{PV}}\ \pi$	>0.05 cm
$p_{\mathrm{T}}({}^{3}\mathrm{He})$	>1.8 GeV/c
$p_{\mathrm{T}}(\pi)$	>0.2 GeV/c
$\cos(\theta_p)$	>0.9995
$\lvert n\sigma_{TPC}\ {}^{3}\mathrm{He}\rvert$	<3
$\lvert n\sigma_{TPC}\ \pi\rvert$	<3
$\mathrm{n}^{\mathrm{clus}}_{\mathrm{TPC}}\ {}^{3}\mathrm{He}$	>80

Tab. 5.9: Topological selections applied at the V^0 level.

systematic uncertainty. Furthermore, the statistical uncertainty obtained with linear selections is $\sim$ 35 % higher than the one obtained with the ML based selections, proving that ML is more efficient in selecting the ${}^{3}_{\Lambda}\mathrm{H}$ signal and rejecting the combinatorial background.

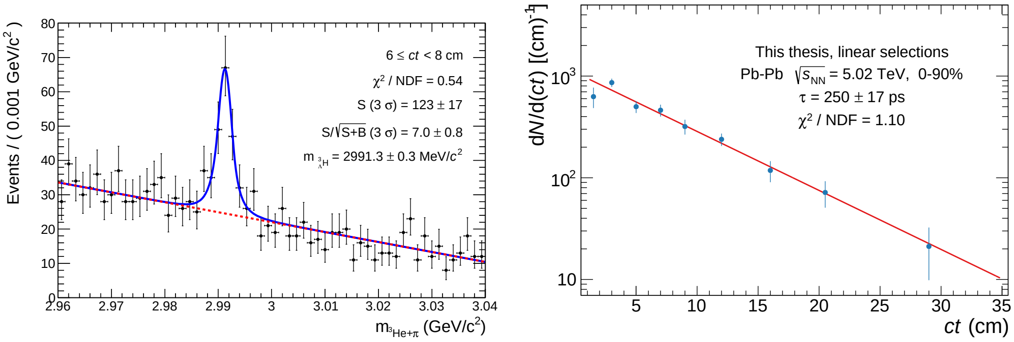

Fig. 5.29: Left panel: signal extraction in the ct interval between 6 and 8 cm obtained by using linear selections. The spectrum is fitted with a DSCB and a linear function to model the signal and the background components, respectively. Right panel: corrected ct spectrum of the ${}^{3}_{\Lambda}\mathrm{H}$ signal fitted with an exponential.

Table 5.10 summaryzes the different sources of systematic uncertainty affecting the ${}^{3}_{\Lambda}\mathrm{H}$ lifetime measurement. The total systematic uncertainty is found to be 6 ps, $\sim 2\%$ of the extracted value of τ.

Systematic contribution	Value (ps)
Signal selection and extraction	5.2
Absorption in the detector	3
BDT hyperparameters	/
Input p_{T} shape	/
Linear selection vs ML	/
Total	6.0

Tab. 5.10: Summary of the different sources of systematic uncertainty affecting the ${}^{3}_{\Lambda}\mathrm{H}$ lifetime measurement.

5.6 Measurement of B_Λ

As mentioned in Sec. 2.2.2, the B_Λ of the ${}^{3}_{\Lambda}\mathrm{H}$ is the energy required to separate the Λ from the deuteron core of the ${}^{3}_{\Lambda}\mathrm{H}$. Hence, it is defined as:

$$\mathrm{B}_\Lambda = m_\mathrm{d} + m_\Lambda - m_{{}^{3}_{\Lambda}\mathrm{H}}, \tag{5.14}$$

where m_d and m_Λ are the masses of the deuteron and the Λ, respectively. The ${}^{3}_{\Lambda}\mathrm{H}$ mass ($m_{{}^{3}_{\Lambda}\mathrm{H}}$) is measured starting from the mean value ($\mu_{{}^{3}_{\Lambda}\mathrm{H}}$) of the signal pdf extracted from the ${}^{3}_{\Lambda}\mathrm{H}$ invariant mass fits in each ct interval, as described in the previous section. As it is done for the lifetime, as ${}^{3}_{\Lambda}\mathrm{H}$ and ${}^{3}_{\overline{\Lambda}}\overline{\mathrm{H}}$ are summed together, in the following $\mu_{{}^{3}_{\Lambda}\mathrm{H}}$ will be simply referred to as μ. The values of μ as a function of ct are shown in Fig. 5.30.

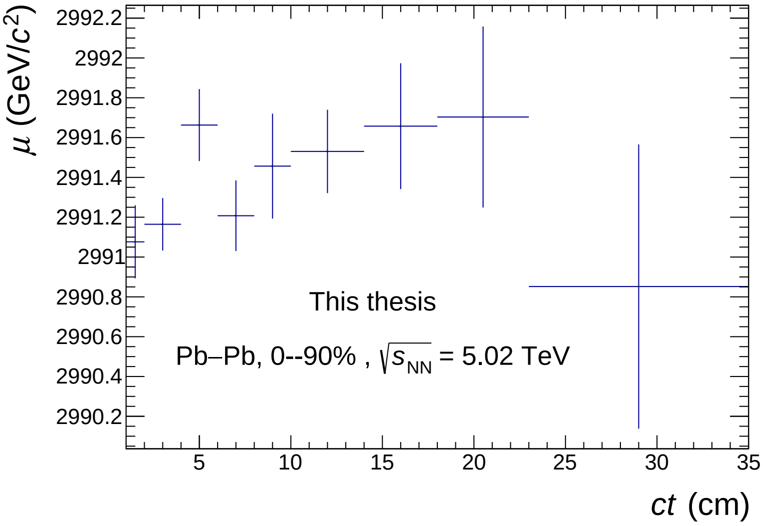

Fig. 5.30: Mean value of the ${}^{3}_{\Lambda}\mathrm{H}$ invariant mass as a function of ct.

The raw value of $\mu_{{}^{3}_{\Lambda}\mathrm{H}}$ extracted in Fig 5.30 has to be corrected for the energy loss of the ${}^{3}_{\Lambda}\mathrm{H}$ in the detector material. In Sec. 3.3.2, a brief description of the global track reconstruction is given, which is based on the iterative update of the track parameters by using a Kalman filter. At each iteration, a noise term is added to the covariance matrix to take into account stochastic processes such as energy losses $\mathrm{d}E/\mathrm{d}x$. If the track propagation goes outward, (PV to TPC, for example), taking into account energy losses means substracting energy to the track parameters, because the charged particle is supposed to loose energy while traversing material. Conversely, for an inward propagation (TPC to PV, for example), energy needs to be added to the track parameters. In the last step of the tracking, all the tracks are propagated inward to the distance of closest approach to the PV, and the energy loss corrections are applied. Once the tracks and the primary vertex are reconstructed, a search for V^0 secondary vertices is executed, as described in Sec. 5.2.2. In order to get the correct V^0 and cascade parameters, the daughter tracks need to be propagated (outward) to the secondary vertex. However energy loss corrections are not applied in this last propagation. This means that the energy added during the final inward propagation of the tracking between the secondary and primary vertex is not subtracted, leading to extra energy/momentum in the track parameters at the secondary decay vertex and therefore to an offset of the invariant mass. This effect can be corrected a posteriori by using the MC information, as it is done for the lifetime measurement. Fig. 5.31 shows the μ^{MC} parameters extracted from the fit to MC candidates passing the BDT selections, as a function of ct. The μ^{MC} value is compared with the injected value of the ${}^{3}_{\Lambda}\mathrm{H}$ mass in the MC (m^{MC}), showing an increase of $\sim$ 0.8 MeV from 1 to 35 cm.

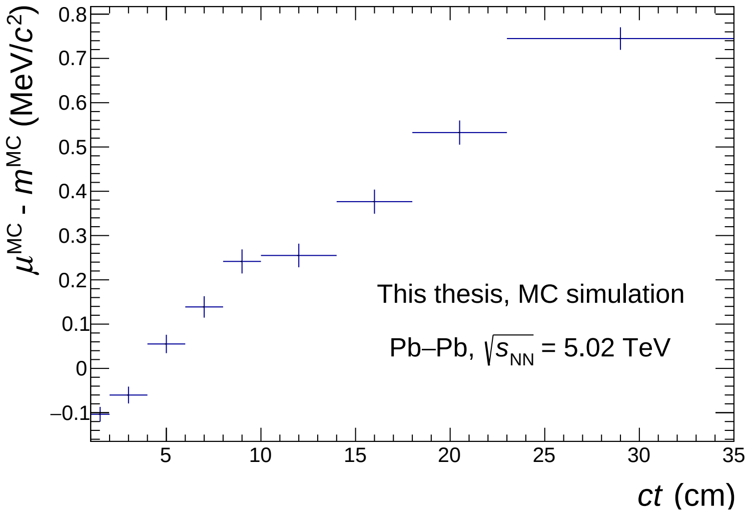

Fig. 5.31: Mass shift of the ${}^{3}_{\Lambda}\mathrm{H}$ signal observed in MC as a function of ct.

The observed shift, δ^{MC}, can be used to correct the μ values found in the data for each ct interval as:

$$m = \mu - \delta^{\mathrm{MC}}, \tag{5.15}$$

where m is the corrected mass of the ${}^{3}_{\Lambda}\mathrm{H}$ + ${}^{3}_{\overline{\Lambda}}\overline{\mathrm{H}}$ candidates. The corrected mass as a function of ct is shown in Fig. 5.32 and it is fitted with a constant (χ^2 fit). The high fit probability indicates that the corrected mass is constant within the statistical uncertainties. The statistical uncertainty on the measurement is $\sim 10^{-3}\,\%$, and it is the most precise measurement of the ${}^{3}_{\Lambda}\mathrm{H}$ mass ever done, as it will be shown in Sec. 5.7.

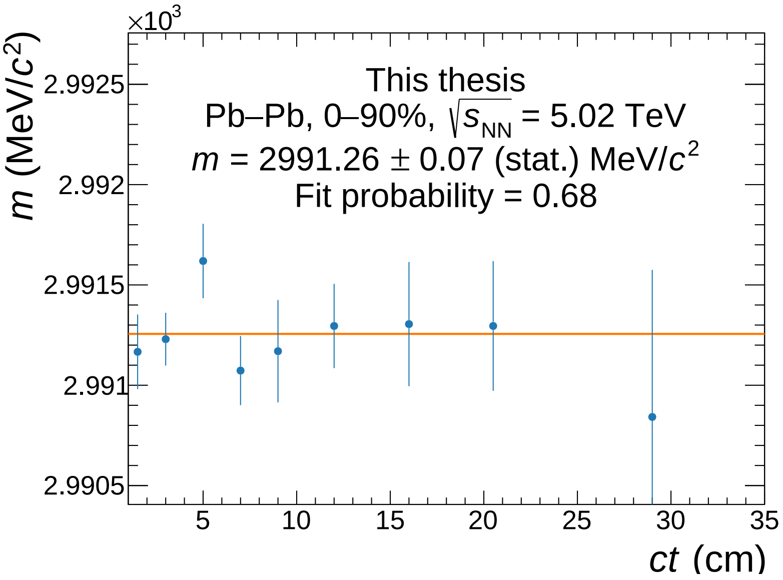

Fig. 5.32: Measured ${}^{3}_{\Lambda}\mathrm{H}$ mass as a function of ct, fitted with a constant.

5.6.1 Systematic uncertainties

The systematic uncertainties on B_{Λ} originate from (1) the ${}^{3}_{\Lambda}\mathrm{H}$ selection and the signal extraction, (2) the uncertainty on the magnetic field, (3) the residual detector misalignement, (4) the material budget. The latter contributions are negligible for the τ computation, as they only affect the position of the ${}^{3}_{\Lambda}\mathrm{H}$ mass peak, while the choice of input p_{T} and ct shape in the MC is proven to have no impact for the mass measurement. A data-driven approach is employed to estimate the systematic uncertainties related to (2) and (3) and (4), as it will be described in the following.

Signal selection and extraction

As it is done in Sec. 5.5.3, a multi-trial approach is implemented to properly take into account the correlation between the BDT selection and signal extraction. A variation range of 10% is applied to the BDT selection efficiency, three different background fit functions (linear, second order polynomial, exponential), and two different signal fit functions (KDE, DSCB) are also employed. For each trial a random combination of the variations is chosen, and the corrected ${}^{3}_{\Lambda}\mathrm{H}$ mass is recomputed. The resulting distribution is shown in Fig. 5.33: the RMS of such a distribution is taken as the systematic uncertainty due to the signal selection and extraction.

Systematic study of the Λ mass

The uncertainties related to the magnetic field, the residual detector misalignement and the material budget are estimated by studying the Λ mass distribution. Indeed, Λ hyperons are ideal probes to study the uncertainties on the reconstruction corrections

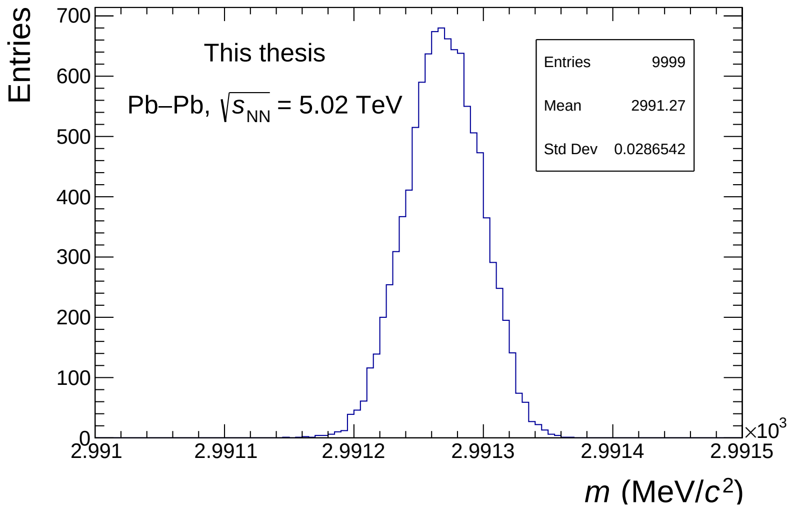

Fig. 5.33: Multi-trial $^{3}_{\Lambda}$H mass distribution.

implemented in the MC simulated nominal values for material budget, magnetic field, detector misalignement, which have a relative uncertainty of $\sim 4.5\%$, $\sim 0.1\%$, and $\sim 0.1\%$ respectively. Two major advantages of using Λ to check potential systematic uncertainties are: (1) the Λ mass is known with a precision of ~ 6 keV [7], and (2) the statistical precision on the Λ mass is negligible with respect to the systematic contributions under study. Furthermore, the Λ is well suited to be used as a proxy for the $^{3}_{\Lambda}$H, as the decay length is the same within uncertainties, and the Q value of the Λ decay is very close to the $^{3}_{\Lambda}$H one. The same analysis procedure of the $^{3}_{\Lambda}$H is applied to the Λ candidates of the same dataset (LHC18qr), and a DSCB function is employed to extract the signal. The raw mass of the Λ (μ_{Λ}) extracted as a function of the ct is shown in the left panel of Fig. 5.34, while in the right panel the raw mass taken from the MC is shown (μ_{Λ}^{MC}). The two distributions show a similar trend, which is also the same as the one observed for the $^{3}_{\Lambda}$H mass.

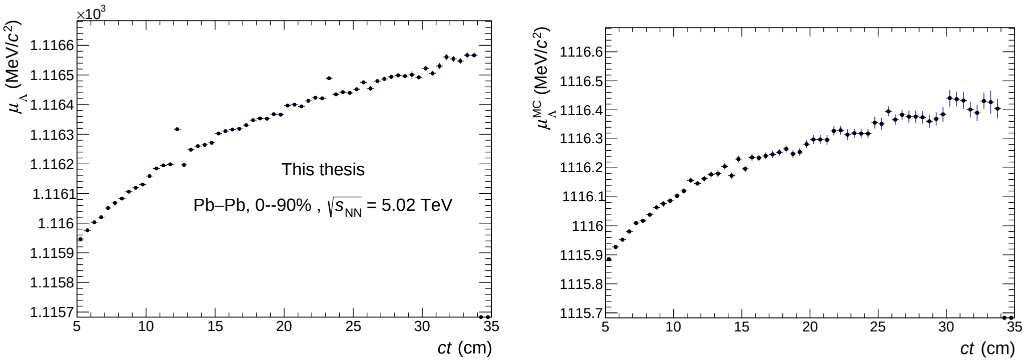

Fig. 5.34: Left: raw mass of the Λ extracted from the data as a function of the ct. Right: raw mass of the Λ extracted from the MC as a function of the ct.

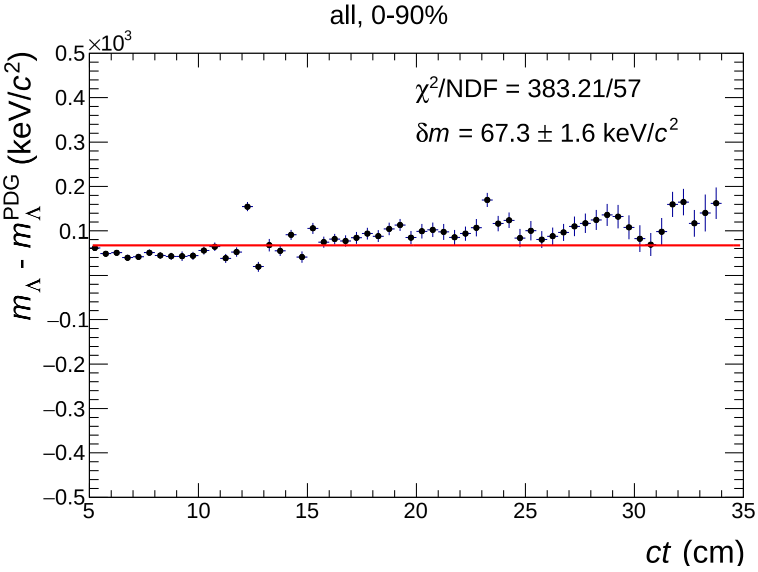

Fig. 5.35: Corrected mass of the Λ as a function of the ct.

Finally, the corrected mass m_Λ is shown in Fig. 5.35 as a function of the ct, showing a little increase as a function of the ct. This clearly represents a systematic due to the data-simulation mismatch that has to be taken into account. Furthermore, by fitting with a constant the corrected mass, a shift of ~ 67 keV is observed with respect to the nominal PDG mass. This shift is taken as a further data driven correction factor to be applied to the ${}^{3}_{\Lambda}\mathrm{H}$ mass, which will be referred to as δ^Λ.

To evaluate the systematic uncertainty related to this correction, the full analysis chain is repeated separately for Λ and $\overline{\Lambda}$, and with splitted magnetic field polarities. Different δ^Λ are extracted for the different cases, and the maximum difference between the δ^Λ factors is employed as systematic uncertainty on the data-driven correction. The result of the systematic study is shown in Table 5.11: in principle Λ with positive polarities and $\overline{\Lambda}$ with negative polarities should exibhit the same δ^Λ (and viceversa), but the residual detector misalignement and the uncertainty on the magnetic and electric fields of the TPC could introduce small but significant differences as the ones observed. This is why the systematic uncertainty related to the data-MC mismatch is evaluated in such a conservative way. The obtained estimate is $\Delta(\delta^\Lambda) = 106 - 45\mathrm{keV} = 61\mathrm{keV}$, which corresponds to a systematic uncertainty of $\sim 10^{-3}\,\%$.

δ^Λ (keV/c^2)	Λ	$\overline{\Lambda}$
B = +0.5 T	44.5 ± 3.0	82.9 ± 3.1
B = -0.5 T	35.1 ± 3.2	106.3 ± 3.3

Tab. 5.11: Data driven δ^Λ splitted for matter and antimatter and for different magnetic field polarities.

Table 5.12 summaryzes the different sources of systematic uncertainty affecting the ${}^{3}_{\Lambda}\mathrm{H}$ mass measurement. As for the τ analysis, the systematic uncertainties related to the BDT hyperparameters, the input p_{T} shape and the linear selection vs ML result in a negligible contribution. The total systematic uncertainty is found to be 6 ps, $\sim 2\%$ of the extracted value of m.

Systematic contribution	Value (keV)
Signal selection and extraction	28
Data-MC mismatch	61
BDT hyperparameters	/
Input p_{T} shape	/
Linear selection vs ML	/
Total	67

Tab. 5.12: Summary of the different sources of systematic uncertainty affecting the ${}^{3}_{\Lambda}\mathrm{H}$ mass measurement.

5.7 Final results

The final ${}^{3}_{\Lambda}\mathrm{H}$ + ${}^{3}_{\Lambda}\overline{\mathrm{H}}$ τ and m are obtained by summing in quadrature all the different systematic contributions, resulting in:

$$\tau = [253 \pm 11\ (\text{stat.}) \pm 6\ (\text{syst.})]\ \text{ps},$$

$$m = [2991.26 \pm 0.06\ (\text{stat.}) \pm 0.07\ (\text{syst.})]\ \text{MeV}.$$

The B_{Λ} of the ${}^{3}_{\Lambda}\mathrm{H}$ is computed by subtracting m to the deuteron and the Λ masses 5.14 and it is found to be:

$$\mathrm{B}_{\Lambda} = [102 \pm 63\ (\text{stat.}) \pm 67\ (\text{syst.})]\ \text{keV},$$

where the deuteron mass is taken from CODATA [153], and the Λ mass from the PDG [7]. The right and left panels of Fig. 5.36 show the final τ and B_{Λ} results, together with their statistical and systematic uncertainties.

The new results can be compared with the previous measurements of the τ and B_{Λ} done so far in Figs. 5.37 and 5.37 : in both cases the most precise measurements of the two quantities are obtained [1]. Both the measurements provide a similar picture of the ${}^{3}_{\Lambda}\mathrm{H}$: the ${}^{3}_{\Lambda}\mathrm{H}$ lifetime is found to be compatible within statistical uncertainty with the free Λ one, while the B_{Λ} is compatible within 1σ with the zero value (${}^{3}_{\Lambda}\mathrm{H}$ unbounded). Even though some local tensions among a few measurements of lifetime and B_{Λ} have been reported in the literature as the "hypertriton puzzle", when performing a global average of the historically available measurements (see also the Mainz hypernuclear data database [46]), the probability of having such a set of measurements, computed with a Pearson test, is 23% for the lifetime and 57% for the B_{Λ}, hence no global tension is found.

---

[1] It is important to remark that the results before [61] lack of a determination of the systematic uncertainties. Hence, the statement above considers only the statistical precision associated with the measurements.

As the most recent theoretical calculations [76, 77] provide different relations between the ${}^{3}_{\Lambda}\mathrm{H}$ lifetime and the B_{Λ}, the new results can be evaluated together as it is done in Fig 5.38. The new set of measurements presented in this work provides tight constraints on the ${}^{3}_{\Lambda}\mathrm{H}$ structure, definitely proving that the ${}^{3}_{\Lambda}\mathrm{H}$ is an extremely weak bound state. Hence, the hypothesis of "compact" ${}^{3}_{\Lambda}\mathrm{H}$ seems to be ruled out by these measurements, thus solving a long-standing problem in the hypernuclear physics.

5.7.1 Testing the CPT symmetry

The standard model Lagrangian is invariant under the simultaneous operations of C (charge conjugation, which interchanges a particle with its antiparticle), P (parity, which reverses the direction of all spatial axes) and T (time reversal) and no CPT violation has ever been observed so far [13]. According to the CPT theorem, particles and their antiparticles should have the same mass and lifetime but opposite charge and magnetic moment. In the previous sections, ${}^{3}_{\Lambda}\mathrm{H}$ and ${}^{3}_{\bar{\Lambda}}\overline{\mathrm{H}}$ signals have been summed together: in the following, the CPT symmetry will be tested by considering separately the ${}^{3}_{\Lambda}\mathrm{H}$ and ${}^{3}_{\bar{\Lambda}}\overline{\mathrm{H}}$ contributions.

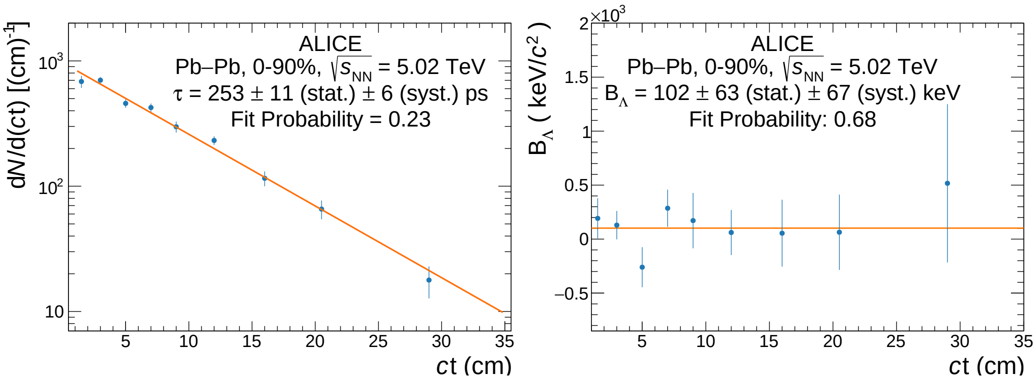

Fig. 5.36: Left: exponential decay spectrum as a function of the proper decay length for ${}^{3}_{\Lambda}\mathrm{H}$, the blue points represent the measured yield, while the orange line represents the best fit to the measurement. Right: B_{Λ} measurement as a function of the proper decay length. Only statistical uncertainties are shown; see the text for a description of the determination of the systematic uncertainties. The fit probability computed with a Pearson test is reported.

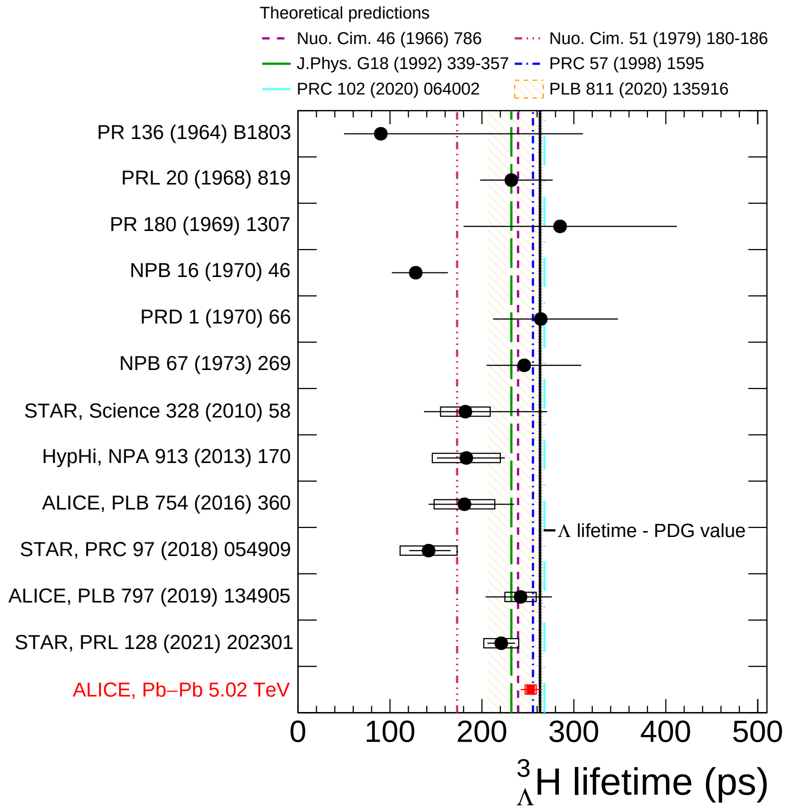

Fig. 5.37: Collection of the ${}^{3}_{\Lambda}\mathrm{H}$ lifetime measurements [61, 65, 70–72, 75, 147, 154–158] obtained with different experimental techniques. The horizontal lines and boxes are the statistical and systematic uncertainties, respectively. The dashed and dash-dotted lines are the corresponding theoretical predictions [60, 68, 76, 77, 159, 160].

The full analysis chain is repeated for both the ${}^{3}_{\Lambda}\mathrm{H}$ and ${}^{3}_{\bar{\Lambda}}\overline{\mathrm{H}}$ separately. The BDT efficiency interval chosen to compute the systematic variations is the same for both ${}^{3}_{\Lambda}\mathrm{H}$ and ${}^{3}_{\bar{\Lambda}}\overline{\mathrm{H}}$, and it is inherited from the ${}^{3}_{\Lambda}\mathrm{H}$ + ${}^{3}_{\bar{\Lambda}}\overline{\mathrm{H}}$ integrated analysis. Choosing different BDT efficiency intervals for ${}^{3}_{\Lambda}\mathrm{H}$ and ${}^{3}_{\bar{\Lambda}}\overline{\mathrm{H}}$ would introduce a further systematic uncertainty due to the different selection efficiencies of the two species. Hence, a common systematic distribution due to the signal selection and extraction is built for the $(\tau_{{}^{3}_{\Lambda}\mathrm{H}}$- $\tau_{{}^{3}_{\bar{\Lambda}}\overline{\mathrm{H}}})/\tau_{{}^{3}_{\Lambda}\mathrm{H}}$ quantity: for each trial the BDT efficiency and the fit functions are varied coherently for ${}^{3}_{\Lambda}\mathrm{H}$ and ${}^{3}_{\bar{\Lambda}}\overline{\mathrm{H}}$. In this way, the central value of the distribution is the quantity that we are interested in, while the spread of the distribution represents the systematic uncertainty due to the signal selection and extraction. The resulting systematic distribution is shown in the left panel of Fig. 5.39, while in the right panel the statistical uncertainties associated to the different trials and summed in quadrature for ${}^{3}_{\Lambda}\mathrm{H}$ and ${}^{3}_{\bar{\Lambda}}\overline{\mathrm{H}}$ are shown. The central value of the statistical distribution represents the statistical uncertainty associated with the measurement.

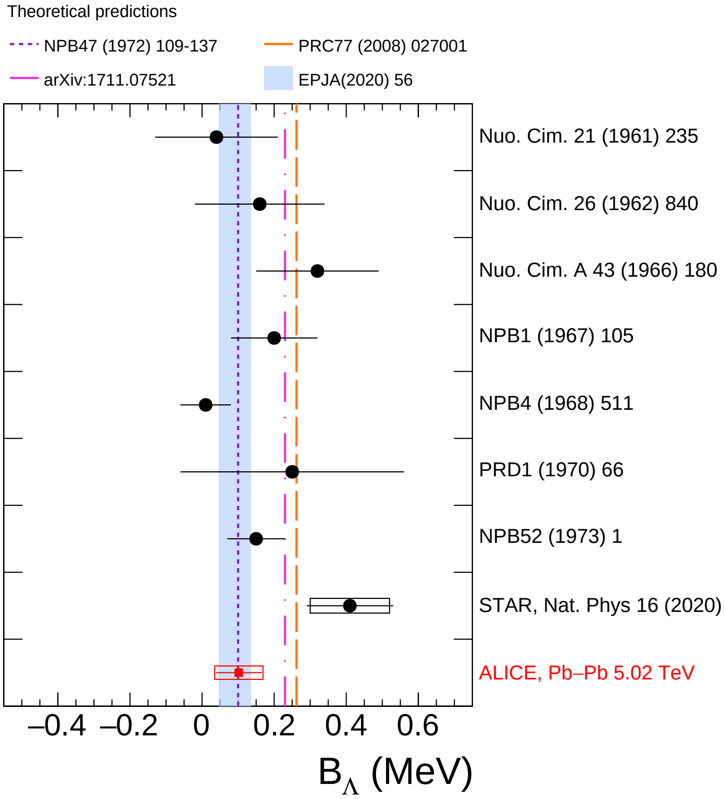

Fig. 5.37: Collection of the ${}^{3}_{\Lambda}\mathrm{H}$ B_{Λ} measurements [64, 65, 73, 161–165] obtained with different experimental techniques. The horizontal lines and boxes are the statistical and systematic uncertainties, respectively. The dashed and dash-dotted lines are the corresponding theoretical predictions [67, 83, 166, 167].

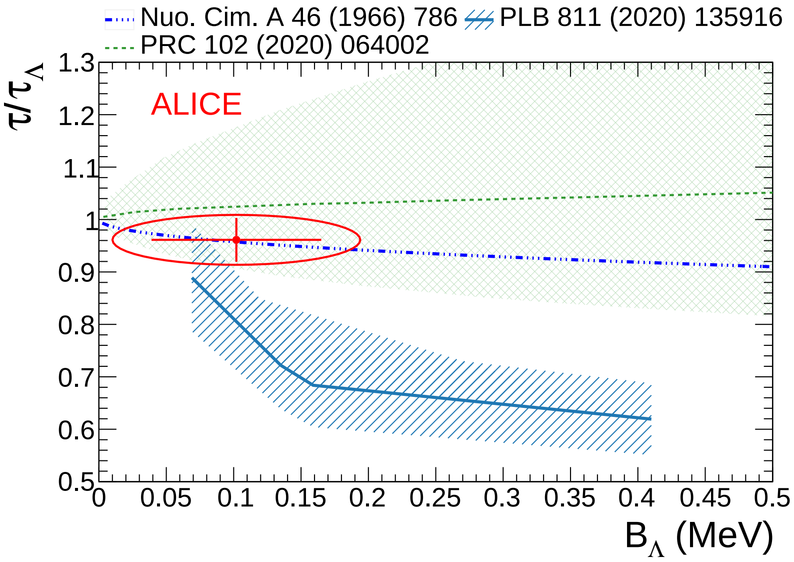

Fig. 5.38: The ${}^{3}_{\Lambda}\mathrm{H}$ lifetime relative to the free Λ lifetime as a function of the B_{Λ} for pionless EFT [76] (green), χEFT [77] (light blue), and the original π exchange calculations [159] (blue). The red point represents the measurement presented in this work with the statistical and total uncertainties depicted with lines and ellipse, respectively.

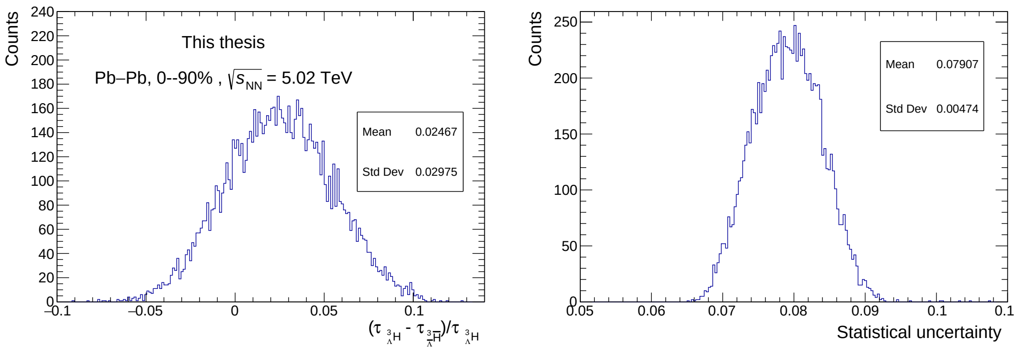

Fig. 5.39: Right panel: systematic distribution of the $^{3}_{\Lambda}\mathrm{H}$ lifetime asymmetry $(\tau_{^{3}_{\Lambda}\mathrm{H}}$- $\tau_{^{3}_{\overline{\Lambda}}\overline{\mathrm{H}}})/\tau_{^{3}_{\Lambda}\mathrm{H}}$. Left panel: statistical uncertainties associated to the different trials and summed in quadrature for $^{3}_{\Lambda}\mathrm{H}$ and $^{3}_{\overline{\Lambda}}\overline{\mathrm{H}}$.

Summing in quadrature the absorption contribution, which amounts to 2 ps, the final lifetime asymmetry is:

$$(\tau_{^{3}_{\Lambda}\mathrm{H}} - \tau_{^{3}_{\overline{\Lambda}}\overline{\mathrm{H}}})/\tau_{^{3}_{\Lambda}\mathrm{H}} = [2 \pm 8\ (\mathrm{stat.}) \pm 3\ (\mathrm{syst.})] \times 10^{-2}\,, \tag{5.16}$$

which is compatible with zero within the statistical and systematic uncertainties.

The same procedure is applied to the $^{3}_{\Lambda}\mathrm{H}$ mass measurement: the mass asymmetry $((m_{^{3}_{\Lambda}\mathrm{H}} - m_{^{3}_{\overline{\Lambda}}\overline{\mathrm{H}}})/m_{^{3}_{\Lambda}\mathrm{H}})$ systematic distribution shown in the left panel of Fig. 5.40 provides both the central value and the systematic uncertainty due to the signal selection and extraction.

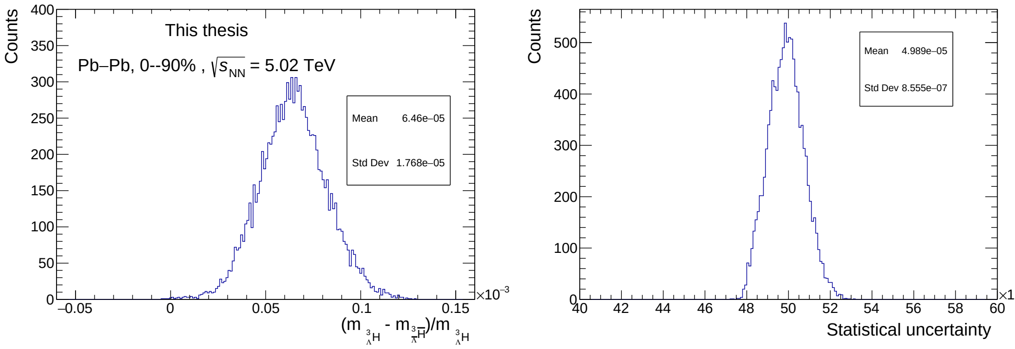

Fig. 5.40: Right panel: systematic distribution of the $^{3}_{\Lambda}\mathrm{H}$ mass asymmetry $(m_{^{3}_{\Lambda}\mathrm{H}} - m_{^{3}_{\overline{\Lambda}}\overline{\mathrm{H}}})/m_{^{3}_{\Lambda}\mathrm{H}}$. Left panel: statistical uncertainties associated to the different trials and summed in quadrature for $^{3}_{\Lambda}\mathrm{H}$ and $^{3}_{\overline{\Lambda}}\overline{\mathrm{H}}$.

The result is:

$$\frac{m_{^{3}_{\Lambda}\mathrm{H}} - m_{^{3}_{\overline{\Lambda}}\overline{\mathrm{H}}}}{m_{^{3}_{\Lambda}\mathrm{H}}} = [6 \pm 5\ (\mathrm{stat.}) \pm 2\ (\mathrm{syst.})] \times 10^{-5}, \tag{5.17}$$

which is fully compatible with zero within the statistical and systematic uncertainties. The statistical precision of the ${}^{3}_{\Lambda}\mathrm{H}$ mass asymmetry measurement improves by a factor of four the only previous measurement available [73]. However, a further dominant systematic contribution ($\delta m_{^{3}\mathrm{He}}$) has to be added to the mass asymmetry to take into account the uncertainty on the ${}^{3}\mathrm{He}$ and ${}^{3}\overline{\mathrm{He}}$ mass difference, as a potential CPT violation on the decay products would impact the measurement of $m_{{}^{3}_{\Lambda}\mathrm{H}} - m_{{}^{3}_{\overline{\Lambda}}\overline{\mathrm{H}}}$. This uncertainty has been taken from the STAR measurement [73] (δ^{STAR}), and propagated to $m_{{}^{3}_{\Lambda}\mathrm{H}} - m_{{}^{3}_{\overline{\Lambda}}\overline{\mathrm{H}}}$ utilizing a Monte Carlo method. Starting from a sample of one million ${}^{3}_{\Lambda}\mathrm{H}$ generated with a Blast Wave momentum distribution, the two body decay of the ${}^{3}_{\Lambda}\mathrm{H}$ is simulated by using the ROOT n-body phase space generator [123]. The ${}^{3}\mathrm{He}$ daughter mass is then smeared by δ^{STAR} and the ${}^{3}_{\Lambda}\mathrm{H}$ invariant mass is recomputed. The RMS of the resulting distribution, which is shown in Fig. 5.41, is then used as a proxy for the systematic uncertainty due to the ${}^{3}\mathrm{He}$ mass difference ($\delta m_{^{3}\mathrm{He}}$).

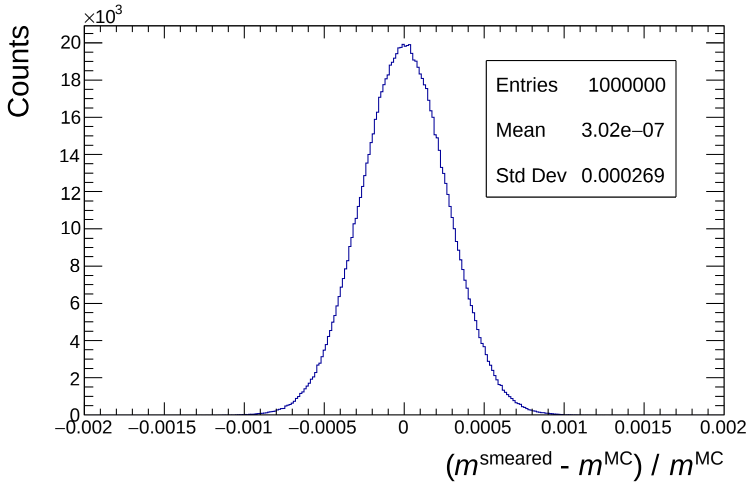

Fig. 5.41: Distribution of the reconstructed ${}^{3}_{\Lambda}\mathrm{H}$ mass after smearing the ${}^{3}\mathrm{He}$ daughter mass by δ^{STAR} minus the nominal ${}^{3}_{\Lambda}\mathrm{H}$ mass.

As the δ^{STAR} uncertainty is ~ 6 times larger than the statistical uncertainty coming from the ${}^{3}_{\Lambda}\mathrm{H}$ mass measurement, the $\delta m_{^{3}\mathrm{He}}$ systematic uncertainty is by far the dominant contribution to the total uncertainty.

The final result considering this further uncertainty separately is:

$$\frac{m_{{}^{3}_{\Lambda}\mathrm{H}} - m_{{}^{3}_{\overline{\Lambda}}\overline{\mathrm{H}}}}{m_{{}^{3}_{\Lambda}\mathrm{H}}} = [6 \pm 5\ (\mathrm{stat.}) \pm 2\ (\mathrm{syst.}) \pm 27(\delta m_{^{3}\mathrm{He}})] \times 10^{-5}. \qquad (5.18)$$

Both the ${}^{3}_{\Lambda}\mathrm{H}$ lifetime and mass asymmetry measurements are fully compatible with zero within the statistical and systematic uncertainties, thus providing a stringent test of the CPT symmetry in the nuclear sector.

6

First measurement of ${}^{3}_{\Lambda}\mathrm{H}$ production in p–Pb collisions

As explained in detail in Chapter 2, the extremely low B_{Λ} measured implies that the ${}^{3}_{\Lambda}\mathrm{H}$ has a large radius extending up to $\sim$ 5 fm [69, 168]. The size of the ${}^{3}_{\Lambda}\mathrm{H}$ wave function is therefore much larger than the hadron emission radius estimated with femtoscopic techniques in p–Pb collisions (1–2 fm, [101, 102]). For this reason, the ${}^{3}_{\Lambda}\mathrm{H}$ yield in p–Pb collisions predicted by the coalescence model, where the ratio of nucleus size to source size directly influences its yield, is suppressed with respect to the statistical hadronisation model expectations [95, 98, 169]. In this Chapter, the first measurement of the ${}^{3}_{\Lambda}\mathrm{H}$ production, which was published with a letter on the Physics Review Letters Journal [170] is presented. The measurement is performed by analysing the p–Pb data sample collected by ALICE at $\sqrt{s_{\mathrm{NN}}}$ = 5.02 TeV during 2013 and 2016, and by selecting the ${}^{3}_{\Lambda}\mathrm{H}$ signals with BDTs.

Data sample

The results presented in this Chapter are based on the p–Pb data sample collected by ALICE at $\sqrt{s_{\mathrm{NN}}}$ = 5.02 TeV during the 2013 and 2016 data taking periods. The minimum bias trigger is used to select the events by requiring a hit in the SPD or in either two V0 detectors. The triggered events are further selected offline with an analogous procedure to the one used in Pb–Pb analysis (see Sec. 5.1.1):

- Primary vertices in a fiducial region of ± 10 cm are selected
- pile-up rejection based on: the number of reconstructed SPD primary vertices, the difference between the global and SPD primary vertices positions.

The event selections are summarized in Table 6.1: in total, about 750 million MB events are selected for analysis, corresponding to an integrated luminosity of $\mathcal{L}_{\mathrm{int}}^{\mathrm{MB}} = 359\ \mu\mathrm{b}^{-1}$, with a relative uncertainty determined by the van der Meer scan to be 3.7% [171].

Tab. 6.1: Summary of the event selection applied for to the data sample employed for this analysis.

Data sample	Selections
p–Pb 2013 + 2016	$\lvert V_z \rvert \leq 10$ cm Reject multiple SPD vertices with more than n contributors $\lvert \Delta V_z \rvert \leq 20\sigma_{\mathrm{track}}$, $\lvert \Delta V_z \rvert \leq 10\sigma_{\mathrm{SPD}}$ and $\lvert \Delta V_z \rvert \leq 0.2$ cm

The centrality distribution of the selected events is shown in Fig. 6.1: the MB trigger provides an almost uniform centrality distribution between 0% and 90% centrality.

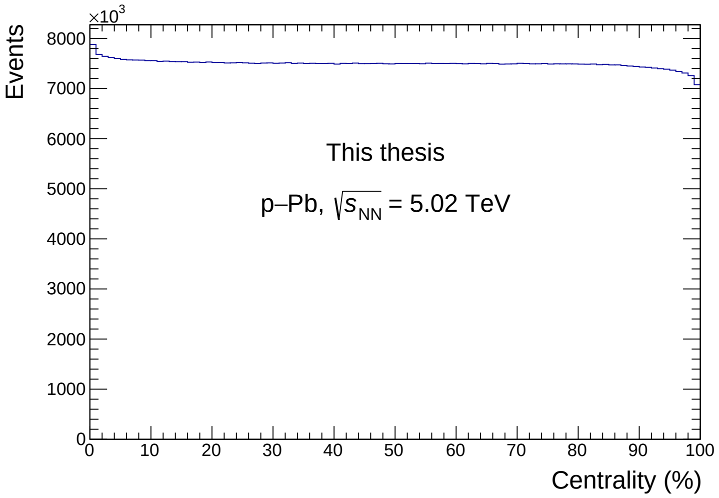

Fig. 6.1: Centrality distribution of the selected events.

As most of the signal is expected to be produced in central collisions, for this analysis, the 40% events with the highest multiplicity measured by the V0A detector are used. It is worth to mention that in p–Pb collisions the V0A estimator does not strictly measure centrality, but is more used to define the percentiles of multiplicity, as the centrality in p–Pb collisions is very difficult to determine In total ~ 400 million events in the 0–40% centrality interval are selected.

6.0.1 Monte Carlo sample

A MC production anchored to both the data taking periods is used similarly to what is done for the ${}^{3}_{\Lambda}\mathrm{H}$ lifetime and binding energy analyses (see Sec. 5.1.2). The MC sample will be employed to compute the efficiency and acceptance corrections. Each MC event is composed by:

- the underlying p–Pb event, generated by using the HIJING [125] event generator;
- five ${}^{3}_{\Lambda}\mathrm{H}$ and five ${}^{3}_{\Lambda}\overline{\mathrm{H}}$ with a uniform momentum distribution between 0 and 10 GeV/c and η between -1 and 1.

The transport of ${}^{3}_{\Lambda}\mathrm{H}$ and ${}^{3}_{\Lambda}\overline{\mathrm{H}}$ in the detector material is simulated by using the GEANT4[128] simulation package. As it is done for the Pb–Pb, only a fraction of the total collected statistics is generated in the MC samples. The centrality of the simulated events is computed starting from the impact parameter (b) of the collision simulated by HIJING. In the MC sample, b is extracted randomly for each event. The input ct distribution is obtained by sampling an exponential function with $\tau = \tau_{\Lambda}$, and it is shown in Fig. 6.2.

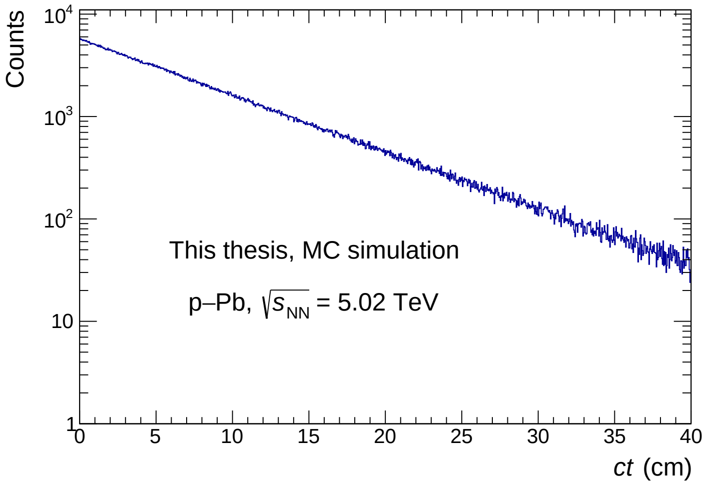

Fig. 6.2: Input ct distribution for the ${}^{3}_{\Lambda}\mathrm{H}$ and ${}^{3}_{\Lambda}\overline{\mathrm{H}}$ in the MC sample.

6.1 ${}^{3}_{\Lambda}\mathrm{H}$ (${}^{3}_{\Lambda}\overline{\mathrm{H}}$) reconstruction

The ${}^{3}_{\Lambda}\mathrm{H}$ and ${}^{3}_{\Lambda}\overline{\mathrm{H}}$ are reconstructed in the same way as in the Pb–Pb analysis (see Sec. 5.2), and in the following they will be summed together and simply referred to as ${}^{3}_{\Lambda}\mathrm{H}$. The daughter track quality selections are listed in Table 5.2, and guarantee a momentum and TPC dE/dx resolutions better than 5% and 6% respectively. The ${}^{3}_{\Lambda}\mathrm{H}$ candidates are reconstructed by combining the daughter tracks with the custom offline V0 finder described in Sec. 5.2. As the daughter tracks combinatorics is much lower than in the Pb–Pb case, only the $\mathrm{DCA}_{\mathrm{daugh}}$ pre-selection is applied during the vertexing: daughter tracks are required to have a minimum distance of closest approach of 1.5 cm. In addition, the PID selection on the ${}^{3}\mathrm{He}$ and π tracks is performed by requiring the $n\sigma^{{}^{3}\mathrm{He}} = \frac{|S_{meas}-S_{exp}|}{\sigma^{{}^{3}\mathrm{He}}} < 4$ or $n\sigma^{\pi} = \frac{|S_{meas}-S_{exp}|}{\sigma^{\pi}} < 4$.

The ^{3}He PID response calibration is performed as described in Sec. 5.2.2. The only important difference introduced at this level is the $^3_\Lambda$H rapidity selection: in p–Pb collisions the centre-of-mass system moves in rapidity by $\Delta y_{\rm cms}$ = 0.465 in the direction of the proton beam. Hence, to match the barrel acceptance of the ALICE detector, only $^3_\Lambda$H candidates with $-1 \leq y_{\rm cms} < 0$ are selected: this will also allow for a direct comparison with other measurements, as it will be explained in the next sections.

The Monte Carlo sample, which is employed for the efficiency correction and for training the BDT Classifier, undergoes the same reconstruction procedure employed for the data. In addition, the reweighting of the $p_{\rm T}$ shape according to the published ^{3}He analysis [172] is applied to the uniform input $p_{\rm T}$ distribution. In [172], different $p_{\rm T}$ shapes are employed for extrapolating the ^{3}He yield at low momentum: $m_{\rm T}$-exponential, $p_{\rm T}$-exponential, Boltzmann, Blast Wave functions (see the definitions in 9). The one employed for reweighting the $^3_\Lambda$H distribution is the $m_{\rm T}$-exponential one, which is the one that better describes the ^{3}He data: the other $p_{\rm T}$ shapes are employed for the systematic uncertainty evaluation. The reweighted $^3_\Lambda$H $p_{\rm T}$ distribution is shown in Fig. 6.3, with superimposed the ^{3}He $p_{\rm T}$ shape from [172].

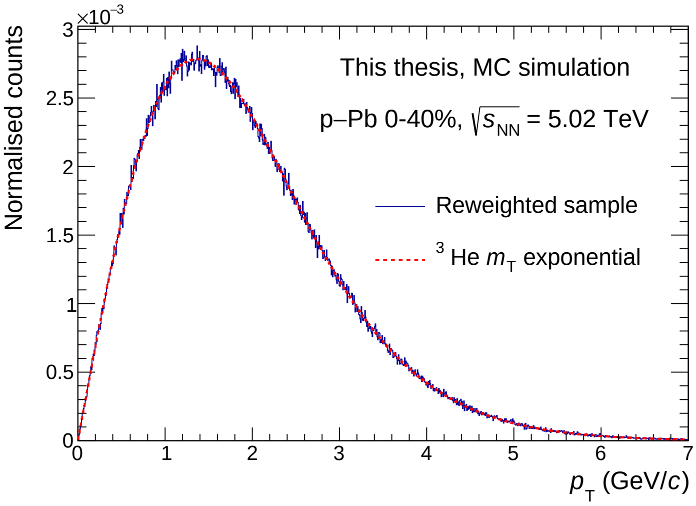

Fig. 6.3: Reweighted $^3_\Lambda$H $p_{\rm T}$ distribution, together with the ^{3}He $p_{\rm T}$ shape from [172].

Finally, the pre-selection efficiency as a function of the $^3_\Lambda$H $p_{\rm T}$ is computed, and it is shown in Fig. 6.4. The efficiency is computed in the rapidity range $-1 \leq y_{\rm cms} < 0$ and in the centrality range 0–40%, and it takes into account the geometrical acceptance of the ALICE detector, the $^3_\Lambda$H reconstruction efficiency, and the $^3_\Lambda$H PID selection. The $p_{\rm T}$ integrated efficiency, which is computed on the reweighted sample from 0 to 9 GeV/c results to be 29%.

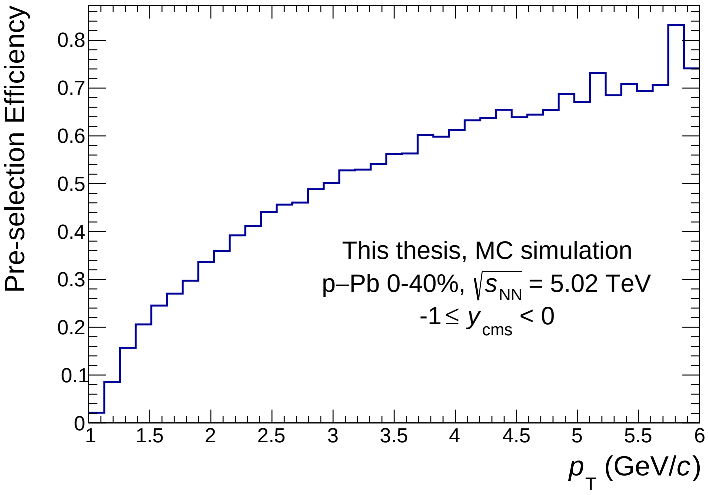

Fig. 6.4: Pre-selection efficiency as a function of the $^{3}_{\Lambda}\mathrm{H}$ p_{T}.

$^{3}_{\Lambda}\mathrm{H}$ selection with the BDT Classifier

The $^{3}_{\Lambda}\mathrm{H}$ signal selection is performed by using the XGBoost BDT Classifier, similarly to what is done in the Pb–Pb analysis (see Sec. 5.3.2). The training sample is composed by:

- the signal sample, built by selecting $^{3}_{\Lambda}\mathrm{H}$ signal in the MC sample;
- the background sample, built by pairing a $^{3}\mathrm{He}$ and a π track of the same sign (Like Sign, LS) in the data sample.

The input variables employed for training the BDT Classifier are the same as the ones employed in the Pb–Pb analysis (listed here 5.3.1) with one exception: the $^{3}_{\Lambda}\mathrm{H}$ ct is used instead of the p_{T}. This is done because the ct distribution is well known and measured, while the p_{T} distribution depends on the collision system and is not measured yet. The combination of both the variables has to be avoided, as it would allow the model to infer on the mass of the $^{3}_{\Lambda}\mathrm{H}$ ($ct = m\frac{L}{p}$). The distribution of the training variables is shown in Fig. 6.5, and it is similar to the one found in the Pb–Pb analysis (see Fig. 5.11). Variables that present strong differences between signal and background, such as the cos(θ_p), the ct, and the $\mathrm{n}^{\mathrm{clus}}_{\mathrm{TPC}}$ $^{3}\mathrm{He}$ will be the most important ones for the BDT Classifier.

The correlations among the training variables are also checked: the BDT is able to exploit the different correlations among the signal and background variables to properly classify an independent sample. The correlation matrices are shown in Fig. 6.6, and they are similar to the ones found in the Pb–Pb analysis (see Fig. 5.13).

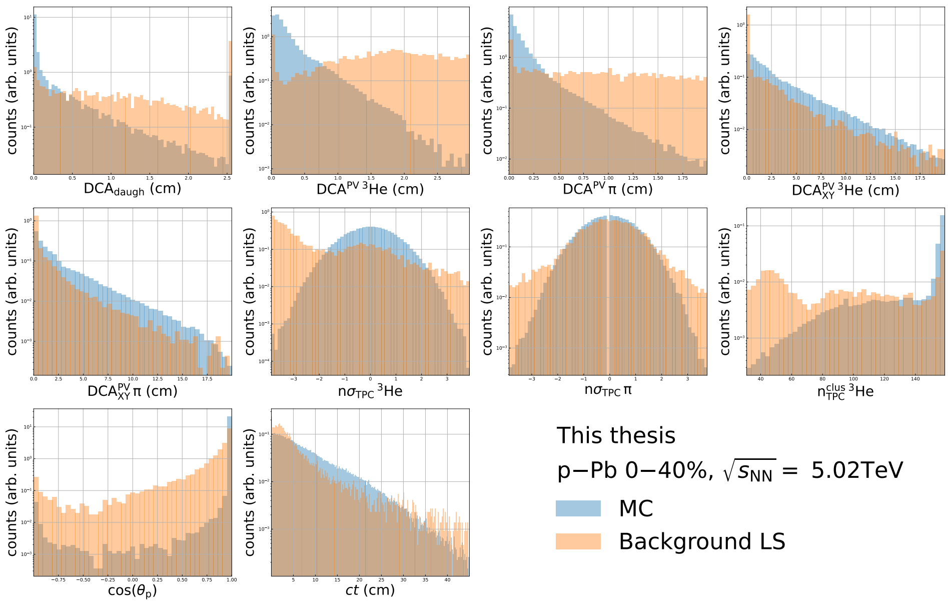

Fig. 6.5: Distribution of the training variables for the $^{3}_{\Lambda}\mathrm{H}$ signal and background.

The ct, which is the new variable introduced in the p–Pb analysis, is correlated with the DCA variables as expected, and it is not correlated with invariant mass, thus avoiding potential mass shaping effects.

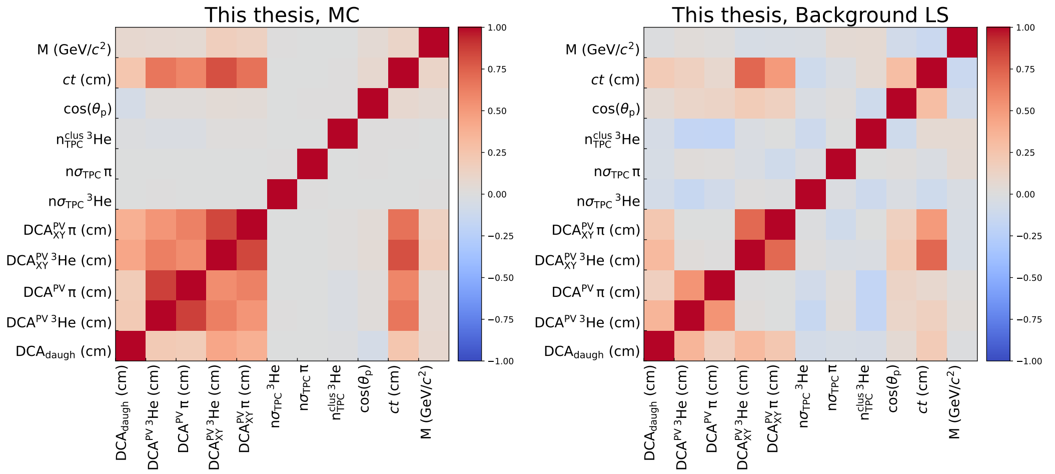

Fig. 6.6: Linear correlations between the training variables and the $^{3}_{\Lambda}\mathrm{H}$ invariant mass, for signal (top) and background (bottom) candidates. The colours, from red (fully correlated) to blue (fully anti-correlated), indicate the correlation level.

6.1.1 Training and testing of the BDT

The BDT Classifier is trained using the XGBoost package, as it is done in the Pb–Pb analysis (see Sec. 5.3.2). As the signal will be extracted in one integrated p_{T} bin between 0 and 9 GeV/c, one single BDT is trained for the whole p_{T} range. The training is performed in two steps: first the best BDT hyper-parameters are found by employing a bayesian optimizer, and then a final training step is performed using the optimal hyper-parameters configuration. The full training sample is split in two parts: the first one is used for training the BDT, while the second one is used for testing the BDT performance (test set).

The hyper-parameters are optimized by maximizing the ROC-AUC score evaluated on five different subsamples, employing the 5-fold cross-validation technique described in Sec. 5.3.2. The search is entrusted to the Hyperopt package [138], the bayesian optimizer already described in Sec. 4.2.2. The best hyperparameter configuration found is summarized in Table 6.2.

Hyper-parameter	Optimization range	Values
max depth	[3, 20]	6
n estimators	[50, 800]	350
learning rate	[0.01, 0.3]	0.1
gamma	[0.3, 1.1]	0.6
min child weight	[1, 12]	7.3
subsample	[0.5, 0.9]	0.8
colsample by tree	[0.5, 0.9]	0.6

Tab. 6.2: Optimized BDT hyper-parameters in the p–Pb analysis.

Once the final training is done, the performance of the BDT are evaluated both on the training and the test sets: for each candidate the BDT score is computed, and the resulting distributions, divided by signal and background, are shown in Fig. 6.7. The distributions, similar to the ones found in the Pb–Pb analysis (see Fig. 5.15), are well separated, demonstrating that the BDT is able to properly classify the signal and the background.

A negligible overfitting behaviour is observed, and can be quantified by comparing the ROC curves obtained on the training and the test sets, as shown in Fig. 6.8. In both the cases the BDT is able to separate the signal from the background with ROC-AUC scores higher than 0.999; while the relative difference between the two scores is $\sim 0.3\%$.

The feature importance is also evaluated in Fig. 6.9 by using the SHAP algorithm, showing a behaviour similar to the one found in the Pb–Pb analysis (see Fig. 4.7): the most important features are the cos(θ_p) and the $\mathrm{n}\sigma_{\mathrm{TPC}}$ $^3\mathrm{He}$ variables, followed by the DCA variables.

6.1.2 Choice of the BDT threshold

After passing all the checks performed during the testing part, the BDT is applied to the real data sample, obtaining a continuous distribution. In order to extract the $^3_\Lambda\mathrm{H}$

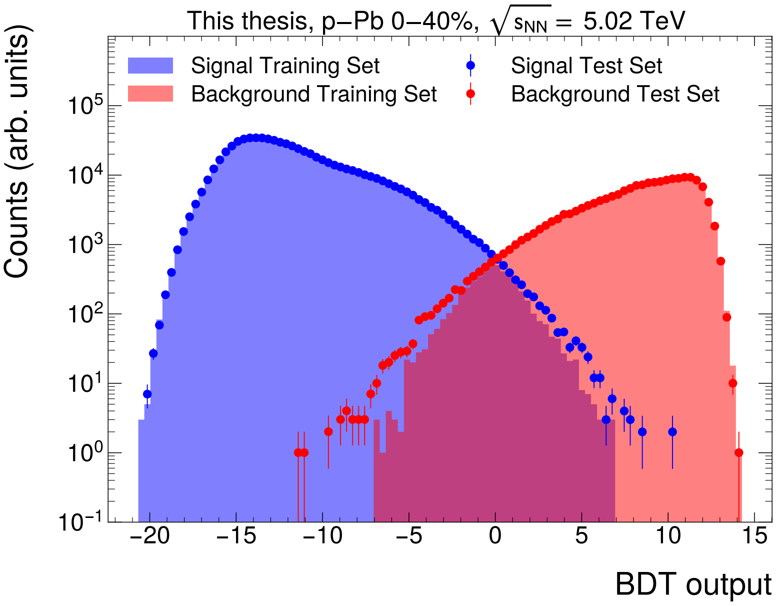

Fig. 6.7: Normalized BDT output distributions for the training (shaded area) and test (points with statistical errors) set. The background is reported in blue, the signal in red.

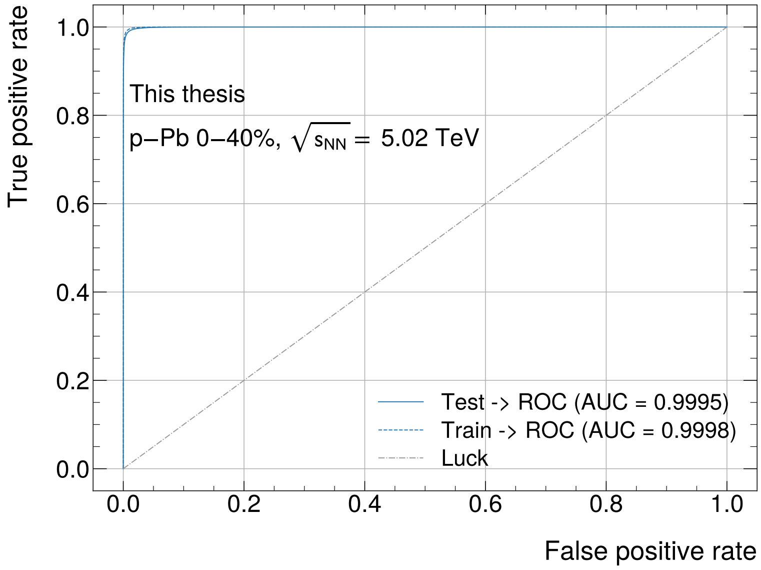

Fig. 6.8: ROC curves for the training and the test sets.

signal, a threshold is applied to the BDT score. First the BDT efficiency as a function of the score threshold is computed on the test set, and it is parametrized by using a spline function between 0.99 and 0.5, as described in Sec. 5.5.3. The result is shown in Fig. 6.10.

The BDT score threshold is then chosen by employing the Significance Scan algorithm, which is described in Sec. 5.3.3. For each threshold the expected significance,

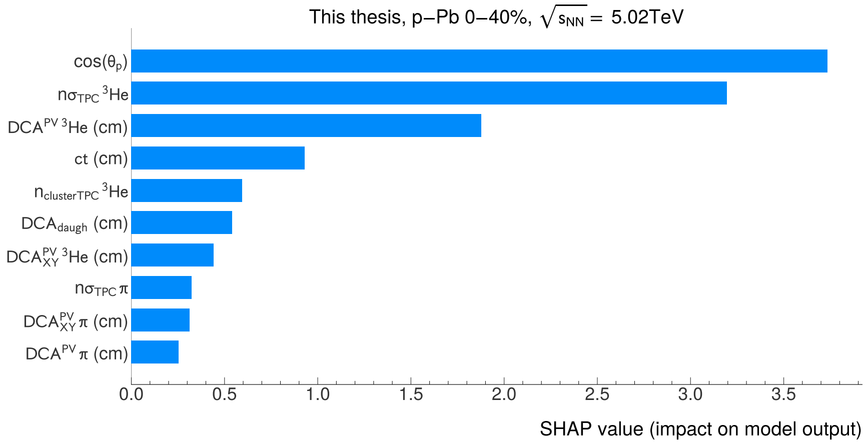

Fig. 6.9: Feature importance computed by using the SHAP algorithm. Features are ordered by decreasing importance.

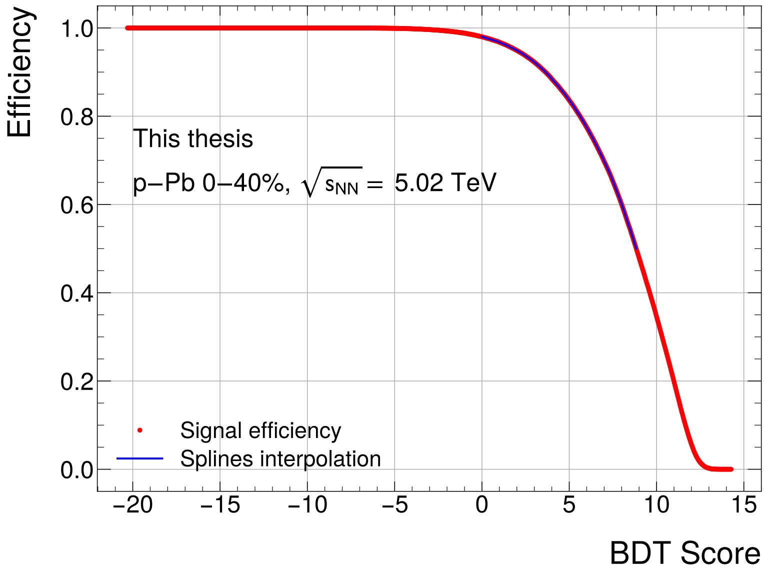

Fig. 6.10: BDT efficiency as a function of the score threshold, computed on the test set (red markers). A spline function is used to parametrize the efficiency curve (blue line).

computed by assuming ${}^{3}_{\Lambda}\mathrm{H}$ thermal production, is evaluated and multiplied by the corresponding BDT efficiency. The result is shown in Fig. 6.11: the expected significance obtained by assuming thermal production is $> 6\sigma$. The BDT threshold efficiency results to be 72%.

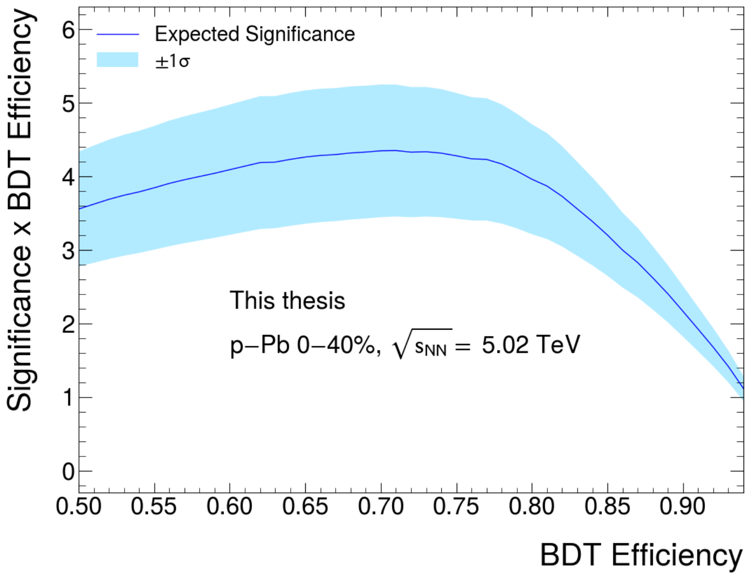

Fig. 6.11: Expected significance as a function of the corresponding BDT threshold efficiency, computed assuming thermal production. The significance is multiplied for the BDT efficiency.

6.2 Measurement of $^{3}_{\Lambda}\mathrm{H}$ production in p–Pb collisions

After passing the BDT threshold, the selected $^{3}_{\Lambda}\mathrm{H}$ candidates are employed to populate the invariant mass spectrum. A clear excess of events is observed around the nominal $^{3}_{\Lambda}\mathrm{H}$ mass, and it is reported in Fig. 6.12. In Fig. 6.12, both the selected candidates for data and LS background are shown. The LS invariant mass spectrum does not exhibit any peak structure, demonstrating that the excess is not due to the mass shaping effect.

The signal extraction is performed on the unbinned invariant distribution in order to avoid biases due to the choice of the binning of the histogram. The signal shape is extracted from the MC sample and smoothed with a KDE function, already described in Sec. 5.4, while the background is parametrized by a first order polynomial. The result of the signal extraction is shown in Fig. 6.13.

The signal is extracted by integrating the KDE function over the full invariant mass range, and it is found to be: $\mathrm{S} = 19.1 \pm 5.6$. As the number of signal events is extremely low, the simple approximation employed in Sec. 5.4 for computing the significance ($\mathrm{Sign} = \mathrm{S}/\sqrt{\mathrm{S}+\mathrm{B}}$) is not applicable, and a more sophisticated approach is needed. The significance associated with the signal is evaluated following the procedure described in [173]: the probability for a background fluctuation to be

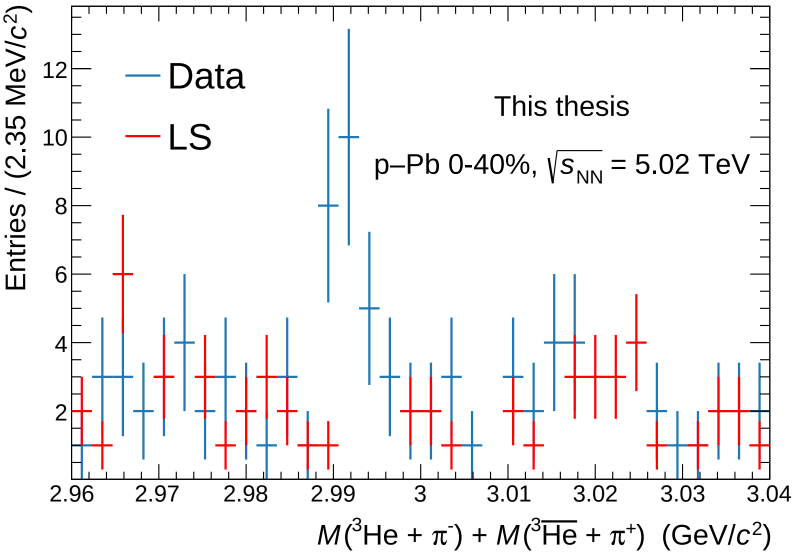

Fig. 6.12: Invariant mass spectrum of the selected $^3_\Lambda\mathrm{H}$ candidates both in the unlike sign pairs (blue) and in the LS background (red). The data points are shown with statistical errors. Entries with zero counts are not shown in the Figure.

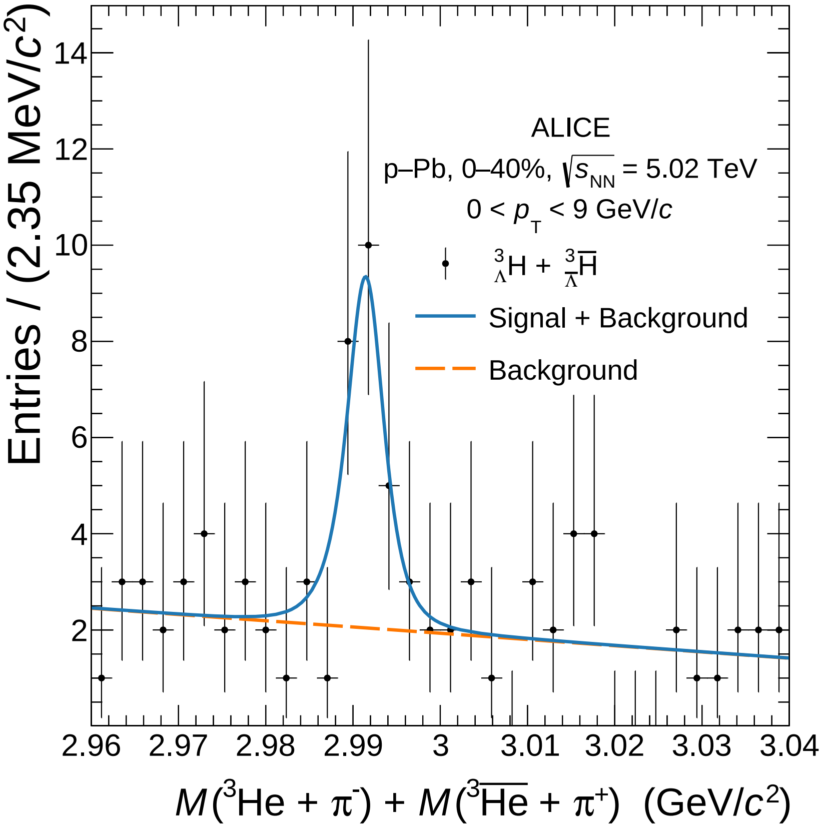

Fig. 6.13: Invariant mass distribution of the $^3\mathrm{He}+\pi^-$ and charge conjugate pairs passing the analysis selections. The invariant mass spectrum is fitted with a two component model: the blue line represents the total fit while the orange dashed line shows the background component only.

at least as large as the observed maximum excess (local p-value) is computed by employing the asymptotic formulae for likelihood-based tests obtained by Cowan et al. The formulae have successfully been employed for the Higgs boson discovery [174], and they are implemented in the RooFit framework [149]. The local p-value can be expressed as a corresponding number of standard deviations using the one-sided Gaussian tail convention. The result of the study is shown in Fig. 6.14: the local p-value in correspondence of the ${}^{3}_{\Lambda}$H mass peak results to be higher than 4σ.

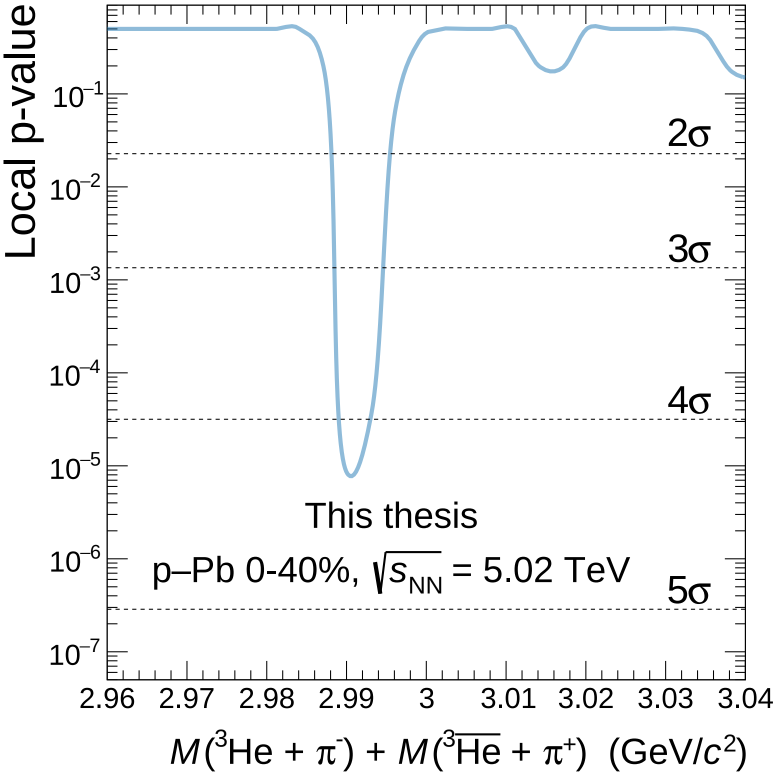

Fig. 6.14: Local p-values as a function of the ${}^{3}_{\Lambda}$H invariant mass. The significance is computed by using the one-sided Gaussian tail convention, and it is reported with horizontal dashed lines.

The capability of extracting the ${}^{3}_{\Lambda}$H signal with high significance in p–Pb represents a huge milestone for the nuclear physics community, as for the first time the hypertriton is observed in hadronic collisions different from the nucleus-nucleus ones.

Production yield

The production yield ($\mathrm{d}N/\mathrm{d}y$) is obtained starting from the signal extracted from the fit to the invariant mass spectrum (S). Then the fitted signal is corrected for the pre-selection efficiency (ϵ_{pres}, includes the ${}^{3}_{\Lambda}$H candidate reconstruction efficiency and the acceptance of the ALICE detector), the BDT efficiency (ϵ_{BDT}), the number of analysed events (N_{ev}), the branching ratio (B.R.) of the ${}^{3}_{\Lambda}$H in the two-body decay channel and the fraction of ${}^{3}_{\Lambda}\mathrm{H}$ that are not absorbed in the ALICE detector $(1 - f_{\mathrm{abs}})$. The expression for the production yield is:

$$\frac{\mathrm{d}N}{\mathrm{d}y} = \frac{1}{\epsilon_{\mathrm{pres}}}\frac{1}{\epsilon_{\mathrm{BDT}}}\frac{1}{\mathrm{N_{ev}}}\frac{1}{\mathrm{B.R.}}\frac{1}{(1 - f_{\mathrm{abs}})} \times \mathrm{S} \tag{6.1}$$

The values of ϵ_{pres}, ϵ_{BDT}, and $\mathrm{N_{ev}}$ have already been discussed and amounts 27%, 72% and 4×10^{8} respectively. The B.R. value is assumed to be 0.25 according to the calculation published in [60], but uncertainty will be added as it will be explained in 6.2. Finally, the value of f_{abs} is determined with the same procedure employed in 5.5.1: the interaction of the ${}^{3}_{\Lambda}\mathrm{H}$ with the ALICE detector is simulated with GEANT4 by using ${}^{3}\mathrm{He}$ as a proxy, after properly reweighting the momentum and the ct distributions. The value of the ${}^{3}_{\Lambda}\mathrm{H}$ cross section given in input to GEANT4 is $\sigma^{inel} = 1.5\sigma^{inel}({}^{3}\overline{\mathrm{He}})$, according to the only calculation available in literature by Evlanov et al. [151]. A slightly but compatible approach is employed to compute the ct integrated f_{abs} value since at the time of the analysis there were only MC samples with increased cross section by a factor 5 and 8. For each of these samples, the ct integrated f_{abs} value is computed, and the value of f_{abs} corresponding to $\sigma^{inel} = 1.5\sigma^{inel}({}^{3}\overline{\mathrm{He}})$ is obtained through an exponential interpolation. The resulting value of f_{abs} is 3%, which is fully compatible with the one obtained in the lifetime analysis by using the sample with $\sigma^{inel} = 1.5\sigma^{inel}({}^{3}\overline{\mathrm{He}})$ employed in Sec. 5.5.1. The factor 1 - f_{abs} is shown as a function of the cross section in Fig. 6.15: different p_{T} shapes have been employed for reweighting the sample (the default one is m_{T}-exponential), and the differences are taken into account in the systematic evaluation.

Systematic uncertainties

The systematic uncertainties are evaluated similarly as in the Pb–Pb analysis. Four different sources are considered: the ${}^{3}_{\Lambda}\mathrm{H}$ signal selection and extraction, the choice of the ${}^{3}_{\Lambda}\mathrm{H}$ input p_{T} shape, the absorption in the ALICE detector, and finally the ${}^{3}_{\Lambda}\mathrm{H}$ branching ratio.

Signal selection and extraction

A multi trial approach is employed to evaluate the systematic uncertainty associated with the signal selection and extraction. As the signal is extracted with significance > 3 only in a narrow ϵ_{BDT} window, the systematic uncertainty is evaluated by varying the BDT threshold around $\pm 5\%$ from the optimal ϵ_{BDT}. For each variation, the signal is extracted with three different background functions (constant, linear, exponential), while the signal shape is not varied as it does not affect the signal

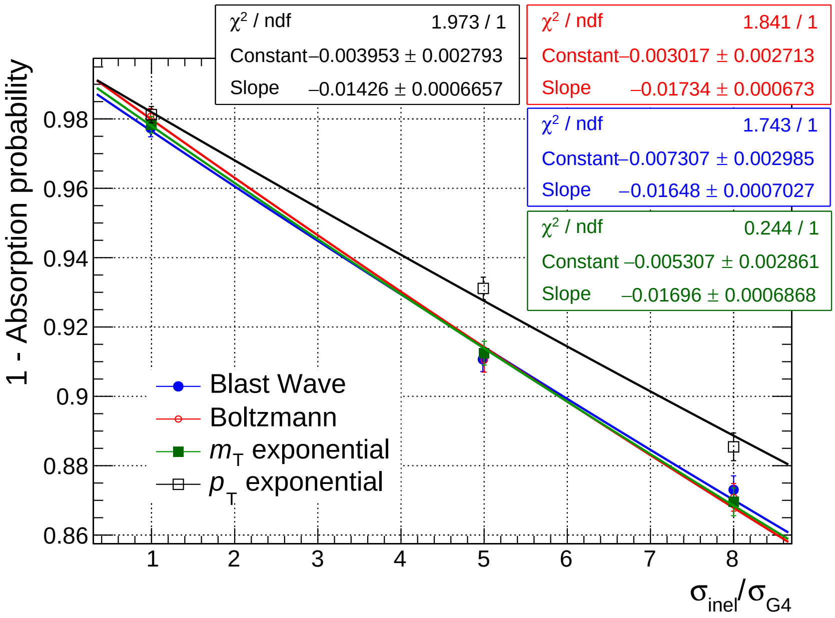

Fig. 6.15: Correction factor 1-f_{abs} as a function of the anti- ^3He inelastic cross-section for the different p_T shapes considered in the analysis. The superimposed exponential fits were used to obtain the correction factor for cross sections that are 1.5 times larger than the anti-^3He inelastic cross section

extraction significantly. Hence, 33 different variations are considered, and for each of them the factor S/ϵ_{BDT} is computed. The RMS of the resulting distribution, which is shown in Fig. 6.16, is used as an estimate of the systematic uncertainty due to the signal selection and extraction. This uncertainty results to be 15% of the signal yield.

Choice of the input p_T shape

As mentioned in section 6.1, the p_T shape of the $^3_\Lambda\text{H}$ candidates in the MC is reshaped according to the ^3He m_T exponential function. The systematic uncertainty due to the choice of this model is evaluated. Since the p_T is not used as a training variable the main contribution for this source of uncertainty is given by the different pre-selection efficiencies. To estimate this systematic uncertainty, four different input p_T shapes are employed to compute different pre-selection efficiencies: Boltzmann, p_T exponential, m_T exponential and Blast Wave. The parameters of the p_T distributions are taken from the published ^3He analysis [172]. The transverse momentum distribution of the sample reshaped according to the different models is shown in Figure 6.17. While the Boltzmann and m_T exponential distributions present similar shape, the fitted p_T exponential and Blast Wave distributions are significantly different. For each function the pre-selection efficiency is re-computed, and the standard deviation between the different corrections is taken as systematic estimate due to the unknown $^3_\Lambda\text{H}$ p_T shape, resulting 7%.

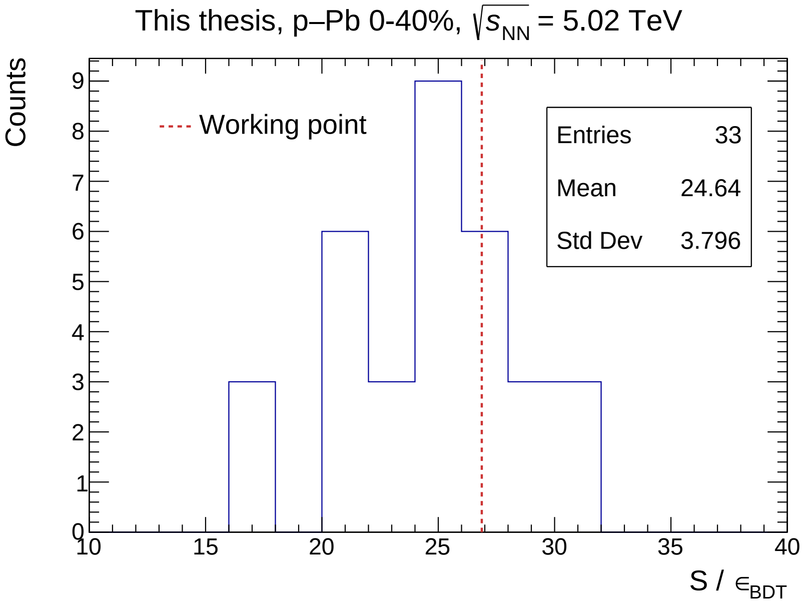

Fig. 6.16: Distribution of the signal yield obtained by varying the BDT threshold around ±5% from the optimal ϵ_{BDT}, and by using three different background functions (constant, linear, exponential). The S/ϵ_{BDT} obtained from the optimal BDT threshold is used as a reference, and it is shown with a vertical dashed red line.

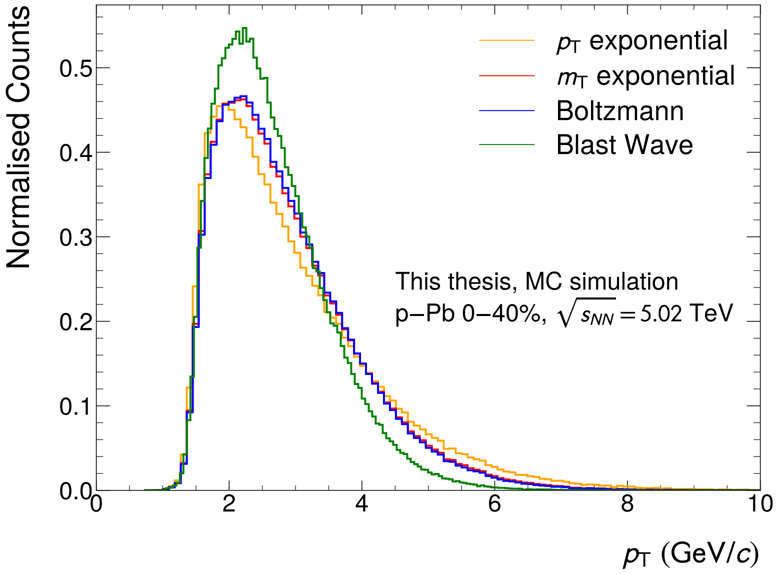

Fig. 6.17: Reconstructed MC sample reshaped according to four different input models.

Absorption in the ALICE detector

The uncertainty due to the unknown ${}^{3}_{\Lambda}\mathrm{H}$ absorption cross section is evaluated by varying the nominal ${}^{3}_{\Lambda}\mathrm{H}$ cross section of ± 50%. Hence, the full difference between f_{abs} computed for $\sigma^{inel} = \sigma^{inel}({}^{3}\overline{\mathrm{He}})$ and $\sigma^{inel} = 2\sigma^{inel}({}^{3}\overline{\mathrm{He}})$ is taken directly from Fig. 6.15, resulting in a systematic uncertainty of 2%.

Branching ratio

The value of B.R. = 0.25 for the $^{3}_{\Lambda}\mathrm{H} \rightarrow {}^{3}\mathrm{He} + \pi$ decay reported in this analysis is computed theoretically in Ref. [60]. Since there are not direct measurement of the full $^{3}_{\Lambda}\mathrm{H}$ branching ratios, an uncertainty is added by evaluating the relative deviation between the theoretical R_3 and the world average of all the R_3 measurements found in [71], where R_3 is defined as:

$$\mathrm{R}_3 = \frac{\mathrm{B.R.}(^{3}_{\Lambda}\mathrm{H} \rightarrow {}^{3}\mathrm{He} + \pi^-)}{\mathrm{B.R.}(^{3}_{\Lambda}\mathrm{H} \rightarrow \text{all } \pi^- \text{ decay channels})}.$$

This uncertainty on R_3 is propagated linearly to the $\mathrm{B.R.}(^{3}_{\Lambda}\mathrm{H} \rightarrow {}^{3}\mathrm{He} + \pi^-)$ and corresponds to a variation range of $\pm 9\%$ around the nominal value. Therefore, the relative uncertainty due to the choice of the B.R. value is 9%.

Table 6.3 summarizes all the systematic contributions evaluated in this analysis: the total systematic uncertainty is 19% of the signal yield.

Systematic contribution	Value (%)
Signal selection and extraction	15 %
Choice of the p_{T} shape	7 %
Absorption in the detector	2 %
Branching ratio value	9 %
Total	19 %

Tab. 6.3: Summary of the different sources of systematic uncertainty affecting the $^{3}_{\Lambda}\mathrm{H}$ yield measurement.

Results

The resulting corrected $^{3}_{\Lambda}\mathrm{H}$ yield in the rapidity interval $-1 < y < 0$ together with its statistical and systematic uncertainties is

$$\frac{\mathrm{d}N}{\mathrm{d}y} = [6.3 \pm 1.8(\mathrm{stat.}) \pm 1.2(\mathrm{syst.})] \times 10^{-7}.$$

The result is compared with the expectations from the canonical SHM [95], defined in Sec. 2.3, which assumes exact conservation of baryon number, strangeness and electric charge across a correlation volume V_c. The SHM predictions are computed using a fixed chemical freeze-out temperature of T_{chem} = 155 MeV and two correlation volumes extending across one unit ($V_c = \mathrm{d}V/\mathrm{d}y$) and three units ($V_c = 3\mathrm{d}V/\mathrm{d}y$) of rapidity [95]. The size of the correlation volume governs the influence of exact quantum number conservation, with smaller values leading to a stronger suppression of conserved charges and $V_c \rightarrow \infty$ leading to the grand canonical ensemble. The $^{3}_{\Lambda}\mathrm{H}$ p_{T}

integrated yield is $1.1\text{x}10^{-6}$ and $2.0\text{x}10^{-6}$ with $V_c = \mathrm{d}V/\mathrm{d}y$ and $V_c = 3\mathrm{d}V/\mathrm{d}y$, respectively. The $\mathrm{d}N/\mathrm{d}y$ predictions by the model were obtained using the code released together with the publication [175]. While the SHM prediction with $V_c = \mathrm{d}V/\mathrm{d}y$ is in agreement with the measured yield within 2.5σ, the prediction with $V_c = 3\mathrm{d}V/\mathrm{d}y$ is more than 6.5 σ away from the data, and thus it can be excluded.

As explained above, in the case of the coalescence model it is not possible to compare directly the measured absolute yield to the model prediction. Hence, this comparison is attained by computing the $^{3}_{\Lambda}\mathrm{H}$ /Λ ratio and the strangeness population factor $S_3 = (^{3}_{\Lambda}\mathrm{H}/^{3}\mathrm{He})/(\Lambda/\mathrm{p})$ [176] using previous ALICE measurements of p, Λ and $^{3}\mathrm{He}$ yields [172, 177], as shown in Figs. 6.19 and6.18. The S_3 parameter quantifies whether there is an extra penalty factor occurring when a bound strange nuclear state is formed ($^{3}_{\Lambda}\mathrm{H}$), compared to a free strange hadron (Λ): hence, a strong suppression is expected in the case of coalescence due to the large system size of the $^{3}_{\Lambda}\mathrm{H}$ nucleus. Figures 6.19 and 6.18 show the $^{3}_{\Lambda}\mathrm{H}$ /Λ ratio and S_3 as a function of the mean charged-particle multiplicity. The mean charged-particle multiplicity associated with the 0-40% p–Pb collisions is inherited from [178], and it is computed by measuring the multiplicity in the central barrel, using SPD tracklets, at the corresponding V0A activity values used in this analysis. For both the S_3 and $^{3}_{\Lambda}\mathrm{H}$ /Λ quantities, in central Pb–Pb collisions the data are consistent with both coalescence and SHM predictions, which are similar. The situation is different for p–Pb collisions where the two models are well separated.

Taking into account the uncertainties of the measurement as well as the model uncertainty, the measured S_3 ratio is compatible with the 2-body (deuteron-Λ) and 3-body (proton-neutron-Λ) coalescence within 1.2σ and 2σ, respectively. With its large uncertainties, also due to the large uncertainty on the $^{3}\mathrm{He}$ yield, the S_3 is compatible within 2σ with the SHM calculations too.

On the other hand, the $^{3}_{\Lambda}\mathrm{H}$ /Λ ratio is a more sensitive quantity for coalescence and SHM predictions, as only the precision measurement of the Λ production enters the ratio. In this case, the measurement is deviating by 3.2σ and 7.9σ from the SHM with $V_c = 1\mathrm{d}V/\mathrm{d}y$ and $V_c = 3\mathrm{d}V/\mathrm{d}y$, respectively. On the other hand, both the coalescence calculations are within 2σ of the measured $^{3}_{\Lambda}\mathrm{H}$ /Λ (1.16σ for the 2-body coalescence, 1.92σ for the 3-body one).

Finally, the assumption on the B.R. is released in Fig. 6.20, where the $^{3}_{\Lambda}\mathrm{H}$ /Λ x B.R. factor is reported as a function of the B.R.: the range of the B.R. is limited by the uncertainty already described in Sec. 6.2. While the 2-body coalescence calculation is compatible with the data for the nominal or larger B.R., a maximum deviation of 2σ is observed between the data and the 3-body coalescence prediction. Furthermore, in the whole B.R. variation interval, the SHM is more than 2.7σ and

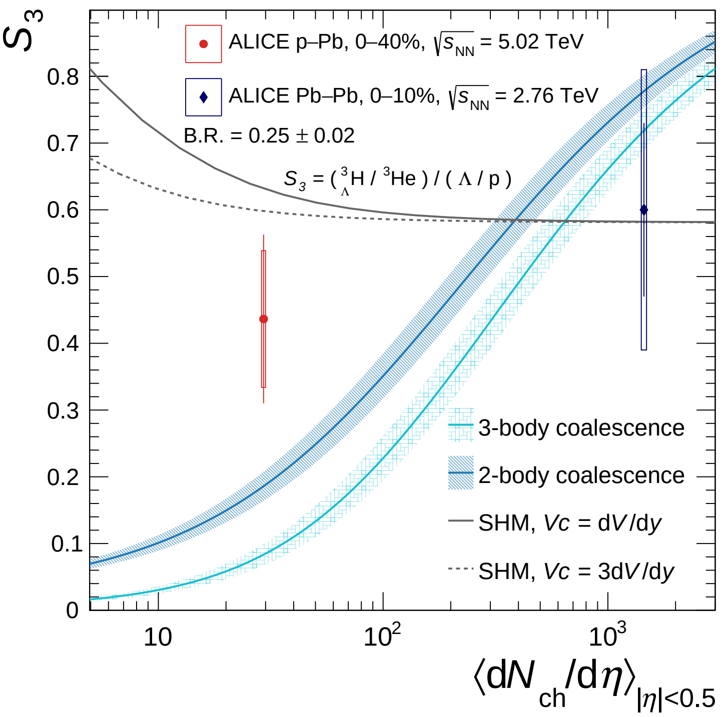

Fig. 6.18: S_3 measurement in p–Pb (in red) and Pb–Pb collisions [179] (in blue) as a function of mean charged-particle multiplicity. The vertical lines and boxes are the statistical and systematic uncertainties (including the uncertainty on the B.R.), respectively. The expectations for the canonical statistical hadronization [95] and coalescence models are shown [98].

6.9σ away from the measured ${}^{3}_{\Lambda}\mathrm{H}/\Lambda \times$ B.R. for the $V_c = 1\mathrm{d}V/\mathrm{d}y$ and $V_c = 3\mathrm{d}V/\mathrm{d}y$ configurations, respectively.

In summary, the first measurement of the ${}^{3}_{\Lambda}\mathrm{H}$ production in p–Pb collisions is achieved by selecting the ${}^{3}_{\Lambda}\mathrm{H}$ signal with a BDT Classifier. The measured p_{T} integrated yield excludes, with high significance, canonical versions of the SHM with $V_c \geq 3\mathrm{d}V/\mathrm{d}y$ to explain the (hyper)nuclei production in p–Pb collisions. It remains to be seen if advanced versions of the SHM using the S-matrix approach to account for the interactions among hadrons [180] will be able to solve this discrepancy. The ${}^{3}_{\Lambda}\mathrm{H}/\Lambda$ ratio is well described by the 2-body coalescence prediction while the 3-body formulation is slightly disfavoured by the measurement. Similar conclusions can be drawn for the S_3 factor, but wilth much less sensitivity.

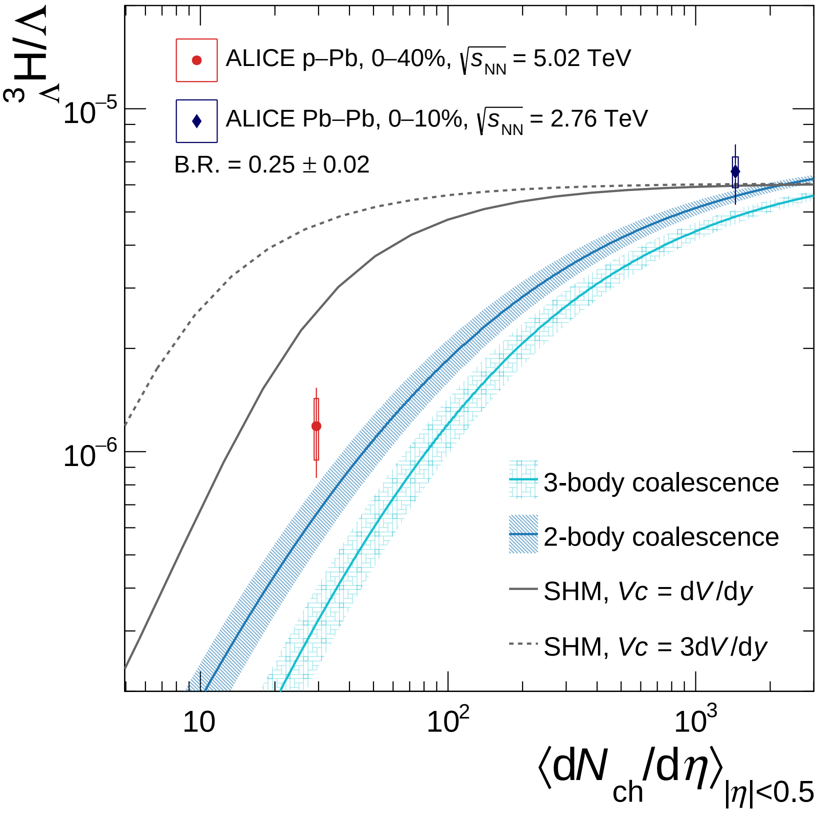

Fig. 6.19: $^{3}_{\Lambda}$H/Λ measurement in p–Pb (in red) and Pb–Pb collisions [179] (in blue) as a function of mean charged-particle multiplicity. The vertical lines and boxes are the statistical and systematic uncertainties (including the uncertainty on the B.R.), respectively. The expectations for the canonical statistical hadronization [95] and coalescence models are shown [98].

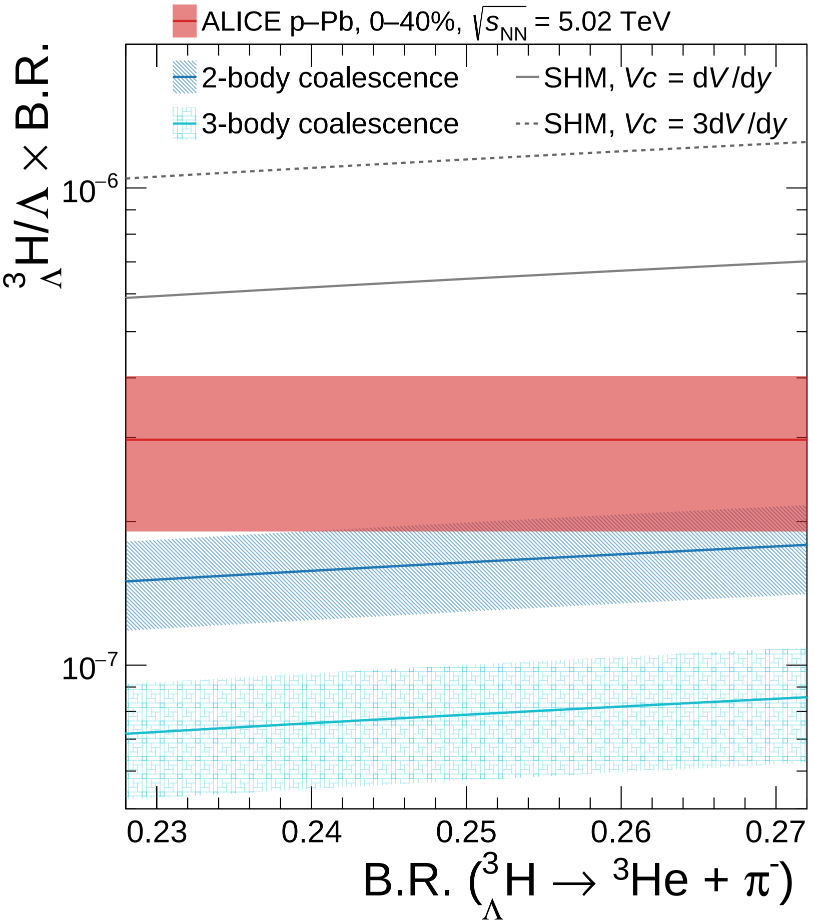

Fig. 6.20: $^{3}_{\Lambda}\mathrm{H}/\Lambda$ times branching ratio as a function of $^{3}_{\Lambda}\mathrm{H} \rightarrow {}^{3}\mathrm{He} + \pi$. The horizontal line is the measured value and the band represents statistical and systematic uncertainties added in quadrature. The expectations for the canonical statistical hadronization [95] and coalescence models are shown [98].

7

New avenues in hypernuclear physics

In the next years, new experimental facilities with a dedicated hypernuclear physics programme will start operating. In particular, in the low energy heavy-ion sector (from $\sqrt{s_{\mathrm{NN}}} = 3$ up to 20 GeV) two new facilities are going to be built: NICA at the DUBNA Laboratory [181] and FAIR at the GSI [182]. Additionally a new experiment at the CERN SPS [183], NA60+, is currently being proposed. At these energies, the production of hypernuclei is largely favoured because of the stopping of the baryonic fragments during the ion collisions. At the same time, the ALICE detector will be able in the next years to fully characterize A<=4 hypernuclear states in all the collision systems, thanks to the unprecedented integrated luminosity that will be collected during the LHC Run 3 and Run 4. In this Chapter, the algorithm for the direct tracking of long-lived hypernuclei developed for the LHC Run 3 will be discussed. Moreover, the expected performance of the new NA60+ experiment for the $^{5}_{\Lambda}\mathrm{He}$ reconstruction will be presented: the result has been included in the NA60+ Letter of Intent [183].

7.1 Tracking hypernuclei with ALICE

During the Run 3 of the LHC, the direct tracking of hypernuclei will be made possible for the first time, thanks to the upgrade of the Inner Tracking System detector of ALICE (ITS2) [184]. This, together with the reconstruction of the decay daughters, will determine the full kinematics of the decay, allowing ALICE to perform the precision measurement of the $^{3}_{\Lambda}\mathrm{H}$ 3-body decay channel, now swamped in a huge combinatorial and correlated background. Furthermore, the direct tracking of the mother particle will provide the first measurement of incomplete decay topologies of hypernuclei, e.g. decays with a neutral daughter particle (such as $^{3}_{\Lambda}\mathrm{H} \rightarrow {}^{3}\mathrm{H} + \pi_0$). A brief description of the ITS2 is provided in the following

7.1.1 Upgrade of the ITS

The Inner Tracking System (ITS2) currently in use was commissioned in 2021 and in the first 6 months of 2022. It was designed to enhance the tracking and readout rate capabilities with respect to the ones of the detector that was in operation during the LHC Run 1 and 2. The ITS2 is composed by seven cylindrical layers (three innermost layers constituting the Inner Barrel, IB, and four outermost layers constituting the Outer Barrel, OB) all equipped with ALPIDE Monolithic Active Pixel Sensors (MAPS) chips of about 30x30 μm^2 pixel size, a large reduction of the material budget ($\sim$0.3% X_0 for the IB and $\sim$1% X_0 for the OB), and a reduced distance of the innermost layer to the interaction point (2.1 cm). A schematic view of the ITS2 is shown in Fig. 7.1, while Table 7.1 summarizes the geometric characteristics of the detector layers.

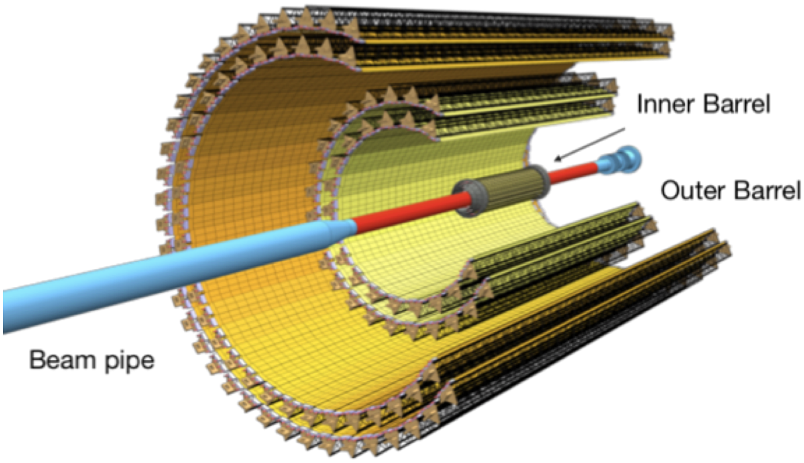

Fig. 7.1: Schematic view of the ITS2 layout.

	Radius (cm)	Length (cm)	# of chips
Layer 0	2.2	27.1	108
Layer 1	3.1	27.1	144
Layer 2	3.8	27.1	180
Layer 3	19.4	84.3	2688
Layer 4	24.4	84.3	3360
Layer 5	34.2	147.5	8232
Layer 6	39.2	147.5	9408

Tab. 7.1: Geometric characteristics of the ITS2 layers.

The ITS2 covers a 10 m^2 active surface with 12.5 billion pixels offering a radius coverage of 22–400 mm and a pseudorapidity coverage of $|\eta| < 1.22$. All the above modifications contribute to the improvement of the impact parameter resolution in the beam direction z by a factor of six, from 240 μm to 40 μm, and in the transverse plane rϕ by a factor of three, from 120 μm to 40 μm at $p_\mathrm{T} = 0.5$ GeV/c.

The high granularity of the ITS2 allows for the reconstruction of ITS only tracks with a dedicated algorithm, which is based on the cellular automaton approach for the hit pattern recognition and a final track fitting done with a Kalman filter. At least four hits are required by the algorithm to build a track, and the momentum resolution of the ITS tracks with hits on all the seven detector layers is less than 6% for $p_{\mathrm{T}} > 0.5$ GeV/c.

To test the ${}^{3}_{\Lambda}\mathrm{H}$ track reconstruction foreseen for the LHC Run 3, a dedicated simulation is built on top of the Run 3 ALICE simulation and reconstruction framework, Alice O2 [185]. In this simulation, one ${}^{3}_{\Lambda}\mathrm{H}$ particle is injected into a pp inelastic collision at $\sqrt{s_{\mathrm{NN}}} = 13.6$ TeV, simulated with the Pythia8 event generator [124]. Then, all the particles are propagated through the ALICE detector using Geant4, which takes care of the decay of the unstable particles during the propagation. The ${}^{3}_{\Lambda}\mathrm{H}$ ITS track is then reconstructed with the ITS tracking algorithm, and the tracking efficiency as a function of the decay radius is shown in Fig. 7.2. As the minimum number of clusters required to reconstruct a track is four, in principle only ${}^{3}_{\Lambda}\mathrm{H}$ with decay radius higher than ~ 19 cm (the radius of the fourth layer of the ITS2) can be reconstructed. However, since the Q-value of the ${}^{3}_{\Lambda}\mathrm{H}$ is small, the ${}^{3}\mathrm{He}$ daughter particle usually points into the ${}^{3}_{\Lambda}\mathrm{H}$ mother direction: this causes a huge number of fake tracks, i.e. tracks with at least one cluster not belonging to the ${}^{3}_{\Lambda}\mathrm{H}$ particle. This effect can be observed in Fig. 7.2, where no ITS tracks containing solely ${}^{3}_{\Lambda}\mathrm{H}$ clusters (referred to as "pure ITS ${}^{3}_{\Lambda}\mathrm{H}$ tracks") are detected with a radius less than 19 cm. However, the tracking efficiency remains around 30% as a result of the presence of ${}^{3}\mathrm{He}$ clusters within the track. For decay radii higher than 19 cm, the tracking efficiency reflects the structure of the ITS2: the highest fractions of fake tracks correspond to the ${}^{3}_{\Lambda}\mathrm{H}$ that decay close to the layers of the detector.

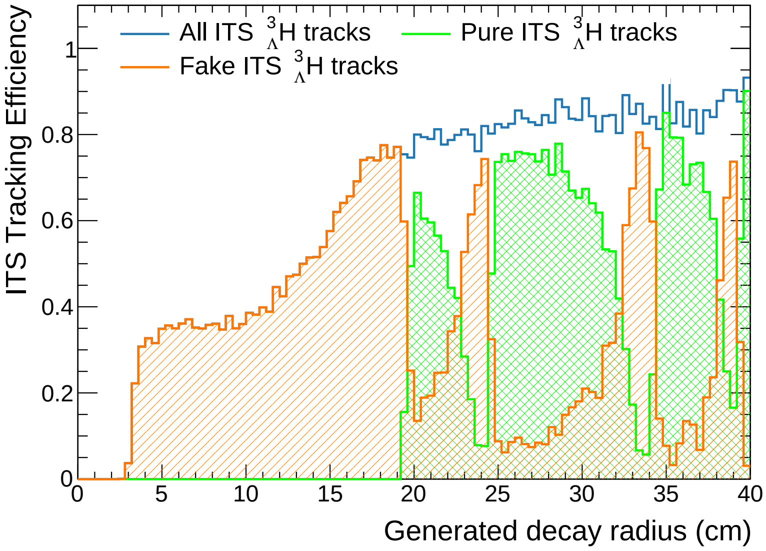

Fig. 7.2: Tracking efficiency of the ${}^{3}_{\Lambda}\mathrm{H}$ particle as a function of the decay radius for all ITS ${}^{3}_{\Lambda}\mathrm{H}$ tracks(blue line), pure ${}^{3}_{\Lambda}\mathrm{H}$ tracks (green area), and fake ones (orange area).

The reconstructed ITS tracks are then matched with the TPC ones, and the TOF and TRD information, when available, to form global tracks. After the primary vertex reconstruction, the secondary vertex algorithm is applied to the tracks looking for particles coming from weak decays, with a similar approach to the one used in the Run 2.

7.1.2 The ${}^{3}_{\Lambda}\mathrm{H}$ matching algorithm

The ${}^{3}_{\Lambda}\mathrm{H}$ matching algorithm is in charge of matching the ${}^{3}_{\Lambda}\mathrm{H}$ ITS track with the decay daughters and fitting the full decay topology by means of a kinematic fit. The development of the algorithm is still ongoing, and the kinematic fit part is not yet implemented. Nevertheless, in this thesis, a few preliminary results are presented. The ITS tracker outlined in the previous section is employed to reconstruct the ${}^{3}_{\Lambda}\mathrm{H}$ ITS track, while the V^0 finder algorithm is used to determine the ${}^{3}_{\Lambda}\mathrm{H}$ decay topology as it is explained in Sec 5.2.2, and a V^0 track is built by combining the daughter ones. The matching algorithm starts by organizing the ITS tracks in an ordered grid based on the ϕ (azimuth angle) and z coordinates of the tracks at their last hit into the ITS2 detector. Then a loop on the reconstructed V^0 tracks is performed, and for each V^0, the ITS tracks compatible within a predefined ϕ and z window are selected. The grid organisation of the ITS tracks allows for speeding up this process. For each compatible ITS track the algorithm tries to attach its clusters to the V^0 by using a Kalman filter: at each attachment step, if the track-cluster matching χ^2 is lower than a certain threshold (10 in this case), the V^0 track parameters and their covariance matrix are updated. An iterative procedure is developed to account for the presence of fake clusters belonging to one of the daughter tracks: if the decay radius reconstructed with the V^0 finder is lower than the layer radius corresponding to the cluster, this cluster is likely a fake. In this case, the cluster is attached to one of the daughter tracks and not to the V^0. A simple sketch of the decay topology into the ITS2 is shown in Fig. 7.3: the outermost cluster is wrongly attached to the mother ITS track, and the algorithm is able to remove it and attach it to the daughter one.

If all the ITS clusters are attached to the V0 track or to its daughters, the full topology is re-fitted trying to minimize the DCA between the three tracks: this should improve the decay vertex position and the momentum resolution of the ${}^{3}_{\Lambda}\mathrm{H}$ particle. This last step is only partially implemented, and it will be improved by constraining the fit to the ${}^{3}_{\Lambda}\mathrm{H}$ mass hypothesis.

The topologies that fulfill the previous requirements are then stored in a dedicated tree and the performance of the algorithm is evaluated. The invariant mass distribution of the simulated ${}^{3}_{\Lambda}\mathrm{H}$ sample before and after requiring the matching of the ITS track is shown in Fig. 7.4. The spectra are fitted with a Double Sided Crystal Ball and a third-order polynomial functions to model the signal and the background,

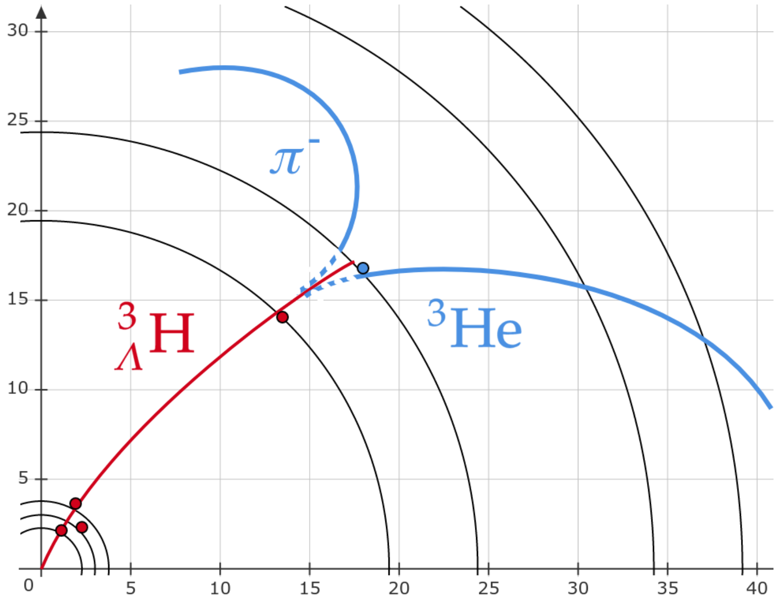

Fig. 7.3: Sketch of the $^{3}_{\Lambda}\mathrm{H}$ decay into the ITS2 detector. The track is wrongly propagated up to the fifth ITS2 layer and includes the $^{3}\mathrm{He}$ daughter cluster.

respectively. It is worth to remark that since there is one injected $^{3}_{\Lambda}\mathrm{H}$ per event, the $^{3}_{\Lambda}\mathrm{H}$ peak is visible without applying any selection. However, the matching algorithm is able to improve the signal over background ratio by a factor 45, thus allowing for a clean selection of the $^{3}_{\Lambda}\mathrm{H}$ signal in the real data.

The algorithm efficiency is evaluated by dividing the number of $^{3}_{\Lambda}\mathrm{H}$ candidates with a matched ITS track by the total number of $^{3}_{\Lambda}\mathrm{H}$ with a reconstructed ITS and V0 track, and it is shown in Fig. 7.5 as a function of the transverse momentum (top panel) and the decay radius (bottom panel) of the $^{3}_{\Lambda}\mathrm{H}$.

The efficiency weakly increases with the p_{T} and the radius of the $^{3}_{\Lambda}\mathrm{H}$ from 50% up to 80%. The non-matched $^{3}_{\Lambda}\mathrm{H}$ tracks are due to the presence of fake clusters attached to the tail of the $^{3}_{\Lambda}\mathrm{H}$ tracks not belonging to any of its daughters. This is a well known behaviour of the ITS tracking algorithm affecting the purity of the short-tracks reconstruction (with less than 7 clusters). However, the current implementation of the matching algorithm already guarantees that around 30% of the V0 candidates have their ITS track matched. This algorithm will open the possibility to study in detail the three body decay of the $^{3}_{\Lambda}\mathrm{H}$ ($^{3}_{\Lambda}\mathrm{H} \rightarrow p + d + \pi^{-}$), now inaccessible because of the huge background coming from the Λ decay products. Furthermore, the direct tracking of the $^{3}_{\Lambda}\mathrm{H}$ will allow for the first time to study decay channels involving neutral particles, such as the $^{3}_{\Lambda}\mathrm{H} \rightarrow {}^{3}\mathrm{H} + \pi^{0}$ decay.

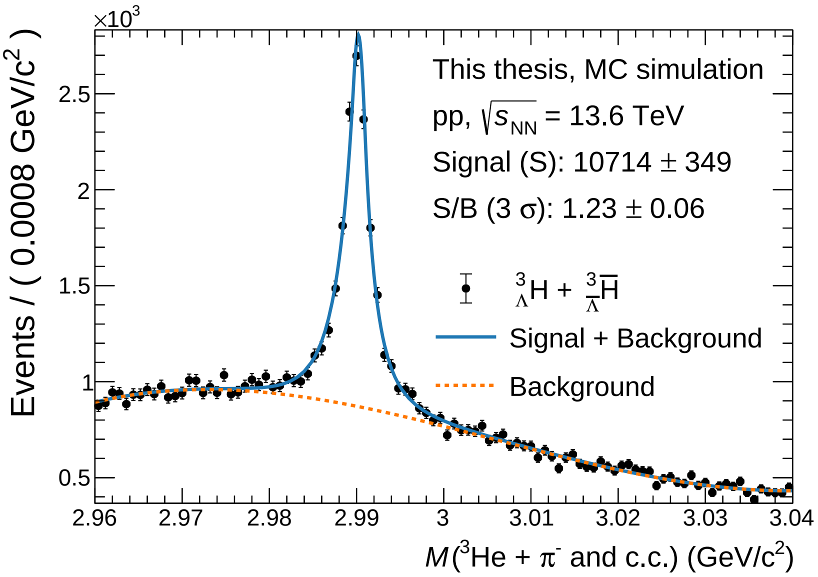

(a) Before ITS track matching

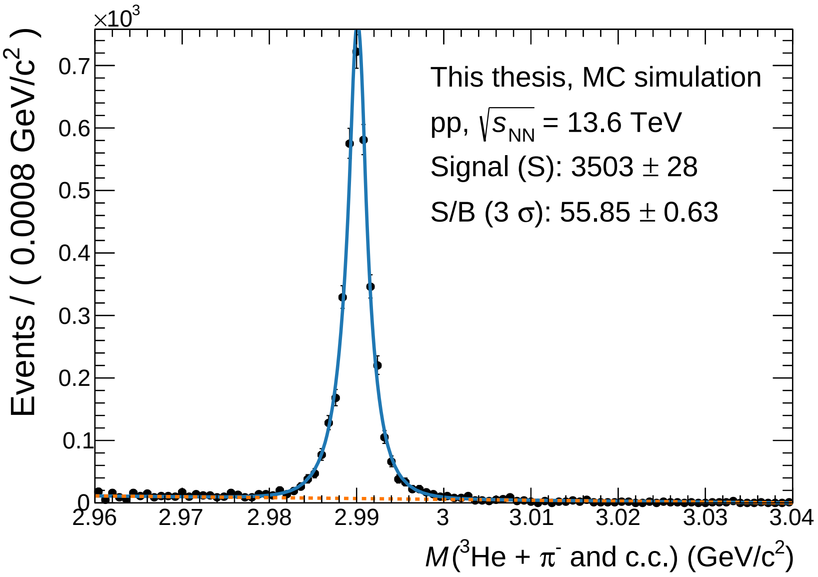

(b) After ITS track matching

Fig. 7.4: Invariant mass distribution of the simulated ${}^{3}_{\Lambda}\mathrm{H}$ sample before and after requiring the matching of the ITS track.

7.2 Heavier hypernuclei with NA60+

The NA60+ project is a proposal for a new heavy-ion experiment to study the QGP properties at CERN SPS energies (from $\sqrt{s_{\mathrm{NN}}} = 6$ up to 17.3 GeV). While the QGP studied at the LHC is characterized by a large initial temperature and a null net baryonic density, collisions at the SPS energies could investigate the QCD phase diagram in a region with a smaller initial temperature and a non-zero net baryonic density. In such conditions, a first order phase transition from nuclear matter to QGP

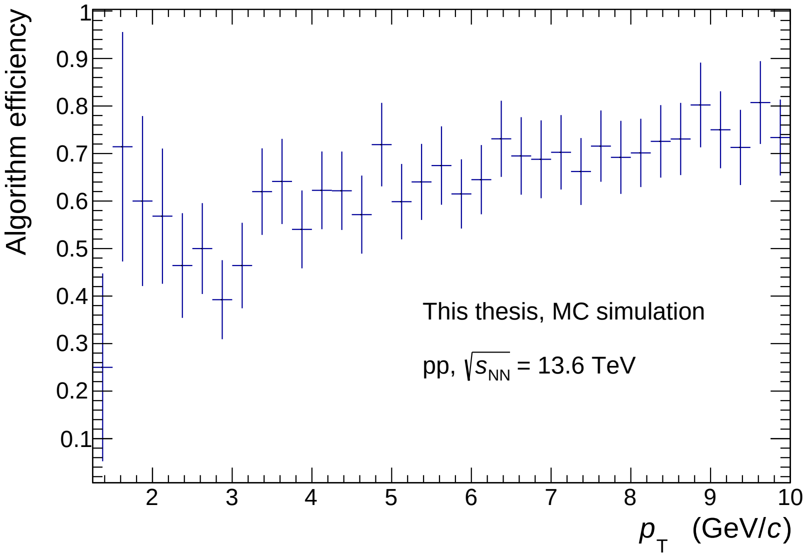

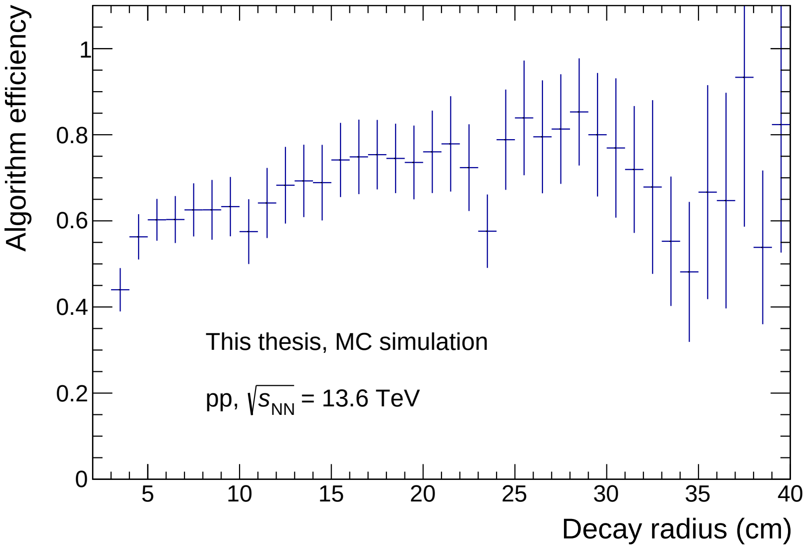

Fig. 7.5: Matching algorithm efficiency as a function of the p_T (top) and the decay radius (bottom) of the ${}^{3}_{\Lambda}$H.

is expected, and the QGP properties could be very different from the ones studied at the LHC. The main observables employed to study the QGP formation and properties with high precision are:

- electromagnetic probes of the QGP, via the measurement of the muon pair spectrum (already described in Sec. 1.4);
- open and hidden charm production, which gives constraints on the transport properties of the QGP (open charm) and on the modification of the QCD binding in a deconfined medium (charmonium).

The concept of the experimental set-up is inspired by the former NA60 experiment relying on a muon spectrometer, covering one unit of rapidity, and a vertex spectrometer. The muon spectrometer will feature a toroidal magnet, and its tracking system will be based on six stations: two of them located upstream, two downstream of the toroid, and the last two stations afterwards a graphite absorber. A schematic view of the NA60+ detector is shown in Fig. 7.6.

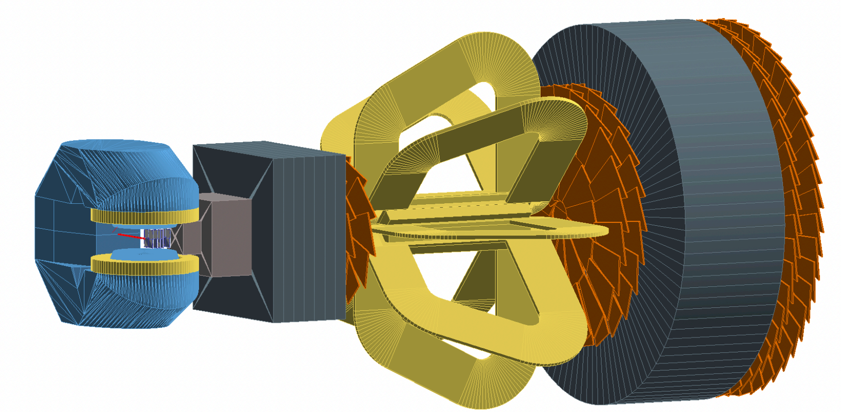

Fig. 7.6: Schematic layout of the NA60+ detector, drawn with Geant4 [183].

The vertex spectrometer, positioned immediately downstream of the targets, will consist of a series of stations (from 5 up to 10) of high-granularity and low material budget monolithic active pixel sensors (MAPS), the same technology employed in the ALICE ITS2. This will guarantee an efficient tracking of the large number of produced charged particles that are expected to be in the order of $\sim$ 400 for central Pb–Pb collisions at top SPS energy.

The NA60+ unique set-up could represent an opportunity to extend the physics programme of the experiment to study the production of hypernuclei up to A=7. Indeed, the low energy heavy-ion collisions delivered at the SPS are particularly interesting for this purpose, since the stopping of the baryonic fragments during the ion collisions favours the formation of hyper-nuclear clusters. Figure 7.7 shows the expected production of hypernuclei in Pb–Pb collisions as a function of the centre of mass energy according to the SHM in [186, 187]: the green band highlights the energy range accessible to the NA60+ experiment. The production rate of hypernuclei in NA60+ is expected to be enhanced with respect to the ALICE one by more than two orders of magnitude for all the hypernuclei. In the following, the expected production of ${}^{5}_{\Lambda}\mathrm{He}$ is used as an example to illustrate the potential of the NA60+ hypernuclear physics programme.

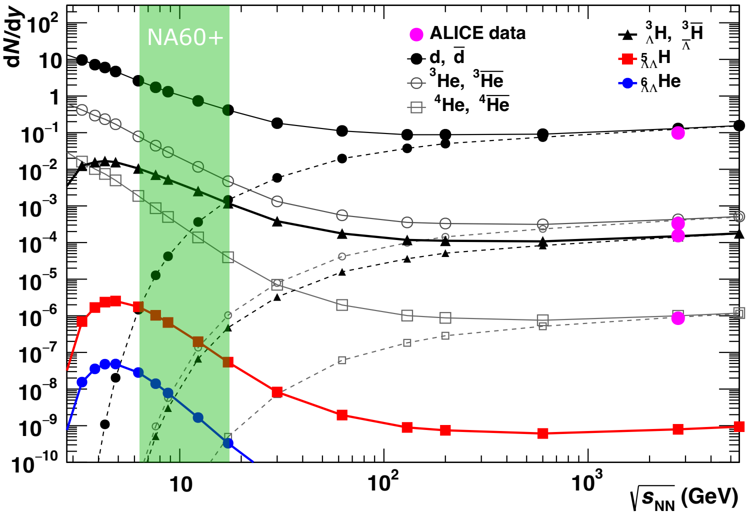

Fig. 7.7: Expected production of hypernuclei in Pb–Pb collisions as a function of the centre of mass energy according to the SHM.

7.2.1 Production of $^{5}_{\Lambda}\mathrm{He}$

The analysed decay channel of the $^{5}_{\Lambda}\mathrm{He}$ is: $^{5}_{\Lambda}\mathrm{He} \rightarrow ^{4}\mathrm{He} + p + \pi^{-}$, which has an expected branching ratio of approximately 32% [188]. In principle, the current concept of the NA60+ detector does not include a PID system, even if the possibility to add silicon timing layers after the MAPS stations is currently under investigation. However, the proposed minimal configuration of the vertex spectrometer (VT) of NA60+, with five tracking stations using MAPS detectors, allows for the separation of heavily ionising particles from ordinary hadrons by looking at the size of the clusters associated with the tracks. This interesting property was studied at the time of the ITS2 TDR [184], and it is confirmed by the preliminary studies performed on the ALICE Run 3 data. In order to study the performance of the NA60+ VT, a dedicated fast simulation and reconstruction tool has been developed featuring:

- layout description module, which allows describing the experimental set-up as a combination of thin sensitive and extended passive material layers;
- a fast simulation engine that, starting from the initial kinematics and position of the particle, performs its transport through the detector and registers the hit positions at all the sensitive layers;
- a Kalman filter based track reconstruction engine, inherited from the ALICE one.

The expected yield and the momentum distribution for the $^{5}_{\Lambda}\mathrm{He}$ are sampled from the Thermal-FIST event generator [175], which produces particles according to the SHM abundances and with a momentum distribution given by the MUSIC hydrodynamical model [189]. The particle is then propagated through the NA60+ detector, and the reconstructed daughter tracks are employed to estimate the projected performance for identifying the $^{5}_{\Lambda}\mathrm{He}$. The signal expected in 10^{10} Pb–Pb collisions at the lowest collision energy provided by the SPS is generated and reconstructed. In order to estimate the background, a sample of 10^{6} central Pb–Pb collisions is generated: under the assumption that Z=2 nuclei can be cleanly identified by means of their cluster size, the main background is expected to come from the combinatorics of primary and secondary Z=2 nuclei with other hadrons from secondary vertices. A sharp selection on the $\cos(\theta_p)$ (0.9999) of the decay products can be applied to reduce the combinatorial background, which is then parametrized with a constant function and rescaled to match the number of events simulated for the signal.

Figure 7.8 shows the projected performance for the $^{5}_{\Lambda}\mathrm{He}$: the reconstructed invariant mass spectrum is fitted with a DSCB and a constant function, to model the signal and the background contributions, respectively.

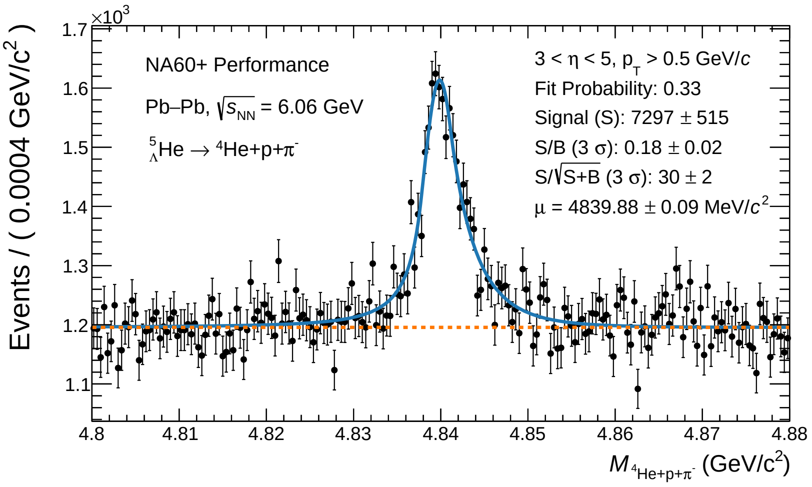

Fig. 7.8: Invariant mass spectrum of the $^{5}_{\Lambda}\mathrm{He}$ reconstructed in NA60+ with a minimal configuration of the vertex spectrometer.

The number of reconstructed $^{5}_{\Lambda}\mathrm{He}$ will be ~ 7 times larger than the number of $^{3}_{\Lambda}\mathrm{H}$ analysed in this thesis in the same collision system. Hence, a complete characterization of this hypernucleus will be achieved. Furthermore, the 90 keV uncertainty associated with the mass peak position (the μ parameter in Fig. 7.8) will allow for a precision study of the binding energy of the $^{5}_{\Lambda}\mathrm{He}$, which is almost unexplored in the literature (see [46]).

Similar analysis strategies can be adopted to study lighter and heavier hypernuclei and to look for evidence of the existence of light Ξ hypernuclear states [190].

Furthermore, the possibility of directly tracking the hypernucleus, as illustrated in the previous section, is here not discussed but it will allow NA60+ to dramatically reduce the background for the hypernuclear measurements.

8 Conclusions

This thesis was focused on the measurements of the properties of the hypertriton ($^{3}_{\Lambda}$H), the lightest Λ-hypernucleus. The goal was to measure with the highest possible precision the $^{3}_{\Lambda}$H lifetime τ and the Λ separation energy B_{Λ}. These quantities, if measured together, can be used to test different theoretical models describing the $^{3}_{\Lambda}$H structure, and to constrain the value of the $^{3}_{\Lambda}$H radius. Both τ and B_{Λ} of the $^{3}_{\Lambda}$H have been measured by exploiting the large Pb–Pb dataset collected by ALICE during 2018, the last year of the LHC Run 2. The $^{3}_{\Lambda}$H signal was selected by employing a Boosted Decision Tree classifier, which was shown to improve the statistical significance of the $^{3}_{\Lambda}$H signal with respect to the previous selection method. The combined measurements of the $^{3}_{\Lambda}$H lifetime and B_{Λ} are presented in Fig. 8.1, and they are shown together with state-of-the-art theoretical predictions based on chiral effective field theory.

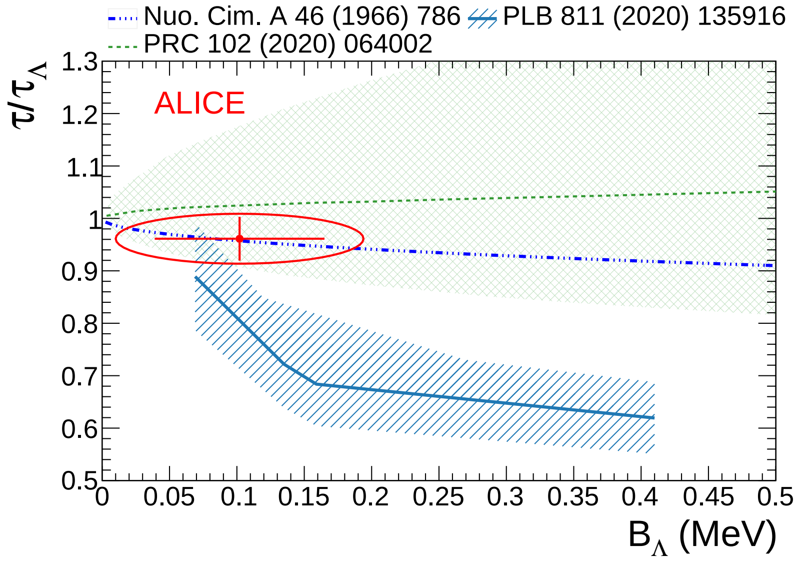

Fig. 8.1: The $^{3}_{\Lambda}$H lifetime relative to the free Λ lifetime as a function of the B_{Λ} for pionless EFT [76] (green), χEFT [77] (light blue), and the original π exchange calculations [159] (blue). The red point represents the measurement presented in this work with the statistical and total uncertainties depicted with lines and ellipse, respectively.

Both the measurements definitely demonstrate the weakly bound nature of the $^{3}_{\Lambda}$H, thus rejecting models predicting a compact structure for this hypernucleus. Furthermore, the B_{Λ} value of 102 ± 63 (stat.) ± 67 (syst.) keV is in close agreement with the B_{Λ} value traditionally used by the theoretical community to describe the $^{3}_{\Lambda}$H structure, $B_\Lambda = 130 \pm 50$ (stat.). According to [69], this translates into an extremely wide deuteron-Λ radius of ~ 11 fm.

One of the main consequences of the weakly bound nature of the ${}^3_\Lambda$H is that the ${}^3_\Lambda$H yield in p–Pb is a sensitive probe to discriminate among the nucleosynthesis models: while coalescence is directly influenced by the ratio of nucleus size to source size, the SHM treats all the particles as point-like [95, 98, 169]. In this thesis, the first measurement of ${}^3_\Lambda$H production in p–Pb collisions was achieved: the use of the BDT Classifier allows for the first time to extract the ${}^3_\Lambda$H signal with a significance higher than 4σ. The ${}^3_\Lambda$H/ Λ yield ratio measured in this thesis favours the coalescence models, and it excludes a very popular interval of configurations of the SHM that successfully describes the light flavour hadron yields. This result is supported by the first measurement of the ${}^3_\Lambda$H/ Λ yield ratio in high-multiplicity pp collisions, which is still in a preliminary stage. The ratios are shown in Fig. 8.2: the 2-body coalescence model clearly describes the suppression of the ${}^3_\Lambda$H production at low charged-particle multiplicity.

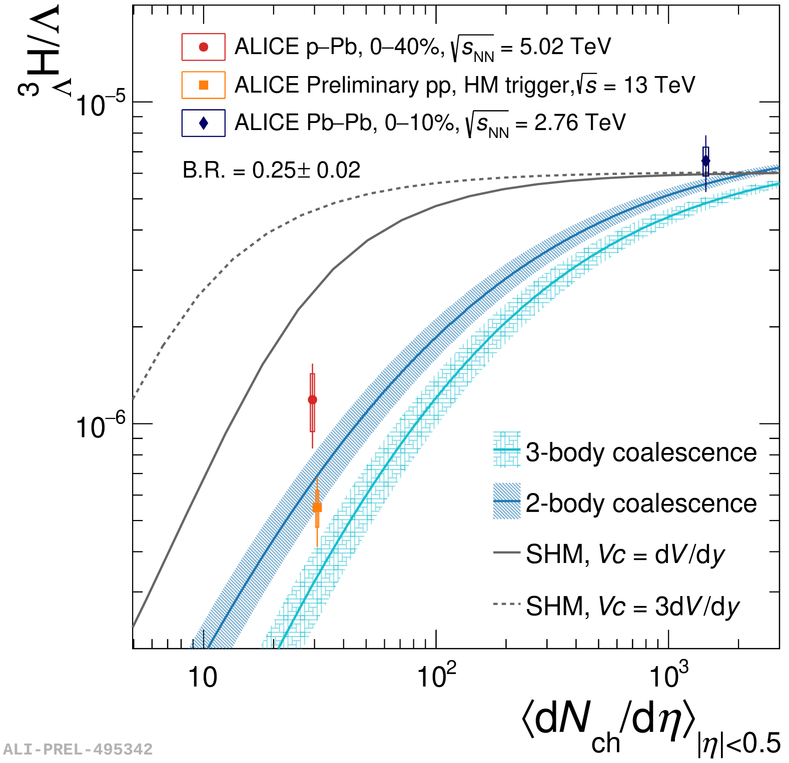

Fig. 8.2: ${}^3_\Lambda$H/Λ measurement in p–Pb (in red), pp (in orange) and Pb–Pb collisions [179] (in blue) as a function of mean charged-particle multiplicity. The vertical lines and boxes are the statistical and systematic uncertainties, respectively. The expectations for the canonical statistical hadronization [95] and coalescence models are shown [98].

The main remaining issue to be addressed for the ${}^3_\Lambda$H is the precise measurement of its two-body / three-body decays relative branching ratios. Indeed, the ${}^3_\Lambda$H signal extraction from its three-body decay channel is a challenging task due to the presence of a Λ-deuteron correlated background, biasing the shape of the ${}^{3}_{\Lambda}\mathrm{H}$ invariant mass spectrum. This will change during the LHC Run 3, when the ${}^{3}_{\Lambda}\mathrm{H}$ track will be reconstructed together with decay products. The new tracking and matching algorithm was presented in Chapter 7, and it will allow for the measurement of the ${}^{3}_{\Lambda}\mathrm{H}$ three-body decay channel. Finally, the possibility to start a wide hypernuclear physics programme with the NA60+ experiment was discussed in Chapter 7: a dedicated performance study was done for the ${}^{5}_{\Lambda}\mathrm{He}$, employed as a case study. The study showed that the NA60+ apparatus will be capable to measure the properties of poorly known hypernuclei, such as the ${}^{6}_{\Lambda}\mathrm{He}$ (see the Mainz hypernuclear database [46]), and possibly to observe for the first time light double-strange Ξ and $\Lambda\Lambda$ hypernuclei.

9

Appendix

Several $p_{\rm T}$ distributions have been employed in this thesis to model the ${}^3_\Lambda$H $p_{\rm T}$ shape. In this appendix these functions are briefly described.

9.1 Blast-Wave distribution

The phenomenological model for producing hadronic matter in heavy ion collisions, as described in [191], serves as the basis for the Blast-Wave distribution. The model is developed by starting out with thermalization as the basic assumption and adding more features as they are dictated by the analysis of the measured hadronic spectra. The distribution is written as:

$$\frac{1}{p_{\rm T}}\frac{dN}{dp_{\rm T}} = \int_0^R r dr m_{\rm T} I_0\Big(\frac{p_{\rm T} sinh\rho}{T_{kin}}\Big) K_1\Big(\frac{m_{\rm T} cosh\rho}{T_{kin}}\Big) \tag{9.1}$$

where the parameter ρ contains the dependence on the velocity profile, since it is expressed as:

$$\rho = tanh^{-1}\Big[\Big(\frac{r}{R}\Big)^n \beta_{\rm T}\Big] \tag{9.2}$$

In the previous equations, $m_{\rm T}$ is the transverse mass, I_0 and K_1 the modified Bessel functions of the first and second kind, respectively, r is the radial distance on the transverse plane, T_{kin} is the kinetic freeze-out temperature, $\beta_{\rm T}$ is the average transverse velocity, and n is the exponent of the velocity profile.

9.2 Maxwell-Boltzmann distribution

The Maxwell-Boltzmann statistics describes the distribution of transverse momentum of particles in a thermalized medium. It is defined as:

$$\frac{1}{p_{\rm T}}\frac{dN}{dp_{\rm T}} = p_{\rm T} \cdot \sqrt{p_{\rm T}^2 + m_{\rm T}^2} \cdot \exp\Big(-\frac{\sqrt{p_{\rm T}^2 + m^2}}{T}\Big) \tag{9.3}$$

9.3 Transverse momentum and mass exponential distributions

The p_{T} and m_{T} exponential distributions have been successfully employed to describe the p_{T} shape of identified particles in high-energy collisions [172, 192, 193]. The p_{T} exponential is defined as:

$$\frac{1}{p_{\mathrm{T}}}\frac{dN}{dp_{\mathrm{T}}} = p_{\mathrm{T}} \cdot \exp\Big(-\frac{\sqrt{p_{\mathrm{T}}^2}}{T}\Big), \tag{9.4}$$

while the m_{T} exponential is:

$$\frac{1}{p_{\mathrm{T}}}\frac{dN}{dp_{\mathrm{T}}} = p_{\mathrm{T}} \cdot \sqrt{p_{\mathrm{T}}^2 + m_{\mathrm{T}}^2} \cdot \exp\Big(-\frac{\sqrt{p_{\mathrm{T}}^2 + m^2}}{T}\Big). \tag{9.5}$$

Bibliography

[1] Limin Wang, RR Caldwell, JP Ostriker, and Paul J Steinhardt. „Cosmic concordance and quintessence“. In: *The Astrophysical Journal* 530.1 (2000), p. 17 (cit. on p. 1).

[2] Peter AR Ade, N Aghanim, M Arnaud, et al. „Planck 2015 results-xiii. cosmological parameters“. In: *Astronomy & Astrophysics* 594 (2016), A13 (cit. on p. 1).

[3] Murray Gell-Mann. „A schematic model of baryons and mesons“. In: *Physics Letters* 8.3 (1964), pp. 214–215 (cit. on p. 1).

[4] George Zweig. „An SU(3) model for strong interaction symmetry and its breaking“. In: *Developments In The Quark Theory Of Hadrons* 1 (1964) (cit. on p. 1).

[5] George Zweig. „An SU(3) model for strong interaction symmetry and its breaking II“. In: *Developments In The Quark Theory Of Hadrons* 1 (1964) (cit. on p. 1).

[6] Harald Fritzsch and Murray Gell-Mann. „Current algebra: Quarks and what else?“ In: *eConf* C720906V2 (1972). Ed. by J. D. Jackson and A. Roberts, pp. 135–165. arXiv: `hep-ph/0208010` (cit. on p. 1).

[7] P.A. Zyla et al. „Review of Particle Physics“. In: *PTEP* 2020.8 (2020), p. 083C01 (cit. on pp. 1, 2, 95, 97).

[8] Michael E. Peskin and Daniel V. Schroeder. *An Introduction to quantum field theory*. Reading, USA: Addison-Wesley, 1995 (cit. on p. 3).

[9] Diogo Boito, Maarten Golterman, Kim Maltman, James Osborne, and Santiago Peris. „Strong coupling from the revised ALEPH data for hadronic τ decays“. In: *Phys. Rev. D* 91.3 (2015), p. 034003. arXiv: `1410.3528 [hep-ph]` (cit. on p. 5).

[10] Clara Peset, Antonio Pineda, and Jorge Segovia. „The charm/bottom quark mass from heavy quarkonium at N^{3}LO“. In: *JHEP* 09 (2018), p. 167. arXiv: `1806.05197 [hep-ph]` (cit. on p. 5).

[11] Johannes Blumlein, Helmut Bottcher, and Alberto Guffanti. „Non-singlet QCD analysis of deep inelastic world data at O(alpha(s)**3)“. In: *Nucl. Phys. B* 774 (2007), pp. 182–207. arXiv: `hep-ph/0607200` (cit. on p. 5).

[12] G. Dissertori, A. Gehrmann-De Ridder, T. Gehrmann, et al. „Determination of the strong coupling constant using matched NNLO+NLLA predictions for hadronic event shapes in e+e- annihilations“. In: *JHEP* 08 (2009), p. 036. arXiv: `0906.3436 [hep-ph]` (cit. on p. 5).

[13] R. L. Workman et al. „Review of Particle Physics“. In: *PTEP* 2022 (2022), p. 083C01 (cit. on pp. 5, 22, 98).

[14]John C. Collins and M. J. Perry. „Superdense Matter: Neutrons Or Asymptotically Free Quarks?“ In: *Phys. Rev. Lett.* 34 (1975), p. 1353 (cit. on p. 5).

[15]N. Cabibbo and G. Parisi. „Exponential Hadronic Spectrum and Quark Liberation“. In: *Phys. Lett. B* 59 (1975), pp. 67–69 (cit. on p. 5).

[16]Gert Aarts. „Introductory lectures on lattice QCD at nonzero baryon number“. In: *J. Phys. Conf. Ser.* 706.2 (2016), p. 022004. arXiv: `1512.05145 [hep-lat]` (cit. on p. 5).

[17]Mark G Alford, Andreas Schmitt, Krishna Rajagopal, and Thomas Schäfer. „Color superconductivity in dense quark matter“. In: *Reviews of Modern Physics* 80.4 (2008), p. 1455 (cit. on p. 6).

[18]Johann Rafelski. „Connecting QGP-Heavy Ion Physics to the Early Universe“. In: *Nucl. Phys. B Proc. Suppl.* 243-244 (2013). Ed. by Roberto Battiston and Sergio Bertolucci, pp. 155–162. arXiv: `1306.2471 [astro-ph.CO]` (cit. on p. 6).

[19]Kenneth Johnson. „The MIT bag model“. In: *Acta Phys. Polon.* 6.MIT-CTP-494 (1975), p. 865 (cit. on p. 6).

[20]A. Bazavov et al. „Equation of state in (2+1)-flavor QCD“. In: *Phys. Rev. D* 90 (2014), p. 094503. arXiv: `1407.6387 [hep-lat]` (cit. on p. 6).

[21]F. Karsch, K. Redlich, and A. Tawfik. „Hadron resonance mass spectrum and lattice QCD thermodynamics“. In: *Eur. Phys. J. C* 29 (2003), pp. 549–556. arXiv: `hep-ph/0303108` (cit. on p. 6).

[22]„New State of Matter created at CERN. Un nouvel état de la matière“. In: (2000). Issued on 10 Feb 2000 (cit. on p. 7).

[23]*BNL Webpage*. `https://www.bnl.gov/rhic/physics.asp`. Accessed: 2010-09-20 (cit. on p. 7).

[24]Prashant Shukla. „Glauber model and the heavy ion reaction cross section“. In: *Physical Review C* 67.5 (2003), p. 054607 (cit. on p. 7).

[25]Michael L. Miller, Klaus Reygers, Stephen J. Sanders, and Peter Steinberg. „Glauber modeling in high energy nuclear collisions“. In: *Ann. Rev. Nucl. Part. Sci.* 57 (2007), pp. 205–243. arXiv: `nucl-ex/0701025` (cit. on pp. 8, 9).

[26]Roger D. Woods and David S. Saxon. „Diffuse Surface Optical Model for Nucleon-Nuclei Scattering“. In: *Phys. Rev.* 95 (1954), pp. 577–578 (cit. on p. 8).

[27]Betty Abelev et al. „Pseudorapidity density of charged particles in p + Pb collisions at $\sqrt{s_{NN}} = 5.02$ TeV“. In: *Phys. Rev. Lett.* 110.3 (2013), p. 032301. arXiv: `1210.3615 [nucl-ex]` (cit. on p. 9).

[28]Ulrich W. Heinz. „Concepts of heavy ion physics“. In: *2nd CERN-CLAF School of High Energy Physics*. July 2004, pp. 165–238. arXiv: `hep-ph/0407360` (cit. on p. 9).

[29]J. D. Bjorken. „Highly Relativistic Nucleus-Nucleus Collisions: The Central Rapidity Region“. In: *Phys. Rev. D* 27 (1983), pp. 140–151 (cit. on p. 11).

[30]Shreyasi Acharya et al. „Prompt D^0, D^+, and D^{*+} production in Pb–Pb collisions at $\sqrt{s_{\mathrm{NN}}}$ = 5.02 TeV“. In: *JHEP* 01 (2022), p. 174. arXiv: `2110.09420 [nucl-ex]` (cit. on pp. 12, 13).

[31] Shreyasi Acharya et al. „Measurement of prompt D_s^+-meson production and azimuthal anisotropy in Pb–Pb collisions at $\sqrt{s_{NN}}$=5.02TeV“. In: *Phys. Lett. B* 827 (2022), p. 136986. arXiv: `2110.10006 [nucl-ex]` (cit. on pp. 12, 13).

[32] Betty Abelev et al. „J/ψ suppression at forward rapidity in Pb-Pb collisions at $\sqrt{s_{NN}} = 2.76$ TeV“. In: *Phys. Rev. Lett.* 109 (2012), p. 072301. arXiv: `1202.1383 [hep-ex]` (cit. on p. 12).

[33] Serguei Chatrchyan et al. „Observation of Sequential Upsilon Suppression in PbPb Collisions“. In: *Phys. Rev. Lett.* 109 (2012). [Erratum: Phys.Rev.Lett. 120, 199903 (2018)], p. 222301. arXiv: `1208.2826 [nucl-ex]` (cit. on p. 12).

[34] Serguei Chatrchyan et al. „Observation and studies of jet quenching in PbPb collisions at nucleon-nucleon center-of-mass energy = 2.76 TeV“. In: *Phys. Rev. C* 84 (2011), p. 024906. arXiv: `1102.1957 [nucl-ex]` (cit. on p. 12).

[35] B. Abelev et al. „Measurement of charged jet suppression in Pb-Pb collisions at $\sqrt{s_{NN}}$ = 2.76 TeV“. In: *JHEP* 03 (2014), p. 013. arXiv: `1311.0633 [nucl-ex]` (cit. on p. 12).

[36] Albert M Sirunyan et al. „Constraints on the Initial State of Pb-Pb Collisions via Measurements of Z-Boson Yields and Azimuthal Anisotropy at $\sqrt{s_{NN}}$=5.02 TeV“. In: *Phys. Rev. Lett.* 127.10 (2021), p. 102002. arXiv: `2103.14089 [hep-ex]` (cit. on p. 13).

[37] Jaroslav Adam et al. „Direct photon production in Pb-Pb collisions at $\sqrt{s_{NN}} = 2.76$ TeV“. In: *Phys. Lett. B* 754 (2016), pp. 235–248. arXiv: `1509.07324 [nucl-ex]` (cit. on p. 13).

[38] Huichao Song, Steffen A Bass, Ulrich Heinz, Tetsufumi Hirano, and Chun Shen. „Erratum: Hadron spectra and elliptic flow for 200 A GeV Au+ Au collisions from viscous hydrodynamics coupled to a Boltzmann cascade [Phys. Rev. C 83, 054910 (2011)]“. In: *Physical Review C* 86.5 (2012), p. 059903 (cit. on p. 14).

[39] Betty Abelev, J Adam, D Adamová, et al. „Pion, kaon, and proton production in central Pb-Pb collisions at$\sqrt{s_{\mathrm{NN}}}$ = 2.76 TeV“. In: *Physical Review Letters* 109.25 (2012), p. 252301 (cit. on p. 14).

[40] Shreyasi Acharya et al. „Production of charged pions, kaons, and (anti-)protons in Pb-Pb and inelastic pp collisions at $\sqrt{s_{NN}}$ = 5.02 TeV“. In: *Phys. Rev. C* 101.4 (2020), p. 044907. arXiv: `1910.07678 [nucl-ex]` (cit. on p. 14).

[41] V. Yu. Naboka, Iu. A. Karpenko, and Yu. M. Sinyukov. „Thermalization, evolution, and observables at energies available at the CERN Large Hadron Collider in an integrated hydrokinetic model of A+A collisions“. In: *Phys. Rev. C* 93.2 (2016), p. 024902. arXiv: `1508.07204 [hep-ph]` (cit. on p. 14).

[42] Gabriel Denicol, Akihiko Monnai, Sangwook Ryu, and Bjoern Schenke. „New insights from 3D simulations of heavy ion collisions“. In: *Nucl. Phys. A* 956 (2016). Ed. by Y. Akiba, S. Esumi, K. Fukushima, et al., pp. 288–291. arXiv: `1512.08231 [nucl-th]` (cit. on p. 14).

[43] Jaroslav Adam et al. „Anisotropic flow of charged particles in Pb-Pb collisions at $\sqrt{s_{\mathrm{NN}}} = 5.02$ TeV“. In: *Phys. Rev. Lett.* 116.13 (2016), p. 132302. arXiv: `1602.01119 [nucl-ex]` (cit. on p. 16).

[44] M. Danysz and J. Pniewski. „Delayed disintegration of a heavy nuclear fragment: I“. In: *The London, Edinburgh, and Dublin Philosophical Magazine and Journal of Science* 44.350 (1953), pp. 348–350 (cit. on pp. 17, 20).

[45] A Bonetti, R Levi Setti, M Panetti, L Scarsi, and G Tomasini. „On the possible ejection of a meson-active triton from a nuclear disintegration“. In: *Il Nuovo Cimento (1943-1954)* 11.2 (1954), pp. 210–212 (cit. on pp. 17, 18).

[46] P. Eckert, P. Achenbach, et al. *Chart of Hypernuclides — Hypernuclear Structure and Decay Data*. hypernuclei.kph.uni-mainz.de. 2021 (cit. on pp. 17, 98, 132, 137).

[47] A. Feliciello and T. Nagae. „Experimental review of hypernuclear physics: recent achievements and future perspectives“. In: *Rept. Prog. Phys.* 78.9 (2015), p. 096301 (cit. on p. 18).

[48] Elena Botta, Tullio Bressani, and Gianni Garbarino. „Strangeness nuclear physics: a critical review on selected topics“. In: *Eur. Phys. J. A* 48 (2012), p. 41. arXiv: `1203.5707 [nucl-ex]` (cit. on p. 18).

[49] Laura Tolos and Laura Fabbietti. „Strangeness in Nuclei and Neutron Stars“. In: *Prog. Part. Nucl. Phys.* 112 (2020), p. 103770. arXiv: `2002.09223 [nucl-ex]` (cit. on p. 19).

[50] V. A. Ambartsumyan and G. S. Saakyan. „The Degenerate Superdense Gas of Elementary Particles“. In: 4 (Oct. 1960), p. 187 (cit. on p. 19).

[51] Shmuel Balberg and Avraham Gal. „An Effective equation of state for dense matter with strangeness“. In: *Nucl. Phys. A* 625 (1997), pp. 435–472. arXiv: `nucl-th/9704013` (cit. on p. 19).

[52] Haris Djapo, Bernd-Jochen Schaefer, and Jochen Wambach. „On the appearance of hyperons in neutron stars“. In: *Phys. Rev. C* 81 (2010), p. 035803. arXiv: `0811.2939 [nucl-th]` (cit. on p. 19).

[53] H. -J. Schulze, A. Polls, A. Ramos, and I. Vidana. „Maximum mass of neutron stars“. In: *Phys. Rev. C* 73 (2006), p. 058801 (cit. on p. 19).

[54] Paul Demorest, Tim Pennucci, Scott Ransom, Mallory Roberts, and Jason Hessels. „Shapiro Delay Measurement of A Two Solar Mass Neutron Star“. In: *Nature* 467 (2010), pp. 1081–1083. arXiv: `1010.5788 [astro-ph.HE]` (cit. on p. 20).

[55] H. T. Cromartie et al. „Relativistic Shapiro delay measurements of an extremely massive millisecond pulsar“. In: *Nature Astron.* 4.1 (2019), pp. 72–76. arXiv: `1904.06759 [astro-ph.HE]` (cit. on p. 20).

[56] Diego Lonardoni, Alessandro Lovato, Stefano Gandolfi, and Francesco Pederiva. „Hyperon Puzzle: Hints from Quantum Monte Carlo Calculations“. In: *Phys. Rev. Lett.* 114.9 (2015), p. 092301. arXiv: `1407.4448 [nucl-th]` (cit. on p. 20).

[57] Domenico Logoteta, Isaac Vidana, and Ignazio Bombaci. „Impact of chiral hyperonic three-body forces on neutron stars“. In: *Eur. Phys. J. A* 55.11 (2019), p. 207. arXiv: `1906.11722 [nucl-th]` (cit. on p. 20).

[58] L. Fabbietti, V. Mantovani Sarti, and O. Vazquez Doce. „Study of the Strong Interaction Among Hadrons with Correlations at the LHC“. In: *Ann. Rev. Nucl. Part. Sci.* 71 (2021), pp. 377–402. arXiv: `2012.09806 [nucl-ex]` (cit. on p. 20).

[59] Alice Collaboration et al. „Unveiling the strong interaction among hadrons at the LHC“. In: *Nature* 588 (2020). [Erratum: Nature 590, E13 (2021)], pp. 232–238. arXiv: `2005.11495 [nucl-ex]` (cit. on p. 20).

[60] H Kamada, J Golak, K Miyagawa, H Witała, and W Glöckle. „π-mesonic decay of the hypertriton“. In: *Physical Review C* 57.4 (1998), p. 1595 (cit. on pp. 20–22, 78, 99, 115, 118).

[61] B. I. Abelev et al. „Observation of an Antimatter Hypernucleus“. In: *Science* 328 (2010), pp. 58–62. arXiv: `1003.2030 [nucl-ex]` (cit. on pp. 20, 24, 97, 99).

[62] A. Pérez-Obiol, D. R. Entem, B. Juliá-Díaz, and A. Parreño. „Non-mesonic weak decay of hypernuclei with effective field theory“. In: *J. Phys. Conf. Ser.* 503 (2014). Ed. by Hannah Petersen, Marco Destefanis, Tetyana Galatyuk, et al., p. 012033 (cit. on p. 21).

[63] Joseph Cohen. „Weak Non-mesonic Decays of Λ Hypernuclei“. In: *Prog. Part. Nucl. Phys.* 25 (1990), pp. 139–234 (cit. on p. 21).

[64] M. Juric et al. „A new determination of the binding-energy values of the light hypernuclei (15>=a)“. In: *Nucl. Phys. B* 52 (1973), pp. 1–30 (cit. on pp. 22, 24, 100).

[65] G. Keyes, M. Derrick, T. Fields, et al. „Properties of ${}_{\Lambda}\mathrm{H}^3$“. In: *Phys. Rev. D* 1 (1970), pp. 66–77 (cit. on pp. 22, 99, 100).

[66] G. Keyes, J. Sacton, J. H. Wickens, and M. M. Block. „A measurement of the lifetime of the (lambda)h-3 hypernucleus“. In: *Nucl. Phys. B* 67 (1973), pp. 269–283 (cit. on p. 22).

[67] R. H. Dalitz, R. C. Herndon, and Y. C. Tang. „Phenomenological study of s-shell hypernuclei with lambda n and lambda n n potentials“. In: *Nucl. Phys. B* 47 (1972), pp. 109–137 (cit. on pp. 22, 100).

[68] J. G. Congleton. „A Simple model of the hypertriton“. In: *J. Phys. G* 18 (1992), pp. 339–357 (cit. on pp. 22, 99).

[69] F. Hildenbrand and H. -W. Hammer. „Three-Body Hypernuclei in Pionless Effective Field Theory“. In: *Phys. Rev. C* 100.3 (2019). [Erratum: Phys.Rev.C 102, 039901 (2020)], p. 034002. arXiv: `1904.05818 [nucl-th]` (cit. on pp. 22, 103, 136).

[70] C. Rappold et al. „Hypernuclear spectroscopy of products from 6Li projectiles on a carbon target at 2 AGeV“. In: *Nucl. Phys. A* 913 (2013), pp. 170–184. arXiv: `1305.4871 [nucl-ex]` (cit. on pp. 22, 99).

[71] L. Adamczyk et al. „Measurement of the ${}^{3}_{\Lambda}\mathrm{H}$ lifetime in Au+Au collisions at the BNL Relativistic Heavy Ion Collider“. In: *Phys. Rev. C* 97.5 (2018), p. 054909. arXiv: `1710.00436 [nucl-ex]` (cit. on pp. 22, 99, 118).

[72] Mohamed Abdallah et al. „Measurements of HΛ3 and HΛ4 Lifetimes and Yields in Au+Au Collisions in the High Baryon Density Region“. In: *Phys. Rev. Lett.* 128.20 (2022), p. 202301. arXiv: `2110.09513 [nucl-ex]` (cit. on pp. 22, 99).

[73] J. Adam et al. „Measurement of the mass difference and the binding energy of the hypertriton and antihypertriton“. In: *Nature Phys.* 16.4 (2020), pp. 409–412. arXiv: `1904.10520 [hep-ex]` (cit. on pp. 22, 24, 100, 102).

[74] Jaroslav Adam et al. „${}^{3}_{\Lambda}\mathrm{H}$ and ${}^{3}_{\bar{\Lambda}}\overline{\mathrm{H}}$ production in Pb-Pb collisions at $\sqrt{s_{\mathrm{NN}}} = 2.76$ TeV“. In: *Phys. Lett. B* 754 (2016), pp. 360–372. arXiv: `1506.08453 [nucl-ex]` (cit. on p. 23).

[75] Shreyasi Acharya et al. „${}^{3}_{\Lambda}\mathrm{H}$ and ${}^{3}_{\bar{\Lambda}}\overline{\mathrm{H}}$ lifetime measurement in Pb-Pb collisions at $\sqrt{s_{\mathrm{NN}}} = 5.02$ TeV via two-body decay“. In: *Phys. Lett. B* 797 (2019), p. 134905. arXiv: `1907.06906 [nucl-ex]` (cit. on pp. 23, 86, 90, 99).

[76] F. Hildenbrand and H. -W. Hammer. „Lifetime of the hypertriton“. In: *Phys. Rev. C* 102 (2020), p. 064002. arXiv: `2007.10122 [nucl-th]` (cit. on pp. 23, 98–100, 135).

[77] A. Pérez-Obiol, D. Gazda, E. Friedman, and A. Gal. „Revisiting the hypertriton lifetime puzzle“. In: *Phys. Lett. B* 811 (2020), p. 135916. arXiv: `2006.16718 [nucl-th]` (cit. on pp. 23, 98–100, 135).

[78] B. Sechi-Zorn, B. Kehoe, J. Twitty, and R. A. Burnstein. „Low-energy lambda-proton elastic scattering“. In: *Phys. Rev.* 175 (1968), pp. 1735–1740 (cit. on pp. 24, 25).

[79] G. Alexander, U. Karshon, A. Shapira, et al. „Study of the lambda-n system in low-energy lambda-p elastic scattering“. In: *Phys. Rev.* 173 (1968), pp. 1452–1460 (cit. on pp. 24, 25).

[80] J. M. Hauptman, J. A. Kadyk, and G. H. Trilling. „Experimental Study of Lambda p and xi0 p Interactions in the Range 1-GeV/c-10-GeV/c“. In: *Nucl. Phys. B* 125 (1977), pp. 29–51 (cit. on pp. 24, 25).

[81] L. Piekenbrock and F. Oppenheimer. „$\Lambda - p$ Elastic Scattering“. In: *Phys. Rev. Lett.* 12 (22 1964), pp. 625–627 (cit. on pp. 24, 25).

[82] Shreyasi Acharya et al. „Exploring the NΛ–NΣ coupled system with high precision correlation techniques at the LHC“. In: *Phys. Lett. B* 833 (2022), p. 137272. arXiv: `2104.04427 [nucl-ex]` (cit. on p. 24).

[83] J. Haidenbauer, U. -G. Meißner, and A. Nogga. „Hyperon–nucleon interaction within chiral effective field theory revisited“. In: *Eur. Phys. J. A* 56.3 (2020), p. 91. arXiv: `1906.11681 [nucl-th]` (cit. on pp. 24, 25, 100).

[84] Enrico Fermi. „High energy nuclear events“. In: *Progress of theoretical physics* 5.4 (1950), pp. 570–583 (cit. on p. 25).

[85] R Hagedorn. „Nuovo Cimento A 56, 1027 (1968)“. In: *Crossref, ISI, ADS* (1968) (cit. on p. 25).

[86] Francesco Becattini. „A Thermodynamical approach to hadron production in e+ e- collisions“. In: *Z. Phys. C* 69.3 (1996), pp. 485–492 (cit. on p. 26).

[87] Peter Braun-Munzinger, Krzysztof Redlich, and Johanna Stachel. „Particle production in heavy ion collisions“. In: (Apr. 2003). Ed. by Rudolph C. Hwa and Xin-Nian Wang, pp. 491–599. arXiv: `nucl-th/0304013` (cit. on p. 26).

[88] „THERMUS–a thermal model package for ROOT“. In: *Computer Physics Communications* 180.1 (2009), pp. 84–106 (cit. on p. 28).

[89] Anton Andronic, Peter Braun-Munzinger, Krzysztof Redlich, and Johanna Stachel. „Decoding the phase structure of QCD via particle production at high energy“. In: *Nature* 561.7723 (2018), pp. 321–330 (cit. on pp. 28, 78).

[90] Giorgio Torrieri, S Jeon, Jean Letessier, and Johann Rafelski. „SHAREv2: fluctuations and a comprehensive treatment of decay feed-down“. In: *Computer physics communications* 175.10 (2006), pp. 635–649 (cit. on p. 28).

[91] Shreyasi Acharya, Dagmar Adamová, Jonatan Adolfsson, et al. „Production of ^{4}He and $^4\bar{He}$ in Pb–Pb collisions at $\sqrt{s_{\mathrm{NN}}}$= 2.76 TeV at the LHC“. In: *Nuclear Physics A* 971 (2018), pp. 1–20 (cit. on p. 28).

[92] Johann Rafelski and Jean Letessier. „Importance of reaction volume in hadronic collisions: Canonical enhancement“. In: *J. Phys. G* 28 (2002). Ed. by J. Tennant, pp. 1819–1832. arXiv: `hep-ph/0112151` (cit. on p. 29).

[93] J. Cleymans, K. Redlich, and E. Suhonen. „Canonical description of strangeness conservation and particle production“. In: *Z. Phys. C* 51 (1991), pp. 137–141 (cit. on p. 29).

[94] F. Becattini and Ulrich W. Heinz. „Thermal hadron production in p p and p anti-p collisions“. In: *Z. Phys. C* 76 (1997). [Erratum: Z.Phys.C 76, 578 (1997)], pp. 269–286. arXiv: `hep-ph/9702274` (cit. on p. 29).

[95] Volodymyr Vovchenko, Benjamin Dönigus, and Horst Stoecker. „Multiplicity dependence of light nuclei production at LHC energies in the canonical statistical model“. In: *Phys. Lett. B* 785 (2018), pp. 171–174. arXiv: `1808.05245 [hep-ph]` (cit. on pp. 29, 30, 33, 103, 118, 120–122, 136).

[96] ST Butler and CA Pearson. „Deuterons from high-energy proton bombardment of matter“. In: *Physical Review* 129.2 (1963), p. 836 (cit. on p. 29).

[97] A Schwarzschild and Č Zupančič. „Production of tritons, deuterons, nucleons, and mesons by 30-GeV protons on A1, Be, and Fe targets“. In: *Physical Review* 129.2 (1963), p. 854 (cit. on p. 30).

[98] Kai-Jia Sun, Che Ming Ko, and Benjamin Dönigus. „Suppression of light nuclei production in collisions of small systems at the Large Hadron Collider“. In: *Phys. Lett. B* 792 (2019), pp. 132–137. arXiv: `1812.05175 [nucl-th]` (cit. on pp. 31, 33, 103, 120–122, 136).

[99] Jaroslav Adam et al. „Production of light nuclei and anti-nuclei in pp and Pb-Pb collisions at energies available at the CERN Large Hadron Collider“. In: *Phys. Rev.* C93.2 (2016), p. 024917. arXiv: `1506.08951 [nucl-ex]` (cit. on p. 32).

[100] Betty Abelev et al. „Centrality dependence of π, K, p production in Pb-Pb collisions at $\sqrt{s_{NN}}$ = 2.76 TeV“. In: *Phys. Rev. C* 88 (2013), p. 044910. arXiv: `1303.0737 [hep-ex]` (cit. on p. 32).

[101] Betty Abelev et al. „Freeze-out radii extracted from three-pion cumulants in pp, p–Pb and Pb–Pb collisions at the LHC“. In: *Phys. Lett. B* 739 (2014), pp. 139–151. arXiv: `1404.1194 [nucl-ex]` (cit. on pp. 33, 103).

[102] J. Adam et al. „Two-pion femtoscopy in p-Pb collisions at $\sqrt{s_{\mathrm{NN}}} = 5.02$ TeV“. In: *Phys. Rev. C* 91 (2015), p. 034906. arXiv: `1502.00559 [nucl-ex]` (cit. on pp. 33, 103).

[103] Fabienne CERN Marcastel. *CERN’s Accelerator Complex*. Tech. rep. 2013 (cit. on p. 36).

[104] Karlheinz Schindl. *The injector chain for the LHC*. Tech. rep. 1999 (cit. on p. 35).

[105] M Benedikt, P Collier, V Mertens, J Poole, and K Schindl. „LHC Design Report, volume III, The LHC injector chain“. In: *CERN, Geneva* (2004) (cit. on p. 35).

[106] D Manglunki, D Kuchler, H Bartosik, et al. „Performance of the CERN Heavy Ion production complex“. In: *Conf. Proc.* Vol. 1205201. CERN-ATS-2012-104. 2012, THPPP012 (cit. on p. 36).

[107] Kenneth Aamodt, A Abrahantes Quintana, R Achenbach, et al. „The ALICE experiment at the CERN LHC“. In: *Journal of Instrumentation* 3.08 (2008), S08002 (cit. on pp. 37, 38).

[108]Alice Collaboration. „Performance of the ALICE Experiment at the CERN LHC“. In: *International Journal of Modern Physics A* 29.24 (2014), p. 1430044 (cit. on pp. 37, 44–48, 60).

[109]K ALICE. „Aamodt et al., JINST 3“. In: *S08002* (2008) (cit. on p. 38).

[110]P Cortese, G Dellacasa, L Ramello, et al. „ALICE: Physics performance report, volume I“. In: *Journal of Physics G: Nuclear and Particle Physics* 30.11 (2004) (cit. on p. 38).

[111]Collaboration Alice, L Bosisio, M Bregant, et al. „ALICE: Physics Performance Report, Volume II“. In: (2006) (cit. on p. 38).

[112]Stefania Beolè, Alice Collaboration, et al. „The ALICE Inner Tracking System: performance with proton and lead beams“. In: *Physics Procedia* 37 (2012), pp. 1062–1069 (cit. on p. 39).

[113]G Dellacasa, X Zhu, M Wahn, et al. *ALICE technical design report of the inner tracking system (ITS)*. Tech. rep. 1999 (cit. on p. 39).

[114]ALICE collaboration et al. „Performance of the ALICE VZERO system“. In: *Journal of Instrumentation* 8.10 (2013), P10016 (cit. on p. 41).

[115]ALICE collaboration et al. „Technical Design Report of the Trigger, Data Acquisition, High Level Trigger and Control System“. In: *CERN, January* (2004) (cit. on p. 42).

[116]Mikolaj Krzewicki, David Rohr, Sergey Gorbunov, et al. „The ALICE high level trigger: Status and plans“. In: *Journal of Physics: Conference Series*. Vol. 664. 8. IOP Publishing. 2015, p. 082023 (cit. on p. 42).

[117]Sergey Gorbunov et al. „ALICE HLT high speed tracking on GPU“. In: *IEEE Trans. Nucl. Sci.* 58 (2011). Ed. by Sascha Marc Schmeling, pp. 1845–1851 (cit. on p. 43).

[118]Yu Belikov, K. Safarik, and B. Batyunya. „Kalman Filtering Application for Track Recognition and Reconstruction in ALICE Tracking System“. In: (1997) (cit. on p. 43).

[119]Shreyasi Acharya et al. „Real-time data processing in the ALICE High Level Trigger at the LHC“. In: *Comput. Phys. Commun.* 242 (2019), pp. 25–48. arXiv: `1812.08036 [physics.ins-det]` (cit. on p. 43).

[120]Rudolf Frühwirth. „Application of Kalman filtering to track and vertex fitting“. In: *Nuclear Instruments and Methods in Physics Research Section A: Accelerators, Spectrometers, Detectors and Associated Equipment* 262.2-3 (1987), pp. 444–450 (cit. on p. 44).

[121]Walter Blum, Werner Riegler, and Luigi Rolandi. *Particle detection with drift chambers*. Springer Science & Business Media, 2008 (cit. on pp. 47, 67).

[122]„Centrality determination in heavy ion collisions“. In: (2018) (cit. on pp. 47, 49).

[123]Rene Brun and Fons Rademakers. „ROOT—an object oriented data analysis framework“. In: *Nuclear Instruments and Methods in Physics Research Section A: Accelerators, Spectrometers, Detectors and Associated Equipment* 389.1-2 (1997), pp. 81–86 (cit. on pp. 49, 102).

[124]Torbjörn Sjöstrand, Stephen Mrenna, and Peter Skands. „PYTHIA 6.4 physics and manual“. In: *Journal of High Energy Physics* 2006.05 (2006), p. 026 (cit. on pp. 50, 125).

[125] Xin-Nian Wang and Miklos Gyulassy. „HIJING: A Monte Carlo model for multiple jet production in pp, pA, and AA collisions“. In: *Physical Review D* 44.11 (1991), p. 3501 (cit. on pp. 50, 62, 105).

[126] Alfredo Ferrari, Paola R Sala, Alberto Fasso, and Johannes Ranft. *FLUKA: A multi-particle transport code (Program version 2005)*. Tech. rep. 2005 (cit. on p. 50).

[127] Rene Brun, L Urban, Federico Carminati, et al. *GEANT: detector description and simulation tool*. Tech. rep. CERN, 1993 (cit. on p. 50).

[128] Sea Agostinelli, John Allison, K al Amako, et al. „GEANT4—a simulation toolkit“. In: *Nuclear instruments and methods in physics research section A: Accelerators, Spectrometers, Detectors and Associated Equipment* 506.3 (2003), pp. 250–303 (cit. on pp. 50, 62, 63, 105).

[129] Jamie Shiers. „The worldwide LHC computing grid (worldwide LCG)“. In: *Computer physics communications* 177.1-2 (2007), pp. 219–223 (cit. on p. 50).

[130] Yaser S Abu-Mostafa, Malik Magdon-Ismail, and Hsuan-Tien Lin. *Learning from data*. Vol. 4. AMLBook New York, NY, USA: 2012 (cit. on p. 51).

[131] Aurélien Géron. *Hands-on machine learning with Scikit-Learn and TensorFlow: concepts, tools, and techniques to build intelligent systems*. " O’Reilly Media, Inc.", 2017 (cit. on pp. 51, 53, 55, 56).

[132] Jin Huang and Charles X Ling. „Using AUC and accuracy in evaluating learning algorithms“. In: *IEEE Transactions on knowledge and Data Engineering* 17.3 (2005), pp. 299–310 (cit. on p. 52).

[133] Fatih Demir. „14 - Deep autoencoder-based automated brain tumor detection from MRI data“. In: *Artificial Intelligence-Based Brain-Computer Interface*. Ed. by Varun Bajaj and G.R. Sinha. Academic Press, 2022, pp. 317–351 (cit. on p. 53).

[134] Alan S. Cornell, Wesley Doorsamy, Benjamin Fuks, Gerhard Harmsen, and Lara Mason. „Boosted decision trees in the era of new physics: a smuon analysis case study“. In: *JHEP* 04 (2022), p. 015. arXiv: `2109.11815 [hep-ph]` (cit. on p. 54).

[135] Wikipedia contributors. *Gradient descent — Wikipedia, The Free Encyclopedia*. [Online; accessed 14-October-2019]. 2019 (cit. on p. 55).

[136] Tianqi Chen, Tong He, Michael Benesty, Vadim Khotilovich, and Yuan Tang. „Xgboost: extreme gradient boosting“. In: *R package version 0.4-2* (2015), pp. 1–4 (cit. on pp. 55, 68, 73).

[137] Jasper Snoek, Hugo Larochelle, and Ryan P Adams. „Practical Bayesian Optimization of Machine Learning Algorithms“. In: *Advances in Neural Information Processing Systems*. Ed. by F. Pereira, C.J. Burges, L. Bottou, and K.Q. Weinberger. Vol. 25. Curran Associates, Inc., 2012 (cit. on p. 56).

[138] Fernando Nogueira. *Bayesian Optimization: Open source constrained global optimization tool for Python*. 2014 (cit. on pp. 56, 109).

[139] Scott M Lundberg, Gabriel Erion, Hugh Chen, et al. „From local explanations to global understanding with explainable AI for trees“. In: *Nature machine intelligence* 2.1 (2020), pp. 56–67 (cit. on p. 58).

[140] Lloyd S Shapley. „A value for n-person games“. In: *Classics in game theory* 69 (1997) (cit. on p. 58).

[141]*Sci-Kit Learn Documentation*. `https://scikit-learn.org/stable/user_guide.html`. Accessed: 2010-09-20 (cit. on p. 58).

[142]„Measurement of the lifetime and Λ separation energy of ${}^{3}_{\Lambda}\mathrm{H}$“. In: (Sept. 2022). arXiv: `2209.07360 [nucl-ex]` (cit. on p. 59).

[143]*Pandas Documentation*. `https://pandas.pydata.org/`. Accessed: 2010-09-20 (cit. on p. 68).

[144]*Uproot Documentation*. `https://github.com/scikit-hep/uproot4`. Accessed: 2010-09-20 (cit. on p. 68).

[145]Luca Barioglio, Fabio Catalano, Matteo Concas, et al. *hipe4ml/hipe4ml*. Version v0.0.14. Apr. 2022 (cit. on p. 69).

[146]„Light (anti)nuclei production in Pb-Pb collisions at $\sqrt{s_{\mathrm{NN}}} = 5.02$ TeV“. In: (Nov. 2022). arXiv: `2211.14015 [nucl-ex]` (cit. on pp. 69, 70, 89).

[147]Jaroslav Adam, Dagmar Adamov, Madan M Aggarwal, et al. „(Anti-)Hypertriton production in Pb-Pb collisions at sNN=5.02 TeV via two-body decay“. In: (2016) (cit. on pp. 75, 99).

[148]Alice Collaboration. „(Anti-)Hypertriton lifetime measurement in Pb–Pb collisions at sNN=5.02 TeV via two-body decay“. In: *Physics Letters B* 797 (2019), p. 134905 (cit. on p. 75).

[149]Wouter Verkerke and David P. Kirkby. „The RooFit toolkit for data modeling“. In: *eConf* C0303241 (2003). Ed. by L. Lyons and Muge Karagoz, MOLT007. arXiv: `physics/0306116` (cit. on pp. 79, 80, 114).

[150]Kyle S. Cranmer. „Kernel estimation in high-energy physics“. In: *Comput. Phys. Commun.* 136 (2001), pp. 198–207. arXiv: `hep-ex/0011057` (cit. on p. 80).

[151]M. V. Evlanov, A. M. Sokolov, V. K. Tartakovsky, S. A. Khorozov, and Yu. Lukstinsh. „Interaction of hypertritons with nuclei at high-energies“. In: *Nucl. Phys. A* 632 (1998), pp. 624–632 (cit. on pp. 84, 115).

[152]Shreyasi Acharya et al. „Measurement of anti-^{3}He nuclei absorption in matter and impact on their propagation in the Galaxy.“ In: (Feb. 2022). arXiv: `2202.01549 [nucl-ex]` (cit. on p. 84).

[153]Peter J. Mohr, David B. Newell, and Barry N. Taylor. „CODATA Recommended Values of the Fundamental Physical Constants: 2014“. In: *Rev. Mod. Phys.* 88.3 (2016), p. 035009. arXiv: `1507.07956 [physics.atom-ph]` (cit. on p. 97).

[154]R. J. Prem and P. H. Steinberg. „Lifetimes of Hypernuclei, ${}_{\Lambda}\mathrm{H}^{3}$, ${}_{\Lambda}\mathrm{H}^{4}$, ${}_{\Lambda}\mathrm{H}^{5}$“. In: *Phys. Rev.* 136 (6B 1964), B1803–B1806 (cit. on p. 99).

[155]G. Keyes, M. Derrick, T. Fields, et al. „New Measurement of the ${}_{\Lambda}\mathrm{H}^{3}$ Lifetime“. In: *Phys. Rev. Lett.* 20 (1968), pp. 819–821 (cit. on p. 99).

[156]R. E. Phillips and J. Schneps. „Lifetimes of light hyperfragments. ii“. In: *Phys. Rev.* 180 (1969), pp. 1307–1318 (cit. on p. 99).

[157]G. Bohm et al. „On the lifetime of the ${}^{3}_{\Lambda}\mathrm{H}$ hypernucleus“. In: *Nucl. Phys. B* 16 (1970). [Erratum: Nucl.Phys.B 16, 523–523 (1970)], pp. 46–52 (cit. on p. 99).

[158]G. Keyes, J. Sacton, J. H. Wickens, and M. M. Block. „A measurement of the lifetime of the ${}^{3}_{\Lambda}\mathrm{H}$ hypernucleus“. In: *Nucl. Phys. B* 67 (1973), pp. 269–283 (cit. on p. 99).

[159] M. Rayet and R. H. Dalitz. „Lifetime of $^3\text{H}_\nu$“. In: *Nuovo Cim. A* 46 (1966), pp. 786–794 (cit. on pp. 99, 100, 135).

[160] H. M. M. Mansour and K. Higgins. „Relativistic treatment of the calculation of binding energy of the triton“. In: *J. Phys. G* 6 (1980), p. 667 (cit. on p. 99).

[161] Y. Prakash, P. H. Steinberg, D. Chandler, and R. J. Prem. „On the binding energies of mesic hypernuclei“. In: *Il Nuovo Cimento (1955-1965)* 21 (1961), pp. 235–248 (cit. on p. 100).

[162] R. G. Ammar, W. Dunn, and M. Holland. „On the Spin and Binding of $^3_\Lambda\text{H}$“. In: (1962) (cit. on p. 100).

[163] C. Mayeur, J. Sacton, P. Vilain, et al. „A determination of the B_Λ values of light hypernucleivalues of light hypernuclei“. In: *Il Nuovo Cimento A (1971-1996)* 43 (1966), pp. 180–192 (cit. on p. 100).

[164] W. Gajewski et al. „A compilation of binding energy values of light hypernuclei“. In: *Nucl. Phys. B* 1 (1967), pp. 105–113 (cit. on p. 100).

[165] G. Bohm et al. „A determination of the binding-energy values of light hypernuclei“. In: *Nucl. Phys. B* 4 (1968), pp. 511–526 (cit. on p. 100).

[166] Diego Lonardoni and Francesco Pederiva. „Medium-mass hypernuclei and the nucleon-isospin dependence of the three-body hyperon-nucleon-nucleon force“. In: (Nov. 2017). arXiv: `1711.07521 [nucl-th]` (cit. on p. 100).

[167] Y. Fujiwara, Y. Suzuki, M. Kohno, and K. Miyagawa. „Addendum: Triton and hypertriton binding energies calculated from SU(6) quark-model baryon-baryon interactions“. In: *Phys. Rev. C* 77 (2008), p. 027001. arXiv: `0710.0047 [nucl-th]` (cit. on p. 100).

[168] Hidekatsu Nemura, Yasuyuki Suzuki, Yoshikazu Fujiwara, and Choki Nakamoto. „Study of light Lambda and Lambda-Lambda hypernuclei with the stochastic variational method and effective Lambda N potentials“. In: *Prog. Theor. Phys.* 103 (2000), pp. 929–958. arXiv: `nucl-th/9912065` (cit. on p. 103).

[169] Francesca Bellini and Alexander Philipp Kalweit. „Testing coalescence and statistical-thermal production scenarios for (anti-)(hyper-)nuclei and exotic QCD objects at LHC energies“. In: *Phys. Rev.* C99.5 (2019), p. 054905. arXiv: `1807.05894 [hep-ph]` (cit. on pp. 103, 136).

[170] Shreyasi Acharya et al. „Hypertriton Production in p-Pb Collisions at $\sqrt{s_{NN}}$=5.02 TeV“. In: *Phys. Rev. Lett.* 128.25 (2022), p. 252003. arXiv: `2107.10627 [nucl-ex]` (cit. on p. 103).

[171] Betty Bezverkhny Abelev et al. „Measurement of visible cross sections in proton-lead collisions at $\sqrt{s_{\text{NN}}} = 5.02$ TeV in van der Meer scans with the ALICE detector“. In: *JINST* 9.11 (2014), P11003. arXiv: `1405.1849 [nucl-ex]` (cit. on p. 103).

[172] Shreyasi Acharya et al. „Production of (anti-)^{3}He and (anti-)^{3}H in p-Pb collisions at $\sqrt{s_{\text{NN}}} = 5.02$ TeV“. In: *Phys. Rev. C* 101.4 (2020), p. 044906. arXiv: `1910.14401 [nucl-ex]` (cit. on pp. 106, 116, 119, 140).

[173] Glen Cowan, Kyle Cranmer, Eilam Gross, and Ofer Vitells. „Asymptotic formulae for likelihood-based tests of new physics“. In: *Eur. Phys. J. C* 71 (2011). [Erratum: Eur.Phys.J.C 73, 2501 (2013)], p. 1554. arXiv: `1007.1727 [physics.data-an]` (cit. on p. 112).

[174] Serguei Chatrchyan et al. „Combined results of searches for the standard model Higgs boson in pp collisions at $\sqrt{s} = 7$ TeV“. In: *Phys. Lett. B* 710 (2012), pp. 26–48. arXiv: `1202.1488 [hep-ex]` (cit. on p. 114).

[175] Volodymyr Vovchenko and Horst Stoecker. „Thermal-FIST: A package for heavy-ion collisions and hadronic equation of state“. In: *Comput. Phys. Commun.* 244 (2019), pp. 295–310. arXiv: `1901.05249 [nucl-th]` (cit. on pp. 119, 132).

[176] S. Zhang, J. H. Chen, H. Crawford, et al. „Searching for onset of deconfinement via hypernuclei and baryon-strangeness correlations“. In: *Phys. Lett. B* 684 (2010), pp. 224–227. arXiv: `0908.3357 [nucl-ex]` (cit. on p. 119).

[177] Betty Abelev et al. „Multiplicity Dependence of Pion, Kaon, Proton and Lambda Production in p-Pb Collisions at $\sqrt{s_{NN}} = 5.02$ TeV“. In: *Phys. Lett. B* 728 (2014), pp. 25–38. arXiv: `1307.6796 [nucl-ex]` (cit. on p. 119).

[178] Betty Bezverkhny Abelev et al. „Multiplicity Dependence of Pion, Kaon, Proton and Lambda Production in p-Pb Collisions at $\sqrt{s_{NN}} = 5.02$ TeV“. In: *Phys. Lett. B* 728 (2014), pp. 25–38. arXiv: `1307.6796 [nucl-ex]` (cit. on p. 119).

[179] Jaroslav Adam et al. „$^{3}_{\Lambda}\mathrm{H}$ and $^{3}_{\bar{\Lambda}}\overline{\mathrm{H}}$ production in Pb-Pb collisions at $\sqrt{s_{\mathrm{NN}}} = 2.76$ TeV“. In: *Phys. Lett. B* 754 (2016), pp. 360–372. arXiv: `1506.08453 [nucl-ex]` (cit. on pp. 120, 121, 136).

[180] Jean Cleymans, Pok Man Lo, Krzysztof Redlich, and Natasha Sharma. „Multiplicity dependence of (multi)strange baryons in the canonical ensemble with phase shift corrections“. In: *Phys. Rev. C* 103.1 (2021), p. 014904. arXiv: `2009.04844 [hep-ph]` (cit. on p. 120).

[181] I. A. Savin et al. „Spin Physics Experiments at NICA-SPD with polarized proton and deuteron beams“. In: *EPJ Web Conf.* 85 (2015). Ed. by Umberto D’Alesio and Francesco Murgia, p. 02039. arXiv: `1408.3959 [hep-ex]` (cit. on p. 123).

[182] Eberhard Widmann. „Low-energy antiprotons physics and the FLAIR facility“. In: *Phys. Scripta T* 166 (2015). Ed. by Peter Egelhof, Yuri Litvinov, and Markus Steck, p. 014074. arXiv: `1502.03687 [physics.ins-det]` (cit. on p. 123).

[183] C. Ahdida et al. „Letter of Intent: the NA60+ experiment“. In: (Dec. 2022). arXiv: `2212.14452 [nucl-ex]` (cit. on pp. 123, 130).

[184] B Abelev et al and (The ALICE Collaboration). „Technical Design Report for the Upgrade of the ALICE Inner Tracking System“. In: *Journal of Physics G: Nuclear and Particle Physics* 41.8 (2014), p. 087002 (cit. on pp. 123, 131).

[185] P. Buncic, M. Krzewicki, and P. Vande Vyvre. „Technical Design Report for the Upgrade of the Online-Offline Computing System“. In: (Apr. 2015) (cit. on p. 125).

[186] A. Andronic, P. Braun-Munzinger, J. Stachel, and H. Stocker. „Production of light nuclei, hypernuclei and their antiparticles in relativistic nuclear collisions“. In: *Phys. Lett. B* 697 (2011), pp. 203–207. arXiv: `1010.2995 [nucl-th]` (cit. on p. 130).

[187] Peter Braun-Munzinger and Benjamin Dönigus. „Loosely-bound objects produced in nuclear collisions at the LHC“. In: *Nucl. Phys. A* 987 (2019), pp. 144–201. arXiv: `1809.04681 [nucl-ex]` (cit. on p. 130).

[188] M. Agnello et al. „New results on Mesonic Weak Decay of p-shell Lambda-Hypernuclei“. In: *Phys. Lett. B* 681 (2009), pp. 139–146. arXiv: `0905.0623 [nucl-ex]` (cit. on p. 131).

[189] Pasi Huovinen and Hannah Petersen. „Particlization in hybrid models“. In: *Eur. Phys. J. A* 48 (2012), p. 171. arXiv: `1206.3371 [nucl-th]` (cit. on p. 132).

[190] E. Hiyama, K. Sasaki, T. Miyamoto, et al. „Possible lightest Ξ Hypernucleus with Modern ΞN Interactions“. In: *Phys. Rev. Lett.* 124.9 (2020), p. 092501. arXiv: `1910.02864 [nucl-th]` (cit. on p. 132).

[191] Ekkard Schnedermann, Josef Sollfrank, and Ulrich Heinz. „Thermal phenomenology of hadrons from 200A GeV S+ S collisions“. In: *Physical Review C* 48.5 (1993), p. 2462 (cit. on p. 139).

[192] Thorsten Renk and Jorg Ruppert. „Dimuon transverse momentum spectra as a tool to characterize the emission region in heavy-ion collisions“. In: *Phys. Rev. C* 77 (2008), p. 024907. arXiv: `hep-ph/0612113` (cit. on p. 140).

[193] S. Damjanovic et al. „NA60 results on the rho spectral function in In-In collisions“. In: *Nucl. Phys. A* 783 (2007). Ed. by P. Jacobs and Xin-Nian Wang, pp. 327–334. arXiv: `nucl-ex/0701015` (cit. on p. 140).

List of Figures

1.1 R ratio as a function of the $\sqrt{s}$ of the collision between electron and positron [7]. The three pads correspond to three different regions of $\sqrt{s}$: the top pad shows the region of the u, d and s quarks resonances, the middle one the region of the c quark resonances and the bottom one the region of the b quark resonances. It is possible to observe how the ratio changes value when new flavours are available. The observed ratio fits with the Quark Model expectations with 3 quarks (green line). The red line shows how the Quark Model predictions are refined taking into account loop corrections in perturbation theory 2

1.2 Quark-gluon interaction vertex 3

1.3 Gluon-gluon interaction vertices 4

1.4 Values of α_s in different experimental conditions [9–12] as a function of the transferred momentum, taken from [13]. The reference value at the energy scale of the Z boson mass $\alpha_s(M_Z)$ has been evaluated using the χ^2 averaging method. 5

1.5 Phase diagram of the QCD matter, taken from [16]. 5

1.6 QCD equation of state [20] as predicted by the Hadron Resonance Gas model and Lattice QCD calculations. 6

1.7 A sketched representation of the heavy-ion collision geometry, taken from [25] 8

1.8 (Left) The total cross section, calculated in the optical approximation and with a Glauber Monte Carlo (MC) both with identical nuclear parameters as a function of σ_{inel}, the inelastic nucleon-nucleon cross section. (Right) N_{coll} and N_{part} as a function of impact parameter, calculated in the optical approximation (lines) and with a Glauber Monte Carlo (symbols). 10

1.9 Evolution of the fireball with from QGP formation to the hadronization phase. 10

1.10 Nuclear modification factor R_{AA} from [30, 31] of prompt D_s^+ mesons (left panel) and non-strange D mesons (right panel) in the 0–10% centrality interval in Pb–Pb collisions at $\sqrt{s_{\mathrm{NN}}} = 5.02$ TeV compared with theoretical calculations based on charm-quark transport in a hydrodynamically expanding QGP. The boxes represent the total systematic uncertainties. The colour bands represent the theoretical uncertainty when available. 13

1.11 Comparison of model calculations with the direct photon spectra in Pb–Pb collisions at $\sqrt{s_{\mathrm{NN}}}$ = 2.76 TeV for the 0–20% (scaled by a factor 100), the 20–40% (scaled by a factor 10) and 40–80% centrality classes. All models include a contribution from pQCD photons. For the 0–20% and 20–40% classes the fit with an exponential function is shown in addition 14

1.12 Transverse momentum distributions of the sum of positive and negative particles (box: systematic errors; statistical errors smaller than the symbol for most data points), fitted individually with a blast wave function, compared to RHIC data and hydrodynamic models. 15

1.13 Anisotropic flow v_n integrated over the p_{T} range 0.2 < p_{T} < 5.0 GeV/ȝ as a function of event centrality. Measurements for Pb–Pb collisions at $\sqrt{s_{\mathrm{NN}}}$ = 5.02 (2.76) TeV are shown by solid (open) markers. The ratios of v_n (green) between Pb–Pb collisions at 5.02 TeV and 2.76 TeV, are shown in the lower panels. Various hydrodynamic calculations are also presented, showing a good agreement with data for low ζ/s values. The statistical and systematical uncertainties are summed in quadrature. 16

2.1 The first observation of the ${}^{3}_{\Lambda}\mathrm{H}$ two-body charged decay channel ${}^{3}_{\Lambda}\mathrm{H} \rightarrow {}^{3}\mathrm{He} + \pi^-$, reported by Bonetti et al. [45]. 18

2.2 Schematic representation of the internal structure of a neutron star, taken from [49]. 19

2.3 Left panel: the equation of state of a NS with hyperons (red) and without hyperons (black). Right panel: the NSs mass as a function of the central baryon number density with hyperons (red) and without hyperons (black). The mass of the Hulse-Taylor pulsar and the observed PSR J1614-2230 [54] and PSR J0348+0432 [55] are shown with horitzontal lines and bands. 20

2.4 Collection of the ${}^{3}_{\Lambda}\mathrm{H}$ lifetime (left) and B_{Λ} (right) measurements obtained with different experimental techniques. The horizontal lines and boxes are the statistical and systematic uncertainties respectively. The dashed-dotted lines are the corresponding theoretical predictions. . . . 23

2.5 Partial decay widths Γ_i in units of the free Λ width Γ_Λ as a function of B_Λ. The experimental values from [64] and [73] are indicated by the shaded light (green) and dark (blue) rectangular areas, respectively. The EFT uncertainties are shown by bands. 24

2.6 Proton-Λ cross sections measured by [78–81] compared with the NLO chiral effective field theory predictions (blue and red bands) [83]. . . . 25

2.7 Thermal model fit to the light-flavoured hadron yields in central Pb–Pb collisions at $\sqrt{s_{\mathrm{NN}}}$ = 2.76 TeV [91], with three different SHM implementations: THERMUS (black line), GSI-Heidelberg (yellow line) and SHARE (blue line). 28

2.8 Predictions for d/p as a function of charged pion multiplicity $\mathrm{d}N_\pi/\mathrm{d}y$ obtained with *Thermal-Fist* package, implemented in [95]. Predictions are reported for $T = 155$ MeV and $V_c = \mathrm{d}V/\mathrm{d}y$ (black solid lines), $T = 155$ MeV and $V_c = 3\ \mathrm{d}V/\mathrm{d}y$ (black dashed lines) and $T = 170$ MeV and $V_c = \mathrm{d}V/\mathrm{d}y$ (blue dash-dotted lines). Experimental points corresponds to the available ALICE measurements at the time of the publication of Ref. [95], from which this picture is taken. 30

2.9 Yield ratios d/p, ^{3}He/p and ^{3}H/^{3}He as a function of charged particle multiplicity. Experimental data are measured in pp collisions at $\sqrt{s}$ = 0.9, 2.76 and 7 TeV [99] and in Pb–Pb collisions at 2.76 [100]. Lines are the predictions of the coalescence model, with theoretical uncertainties on the emission source radius given by the shaded bands. For ^{3}He/p and ^{3}H/^{3}He the magenta and the blue lines correspond to two-body and three-body coalescence, respectively. 32

2.10 Ratio between the p_{T}-integrated yields of (anti)deuterons and protons as a function of multiplicity. The measurements are performed in high-multiplicity pp collisions at $\sqrt{s}$ = 13 TeV, in minimum bias pp collisions at $\sqrt{s}$ = 13 TeV and at $\sqrt{s}$ = 7 TeV, in p–Pb collisions at $\sqrt{s_{\mathrm{NN}}}$ = 5.02 TeV, and in Pb–Pb collisions at $\sqrt{s_{\mathrm{NN}}}$ = 2.76 TeV. Vertical bars and boxes represent statistical and systematic uncertainties, respectively. The two black lines are the theoretical predictions of the Thermal-FIST CSM [95] for two sizes of the correlation volume VC. The green line represents the expectation from the coalescence model [98] 33

2.11 The $^3_\Lambda$H/Λ The expectations for the canonical statistical hadronization(with two different V_c) and coalescence (2-body and 3-body) models. The ALICE measurement in Pb–Pb collisions at $\sqrt{s_{\mathrm{NN}}}$ = 2.76 TeV is also shown. 34

3.1 View of the CERN accelerator complex and the LHC experiments [103] 36

3.2 ALICE integrated luminosity for different trigger configurations. 37

3.3 Schematic view of the ALICE layout. 38

3.4 Layout of the ALICE Inner Tracking System, with three different subdetectors: Silicon Pixel Detector (SPD), Silicon Drift Detector (SDD) and Silicon Strip Detector (SSD). 40

3.5 Layout of the ALICE Time Projection Chamber. 41

3.6 Sketches of V0A (left) and V0C (right) arrays showing their segmentation. Scintillator thicknesses are 2.5 and 2 cm, respectively. The scintillator segments on both sides of the dashed lines are connected to the same photomultiplier tube. 42

3.7 Total HLT TPC data compression ratio in Run 2 on 2017 pp data as a function of the input data size expressed in terms of the number of TPC clusters. 43

3.8 Primary vertex position resolution in pp collision at $\sqrt{s} = 7$ TeV with SPD-tracklets (SPD) and full tracks (TRK) [108]. 44

3.9 TPC reconstruction efficiency as a function of the transverse momentum in pp and Pb–Pb collisions from [108]. 45

3.10 ITS–TPC matching efficiency vs. p_{T} for data and Monte Carlo for pp (left) and Pb–Pb (right) collisions from [108]. 46

3.11 Resolution on the $1/p_{\mathrm{T}}$ parameter as a function of $1/p_{\mathrm{T}}$ in p-Pb collisions. The resolution is reported for $1/p_{\mathrm{T}}$ because this quantity can be extracted directly from the Kalman filter fit. 46

3.12 Specific energy loss as a function of the rigidity (p/z) for different anti-particles in Pb–Pb collisions at $\sqrt{s_{\mathrm{NN}}}$ = 5.02 TeV from [108]. . . . 48

3.13 Distribution of the V0A+V0C amplitude. The centrality percentiles are determined integrating the distribution while the red line represents the Glauber fit. 49

3.14 Centrality resolution for different estimators in the ALICE experiment [122]. 49

4.1 Generic output of a supervised model for a binary classification problem 52

4.2 Table illustrating the definition of TPR and FPR, taken from [133] . . . 53

4.3 Example of a ROC curve taken from [131]. The red dashed line represents the FPR and TPR for a fixed threshold value. 53

4.4 Simple scheme of a decision tree. This example uses the Titanic data set for predicting whether a passenger will survive or not. The model uses 3 features from the data set, namely sex, age and sibsp (number of spouses or children along). The decision tree is drawn upside down with its root at the top. In the image, the text in black represents the test, namely *internal node*, based on which the tree splits into *branches*. The end of the branch that does not split anymore is the decision/*leaf*, in this case, whether the passenger died or survived, represented as red and green text respectively. Since this DT is not a perfect classifier, the DT leaves contain samples from both the classes. Under each leaf node is probability of survival given as a decimal value and the percentage of the samples filtered into each leaf. 55
4.5 Score assignment in the XGBoost BDT: the algorithm tries to determine whether someone will like a hypothetical computer game. The prediction scores of each individual tree are summed up to get the final score. 56
4.6 Schematization of the 5-fold cross-validation procedure 57
4.7 SHAP feature importance for the BDT trained on the adult census income dataset available in the Scikit-learn library [141]. The features are ordered by their mean SHAP value. 58

5.1 Vertex position in the beam direction: selection of the primary vertices within a fiducial region of ± 10 cm. A shift with respect to the nominal interaction point position is observed in all the Run 2 Pb–Pb analyses, due to an offset of the LHC machine. 60
5.2 Primary vertex position in the beam direction: ΔV_z distribution before and after the event selection. 61
5.3 Centrality distribution of the analysed events. 62
5.4 Input p_{T} and ct distributions of the ${}^{3}_{\Lambda}\mathrm{H}$ sample in the MC production. . 63
5.5 Sketch of the ${}^{3}_{\Lambda}\mathrm{H}$ decay topology. 65
5.6 Example of ${}^{3}\mathrm{He}$ TPC signal extraction for $1.68 \leq p/z < 1.72$ GeV/c. . . 66
5.7 Bethe-Bloch ALEPH [121] parametrization applied to the ${}^{3}\mathrm{He}$ TPC signal. 67
5.8 Efficiency of the ${}^{3}_{\Lambda}\mathrm{H}$ reconstruction as a function of the p_{T} and the ct of the ${}^{3}_{\Lambda}\mathrm{H}$ candidates. 68
5.9 Blast Wave distributions from the analysis of the ${}^{3}\mathrm{He}$ production in five centrality classes [146]. These distributions are employed to reweight the p_{T} shape of the ${}^{3}_{\Lambda}\mathrm{H}$ candidates in the MC. 70
5.10 Transverse momentum distribution of the ${}^{3}_{\Lambda}\mathrm{H}$ candidates in the MC sample after the B-W reweighting. 70
5.11 Normalised distribution of the training variables for the signal (from MC) and the background (from real data) samples. 72

5.12 Normalized distribution of the training variables for the LS background and the real data samples. 73

5.13 Linear correlations between the training variables and the $^{3}_{\Lambda}\mathrm{H}$ invariant mass, for signal (left) and background (right) candidates. The colours, from red (fully correlated) to blue (fully anti-correlated), indicate the correlation level. 73

5.14 ROC curves for the training and the test sets for ct between 1 and 2 cm. 74

5.15 Normalized BDT output distributions for the training (shaded area) and test (points with statistical errors) set. The background is reported in blue, the signal in red. 75

5.16 Feature importance for the training set for ct between 1 and 2 cm (top) and 18 and 23 cm (bottom). 76

5.17 Normalized distribution of the BDT output of the real data sample for ct between 1 and 2 cm. 77

5.18 BDT threshold efficiency as a function of the threshold (or score) for ct between 1 and 2 cm. 77

5.19 $2 \leq ct < 4$ cm. Left: expected signal significance × BDT efficiency as a function of the threshold value applied on the BDT output. The light blue region is the confidence interval within 1σ associated to the estimation. Right: invariant mass spectrum for the performance BDT analysis. The signal region counts (red bullets) and the background region counts (blue bullets) are reported with the statistical error. . . . 79

5.20 Invariant mass distribution of the selected MC sample, for ct between 1 and 2 cm with superimposed a KDE and DSCB fitting functions. The KDE is shown in blue, while the DSCB is shown in green. 80

5.21 Distribution of the invariant-mass of the $^{3}_{\Lambda}\mathrm{H}$ and $^{3}_{\Lambda}\overline{\mathrm{H}}$ candidates in nine ct intervals from 1 to 35 cm. The statistical uncertainties of the bin counts are represented with vertical lines. The distribution is fitted with a two-component model; the blue line depicts the overall fit, and the orange dashed line displays the background component. 82

5.22 Distribution of the invariant-mass of the LS candidates in the first ct interval. The statistical uncertainties of the bin counts are represented with vertical lines. 83

5.23 Fraction of $^{3}_{\Lambda}\mathrm{H}$ and $^{3}_{\Lambda}\overline{\mathrm{H}}$ absorbed in the ALICE detector material as a function of the ct. 85

5.24 $^{3}_{\Lambda}\mathrm{H}$ production spectrum as a function of the proper decay length , the blue points represent the measured yield, while the orange line represents the best fit to the measurement. 86

5.25 BDT efficiency as a function of the BDT score parametrized with a spline function, in the ct interval between 2 and 4 cm. 87

5.26 Distribution of the τ value from the exponential fit of the ct spectra obtained by varying the BDT score selection and the signal extraction procedure. The RMS of this distribution is assigned as systematic uncertainty to the final estimation of the ${}^{3}_{\Lambda}\mathrm{H}$ lifetime. 88

5.27 Absorption correction as a function of the proper decay length for ${}^{3}_{\Lambda}\mathrm{H}$, for two different values of the ${}^{3}_{\Lambda}\mathrm{H}$ absorption cross section. 89

5.28 Ratio between the efficiency obtained with the nominal p_{T} shape and the efficiency obtained with the Boltzmann and m T -exponential distributions. 90

5.29 Left panel: signal extraction in the ct interval between 6 and 8 cm obtained by using linear selections. The spectrum is fitted with a DSCB and a linear function to model the signal and the background components, respectively. Right panel: corrected ct spectrum of the ${}^{3}_{\Lambda}\mathrm{H}$ signal fitted with an exponential. 91

5.30 Mean value of the ${}^{3}_{\Lambda}\mathrm{H}$ invariant mass as a function of ct. 92

5.31 Mass shift of the ${}^{3}_{\Lambda}\mathrm{H}$ signal observed in MC as a function of ct. 93

5.32 Measured ${}^{3}_{\Lambda}\mathrm{H}$ mass as a function of ct, fitted with a constant. 94

5.33 Multi-trial ${}^{3}_{\Lambda}\mathrm{H}$ mass distribution. 95

5.34 Left: raw mass of the Λ extracted from the data as a function of the ct. Right: raw mass of the Λ extracted from the MC as a function of the ct. 95

5.35 Corrected mass of the Λ as a function of the ct. 96

5.36 Left: exponential decay spectrum as a function of the proper decay length for ${}^{3}_{\Lambda}\mathrm{H}$, the blue points represent the measured yield, while the orange line represents the best fit to the measurement. Right: B_{Λ} measurement as a function of the proper decay length. Only statistical uncertainties are shown; see the text for a description of the determination of the systematic uncertainties. The fit probability computed with a Pearson test is reported. 98

5.37 Collection of the ${}^{3}_{\Lambda}\mathrm{H}$ lifetime measurements [61, 65, 70–72, 75, 147, 154–158] obtained with different experimental techniques. The horizontal lines and boxes are the statistical and systematic uncertainties, respectively. The dashed and dash-dotted lines are the corresponding theoretical predictions [60, 68, 76, 77, 159, 160]. 99

5.37 Collection of the ${}^{3}_{\Lambda}\mathrm{H}$ B_{Λ} measurements [64, 65, 73, 161–165] obtained with different experimental techniques. The horizontal lines and boxes are the statistical and systematic uncertainties, respectively. The dashed and dash-dotted lines are the corresponding theoretical predictions [67, 83, 166, 167]. 100

5.38 The ${}^{3}_{\Lambda}$H lifetime relative to the free Λ lifetime as a function of the B_{Λ} for pionless EFT [76] (green), χEFT [77] (light blue), and the original π exchange calculations [159] (blue). The red point represents the measurement presented in this work with the statistical and total uncertainties depicted with lines and ellipse, respectively. 100

5.39 Right panel: systematic distribution of the ${}^{3}_{\Lambda}$H lifetime asymmetry ($\tau_{{}^{3}_{\Lambda}\mathrm{H}}$-$\tau_{{}^{3}_{\Lambda}\overline{\mathrm{H}}}$)/$\tau_{{}^{3}_{\Lambda}\mathrm{H}}$. Left panel: statistical uncertainties associated to the different trials and summed in quadrature for ${}^{3}_{\Lambda}$H and ${}^{3}_{\Lambda}\overline{\mathrm{H}}$. 101

5.40 Right panel: systematic distribution of the ${}^{3}_{\Lambda}$H mass asymmetry $(m_{{}^{3}_{\Lambda}\mathrm{H}} - m_{{}^{3}_{\Lambda}\overline{\mathrm{H}}})/m_{{}^{3}_{\Lambda}\mathrm{H}}$. Left panel: statistical uncertainties associated to the different trials and summed in quadrature for ${}^{3}_{\Lambda}$H and ${}^{3}_{\Lambda}\overline{\mathrm{H}}$. 101

5.41 Distribution of the reconstructed ${}^{3}_{\Lambda}$H mass after smearing the ${}^{3}\mathrm{He}$ daughter mass by δ^{STAR} minus the nominal ${}^{3}_{\Lambda}$H mass. 102

6.1 Centrality distribution of the selected events. 104

6.2 Input ct distribution for the ${}^{3}_{\Lambda}$H and ${}^{3}_{\Lambda}\overline{\mathrm{H}}$ in the MC sample. 105

6.3 Reweighted ${}^{3}_{\Lambda}$H p_{T} distribution, together with the ${}^{3}\mathrm{He}$ p_{T} shape from [172]. 106

6.4 Pre-selection efficiency as a function of the ${}^{3}_{\Lambda}$H p_{T}. 107

6.5 Distribution of the training variables for the ${}^{3}_{\Lambda}$H signal and background. 108

6.6 Linear correlations between the training variables and the ${}^{3}_{\Lambda}$H invariant mass, for signal (top) and background (bottom) candidates. The colours, from red (fully correlated) to blue (fully anti-correlated), indicate the correlation level. 108

6.7 Normalized BDT output distributions for the training (shaded area) and test (points with statistical errors) set. The background is reported in blue, the signal in red. 110

6.8 ROC curves for the training and the test sets. 110

6.9 Feature importance computed by using the SHAP algorithm. Features are ordered by decreasing importance. 111

6.10 BDT efficiency as a function of the score threshold, computed on the test set (red markers). A spline function is used to parametrize the efficiency curve (blue line). 111

6.11 Expected significance as a function of the corresponding BDT threshold efficiency, computed assuming thermal production. The significance is multiplied for the BDT efficiency. 112

6.12 Invariant mass spectrum of the selected ${}^{3}_{\Lambda}$H candidates both in the unlike sign pairs (blue) and in the LS background (red). The data points are shown with statistical errors. Entries with zero counts are not shown in the Figure. 113

6.13 Invariant mass distribution of the $^3\mathrm{He} + \pi^-$ and charge conjugate pairs passing the analysis selections. The invariant mass spectrum is fitted with a two component model: the blue line represents the total fit while the orange dashed line shows the background component only. 113

6.14 Local p-values as a function the $^3_\Lambda\mathrm{H}$ invariant mass. The significance is computed by using the one-sided Gaussian tail convention, and it is reported with horizontal dashed lines. 114

6.15 Correction factor 1-f_{abs} as a function of the anti- $^3\mathrm{He}$ inelastic cross-section for the different p_{T} shapes considered in the analysis. The superimposed exponential fits were used to obtain the correction factor for cross sections that are 1.5 times larger than the anti-$^3\mathrm{He}$ inelastic cross section 116

6.16 Distribution of the signal yield obtained by varying the BDT threshold around $\pm5\%$ from the optimal ϵ_{BDT}, and by using three different background functions (constant, linear, exponential). The S/ϵ_{BDT} obtained from the optimal BDT threshold is used as a reference, and it is shown with a vertical dashed red line. 117

6.17 Reconstructed MC sample reshaped according to four different input models. 117

6.18 S_3 measurement in p–Pb (in red) and Pb–Pb collisions [179] (in blue) as a function of mean charged-particle multiplicity. The vertical lines and boxes are the statistical and systematic uncertainties (including the uncertainty on the B.R.), respectively. The expectations for the canonical statistical hadronization [95] and coalescence models are shown [98]. 120

6.19 $^3_\Lambda\mathrm{H}/\Lambda$ measurement in p–Pb (in red) and Pb–Pb collisions [179] (in blue) as a function of mean charged-particle multiplicity. The vertical lines and boxes are the statistical and systematic uncertainties (including the uncertainty on the B.R.), respectively. The expectations for the canonical statistical hadronization [95] and coalescence models are shown [98]. 121

6.20 $^3_\Lambda\mathrm{H}/\Lambda$ times branching ratio as a function of $^3_\Lambda\mathrm{H} \rightarrow {}^3\mathrm{He} + \pi$. The horizontal line is the measured value and the band represents statistical and systematic uncertainties added in quadrature. The expectations for the canonical statistical hadronization [95] and coalescence models are shown [98]. 122

7.1 Schematic view of the ITS2 layout. 124

7.2 Tracking efficiency of the $^3_\Lambda\mathrm{H}$ particle as a function of the decay radius for all ITS $^3_\Lambda\mathrm{H}$ tracks(blue line), pure $^3_\Lambda\mathrm{H}$ tracks (green area), and fake ones (orange area). 125

7.3 Sketch of the ${}^{3}_{\Lambda}\mathrm{H}$ decay into the ITS2 detector. The track is wrongly propagated up to the fifth ITS2 layer and includes the ${}^{3}\mathrm{He}$ daughter cluster. 127
7.4 Invariant mass distribution of the simulated ${}^{3}_{\Lambda}\mathrm{H}$ sample before and after requiring the matching of the ITS track. 128
7.5 Matching algorithm efficiency as a function of the p_{T} (top) and the decay radius (bottom) of the ${}^{3}_{\Lambda}\mathrm{H}$. 129
7.6 Schematic layout of the NA60+ detector, drawn with Geant4 [183]. . . 130
7.7 Expected production of hypernuclei in Pb–Pb collisions as a function of the centre of mass energy according to the SHM. 131
7.8 Invariant mass spectrum of the ${}^{5}_{\Lambda}\mathrm{He}$ reconstructed in NA60+ with a minimal configuration of the vertex spectrometer. 132

8.1 The ${}^{3}_{\Lambda}\mathrm{H}$ lifetime relative to the free Λ lifetime as a function of the B_{Λ} for pionless EFT [76] (green), χEFT [77] (light blue), and the original π exchange calculations [159] (blue). The red point represents the measurement presented in this work with the statistical and total uncertainties depicted with lines and ellipse, respectively. 135
8.2 ${}^{3}_{\Lambda}\mathrm{H}/\Lambda$ measurement in p–Pb (in red), pp (in orange) and Pb–Pb collisions [179] (in blue) as a function of mean charged-particle multiplicity. The vertical lines and boxes are the statistical and systematic uncertainties, respectively. The expectations for the canonical statistical hadronization [95] and coalescence models are shown [98]. 136

List of Tables

2.1 Partial mesonic and non mesonic decay rates of the ${}^{3}_{\Lambda}$H. 22
2.2 $\Gamma({}^{3}_{\Lambda}\mathrm{H} \to {}^{3}\mathrm{He} + \pi^{-})$ (GHz) and $\tau_{{}^{3}_{\Lambda}\mathrm{H}}$ (ps) calculated for several B_{Λ} values (keV), up to B_{Λ} = 410 keV from [77]. 23

3.1 Details about the material budget and spatial resolution of the ITS sub-detectors. 40

5.1 Summary of the event selection applied for to the data sample employed for this analysis. 61
5.2 Track selection criteria. 64
5.3 Topological selections applied at the V^0 level. 66
5.4 Number of signal and background candidates that compose the training set. 71
5.5 Optimized hyper-parameters for the BDT. 74
5.6 BDT threshold and efficiency for each ct bin. 79
5.7 Results of the fit to the ${}^{3}_{\Lambda}$H invariant mass distributions in the nine ct intervals. 81
5.8 Default XGBoost hyper-parameters. 90
5.9 Topological selections applied at the V^0 level. 91
5.10 Summary of the different sources of systematic uncertainty affecting the ${}^{3}_{\Lambda}$H lifetime measurement. 91
5.11 Data driven δ^{Λ} splitted for matter and antimatter and for different magnetic field polarities. 96
5.12 Summary of the different sources of systematic uncertainty affecting the ${}^{3}_{\Lambda}$H mass measurement. 97

6.1 Summary of the event selection applied for to the data sample employed for this analysis. 104
6.2 Optimized BDT hyper-parameters in the p–Pb analysis. 109
6.3 Summary of the different sources of systematic uncertainty affecting the ${}^{3}_{\Lambda}$H yield measurement. 118

7.1 Geometric characteristics of the ITS2 layers. 124

Acknowledgements

I would like to express my gratitude to Massimo Masera, Stefania Beolè and Stefania Bufalino, for their invaluable support, patience, and engaging discussions that consistently improved the quality of my research. I reserve a special acknowledgment for Maximiliano Puccio, whose infinite enthusiasm, passion, and dedication have inspired me since the beginning of my Master thesis. Thanks to all my colleagues, both at the Turin University and at CERN, for the time spent together that contributed to my personal and professional development. Finally, I would like to thank my family and Elena for their constant presence and support throughout this journey.